MONITORING PARTICLE IMPACT ENERGY USING ACOUSTIC EMISSION TECHNIQUE

Mohamad Ghazi Droubi

A dissertation submitted for the degree of Doctor of Philosophy

Heriot-Watt University

School of Engineering and Physical Sciences

April 2013

This copy of the thesis has been supplied on condition that anyone who consults it is understood to recognise that the copyright rests with its author and that no quotation from the thesis and no information derived from it may be published without the prior written consent of the author or of the University (as may be appropriate).

ACADEMIC REGISTRY
Research Thesis Submission

Name*:*	Mohamad Ghazi Droubi		
School/PGI:	School of Engineering and Physical Sciences		
Version: *(i.e. First, Resubmission, Final)*	Final	Degree Sought (Award **and** Subject area)	PhD Mechanical Engineering

Declaration

In accordance with the appropriate regulations I hereby submit my thesis and I declare that:

1) the thesis embodies the results of my own work and has been composed by myself
2) where appropriate, I have made acknowledgement of the work of others and have made reference to work carried out in collaboration with other persons
3) the thesis is the correct version of the thesis for submission and is the same version as any electronic versions submitted*.
4) my thesis for the award referred to, deposited in the Heriot-Watt University Library, should be made available for loan or photocopying and be available via the Institutional Repository, subject to such conditions as the Librarian may require
5) I understand that as a student of the University I am required to abide by the Regulations of the University and to conform to its discipline.

* *Please note that it is the responsibility of the candidate to ensure that the correct version of the thesis is submitted.*

Signature of Candidate*:*		Date:	

Submission

Submitted By *(name in capitals):*	
Signature of Individual Submitting:	
Date Submitted:	

For Completion in Academic Registry

Received in the Academic Registry by *(name in capitals):*			
Method of Submission *(Handed in to Academic Registry; posted through internal/external mail):*			
E-thesis Submitted (mandatory for final theses from January 2009)			
Signature:		Date:	

Abstract

The estimation of energy dissipated during multiple particle impact is a key aspect in evaluating the abrasive potential of particle-laden streams. A systematic investigation of particle impact energy using acoustic emission (AE) measurements is presented in this thesis with experiments carried out over a range of particle sizes, particle densities and configurations. A model of the AE impact time series is developed and validated on sparse streams where there are few particle overlaps and good control over particle kinetic energies. The approach is shown to be robust and extensible to cases where the individual particle energies cannot be distinguished.

For airborne particles, a series of impact tests was carried out over a wide range of particle sizes (from 125 microns to 1500 microns) and incident velocities (from 0.9 ms^{-1} to 16 ms^{-1}). Two parameters, particle diameter and particle impact speed, both of which affect the energy dissipated into the material, were investigated and correlated with AE energy. The results show that AE increases with the third power of particle diameter, i.e. the mass, and with the second power of the velocity, as would be expected. The diameter exponent was only valid up to particle sizes of around 1.5mm, an observation which was attributed to different energy dissipation mechanisms with the higher associated momentum. The velocity exponent, and the general level of the energy were lower for multiple impacts than for single impacts, and this was attributed to particle interactions in the guide tube and/or near the surface leading to an underestimate of the actual impact velocity in magnitude and direction.

In order to develop a model of the stream as the cumulation of individual particle arrival events, the probability distribution of particle impact energy was obtained for a range of particle sizes and impact velocities. Two methods of time series processing were investigated to isolate the individual particles arrivals from the background noise and from particle noise associated with contact of the particles with the target after their first arrival. For the conditions where it was possible to resolve individual impacts, the probability distribution of particle arrival AE energy was determined by the best-fit lognormal probability distribution function. The mean and variance of this function was then calibrated against the known nominal mass and impact speed. A pulse shape function was devised for the target plate by inspection of the records, backed up by pencil lead tests and this, coupled with the energy distribution functions allowed the records to be simulated knowing the arrival rate and the nominal mass and velocity of the particles. A comparison of the AE energy between the recorded and simulated records showed that the principle of accumulating individual particle impact signatures could be applied to records even when the individual impacts could not be resolved.

For particle-laden liquid, a second series of experiments was carried out to investigate the influence of particle size, free stream velocity, particle impact angle, and nominal particle concentration on the amount of energy dissipated in the target using both a slurry impingement erosion test rig and a flow loop test rig. As with airborne particles, the measured AE energy was found overall to be proportional to the incident kinetic energy of the particles. The high arrival rate involved in a slurry jet or real industrial flows poses challenges in resolving individual particle impact signatures in the AE record, hence, and so the model has been further developed and modified (extended) to account for different particle carrier-fluids and to situations where arrivals cannot necessarily be resolved. In combining the fluid mechanics of particles suspended in liquid and the model, this model of AE energy can be used as a semi-quantitative diagnostic indicator for particle impingement in industrial equipments such as pipe bends.

Dedication

I DEDICATE THIS WORK TO:

THE MARTYRS OF THE SYRIAN REVOLUTION

Acknowledgements

This journey would never have begun, or for that matter reached its end, if it was not for the generosity and help of ALLAH, then many organizations and individuals along the way.

All praises and thanks are due to Almighty Allah for providing me this opportunity to complete this work. Acknowledgement is due to Aleppo University, Technical Engineering School for granting me the Research Assistantship to pursue my graduate studies. I express my profound gratitude to Heriot–Watt University, school of Mechanical and Chemical Engineering for providing me with a decent environment to carry out my research.

I would like to express my sincere thanks and gratitude to my thesis supervisors, Professor R L (Bob) Reuben for his valuable supervision, inspiration, constructive suggestions, constant help and guidance throughout the entire period of my research, Professor Graeme White for his valuable comments and helpful discussions. I consider them as my mentors and will continue to seek their guidance in the future.

I am also grateful to all mechanical and electrical technicians in the school of Engineering and Physical Science for their help in designing, manufacturing, running and maintaining all my experimental apparatuses. Thanks are also due to my colleagues, past and present, who made my time very memorable and extremely enjoyable, in particular, Dr. Mohamad El-Shaib, Dr. Faissal, Dr. Angus, Wael, and Dr. Mansour.

Special thanks for all members of the Syrian community (Together For Syria) for their wonderful company throughout the course of my research. Special gratitude goes to Monkiz, Ali, Manhal, and Hassan for motivating me to complete the research with their unlimited support and love.

Finally and most importantly, I am grateful to my parents and all my family members for their constant prayers and support, to my loving wife Ruan…. For your love, support, patience, resilience, and forgiveness, no words will ever express the true extent of my appreciation, to my small angel Sedra…. Who shared this journey with us and beard all my stressful moments.

Table of contents

List of Tables

List of Figures

Nomenclature

δ	Normal displacement (mm)
δ_e, δ_m	Relative approaches at the onset of plastic yielding and at the maximum compression (mm)
ν	Poisson ratio
λ	Tube skin friction coefficient
ρ_p	Density of sphere/particle (kg.m^{-3})
ρ_o	Density of target material (kg.m^{-3})
ρ_f	Density of fluid
ρ_{air}	Density of air
σ_y	Contact yield stress (N.m^{-2})
ε	Deformation wear factor
$\beta\delta$	Dimensionless quantity dependent only on Poisson's ratio ν
α	Dimensionless function of the coefficient of restitution
θ	Impact angle
q	Sin impact angle exponent
β	Particle concentration exponent
ς	Cutting wear factor
	Particle size exponent
τ	Dimensionless parameter describing the tendency of the stream to diverge
η_e	Erosion coefficient
f	Volume fraction of sand in the stream
	kinematic viscosity of the fluid
ζ	Erosion wear after a given time
A_p	Particle projected area
a	Contact area radius (mm)
a_y	Contact area radius at which yield first occurs (mm)
a_m	Maximum contact radius during the impact (mm)
C	Particle concentration
C_d	Drag coefficient
c	Proportion of particles which collide with others before reaching the surface
c_1	Velocity of longitudinal waves (m.s^{-1})

c_2	Velocity of shear waves ($\mathrm{m.s^{-1}}$)
c_0	Velocity of longitudinal waves along a thin rod of the target material ($\mathrm{m.s^{-1}}$)
D	Particle diameter (mm)
d_p	Average particle diameter (mm)
d_{tube}	Internal diameter of the tube (mm)
E	Acoustic emission energy ($\mathrm{V^2.sec}$)
$E^{'}$	Young modulus
E_*	Effective Young modulus
E_r	Erosion rate
	Radial distribution of dimensionless incident energy per particle in a diverging stream with no collisions
	Radial distribution of dimensionless incident energy per particles which do not undergo inter-particle collision
	Radial distribution of dimensionless incident energy per particles which undergo inter-particle collision
e	Coefficient of restitution
F	Compressive normal contact force (N)
F_1	Peak impact force indicated by the Hutchings model
F_0	Maximum force acting on the sphere (N)
F_r, F_i	Contact force after and before impact (N)
g	Gravity ($\mathrm{m^2sec^{-1}}$)
H	Surface hardness
k	Decay constant
l_{tube}	Length of the tube (mm)
M	Total mass of particles (kg)
m	Particle mass (kg)
m_1, m_2	Masses of the tow contacting bodies (kg)
m_*	Effective mass (kg)
n	Velocity exponent
P	Plastic indentation pressure acting during the loading cycle
P_0	Maximum normal pressure at the contact centre ($\mathrm{N.m^{-2}}$)
P_n / ΔP	Pressure drop along the nozzle ($\mathrm{N.m^{-2}}$)
$P(r)$	Distribution of contact pressure within the contact area
$P(\theta)$	the probability density function of particle angles

P_y	Maximum contact pressure at which yield first occurs ($N.m^{-2}$)
P_{my}	Mean contact pressure at which the onset of plastic deformation occurs($N.m^{-2}$)
Q	Total volume removed by cutting wear
R_1, R_2	Radii of the two contacting bodies (mm)
R_*	Effective radius (mm)
r	Distance from the contact centre (mm)
$\overline{r}*$	Average dimensionless radius at which particles which do not collide with others strike the surface
r_1*	Dimensionless radial distance from centre of impacting stream
s	Nozzle-to-surface stand-off distance
T	Duration of elastic contact (s)
T_s	Time between two successive arrivals (s)
T_r	Time between the first arrival and re-arrival of rebounding particle
t	Impact time according to Hutchings' model
U	Air velocity (ms^{-1})
V_1	Normal component of particle impact velocity (ms^{-1})
V_2	Parallel component of particle impact velocity (ms^{-1})
V_{re}	Relative velocity between the two contacting bodies ($m.s^{-1}$)
V_y	Impact velocity below which the interaction behaviour can be assumed to be elastic ($m.s^{-1}$)
V/V_i	Impact/incident velocity ($m.s^{-1}$)
V_r	Rebound velocity ($m.s^{-1}$)
V_p	Particle impact velocity ($m.s^{-1}$)
V_j	Jet velocity ($m.s^{-1}$)
W	Total elastic energy
W_D	Material loss due to plastic deformation
W_C	Material loss due to cutting deformation
W_{tot}	Total material loss
Y	Yield stress ($N.m^{-2}$)
KE_i	Incident kinetic energy (J)
KE_r	Rebound kinetic energy (J)
Re	Reynolds number
CM	Comparative measure
abs	Absolute value

p.d.f	Probability distribution function
AE	Acoustic emission
FFT	Fast Fourier transform
PSD	Power spectrum density

List of publications from this thesis

1. Droubi M G, Reuben R L and White G. *Acoustic emission monitoring of abrasive particle impacts on carbon steel*. Proceedings of the Institution of Mechanical Engineers, Part E. Journal of Process Mechanical Engineering, 2011. **226**: p. 187-204.

2. Droubi M G, Reuben R L and White G. *Statistical distribution models for monitoring acoustic emission (AE) energy of abrasive particle impacts on carbon steel.* Mechanical Systems and Signal Processing, 2012. **30**: p. 356-372.

3. Droubi M G, Reuben R L and White G. *Monitoring acoustic emission (AE) energy in slurry impingement using a new model for particle impact.* Manuscript submitted to Mechanical Systems and Signal Processing.

4. Reuben R L, Abdou W, Cunningham S, Droubi M G, Nashed M S and Thakkar N A. *Processing techniques for dealing with pulsatile AE signals.* Proceedings WCAE, 2011, Beijing, 24-26 August 2011, p. 85-89.

5. Droubi M G, Reuben R L and White G. *Monitoring acoustic emission (AE) energy in flow loop using statistical distribution model for particle impact* (Manuscript in preparation for Mechanical Systems and Signal Processing)

Chapter 1

Introduction

Erosion due to the impact of fluid-suspended solid particles affects many industrial applications, from bulk solids handling, where the fluid is gaseous, to oil production, where the fluid is liquid. Moreover, slurry erosion has been recognized as a serious problem in a range of industrial applications such as slurry transport pipelines, slurry handling systems and hydraulic components, causing thinning of components, surface roughening and degradation, and reduction in functional life. The basic element of material removal is the impact of a hard particle, carried in the fluid stream, with the surface of the target. Therefore, there is a need for monitoring particle impact as a first step in the development of techniques for monitoring erosion in pipes. This work relates to the application of acoustic emission (AE) techniques in condition monitoring of particle impacts. This chapter introduces the background and significance of the work as well as presenting the motivation for the research.

1.1 Background

Material removal (erosion) occurs as a result of interaction between a large number of impacts of particles whose shape can range from spherical to angular, usually carried in pressurized fluid streams, and a steel surface. Several models have been proposed to describe the rate of material removal in terms of the applied conditions [1-9], which can be classified as; impingement-related (particle velocity, particle concentration and impact angle), particle–related (size, shape and density), and material-related (elastic properties, hardness and toughness of both particle and target). A comprehensive review carried out by Meng and Ludema [10] has revealed more than 28 equations for erosion by solid particle impingement involving 33 variables and constants. However, most researchers agree that particle impact velocity, particle size and impact angle are the primary variables affecting erosion rate.

On the empirical side, many researchers have observed that the erosion rate increases with increasing particle size, being proportional to D^{φ}, where φ is the particle size exponent [11-14]. For example, Feng and Ball [13], using silica sand erodent of sizes 63 to 1000 μm impacting a stainless steel target, observed that the value of particle size exponent was approximately 3 ± 0.1. Whereas most authors agree that particle impact velocity has a significant effect on the erosion rate [11, 13, 15], values of velocity exponent reported in the literature vary between 1.1 and 3.4 depending on target material and impingement angle [13]. Levin *et al* [16] investigated the erosion resistance of a number of target materials of different hardness and toughness and concluded that target materials which combine high hardness (which reduces the energy transferred from the incident particle into the target) and high toughness (which reflects the ability of the target material to absorb impact energy without fracture) offer the highest erosion resistance. It is also well established [11, 15, 17, 18] that the effect of impact angle on erosion rate is fundamentally different for ductile target materials than if is for brittle ones, this being dictated by the material removal mechanism.

From a monitoring point of view, it is important to isolate how individual particle impacts give rise to a sensor signal, so that the effects of multiple particle impacts can be properly understood. Therefore, the monitoring of single particle impact is an essential step towards monitoring particle erosion. Because of its very high temporal resolution, Acoustic Emission (AE) has the potential to be a very useful tool in monitoring high particle arrival rates [19-21]. Monitoring of particle impact using acoustic emission relies upon a fraction of the incident kinetic energy of each impacting particle dissipating as elastic waves, which propagate through the target material before being detected by a suitably placed AE sensor. Some of the investigators in this area have concentrated on monitoring the erosion variables [22, 23] and others have concentrated on monitoring the amount of erosion [24, 25].

Thus, although some work has been done on correlating AE signals with the variables known to affect erosion and, to an extent, with wear rate, these correlations have not, so far been linked with established models to offer a general, quantitative approach to predicting the material removal rate using AE. The theoretical analyses described above have not generally been supported by experimental measurements of the energy dissipated due to particle impact. Since the primary cause of erosion is the energy transmitted from impinging particles to the target [26], the main objective of this work is, over a wide range of impact conditions, to develop a way of measuring this energy in a way that can be calibrated against the incident kinetic energy and, consequently, to use AE as a semi-quantitative diagnostic indicator for particle impingement.

1.2 Research methodology and objectives

To the best of the author's knowledge, there is no systematic work on particle impacts using the AE technique which spans the range from individual well-controlled impacts to practical particle-laden flows. Therfore, three experimental arrangements were devised in this work to assess the feasibility of using the AE technique in monitoring particle impacts semi-quantitativelly. Therefore the main research objectives were:

1 Develop a way of measuring AE energy due to particle impact in a way that can be calibrated against the incident kinetic energy.
2 Develop a model describing the AE time series associated with a particle stream, which accumulates the effect of incident particles, is based on observations of individual impacts, and can be extended to situations where the particle arrivals cannot be resolved.
3 Examine, over a wide range of impact conditions, the relationship between measured AE energy and impingement parameters and adjust the model as necessary.
4 Extend the applicability of the model further to situations where no control over particles is possible, and make recommendations on using AE as a semi-quantitative diagnostic indicator for particle impingement.

1.3 Thesis outline

This thesis is structured in 8 chapters, a brief summary of each of which is given below.

Chapter 1: Introduction

This chapter introduces the general background of theoretical and experimental understanding of erosion caused by solid particle impacts and summarises the state of knowledge of AE monitoring of particle impacts. It also outlines the research objectives, the claimed contribution to knowledge and offers a summary of the thesis.

Chapter 2: Literature Review

This chapter presents a critical review of three key research areas related to the thesis. The first is the extent to which the phenomenon of energy dissipation and material damage mechanisms in erosion are understood as a background to what aspects of erosion that might be feasible to monitor using AE. The second area is the state of knowledge on the reproduction of erosion in the laboratory and the key experimental variables that might be used. The last area is to review critically the work that has already been done in monitoring erosion using AE with a view to encompassing and extending it.

Chapter 3: Experimental Method

This chapter describes the solid particle types and target details, the AE measurement system, and all the experimental procedures and arrangements for this study including calibration tests. Three distinct types of experiments are presented the first related to AE monitoring of free-fall and air-assisted particle impacts, the second related to the AE monitoring of slurry impact using a slurry jet impingement rig, and the third related to the AE monitoring of particle impacts in a flow loop bend.

Chapter 4: Experimental Results

This chapter presents the results of the main systematic experiments. First, the results of three experimental arrangements which were used to investigate three dry impact regimes; low velocity-low mass (impact speeds of 1.5 ms^{-1} to 3 ms^{-1} and masses of 4.9×10^{-6} to 2.3×10^{-4} g), low velocity-high mass (sphere masses of 0.001 to 2 g), and high velocity-low mass (impact speeds of 4 to 16 ms^{-1}) are presented. Within each of these regimes, results for both single-particle and multiple-particle impacts are presented. Next, the results of two distinct types of experiments, both of which used water as different particle carrier medium are also presented. The first is the slurry impingement jet experiment and the second is the flow loop experiment.

Chapter 5: AE time series model

This chapter presents the basis of the AE time series model applied to the particle laden airflow. Two time-domain processing techniques used to isolate the individual particle arrivals from the background noise are presented; the dynamic threshold method and the truncated distribution method in order to arrive at a suitable statistical distribution function to represent AE energy per impact in terms of the incident conditions.

A model, developed by the author, for describing the AE time series associated with a particle stream is then presented along with time series simulations, and the findings are discussed in relation to the literature.

Chapter 6: Analysis and Discussion

This chapter analyses and discusses the results presented in Chapter 4 in order to provide an overall interpretation of the measurements of AE energy dissipated in the carbon steel target during particle impacts. The analysis is developed to account for the presence of noise due to fluid impingement, and techniques for separating flow noise from the AE activity of interest are discussed. Again, the findings are discussed with reference to the literature.

Chapter 7: Conclusions and Recommendations for Future Work

This chapter summarises the main findings emerging from the preceding chapters and provides recommendations for practical application and also future studies that could complement and extend the findings of this thesis.

1.4 Contribution to knowledge

The claimed contribution to knowledge centres around a systematic study of AE associated with particle impacts. This study links the AE associated with single particle impacts where the incident conditions are likely controlled through to AE from particle-laden flows with multiple overlapping impacts where the carrier fluid itself generates some AE. At the heart of this integrated approach is a model of the AE time series which, when “calibrated” using single particle impacts, can be applied to cases where the particles can no longer be resolved.

Chapter 2

Literature review

This chapter reviews the literature relevant to the monitoring of fluid-suspended solid particle impacts using AE technology. The review is divided into three main sections. The first section provides a general overview of impact analysis, then focussing on the generation of elastic waves in the impact target. The second section reviews the state of knowledge of erosion phenomena, including the types of apparatus used for erosion testing, empirical studies of the factors affecting erosion rate, and models which have been developed to describe particle erosion. The third section deals with AE techniques, particularly insofar as these have been applied to material removal studies, including particle impact monitoring.

2.1 Impact dynamics and elastic waves

The study of impact is a large area of engineering study, with analytical and numerical models having been developed for a wide range of applications, from ballistics to materials testing. Here, the interest is in isolating those aspects of particle impact which are relevant in generating AE, for which it is sufficient to focus on the contact/impact behaviour of a sphere with a half-space, which exhibits the principal mechanisms of impact.

2.1.1 Hertz theory of elastic contact/impact

The first analysis of the stresses at the contact of two elastic solids was given by Hertz (1896). Johnson [27] has summarised the assumptions made in the Hertz theory as follows,

- the contacting surfaces are continuous and non-conforming, and their profiles are described by quadratic formulae,
- the strains are small,
- each solid can be considered as a linear elastic half-space,

- the surfaces are frictionless and the surface tractions are only induced by normal contact forces, i.e. neither tangential forces nor adhesive forces are considered.

Based on the above assumptions, Hertz obtained an analytical solution for the elastic contact problem, and showed that, as the contact region spreads to a radius a for a given contact force, there is an elliptical distribution of contact pressure within the contact area, given by:

$$P(r) = P_0\left(1-\left(\frac{r}{a}\right)^2\right)^{1/2}, r \le a \qquad (2.1)$$

where P_0 is the maximum normal pressure at the contact centre and r is the distance from the contact centre. This contact pressure generates local elastic deformations and surface displacements and accounts for the compressive contact force F between the two bodies:

$$F = \int_0^a P(r) 2\pi r dr = \frac{2\pi}{3} a^2 P_0$$

Thus,

$$P_0 = \frac{3F}{2\pi a^2} \qquad (2.2)$$

For elastic collisions, it is of interest to know the relationship between contact force and normal displacement, δ. If the two bodies have the same Poisson's ratio and Young's modulus, v and E' the normal displacement induced by the contact pressure at any arbitrary point at a distance r from the contact centre is given by [27],

$$\delta = \frac{1-v^2}{E'} \frac{\pi P_0}{4a} \left(2a^2 - r^2\right)$$

For the more general case where the two bodies have different radii of curvature, R_1 and R_2 and different isotropic elastic properties, E'_1 and E'_2 and ν_1 and ν_2, an effective radius R_* and modulus E_* can be defined as Stronge [28]:

$$\frac{1}{R_*} = \frac{1}{R_1} + \frac{1}{R_2} \tag{2.3}$$

$$\frac{1}{E_*} = \frac{1-\nu_1^2}{E'_1} + \frac{1-\nu_2^2}{E'_2}$$

and the (maximum) normal displacement at the centre of the contact can be related to the maximum pressure by:

$$\delta = \frac{\pi a P_0}{2E_*} \tag{2.4}$$

and the radius of the contact circle by:

$$a = \frac{\pi P_0 R_*}{2E_*} \tag{2.5}$$

Using **Equations 2.2**, **2.4** and **2.5** the relationship between the normal force and the resulting normal displacement can be determined:

$$F = 1.25\delta^{3/2} R_*^{1/2} E_* \tag{2.6}$$

and, using **Equations 2.2** and **2.5** the relationship between the contact area radius and normal force can be obtained:

$$a = \left(\frac{3FR_*}{4E_*} \right)^{1/3} \tag{2.7}$$

When, as is the case for particle contacts, the radius of curvature of the contactor is much smaller than that of the target, the effective radius is simply equal to the particle radius (**Equation 2.3**).

Once a static force-displacement relationship (**Equation 2.6**) has been determined, it is then possible to develop the dynamics of the normal impact of elastic bodies. For instance, the duration of elastic contact between two bodies of masses m_1 and m_2 coming into contact with an initial relative velocity, V_r, has been determined by numerical integration of the relative velocity [27], and using some additional assumptions (over those of Hertz theory) : 1) the deformation is assumed to be restricted to the vicinity of the contact area and to be given by the static theory, 2) elastic wave motion in the bodies is ignored, and 3) the total mass of each body is assumed to be moving with the velocity of its centre of mass at any instant, the contact time is:

(2.8)

where the effective mass is given by: $\frac{1}{m_*} = \frac{1}{m_1} + \frac{1}{m_2}$

Again, if the mass of the target is much greater than the mass of the contacting particle, the effective mass is simply the mass of the particle so that, for the case of a moving elastic sphere contacting a static elastic half-space, **Equation 2.8** becomes:

where, in this case, ρ, R_1, V_p are the density, radius, and velocity of the sphere, respectively. Thus, for normal particle impacts of elastic spheres on a flat, static target the duration of contact might be expected to be proportional to the radius of the sphere and inversely proportional to $V^{1/5}$ [29].

Quoc *et al* [30] applied finite element analysis to the problem of two identical elastic spheres in contact and subject to normal loading. They compared their solutions to the analytical ones for the pressure distribution on the contact area **Equation 2.1**, the relationship between normal force and normal displacement, **Equation 2.6**, and the variation of the radius of the contact area with normal force **Equation 2.7** and found agreement between FEA and Hertz theory for both loading and unloading stages. Hertz theory has been also validated by Tsai [31] who measured the dynamic contact stresses (normal contact stress and radial surface stress) caused by the impact of a projectile on an elastic-half space. These stresses were taken as the sum of the Hertz contact stresses and the effect of stress waves, and compared with those predicted by the Hertz theory in terms of contact time and contact radius. They found that Hertz theory was a good approximation for determining the total force produced by the projectile, while, for the radial surface stress, Hertz theory only applies for moderate impact velocities where the contact time is more than 40 μs.

Generally, the impact period can be divided into compression and restitution phases, where the bodies continue to approach each other and separate, respectively. During elastic compression, the initial kinetic energy is converted into elastic strain energy stored in the contacting bodies and some is converted into propagating elastic waves. Thus, the contact force does work that reduces the initial relative velocity of the colliding bodies and also does work that increases the internal deformation energy of both bodies. Hence the relative velocity reduces to zero during the compression phase at the end of which the maximum compression is reached. During restitution, the stored elastic strain energy is released and accelerates the bodies apart so that the relative velocity increases to a maximum at the end of restitution when the contacting bodies separate. Overall, the contacting bodies rebound with a kinetic energy that is somewhat less than the initial kinetic energy, the remainder, in the case of elastic contacts, being dissipated as stress wave propagation.

2.1.2 Elastic plastic contact

In many contact problems, most notably in hardness testing, the main assumptions of Hertz theory, that of continued elastic deformation of both bodies for the entire duration of contact, no longer holds. Also, aside from the hardest target materials, some plastic deformation in the contact zone is a necessary precursor to wear, so it is important to acknowledge the effect of plastic deformation on contact mechanics and dynamics.

As the contact load increases elastic indentation will continue until some point in the contact region reaches a state of stress satisfying the yield criterion. For the case of axisymmetric contact of two spheres both with $\nu = 0.3$, both the von Mises and Tresca criteria predict that yield occurs when the maximum contact pressure reaches a particular value P_y [27],

$$P_y = 1.6Y$$

where Y is the yield stress. Tabor [32] has expressed this in terms of the mean contact pressure at which the onset of plastic deformation occurs P_{my}:

$$P_{my} = 1.1Y$$

For a sphere of density ρ impacting a plane surface, Thornton [33] defined a "contact yield stress σ_y", using **Equations 2.2** and **2.5**:

$$\sigma_y = \frac{2E_* a_y}{\pi R_*}$$

where a_y, is the contact radius at which yield first occurs, and obtained an expression for the impact velocity below which the interaction behaviour can be assumed to be elastic,

$$V_y = 1.56\left(\frac{\sigma_y^5}{E_*^4 \rho}\right)^{1/2} \qquad (2.9)$$

It might be noted that the impact velocity required to cause yield on metal surfaces is very small; for example, for a hard steel ball impacting a mild steel target, it is about 0.05 m/s [34].

Plastic deformation will occur first in the body of the material with the lower yield stress (Y) at some distance from the centre of the contact surface (see **Figure 2.1a**) and, as the load increases, the plastic zone grows and finally breaks out to the free surface at which point the displaced material is free to escape by plastic flow and the whole of the material around the contact area undergoes plastic deformation (see **Figure 2.1b**) [3].

(a) (b)

Figure 2.1: Plastic deformation process during the compression of a spherical indenter into a plastic solid (a) the onset of plastic deformation, (b) expansion of plastic zone [29]

Thus, the contact deformation process can be divided into three phases [28]:

1. elastic phase, in which the deformations of both contacting bodies are elastic and Hertz theory can be applied,
2. elastic-plastic phase, in which part of the contact is plastic, starting when the mean pressure P_m between the contacting bodies reaches $1.1Y$ and terminating in full plasticity,
3. fully plastic phase, which occurs once the plastic zone reaches the surface and the material surrounding the contact area undergoes plastic deformation.

Generally, plastic deformation starts in one of the two contacting bodies, but, as the contact deformation proceeds and the maximum contact pressure increases it may exceed $1.6Y$ of the other contacting body. Thus, as a result of impact, one or both bodies may be partially or fully plastically deformed around the contact zone.

An analytical solution for the fully plastic contact pressure has been derived by Ishlinsky (see Tabor [32]) using slip-line theory. He showed that the pressure over the contact area is not uniform but is somewhat higher in the centre than at the edge. The mean contact pressure for fully plastic contact P_m was given by to . Based on available numerical analyses at the time and on experimental measurements published in the literature of the spherical indentation of an elastic-plastic half-space, with or without work hardening, Johnson [27] has given a relationship between the mean contact pressure P_m and the yield stress Y for fully plastic contact as $P_m = 2.8Y$. Johnson [27] also observed that P_m is a function of the dimensionless parameter $E_* a / Y R_*$ for a spherical indenter. For an incompressible material indented by a spherical indenter of radius R, the pressure P_m is given by

$$\frac{P_m}{Y} = \frac{2}{3}\left(1 + \ln\left[\frac{E_* a}{3YR_*}\right]\right) \tag{2.10}$$

Figure 2.2 shows how the mean contact pressure increases from $P_m \approx 1.1Y$ (the onset of plastic deformation) to $3Y$ (full plastic deformation) as the size of the contact a/R_* increases, based on the prediction of **Equation 2.10** for spherical indentation. Fully plastic deformation occurs at a value of $E_* a / Y R_*$ = 40, which is about 16 times greater than the value for first yield. For the case of a hard steel sphere pressed into the surface of a fully work-hardened mild steel specimen, Tabor [32] showed that the load increases by a factor of about 300 and the contact radius increases by a factor of about 10 from the onset of plastic deformation until fully plastic deformation, which is consistent with what is described in **Figure 2.2**.

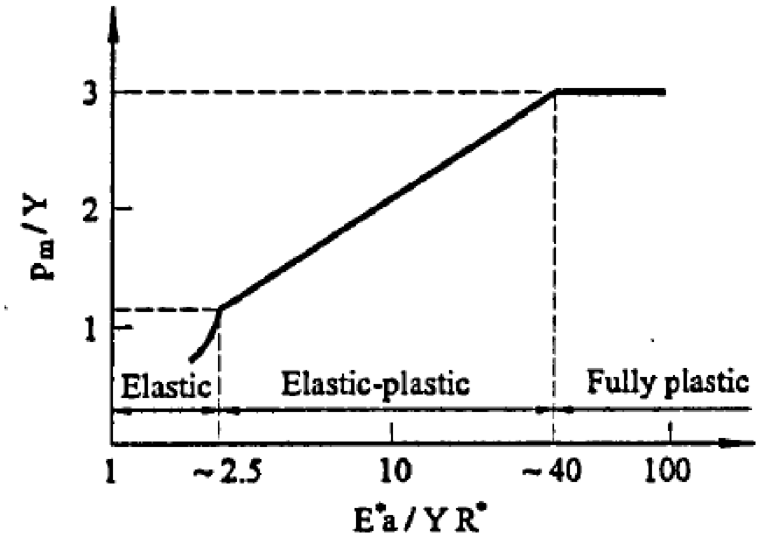

Figure 2.2: Régime diagram for elastic-plastic contact [27]

2.1.3 Contact force-displacement relationships

The relationship between the instantaneous force on the particle F and the penetration of the particle into the substrate δ is fundamental to the impact behaviour of elastic-plastic contacts. This can be approached by determining the contact pressure distribution and the relationship between the relative approach, δ, and the contact radius, a.

For fully plastic contact, it is generally accepted (e.g. Johnson [27] and Tabor [32]) that the mean contact pressure is constant at $(2.8 - 3.0)Y$ as shown in **Figure 2.2** and the relative approach is related to the contact radius by $\delta = a^2 / R_*$ provided that neither piling-up nor sinking-in occurs. Hence, the force-displacement relationship can be determined in the plastic régime.

For the elastic-plastic régime, an accurate determination of the contact pressure distribution and the relationship between relative approach and contact radius becomes more complicated usually requiring some simplifying assumptions. For example, Bitter [2, 3] assumed that, after yield is initiated, the pressure remains constant and the area that is loaded to the constant pressure increases upon further penetration of the particle into the body. A flattened contact pressure distribution, obtained by truncating the Hertzian pressure profile, was proposed by Thornton [33], who also assumed that the Hertzian substitution $a^2 = R_*\delta$ is still valid for the elastic-plastic regime.

Vu-Quoc *et al* [30] developed an elastoplastic normal force-displacement model in which the contact radius is decomposed into an "elastic" part and a "plastic" part, and the contact curvature is modified by an adjustable coefficient to account for plastic deformation. In addition, the pressure distribution is assumed to be of similar pattern to the Hertzian distribution. Yigit and Christoforou [35] combined the classical Hertz theory with the elastic-plastic indentation theory of Johnson [27] to give three force-displacement equations for elastic loading, elastic-plastic loading and elastic unloading as follow:

Elastic loading (Hertz theory):

$$F = 1.25\delta^{3/2}R_*^{1/2}E_*$$

Elastic-plastic loading:

$$F = K_e(\delta - \delta_e) + 1.25\delta^{3/2} R_*^{1/2} E_*$$

Elastic unloading:

$$F = 1.25 E_* R_*^{1/2}(\delta^{3/2} - \delta_m^{3/2} + \delta_e^{3/2}) + K_e(\delta_m - \delta_e)$$

where δ_e and δ_m are the relative approaches at the onset of plastic yielding and at the maximum compression, respectively and K_e is given by: $K_e = 2E_* R_*^{1/2} \delta_e^{1/2}$

2.1.4 Coefficient of restitution

The coefficient of restitution, which is normally used to characterise the change in kinetic energy during an impact, is a useful concept when dealing with monitoring of particle impacts. There are several definitions for the coefficient of restitution [29]:

1. In Newton's definition, the coefficient of restitution *e* is defined as a ratio of the rebound velocity V_r, to the incident velocity V_i. This is usually referred to as Newton's Law of restitution and the ratio as the kinematic coefficient;
2. Poisson defined the coefficient of restitution as the ratio of the impulse during the restitution phase to the impulse during the compression phase of the impact as, ———, where F_r, F_i are the contact forces after and before the impact, respectively. This definition is normally known as Poisson's hypothesis and the ratio as the kinetic coefficient;
3. An energetic coefficient of restitution proposed by Stronge [36] as the ratio of work done by the normal force during the restitution to that during the compression as, ——— .

Using Hertz theory where energy dissipation due to elastic wave motion is neglected and there is no plastic deformation, the incident kinetic energy KE_i can be assumed to be completely converted to elastic strain energy stored in the contact bodies during the compression:

$$KE_i = \frac{1}{2} m V_i^{\,2} = \int_0^{\delta} F d\delta = \frac{8}{15} E_* R_*^{1/2} \delta_m^{\;5/2} = \frac{8}{15} \frac{E_* a_m^5}{R_*^2}$$

where δ_m and a_m are the maximum relative approach and maximum contact radius during the impact.

This elastic strain energy will be recovered and becomes the rebound kinetic energy KE_r, so that, for a sphere striking a fixed target, the rebound velocity, V_r, is the same as the initial impact velocity V_i and the coefficient of restitution is unity. In the more general case, the incident kinetic energy is converted to elastic strain energy stored in the contacting bodies, plastic strain energy to deform the materials plastically (if the stress is high enough anywhere to initiate plastic deformation) and any energy lost by propagation of elastic waves in either body. Only the stored elastic strain energy can be recovered as the rebound kinetic energy, so, at impact velocities greater than the value defined in **Equation 2.9**, some energy is lost due to plastic deformation, and the coefficient of restitution becomes lower and lower as the impact velocity is increased.

Several theoretical models have been developed to predict the coefficient of restitution during the impact of elastic-plastic spheres, in most of which the energy losses due to stress waves are neglected. Starting from a simplified theoretical model for the normal contact interaction of two elastic-perfectly plastic spheres, Thornton [33] developed a theoretical model using a Hertzian pressure distribution with a cut-off pressure, P_y, assumed to be constant during plastic loading, making it possible to obtain an explicit analytical solution for the coefficient of restitution for the case of a sphere impacting a plane surface as follows,

$$e = 1.324 \left(\frac{P_0^5}{E_*^4 \rho} \right)^{1/8} V_i^{-1/4}$$

where V_i is the impact velocity and P_0 is the maximum pressure below which the contact deformation can be considered to be elastic and is defined by **Equation (2.2)**.

Considering only the fully plastic deformation regime, Johnson [27] has assumed that the relative approach is related to the contact radius by $\delta = \frac{a^2}{2R_*}$ (which implies neither "pile-up" nor "sinking in" at the edge of the indentation) as well as taking the mean contact pressure P_m to be constant and equal to $3Y$. Johnson then was able to obtain an expression for the coefficient of restitution for the case of a sphere impacting a wall as:

$$e = 1.718\left(\frac{P_0^5}{E_*^4 \rho}\right)^{1/8} V_i^{-1/4}$$

2.1.5 Elastic wave dissipation during contact/impact

During any impact, the local elastic deformation of the contacting bodies can generate elastic waves that radiate away from the contact region. Elastic waves can propagate within the body of solid materials as either longitudinal (compression) waves or transverse (shear) waves where the particle motion in a longitudinal wave is parallel to the wave propagation direction (**Figure 2.3a**) whereas transverse waves are characterised by particle motion perpendicular to the wave propagation direction, (**Figure 2.3b**). The velocities of both longitudinal waves (c_1) and shear waves (c_2) are frequency independent and are given by the following expressions:

$$c_1 = \sqrt{\frac{E^{'}(1-\nu)}{\rho(1+\nu)(1-2\nu)}}$$

$$c_2 = \sqrt{\frac{E^{'}}{2\rho(1+\nu)}}$$

where $E^{'}$ is Young’s modulus of elasticity for the material, ρ is the density of the material, and ν is Poisson’s Ratio for the material.

For semi-infinite media, a third type of wave can also exist, called Rayleigh waves, (**Figure 2.3c**). These waves propagate over the surface of the medium at a speed a little lower than that of shear waves [27], typically about 0.9 of the shear wave velocity [37].

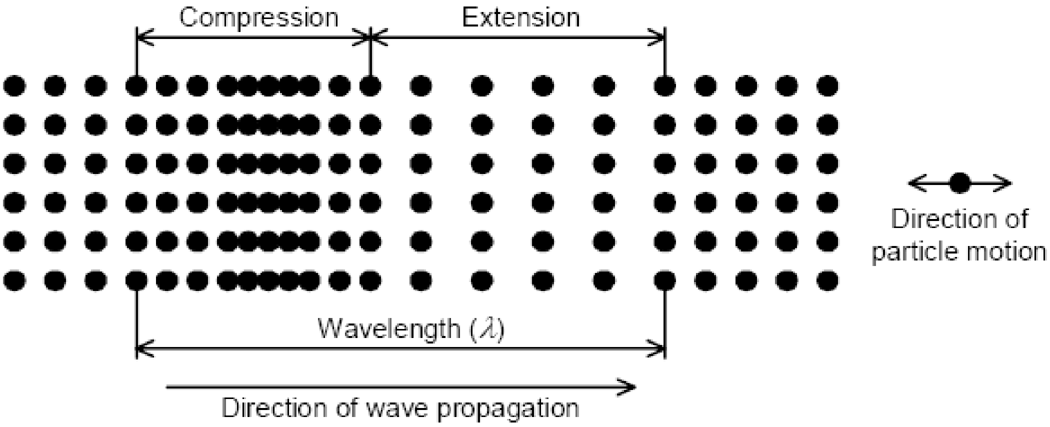

a) Longitudinal wave

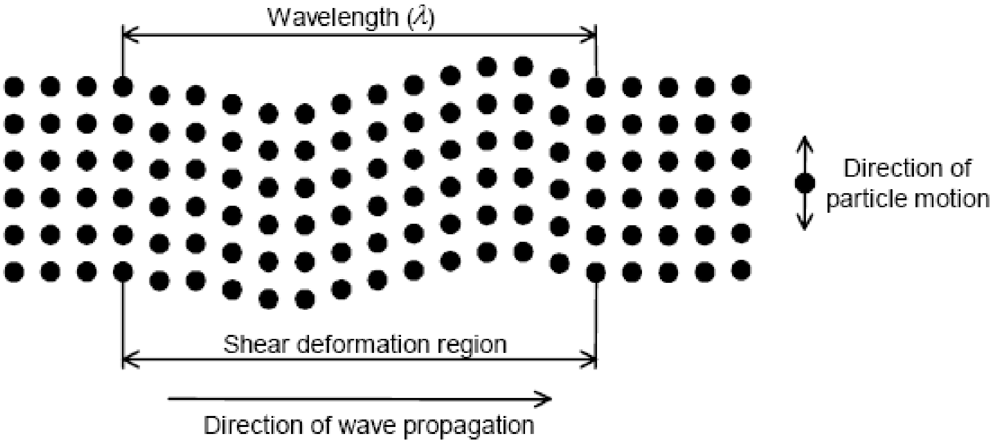

b) Shear wave

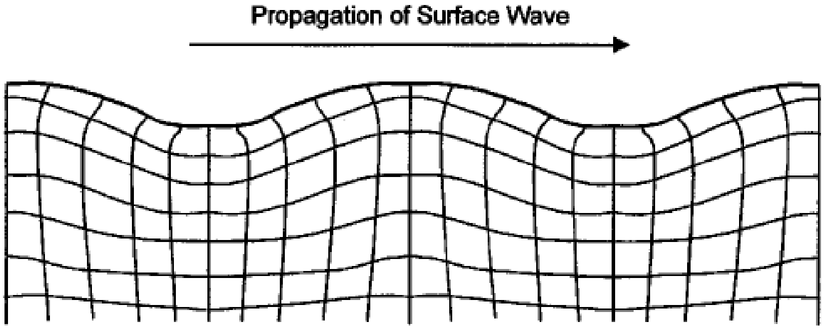

c) Rayleigh wave

Figure 2.3: The main AE waves in infinite and semi-infinite media [37]

In an infinite medium bounded by two surfaces, such as a plate, the waveforms couple at the surfaces to produce more complex propagation modes called Lamb waves. The two basic Lamb wave mode classes are shown in **Figure 2.4**, normally referred to as symmetric (s_0) or extensional and asymmetric (a_0) or flexural wave modes.

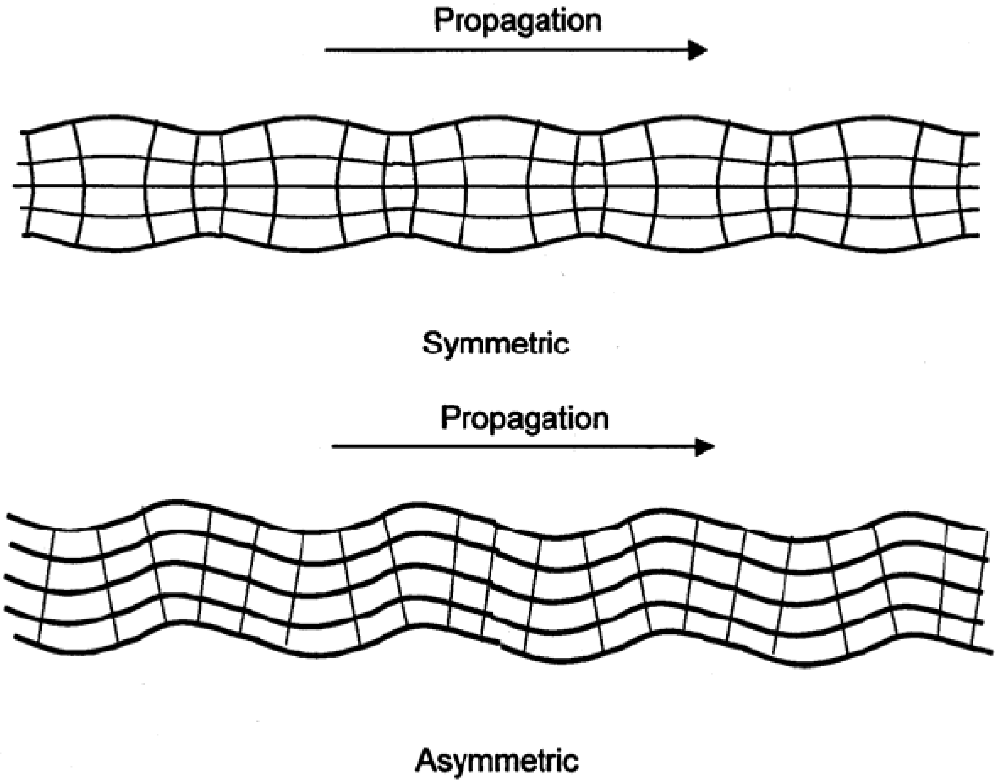

Figure 2.4: Zero-order Lamb wave [37]

In Lamb waves, the particles move in ellipses, and the relative magnitudes of the motion parallel and perpendicular to the plate depend on mode and frequency in a complicated manner.

Elastic waves are only generated if some aspect of the impact takes place at a speed of the order of the wave speed, which is well above the particle arrival speed in most particle impingement situations. However, local plastic deformation, particle fracture and fracture of microscopic components can all contribute to the generation of elastic waves although, in practical situations, these are not very well-conditioned events and can lead to any or all of the above types of waves being generated in either of the contacting bodies.

Hunter [38] calculated the energy contained in elastic waves in terms of the Fourier components of a transient normal force and solved a force-time relationship for the case of purely elastic deformation around an indentation. He estimated the energy converted into elastic waves during normal elastic impact of a hard steel sphere on a steel target to be less than 1% of the incident kinetic energy and found that this total elastic energy, W, can be written in terms of the particle impact velocity, V_p , and the particle diameter, D, as:

$$W = KD^3 V_p^{2.6} \tag{2.11}$$

where K is a constant of proportionality. The same power dependence for both impact velocity and particle diameter, but with a different value of K, was obtained by Reed [39], who estimated the elastic wave energy to be more like 4.5% of the incident kinetic energy using a modified approximation to the force-time relationship for an elastic impact.

It should be noted that both the Hunter and Reed analyses assume elastic impact at right angles to the surface. For impacts at a velocity high enough to cause plastic deformation in the target, the force between the particle and the substrate will not be accurately represented by the Hertz equation and hence the assumptions made above will no longer be valid. To overcome this problem, Hutchings [34] modified Hunter's analysis by assuming a constant plastic pressure to act on the sphere during the loading cycle while making use of Hunter's numerical analysis to predict the force during the unloading cycle and then solving the force-time relationship for the complete cycle. Hutchings made a similar estimate to Reed for the proportion of the original kinetic energy of a sphere dissipated in the elastic wave field (mostly as Rayleigh waves) for normal impacts where some plastic deformation of the target has occurred. The total energy dissipated as elastic waves in the solid was given by Hutchings [34]:

$$W = \beta\delta \frac{F_0^2 w_0 \alpha}{\rho_0 C_0^3} \tag{2.12}$$

where $\beta\delta$ is a dimensionless quantity dependent only on Poisson's ratio ν, ρ_0 is the density of the target material, C_0 is the velocity of longitudinal elastic wave along a thin rod of the target material, α is a dimensionless function of the coefficient of restitution,

e, which was found to be about 1 and F_0 is the maximum force acting on the sphere and can be given by:

$$F_0 = \frac{4}{3}\pi R^2 \rho_p V_p (3P/2\rho_p)^{1/2} \qquad (2.13)$$

where, ρ_p is the density of the sphere, P is the (constant) plastic indentation pressure acting during the loading cycle and w_0 is given by,

$$w_0 = \frac{2(3P/2\rho_p)^{1/2}}{D(1+e)} \qquad (2.14)$$

Substituting **Equations 2.13** and **2.14** into **Equation 2.12,** yields:

$$W = K' \frac{D^3 V_p{}^2}{(1+e)}$$

where K' is again a constant of proportionality. This equation suggests a different dependence of elastic energy on velocity than Hunter or Reed (**Equation 2.11**).

As mentioned above, Hutchings assumed that, during the loading cycle, the force between the sphere and the plane can be represented by a constant pressure acting over the area of contact, while, according to Tabor [40], this pressure varies during collision for two reasons. The first is the dynamic effect associated with the kinetic displacement of the metal during impact which tends to increase the pressure at the initial stages of the deformation when the velocity of displacement is a maximum. The second reason is that work-hardening of the deformed material will occur during the formation of the indentation. As a result, the pressure will tend to increase during impact.

More recently, Wu *et al* [41] have applied FE analysis to the energy dissipation mechanisms during the impact of an elastic sphere with elastic and elastic-perfectly plastic substrates. In this simulation, the number of reflections of the elastic waves during the contact varied with substrate thickness. For elastic impacts where more than one reflection occurs, the results were consistent with Hunter’s earlier finding that the energy converted into elastic waves is less than 1% of the incident, while a significant amount of energy (approximately 6% of the incident) was found to dissipate by this mechanism if there was no reflection at all. For impacts involving plastic deformation, the proportion of the energy dissipated as elastic waves was found to be small compared with that due to plastic deformation.

The foregoing discussion has shown some uncertainties associated with each theoretical model, since all have embedded assumptions that are likely to affect the accuracy of estimating the kinetic energy dissipated as elastic waves through the material. Moreover, the discussion highlights the fact that there is a necessity for some structured observations of elastic wave energy dissipation to compare with the model predictions.

2.2 Erosive wear of materials

Erosive wear is caused by the interaction of solid particles suspended in a gas or liquid stream and a surface which experiences a loss of mass due to successive impacts of hard particles travelling at velocities sufficient to give them a kinetic energy which will damage metallic surfaces [42]. Erosive wear by solid particle impacts can be found in many engineering applications such as pneumatic and hydraulic systems, causing thinning of components, surface roughening and degradation, and reduction in functional life of equipment. For this reason, the subject has received a great deal of attention and a large body of literature exists dealing with solid particle erosion of materials.

2.2.1 Mechanisms of particle erosion

Generally speaking, erosion can arise from mechanical, chemical or thermal actions. The main mechanisms for solid particle erosion are; cutting or abrasive action, fatigue or delamination, brittle fracture, deformation, and melting [12, 13, 43]. Thapa [42] has categorized erosion mechanisms according to the impingement angle and impact velocity into the following:

- Cutting (abrasive) erosion

When particles strike the target at an acute impingement angle (**Figure 2.5a**) and remove material by cutting chips out of the abraded material, the erosion mechanism is called abrasive erosion.

- Surface fatigue (delamination)

When the particles strike the surface with a large impact angle at low velocity as shown in (**Figure 2.5b**), the surface may not be plastically deformed. Even so, contact fatigue can occur leading to cracks being initiated below the surface after repeated collisions. Eventually, the cracks will emerge at the surface, leading to spalling and detachment of particles from the target.

- Brittle fracture

When particles strike a brittle surface with a large impingement angle with medium velocity, erosion takes place by brittle fracture (**Figure. 2.5c**). If the impinging particles are sharp, then brittle fragmentation is more likely and pieces detach from the target following subsurface cracking.

- Plastic deformation

Plastic deformation of the surface can lead to the formation of flakes around the striking point if the particles strike the elastic surface with medium speed and large impingement angle as shown in (**Figure 2.5d**). With repeated strikes on the flakes, the material will detach as debris.

- Melting

When a particle impinges upon the surface of material, it loses some kinetic energy. Most of this lost energy is transformed into plastic energy and then into heat within the target. If this heat is generated sufficiently quickly and within a small enough volume of the target, the temperature can reach the melting point. Consequently, material can be removed more easily due to its much reduced cohesive strength.

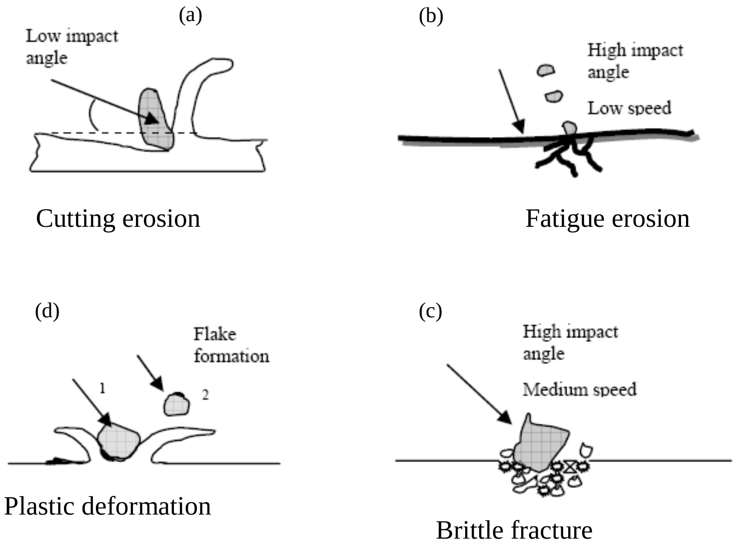

Figure 2.5: Basic mechanisms of particle erosion [42].

It is well known that there is a dramatic difference in impact material removal mechanisms for ductile and brittle materials. Ceramics and other brittle materials are eroded by cracking and chipping, **Figure 2.6**, while ductile materials erode due to mechanisms involving the sequential steps of micro extrusion, forging, and plastic deformation, **Figure 2.7** [1].

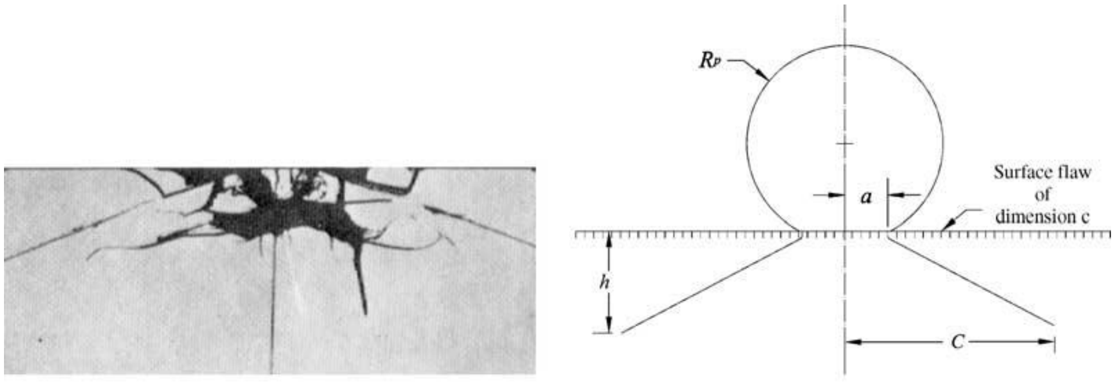

(a) Crater shape (b) Crack propagation

Figure 2.6: Impact material removal mechanism for a brittle material [1]

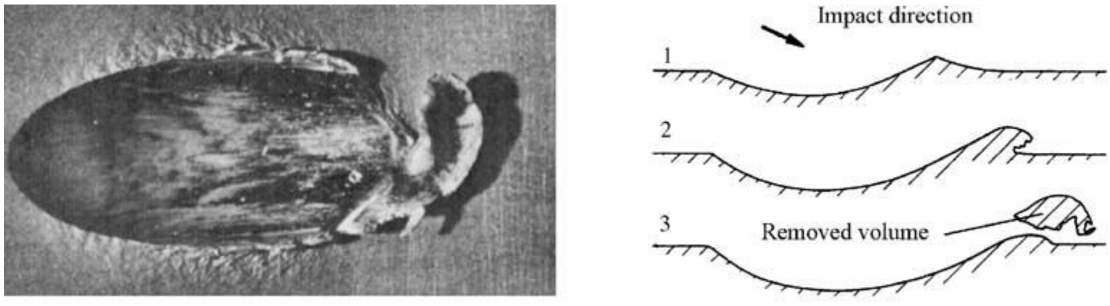

(a) Crater shape (b) Material removal

Figure 2.7: Impact material removal mechanism for a ductile material [1]

Finnie’s seminal paper [4] sets out the basis of our current understanding of material removal mechanisms for ductile and brittle materials. It has been suggested that the particle acts as a miniature machine tool which cuts out a chip of surface material. Bitter [2, 3] has attributed the material removal to the sum of material lost as a result of plastic deformation (where the elastic limit is exceeded, the surface layer is destroyed and its fragments are removed) and that lost due to a cutting mechanism (where the particles strike the body and scratch out some material from the surface). A later review by Finnie [44] presented further understanding of erosion behaviour and traced the history of publications on erosion mechanisms from 1807. He reported a number of different mechanisms that have been proposed for material removal due to impingement at high impact angles, including brittle behaviour brought about by work hardening, fragmentation of particles, low cycle fatigue, temperature effects due to high strain rates, delamination wear, an extrusion mechanism and platelet formation. Finnie also concluded that plastic deformation was believed to be the main erosion mechanism.

Hutchings and his co-workers have provided valuable insights into the different mechanisms of solid particle erosion using both irregular and spherical particles at normal and oblique impingement angles. Hutchings and Winter [45] have shown that, during oblique impact by an individual spherical particle, a lip can be formed from surface material sheared in the direction of motion of the particle and that above a critical velocity, this lip can become detached. This mechanism of material removal was named ploughing deformation, (**Figure 2.8c**).

In another study of erosion by angular particles, Winter and Hutchings [46] identified two distinct modes according to the angle between the leading face of the particle and the target surface. When the leading face of the square particle makes a large angle with the target surface (**Figure 2.8a**), a micro machining action takes place through which a lip is displaced above the surface. When the angle between the particle and the surface is very small (**Figure 2.8b**) ploughing deformation occurs, by which material is forced ahead of the particle and forms a lip at the exit end of the impact crater. Winter and Hutchings believed that both mechanisms are adversely affected if the particle executes a rolling type rotation during its time of contact with the surface rather than sliding along it, because some of the initial particle kinetic energy is lost in the rotation kinetic energy.

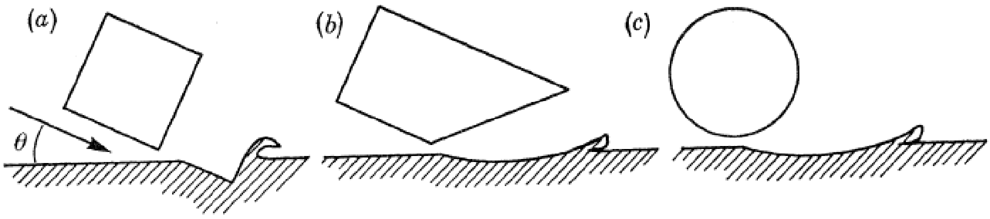

Figure 2.8: Modes of deformation, (a) cutting deformation, (b) ploughing deformation with an angular particle, (c) ploughing deformation with a sphere [7]

Hutchings [5] has divided the cutting deformation mechanism caused by angular particles (modelled as square plates) at oblique impacts into two types according to the rotation direction of the particle after impact. He suggested that, for particles that exhibit a forward rotation, all the metal displaced from the indentation is pushed forward into the large lip at the exit end, which is clearly vulnerable to removal by subsequent impacts. However, for particles that execute a backward rotation, a complete machining action was observed in which a chip of metal was thrown out from the target (see **Figure 2.7**). More recently, Dhar *et al* [47] have identified two primary erosion mechanisms when angular steel particles were launched against a soft aluminium alloy target, ploughing resulting from forward rotating particles and machining resulting from backward rotating particles. The backward rotating particles were not found to machine a chip to complete removal leaving a smooth cut profile (as was found by Hutchings [5]), but, instead, the chip was found to break off prior to completion of the machining action. They explained this apparent contradiction by suggesting that angular particles, in contrast to square particles, tend to tunnel below the surface and then pry themselves out, rather than cut a chip.

For normal incidence, Hutchings *et al* [6] have proposed a platelet mechanism of erosion, whereby the material from which platelets are formed becomes detached from the surface only after many cycles of plastic deformation. Recently, Abouel-Kasem [48] examined the surface morphology of a steel target subjected to silica sand particle impacts at 30^o impingement angle using a whirling arm slurry tester and concluded that the erosion mechanism depends on the particle size, as indentation and material extrusion were observed for particle sizes below 200 µm whereas, for bigger particles, a ploughing mechanism was observed.

Microscopy and other surface techniques can help identify the type of erosion which has occurred as well as reveal valuable information on erosion mechanisms. Albukhaiti *et al* [49] have used scanning electron microscopy, image analysis, optical microscopy as well as gravimetric and microhardness measurements to identify the slurry erosion mechanisms of 1017 steel using a whirling arm slurry test rig. Shallow ploughing and particle rolling was observed at low impact angles then deeper ploughing and microcutting at intermediate angles followed by indentation and material extrusion at higher angles. Ferer *et al* [21] have examined the damaged surfaces impacted by a slurry jet microscopically. Two damage mechanisms, extrusion and forging, were observed where impacts are not sufficient to tear the material at the surface, and no weight loss can be measured. When the impacts are sufficiently energetic for the surface to be removed, the contact time has to be long enough for deformation of the formed flakes to lead to tearing of the material.

Zhang *et al* [25] have investigated the material removal mechanisms in the mechanical erosion of boiler tubes caused by particle impacts. Four regimes with different mechanisms of material removal, according to the particle impact angle, were identified with the aid of scanning electron microscopy. They are; a rubbing and scratching regime when the particle collision angle is below 20°, a cutting and cracking regime when it is between 20° and 30°, a forging and extrusion regime between 30° and 80°, and a sputtering and adhering regime when the angle is beyond 80°, but less than 90°.

2.2.2 Erosion testing

Erosion is a slow process and hence it is costly to be observed from an experimental point of view in practical environments. Consequently, many attempts have been made to construct small-scale rigs to simulate and accelerate material erosion. Since most of the observations and models of erosion mechanisms have been made on such rigs and since the current work will involve simulation of erosion conditions, it is appropriate to review these together here.

2.2.2.1 Erosion testers

For solid-gas flow, two major types of laboratory erosion testers have been widely used to simulate industrial applications. These are the gas-blast erosion testers [13, 16-18, 26, 50-57] and the centrifugal accelerator erosion testers [58, 59]. Gas-blast erosion testers are the subject of an ASTM standard [60]. Other types of erosion testers have been reported from time to time in the literature, for example a gas gun erosion tester [61] and a free-fall test rig [62]. Very recently, Deng *et al* [63] studied the particle dynamics in the centrifugal erosion tester and the gas-blast erosion tester and noted considerable differences in particle acceleration which may lead to significant differences in results under nominally the same conditions.

For solid-liquid (slurry) erosion, there is a wide variety of established test rigs, the most commonly used bench-scale ones being the slurry pot tester [12, 64-69] and the abrasive water jet (jet impingement tester) [20, 21, 70-73]. Nevertheless, many other types of slurry erosion testers have been used, including the Coriolis erosion tester [74] and the whirling arm slurry tester [49].

Centrifugal accelerator erosion testers use the centrifugal force imposed on the particles flowing through radially positioned tubes in a rotating disc to accelerate the particles to the required velocity, as shown in **Figure 2.9**. Targets are arranged around the perimeter of the rotating disc and eroding particles are continuously fed into the central hole of the rotating disc then accelerate in the acceleration tubes to achieve the desired impact velocity upon striking on the targets. The edges and the back sides of the targets are protected in specimen holders in order to prevent erosion in unwanted locations [63].

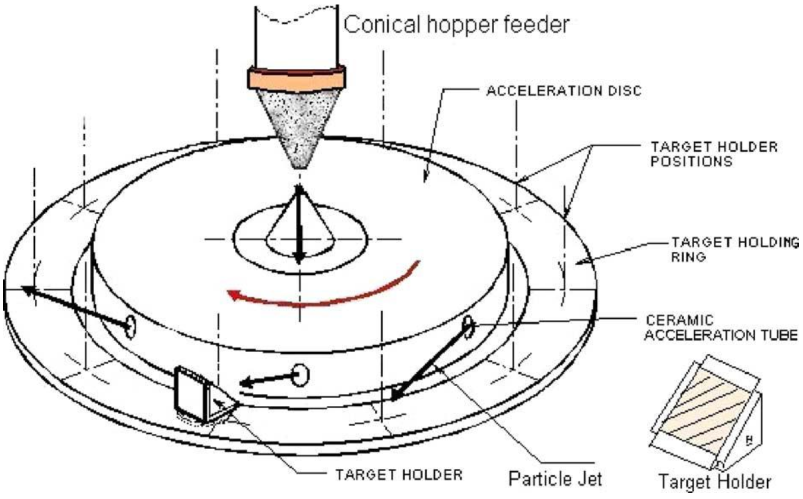

Figure 2.9: Centrifugal accelerator type erosion tester [75]

The principle of the gas blast erosion tester is that pressurized gas is allowed to expand through a narrow bore tube (acceleration tube) hence developing a high-velocity gas flow inside the tube. At the entrance of the tube, a constant feed rate of abrasive solid particles is introduced into the stream. The drag force of the expanding gas accelerates the particles to a desired speed, and then the particles strike a target that is placed at a known distance away from the tube nozzle. The target holder can be rotated relative to the particle jet to achieve a desired impact angle. A schematic diagram of a version used by Shipway and Hutchings [56] to investigate the effect of the acceleration tube internal roughness on the velocity of the erodent particles is shown in **Figure 2.10**. They found that a rough nozzle results in lower erodent velocity and a greater spread of velocities. Due to the influence of the acceleration tube and turbulent air, the particles contained in the acceleration tube do not travel parallel to the nozzle axis. Also, as the pressurized gas expands at the end of the acceleration tube, the particles tend to spread out and this divergence into a particle plume (jet) is attributed to two mechanisms, aerodynamic and particle-particle interaction. Shipway [55] has investigated the jet divergence angle by examining the profile of the wear scars. Although he did not introduce any particle flux distribution or particle velocity distribution in the jet, he suggested that the profile of the wear scar observed can be caused by particles exiting the jet at different angles and possibly at different velocities.

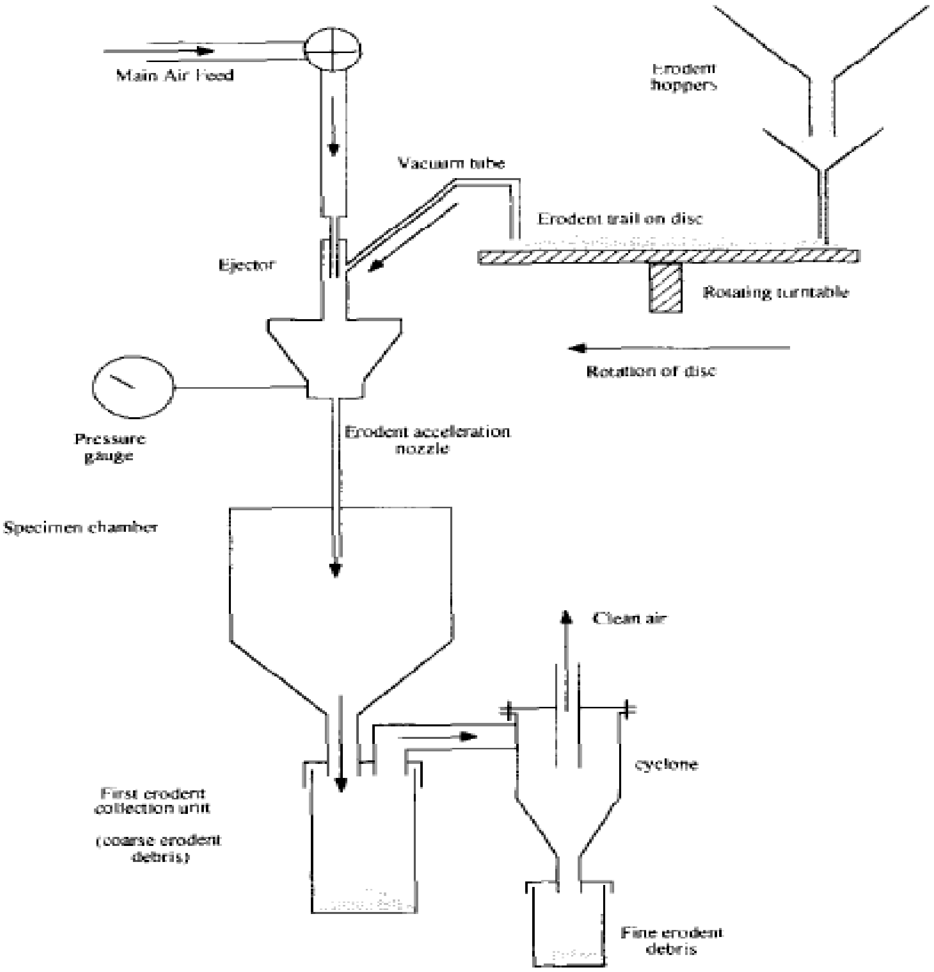

Figure 2.10: The gas-blast type erosion tester [56]

The slurry pot tester relies on the relative motion between the particle-liquid mixture and the specimen. Generally, two cylindrical test specimens are rotated in a pot containing the mixture. One design, by Desale *et al* [66] (see **Figure 2.11**) used a shaft with a mixer propeller inserted from the bottom to ensure a homogenous mixture. Another shaft was inserted from the top incorporating flat arms to hold the specimen inside the pot, this shaft being driven by a variable speed motor to achieve the required relative speed.

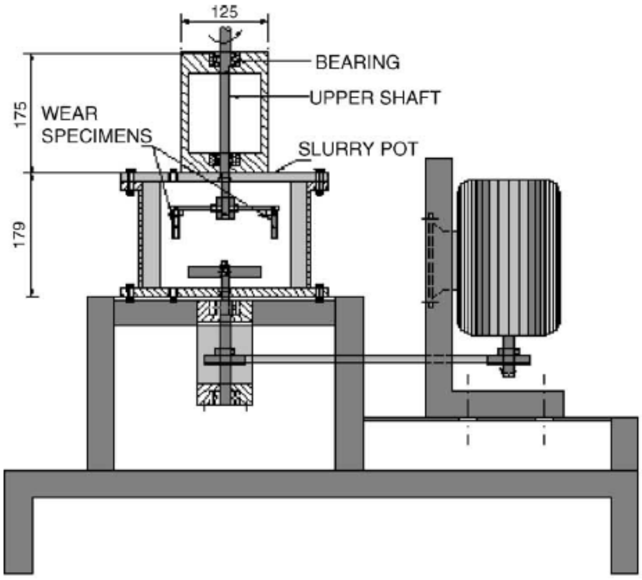

Figure 2.11: Pot tester used for conducting wear studies [66]

The slurry jet impingement tester is popular for research use since it allows fine control over a number of the most important impact parameters. The principle is that a pre-prepared mixture flows through a tank and enters a pump which is used to circulate the mixture through a flow loop. Valves are used to control the flow rate by adjusting the amount of mixture passing through a by-pass line, hence obtaining the desired impact speed. The particles carried by the fluid circulate in the main circuit and then impinge upon a target that is placed at a defined distance from the nozzle inside the erosion chamber. The target can be adjusted to achieve a range of impact angles. A schematic diagram of a version of this type erosion tester used by Ferrer *et al* [21] is shown in **Figure 2.12.**

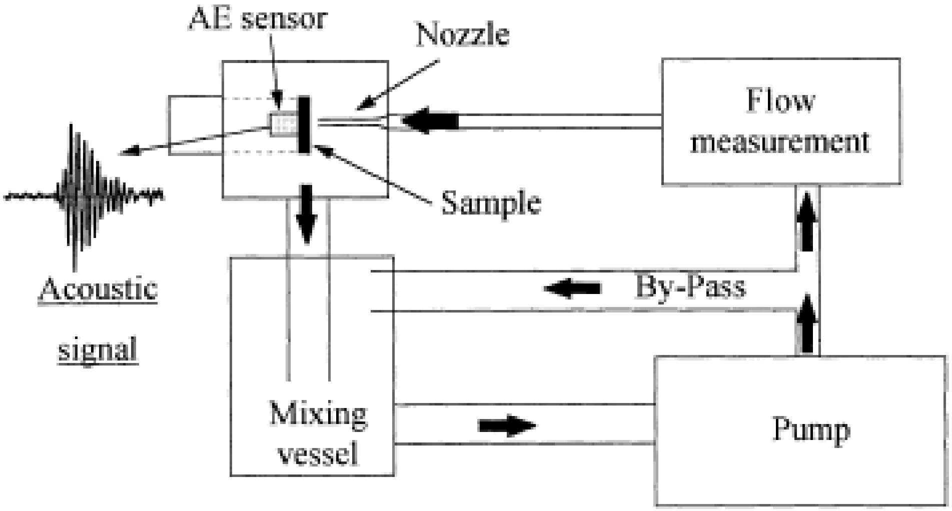

Figure 2.12: Schematic view of the jet impingement tester used by Ferrer *et al* [21]

2.2.3 Empirical observations of factors affecting erosion

Erosive wear is a complex phenomenon due to the many interrelated factors, which act simultaneously and interactively and affect the erosion to a greater or lesser degree. These factors can be split into three categories, those associated with the erosion conditions, those associated with the impacting particles and those associated with the target, as discussed in the following sections. In this context, numerous empirical models [1-9] have been proposed to describe the rate of material removal in terms of parameters which, again, can be classified as; impingement-related (particle velocity, particle concentration and impact angle), particle–related (size, shape and density), and material-related (elastic properties, hardness and toughness of both particle and target). A comprehensive review carried out by Meng and Ludema [10] has revealed more than 28 equations for erosion by solid particle impingement involving 33 variables and constants. However, most researchers agree that particle impact velocity, particle size and impact angle are the primary variables affecting erosion rate.

2.2.3.1 Factors associated with erosion conditions

Among these parameters, impingement angle, particle velocity, and particle concentration play an important role on the material removal process.

The impingement angle is usually defined as the angle between the target material and the trajectory of the impacting particle immediately before the collision [14]. It is well known that impact angle is one of the most significant parameters affecting the erosion behaviour of materials [11, 15, 17, 18]. In the literature, materials are broadly classified into two groups according to their response to their very different dependence of erosion rate on the impingement angle. The group in which plastic deformation predominates and which displays the most severe erosion rate at low impingement angles (between 10° and 30°) is generally known as “ductile material”, while the group in which cutting and fracture dominates and which displays a maximum erosion rate at normal incidence (i.e. 90°) is known as “brittle material”. **Figure 2.13** illustrates schematically the variation in erosion rate with impact angle for a ductile and a brittle material when impacted by silica sand particles. As can be seen, these materials show a very significant difference in both general erosion rate and the effect of impact angle.

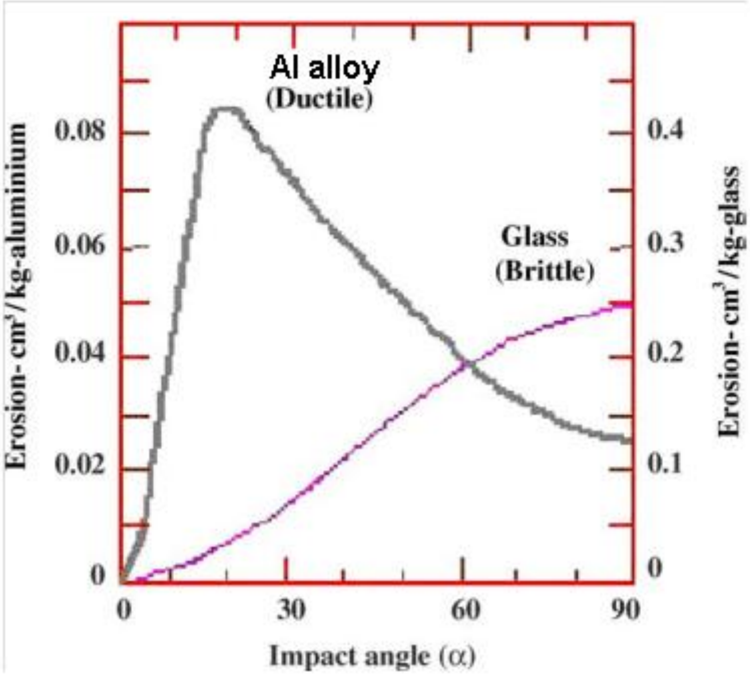

Figure 2.13: Effect of impact angle on erosion for brittle and ductile materials [17]

Al-Bukhaiti *et al* [49] investigated the effect of impact angle on slurry erosion behaviour and mechanisms for two materials, 1017 steel (ductile) and high-Cr white cast iron (brittle), using a constant impingement velocity in a whirling arm slurry test rig. In addition to its well known effect on erosion rate, impact angle was found to influence significantly the erosion mechanism involved. Al-Bukhaiti *et al* concluded that the main erosion mechanisms for 1017 steel could be divided into three regions, according to impact angle (see **Figure 2.14**).

1. Region of small angles, $\Theta<15^o$, where shallow ploughing is the predominant erosion mechanism.
2. Region of intermediate angles, ($15^o<\Theta<70^o$), where deep ploughing and micro cutting are the main erosion mechanisms.
3. Region of high impingement angle, ($70^o<\Theta<90^o$), where indentation and material extrusion are dominant.

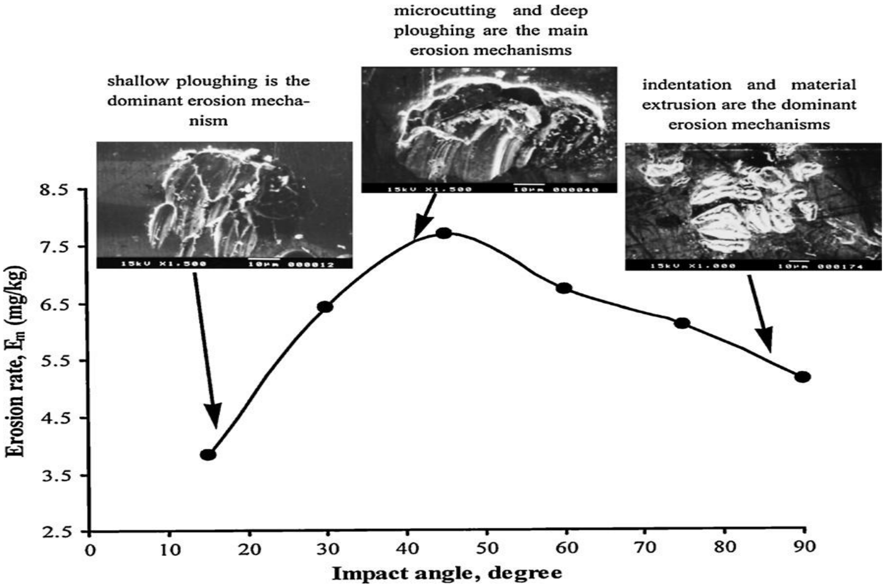

Figure 2.14: Variation of erosion rate and erosion mechanism of 1017 steel (ductile) as a function of impingement angle at impact velocity of 15 m/s [49]

The main erosion mechanisms for high-Cr cast iron could be divided into two regions, (see **Figure 2.15**),

1. Region of low impingement angles, up to 45^o, where ploughing and micro cutting are the main mechanisms of material removal.
2. Region of high impingement angles, from 45^o up to 90^o, involving plastic indentation with extrusion lips and gross fractures and cracking.

Zhang *et al* [25] have investigated the effect of impact angle on the erosion of steel (AISI 1015) under various impact conditions. They reported low wear at very small angles, reaching a maximum between 20^o and 30^o, decreasing steadily until the angle becomes 80°, finally increasing between 80° and 90°.

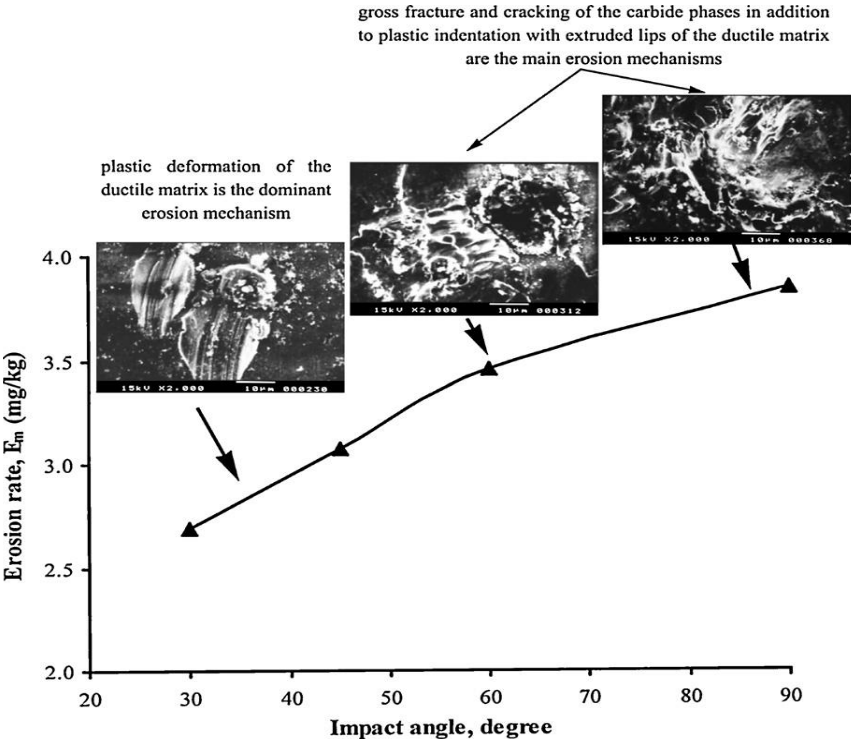

Figure 2.15: Variation of erosion rate and erosion mechanism of high-Cr white cast iron as a function of impingement angle at impact velocity of 15 m/s [49]

The velocity of the erosive particles has a very strong effect on the erosion rate [11, 17, 18, 59]. Erosion occurs only when the impact velocity exceeds a critical value known as the threshold velocity. Yabuki *et al* [43] found this critical velocity to be dependent on the mechanical properties of the erosive particles and the target, as well as on the shape and size of the erodent. For example, they found the threshold velocity to be 2.5 m/s for 0.26 mm silica sand particles impinging on carbon steel. As the velocity increases above the critical velocity, both the cutting and plastic deformation components increase, which amplifies the erosion rate drastically. The modes of erosion also vary depending on the velocity of the particles. At low velocity, the particles do not have enough energy to erode the material by cutting action, but elastic deformation or fatigue effects may be observed [42].

Many investigators e.g. [2, 4, 7, 11, 13, 17, 18, 54, 59, 68] agree that erosive wear rates of materials are strongly dependent on the particle impact velocity and a number have attempted to correlate the erosion rate with particle velocity. For example, Chen *et al* [11] have reported a linear logarithmic relationship between erosion loss and erodent velocity for both ductile and brittle materials. More generally, the dependence is commonly expressed as a power law, in which the erosion rate is proportional to the impact velocity raised to some power n as follows:

$$E_r = kV_p^n$$

where E_r is the erosion rate, k is a constant, V_p is the impact velocity of particles, and n is the velocity exponent. The value of the velocity exponent n varies with target material and erodent particle type and many other operating conditions. In a systematic study carried out by Feng and Ball [13], the erosion of four materials using seven different erodents has shown the velocity exponent to vary in the range of 1.5-2.7 according to the material properties and erodent characteristics. Ghandi *et al* [69] used a slurry pot tester to study the effect of velocity on erosion rate of brass wear pieces at different concentrations and found an n value of 2.56. Oka *et al* [53] have examined the effect of various types of particle on the impact velocity dependence of erosion damage for both ductile and brittle materials. They found the velocity exponent to vary between 2 and 2.9 for (ductile) aluminium alloy, and between 2.1 and 3.1 for (brittle) cast iron material. Harsha and Thakre [18] observed velocity exponents are in the range of 2-2.8 for various polymer composites at different impingement angles (15°-90°) and impact velocities (30-88 ms^{-1}).

Since the impact velocity has such a significant influence on the erosion rate, it is important that its value can be controlled and measured. Accordingly, several methods have been implemented in the literature to measure the particle velocity such as a laser Doppler velocimeter [16], and photographic techniques using a high-speed light source [4].

It is generally agreed that the erosion rate increases with increasing particle concentration within a dilute suspension [25, 59, 69] and then decreases when the concentration rises beyond a critical value. Particle concentration can be defined as the mass (or volume) of particles present in a unit mass (or volume) of fluid, as a fraction or percentage [59, 66, 69].

Desale *et al* [66] reported that the wear rate of aluminium alloy (AA6063) decreases with increasing solid concentration (10-30 wt%) at all impingement angles between 15° and 90°, **Figure 2.16**, attributing this phenomenon to the decrease in collision efficiency due to increased particle interaction at higher concentrations. Deng *et al* [58] have observed a similar effect and again ascribed the reduction in erosion rate to the shielding effect whereby particles act as a defensive barrier, impeding the progress of further particles travelling towards the surface.

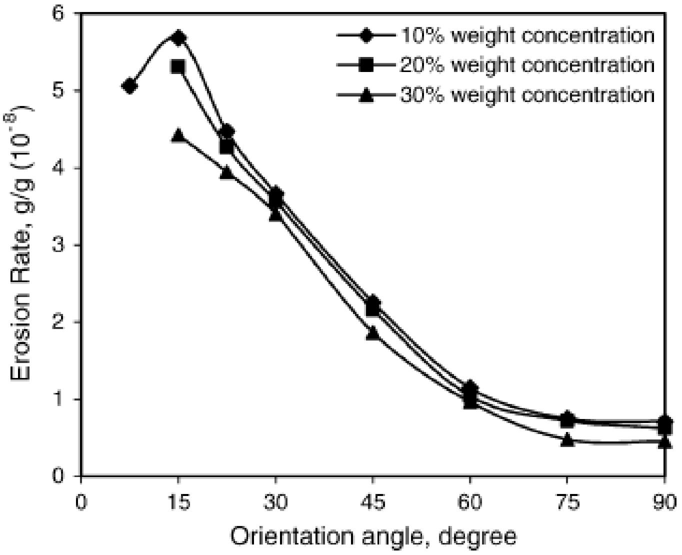

Figure 2.16: Variation of erosion rate for AA6063 material by a narrow size range of particles (550 µm) with impact angle at different concentrations [66]

On the other hand, some researchers e.g. [25, 59, 69] have examined the effect of concentration of particles on erosion rate using dilute suspensions where the shielding effect is less likely and increasing particle concentration might be expected to cause more particle impacts onto the surface in a given time and hence greater wear. However, only a very slight increase in erosion rate is observed as a result of increasing particle concentration [25] and this increase depends on the dominant mechanism of wear when the particle impact angle changes. At low concentration, these investigators [59, 66] have proposed a power law relationship between erosion rate and particle concentration as follows:

$$E_r = kC^{\beta}$$

where E_r is the erosion rate, k is a constant, C is the particle concentration, and β is the concentration exponent. The value of the concentration exponent β was found in the literature [25, 59, 69] to vary between 0.2 and the expected value of 1 according to the target material and erodent particle type.

2.2.3.2 *Factors associated with erodent particles*

The properties of the erodent are also very significant in affecting erosion rate [48], with particle size, shape and properties all having an effect.

The effect of particle on erosion rate has been studied over a number of years e.g. [11-13, 15, 25, 69, 74]. Gandhi *et al* [69] evaluated the effect of particle size on the erosion rate of brass targets by zinc erodents in a slurry pot tester. The erosion rate was found to increase linearly with increase in particle diameter for all velocities and concentrations investigated. Using a Coriolis wear tester, Tian *et al* [74] have examined the same effect using three different target materials and silica sand slurry with particle size range (25-1400 µm). For all materials considered (see **Figure 2.17**), it was observed that larger solid particles generate more wear damage at a given impact speed and concentration, not only for the obvious reason but also due to the fact that the larger mass and hence higher kinetic energy tend to be more effective in getting the erodent onto the surface of the material, while smaller particles are more likely to follow the streamlines.

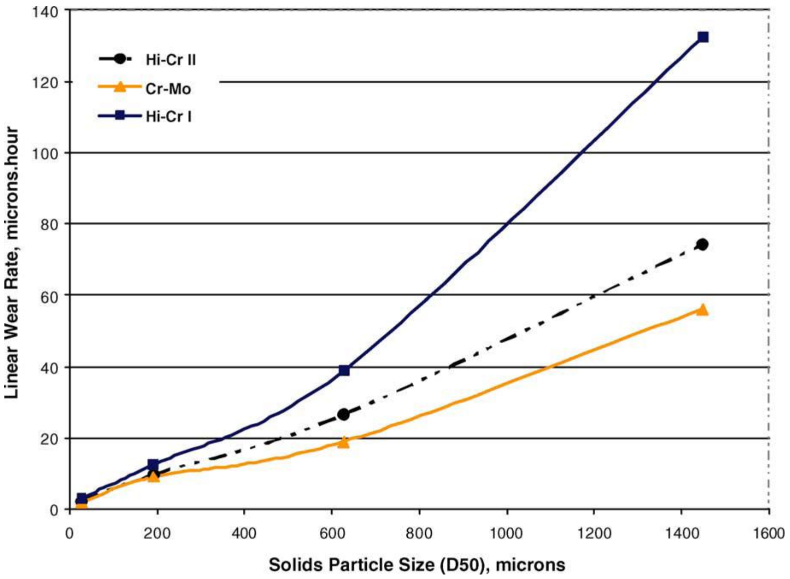

Figure 2.17: Variation of linear wear rate with respect to solid particle size [74]

Many researchers have found a strong dependence of erosion on particle size [12, 13, 25, 69], and have used a power law correlation to describe the relationship between erosion wear and particle size as follows:

$$E_r = kd_p^{\phi}$$

where E_r is the erosion rate, k is a constant, d_p is the particle size, and φ is the particle size exponent. Reported values of the size exponent φ vary; Feng *et al* [13] found it to be in the range between 2.4 and 4 according to the target material and erosive particle type (e.g. being 3 for silica sand erodents impacting a stainless steel target), Clark *et al* [12] found it to be 2 for SiC erodents in the size range between 100 and 780 µm impacting aluminium targets.

Most experimenters prepare erodents by sieving materials into fractions that will contain a distribution of sizes between the mesh sizes of the upper and lower sieves, and so some uncertainty is always associated with the size range distribution of any given erodent sample [12]. Notwithstanding this, Zhang et al [25] have observed a linear relationship between the amount of wear and the particle size for gas-solid erosion when the average particle diameter is <350 µm, but a stronger linear dependence was observed beyond 350 µm.

Erosion is also affected by the shape of the erodent particles, which are usually classified as round, angular, or semi-round, based on visual observation. Many naturally occurring particles are rounded and uniform, but newly or artificially-formed particles can be sharp and complex, and difficult to describe in simple quantitative terms. The general shape of a particle is an indicator of its erosive effect; for instance, irregular shapes with sharp edges increase erosion rate, whereas blunt particles with round edges retard it [42]. Desale *et al* [67] have investigated the effect of erodent shape on erosion wear of two ductile materials by using three different erodents; quartz, alumina and silicon carbide. They compared erosion rates for two shapes of particles, spherical and angular, having the same size and density (see **Figure 2.18**) and pointed out that the reduction in contacting area of angular particles leads to an increase in kinetic energy dissipated per unit area, leading to higher stress intensity which enhances the severity of impact.

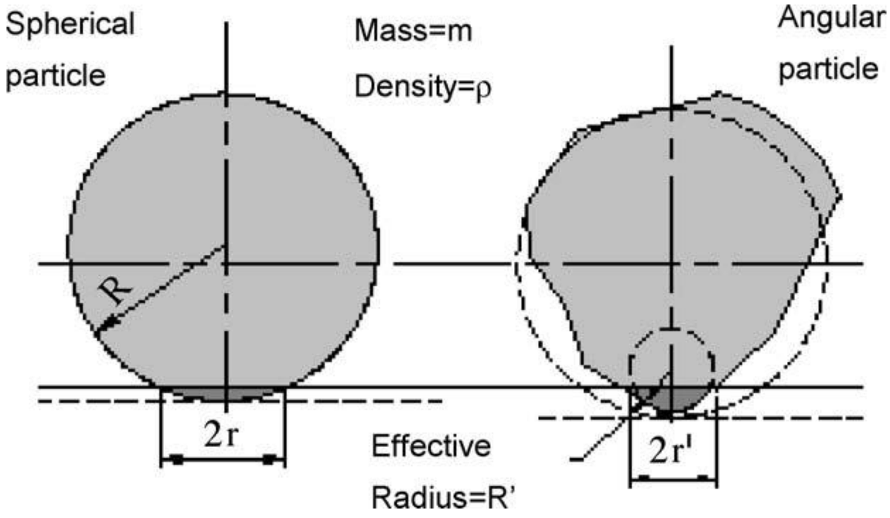

Figure 2.18: Contact area due to impact of spherical and angular particles [67]

It is well established that more angular particles penetrate more deeply and cause more effective material removal than do spherical particles, if all other factors remain the same [4, 14, 74]. The effect of erodent shape was found by Desale *et al* [67] to be more dominant at shallow impact angles compared to high impact angles. They suggested that the erosion rate by angular particles is higher than rounded particles because they were observed to produce deeper craters and higher average surface roughness.

Chen and Li [11] have simulated the erosion process using a computer model (two-dimensional, micro-scale, dynamic model) and have investigated the influence of particle shape, including triangular, square, and circular cross-sections on erosion. The highest calculated single particle impact erosion loss in the orientation shown in **Figure 2.19** was by triangular particles followed by circular then square particles. This observation was attributed to the contact area of each particular shape and its consequent contact stress.

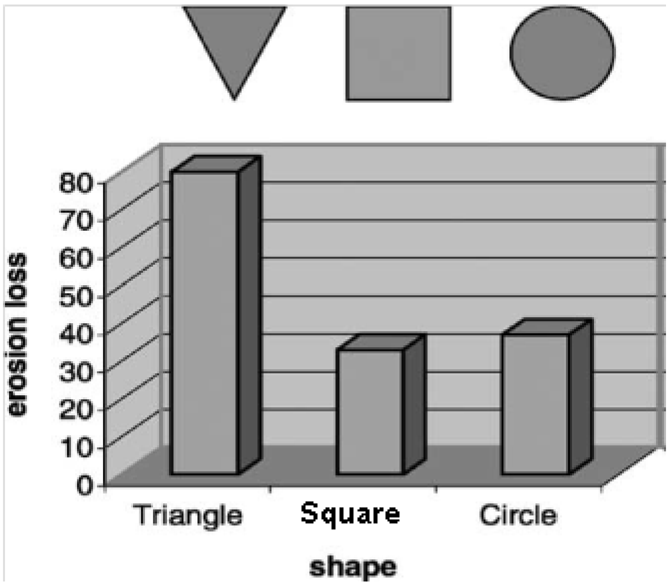

Figure 2.19: Erosion rate due to particles of different shapes [11]

The effect of particle shape has also been studied in detail by Winter and Hutchings [46] who introduced the term ‘‘rake angle’’ to denote the angle between the front face of the particle and the normal to the target surface. This angle is dependent on the particle shape, for example always being large and negative for spherical particles. They showed that rake angle caused a change in erosion mechanism from a ploughing or smearing type of impact crater with large rake angles to a cutting mechanism at small rake angles. Angular particles were generally found to cause a greater proportion of cutting type of material removal [13].

As might be expected, the particle property which most affects erosion is the hardness relative to the target material. For example, Truscott [15] indicated that, for metals in general, wear increases rapidly once the particle hardness exceeds that of the metal being abraded. Beyond this, the wear rate may become fairly constant or may even reduce with increasing abrasive hardness. The same effect was observed by Sundararajan and Roy [14] who pointed out that, as long as the hardness of the erodent is at least twice that of the target material, the erosion rate is independent of particle hardness. Feng *et al* [13] studied the effect of eight erodents of different hardness on erosion rates for brittle and ductile materials. It appeared from their results that the erosion rate increases with particle hardness once the particles are harder than the target to be eroded. They also noted that the dependence of erosion rate on particle hardness and toughness is stronger for brittle materials than for ductile materials.

2.2.3.3 Factors associated with target material

A wide range of materials including metals, ceramics, and polymers are used in applications exposed to erosive environments and the characteristics of these materials have a strong effect on erosion. Chemical composition, elastic properties, hardness [74] and surface morphology [67] are some of the major parameters of the target materials which affect the erosion rate. Among these, hardness is the most widely used target property to control erosion rate and its effect has been explored by many investigators [4, 13, 74]. When hard angular particles strike a relatively soft target, the target surface will deform plastically. On the other hand, when soft erodent particles are used, they may fracture upon impact, and hence, erosion damage will decrease as the target hardness increases.

Levin *et al* [16] have investigated the effect of target material hardness and toughness on erosion resistance. It was noted that, at low particle velocities, materials with high hardness may offer good erosion resistance. However, at high particle velocities, when plastic deformation and/or cracking are more likely, hardness may not improve the erosion resistance of the target. They concluded that materials that combine high hardness (which reduces the energy transferred from the incident particle into the target) and toughness (the ability of the target material to absorb this energy without fracture) may offer high erosion resistance.

Using a slurry jet impingement rig, Wood [76] has correlated erosion rates, expressed as volume loss (μm^3) per particle impact, with material surface hardness for 21 typical engineering surfaces including both ductile and brittle materials. He reported that the erosion rate of brittle materials is more sensitive to hardness with erosion rate proportional to $H^{-3.2}$ (see **Figure 2.20**) while ductile surfaces showed erosion rates proportional to $H^{-1.6}$, where H is the surface hardness.

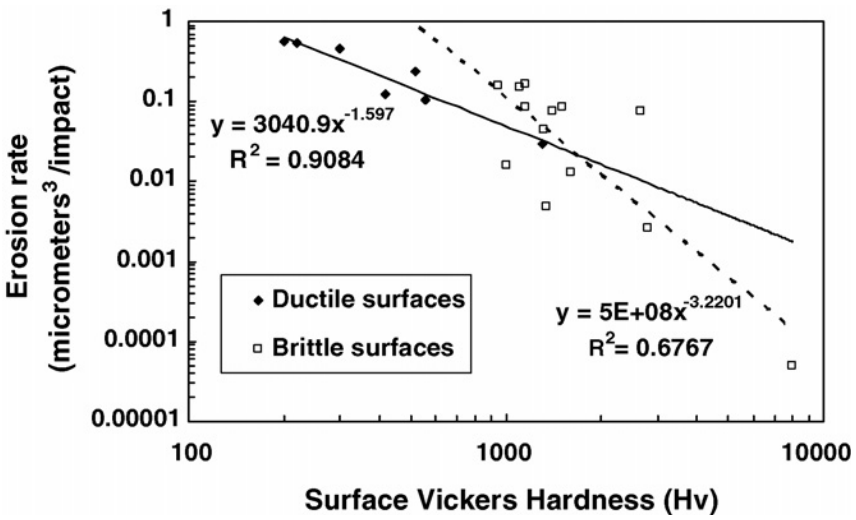

Figure 2.20: Effect of hardness on erosion rate for a range of ductile and brittle materials [76]

2.2.4 Erosion models

Erosion models are useful for the design of slurry components and, in the context of this work, are also useful in designing experiments which are relevant to real systems.

Over the last 50 years, many models have been proposed to evaluate the rate of material removal under various eroding conditions. The pioneering work in the prediction of cutting action damage due to the impact of single particles against a ductile target was due to Finnie [4]. In his model, the particles were assumed to be rigid (non-deforming) with sharp edges and the target was assumed to reach a constant flow pressure (perfectly plastic target) immediately upon impact. Finnie further assumed that no rotation of the particle occurs during the impact process and hence was able to solve the equation of motion for the particle trajectory as it cuts the surface by considering all forces acting on it, and thus predicting the shape of the crater or scratch left by the impacting particle. The resulting expression was further extended to take into account impacts by several free moving particles of total mass, *M*. This resulted in two expressions for total volume, *Q*, removed by cutting wear,

— for

— for

where V_p is the velocity of the particles, θ is the impingement angle and P is the flow pressure (constant horizontal pressure between particle and target).

Finnie indicated that no erosion could occur at normal impingement impact, which is contradictory to other works [6, 61] and noted that the prediction of material removal for brittle materials is difficult to obtain due to the complex nature of cutting of such materials [26].

Finnie's theory formed the foundation for later models, and a more general model was developed by Bitter [2, 3] who considered both ductile and brittle materials. The Bitter model makes the hypothesis that the loss of material is the sum of material lost due to plastic deformation, W_D (deformation due to repeated impact of particles normal to the target where the material elastic limit is exceeded and the surface layer is destroyed and fragments of it are removed), and that lost due to cutting deformation W_C (when the particles strike the body at an acute angle scratching out some material from the surface). Using an approach based on Hertzian theory and making use of the energy balance equation, Bitter derived an equation for deformation wear, W_D using a deformation wear factor, ε, which is the ratio of the energy absorbed by the surface layer during collision and the amount of energy needed to remove a unit volume of material:

—

This equation is valid if $V_p \sin\alpha \geq V_y$, where V_y represents the maximum particle velocity at which the collision is still purely elastic and hence no deformation wear occurs. The effect of target mechanical properties on deformation wear is encapsulated in V_y, which can also be considered to be a threshold velocity, below which deformation wear does not take place and is given by **Equation 2.9**.

The velocity of impinging particles can be resolved into two components, one normal to the surface (V_1) which is responsible of the particle penetration into the target and one parallel to the surface (V_2) causing a scratching action. Depending on whether the parallel component of particle velocity becomes zero during the collision process, two expressions of the material removed by cutting wear can be suggested. In the first one the particle velocity has a parallel component to the surface when it leaves the target and the material removed is given by:

$$W_{C1} = \frac{2MK(V_p\sin\theta - V_y)^2}{\sqrt{(V_p\sin\theta)}}\left[V_p\cos\theta - \frac{K(V_p\sin\theta - V_y)^2}{\sqrt{(V_p\sin\theta}}\varsigma\right], V_2 \neq 0$$

On the other hand, if the velocity component parallel to the surface becomes zero during the collision, the expression for the material removal due to cutting action is

$$W_{C2} = \frac{\frac{1}{2}M\left[V_p{}^2\cos^2\alpha - K_1(V\sin\alpha - K_T)^{\frac{3}{2}}\right]}{\varsigma}, V_2 = 0$$

where, K and K_1 are constants which depend on material properties, ς is a cutting wear factor which is defined as the quantity of energy needed to scratch out a unit volume from a surface.

The total wear in any instance is therefore,

$$W_{TOT} = W_D + W_{C1} \text{ or } W_{TOT} = W_D + W_{C2}$$

Finnie’s restriction of no particle rotation during the impact process was removed by Hutchings *et al* [5-7] who developed a rigid-plastic theory (the particle is undeformable and the target reaches the fully plastic condition very quickly in the impact process) to predict collision kinematics and crater dimensions for impacts of single spheres and square plates on ductile targets. The theory assumed that the elastic effect can be neglected and predicted the kinematics of the particle as it ploughs or cuts through the material, under the assumption that the instantaneous resisting force could be calculated by multiplying a constant plastic flow pressure by the instantaneous contact area. Because the contact area changes as the particles travel through the target material, the force resisting the particle motion changes in both direction and magnitude. Hutching’s theory thus resulted in equations of motion for the particle that had to be solved numerically, and comparison with experimental measurements of crater volume, energy loss, and particle kinematics revealed a reasonable agreement.

Hutchings' theory was subsequently generalized by Papini and Spelt [8, 9] so that the impact of particles of arbitrary shape against targets of arbitrarily dynamic hardness and dynamic friction coefficient could be analysed. Papini and Spelt [9] further studied the special case of two dimensional 'diamond particles' of various angularities by constructing a computer programme capable of describing the trajectories of particles as they form impact craters, so that their size and shape can be predicted. Experimental work carried out by Papini and Dhar [77] has shown that the agreement between experimental and predicted rebound linear, angular velocity, and energy loss was good, while the model generally overestimates the measured crater volume, and underestimates the rebound angle.

In addition to the contact mechanics-based approaches discussed above, empirical correlations between impact parameters and erosion damage caused by solid particle impact offer an alternative approach taken in the literature in order to estimate the material erosion rate [16, 53]. Based on empirical expressions derived from a wide range of experiments and observations, the simplest way of writing an equation for erosion is parametrically [42]:

Erosion = f (operating condition, properties of particles, properties of base material).

However, each equation reflects a very specific and individual case and there are no predictive equations for erosion damage that can be applied to many types of metallic materials under various impact conditions. The great variability of the such models together with the high expense involved in carrying out erosion experiments has led some authors [78] to develop a numerical model based on the finite element method to evaluate the removed volume of material due to particle impacts.

2.2.5 Particle interference effects

The work reviewed above focuses on the analysis of single particles striking a surface, but the importance of multiple overlapping impacts in real eroding flows is now recognized and currently receives considerable attention. In solid particle erosion testing, the dependency of the erosion rate on incident particle flux (stream density) can be attributed to the effects of interference between impacting and rebounding particles in the collision zone, an effect that limits the erosive potential of the particles at the surface and hence reduces the efficiency of solid particle erosion with increasing particle flux. Shipway and Hutchings [79] considered the interference between an incident stream of particles and those rebounding from a flat surface. They describe a method to determine experimentally both the particle flux below which inter-particle collisions are insignificant, and the spatial distribution of particles in the incident stream, for a sand blast type erosion setup. The method is based on the observation that the erosion scar produced by particles impinging on a coated substrate abruptly increases in size at a critical particle flux. This increase in scar radius is attributed to increased particle interactions, as incoming particles are scattered by rebounding particles.

A computer model that simulates a stream of spherical particles impacting a flat surface was devised by Ciampini *et al* [80, 81] in order to determine the interference effect between rebounding and incident streams of spheres. The simulations allowed for multiple spherical particle collisions by tracking the movement and collision of individual particles in three dimensions, so that interference effects could be determined as a function of stream angle of incidence, incident particle velocity and size, nozzle divergence angle, particle flux, stand-off distance, and coefficient of restitution for both particle-particle and particle-surface interactions. A dimensional analysis allowed for presentation of generalized results, and a parametric analysis identified the dimensionless groups that were proposed to assess the reduction, due to interference effects, in stream power from that available at the nozzle exit. In erosion testing, to avoid confusion between effects due to interference with more fundamental parameters such as particle size, shape, angle of attack, and material, care must be exercised to ensure that the particle flux is low enough that only a small proportion of incident particles undergo collisions. Ciampini *et al* [80, 81] show that the results of their simulation can be used to determine the optimum particle flux to be used in such experiments.

A number of investigators have attempted to construct models that allow assessment of particle interference effects to be measured analytically [82, 83]. Gomes-Ferreira *et al* [84] have simulated particle streams allowing for divergence and for inter-particle collisions both on the way to the surface and after rebound. Modifying the model of Shipway and Hutchings [79] for the probability density function (p.d.f.) of particle angles: —— , where τ is a dimensionless parameter describing the tendency of the stream to diverge, Gomes-Ferreira *et al* developed an expression for the radial distribution of dimensionless incident energy per particle in a diverging stream with no collisions:

, where the subscript *0%* indicates no particle interference effect, r_1* is a dimensionless radial position equal to , where s is the nozzle-to-surface stand-off distance, and r is the radial distance from the centre of impacting stream.

When collisions are taken into account, two distributions arise, one for particles which reach the surface without colliding with other particles:

and one for particles which collide before they reach the surface:

where c is the proportion of particles which collide with others before reaching the surface, $\bar{r}*$ and $\bar{r}*$ is the average dimensionless radius at which particles which do not collide with others strike the surface. All of the parameters c, $\bar{r}*$, α, A, B, C, D, E, F, G, H and M were determined by fitting the above distributions to the results of simulations of the particle stream and the entire distribution was obtained by adding the two.

Simpler distribution functions of particle energies have been considered for other situations where the flux and velocity are somewhat lower. For example, Crespo [85] has taken the energy p.d.f. of balls in a ball mill to be given by a Boltzmann distribution:

$g \;\; e \; = \frac{1}{P}\exp\left(\frac{-e}{P}\right)$, where P is the average energy.

In a rather different sphere of engineering Brodie and Rosewell [86] have considered the intensity of rainfall in models of particle wash-off. Whereas these authors were primarily interested in the total kinetic energy of a given storm, they calculated this from an empirical distribution of raindrop size, D:

$N_V \;\; D \; = N_0 \exp \;\; -\Lambda D$

and an empirical relationship between raindrop size and velocity:

$$V_F = 4.854D\exp\ -0.195D$$

2.2.6 Particle-laden liquids

The presence of a liquid carrying the particles influences the movement of the abrasive particles near the test surface much more than in dry erosion. Therefore, it is necessary to understand the fluid dynamic behaviour of particle-laden liquids and their interaction with flat surfaces.

Turenne *et al* [87] have investigated the effect of particle concentration in a slurry on the erosion rate of aluminium samples using a narrow slurry jet of (200-300 μm) sand particles in water at normal incidence angle at a fixed velocity of 17 ms^{-1}, whilst varying the slurry concentration between 1 and 20% by weight. They characterised the so-called "blanketing effect" in dense slurries by identifying an erosion efficiency, η_e, (ratio of mass lost by erosion to mass of erodent used) which decreased with the inverse cube root of the volume fraction of sand in the stream, f:

$$\eta_e = \frac{K}{f^{0.33}}$$

where K is a constant which will depend on the erodent, the target, the jet size and the fluid velocity.

On examination of the eroded surfaces, Turenne *et al* also noted that they expected that different impingement angles could result in very different effects of slurry concentration even to the extent that efficiency could increase with concentration at low angles of incidence.

Fang *et al* [88] directed a jet of silica sand (particle size 600-850 μm) suspended in water at samples of four different ceramics and found that the erosion rate did not change in a consistent way in the concentration range 3 to 7.5 wt.%, although the maximum erosion rate for all the materials investigated was at an impact angle of 90°. Iwai *et al* [89] investigated the slurry wear rate of 13 materials and found that the effect of changing one of the experimental conditions such as jet velocity Vj, particle size D, or particle concentration C on the erosion rate of the target E_r was characterised typically by exponents whose values were chosen to fit the experimental data as follows:

Particularly when the carrier fluid is a liquid, fluid-particle-surface interactions can have a significant effect on particle trajectories and velocities near the target, and hence on the AE energy transferred to the target. Laitone [90] was one of the first to comment that particles approaching a surface always impinge with angles of less than 90° indicating that there is always a difference between the true incidence angle and the angle of the approaching flow. Benchaita *et al* [91] have noted that the form and dimensions of the erosion crater in a copper target subject to a 20 mm square section jet consisting of a 0.3 wt.% suspension of silica sand in water were consistent with a spread in particle trajectories from normal to more inclined angles. They identified three regions in a jet with normal incidence; a uniform flow at the nozzle exit, a streamlined flow near the target and a uniform exit flow parallel to the surface. In the streamlined region, the components of the flow are given by:

and

where *x* and *y* are measured from the stagnation point and *Z* is a flow parameter which depends on the jet velocity, the nozzle width and the stand-off distance. These authors also noted that the boundary layer thickness, given by $\overset{-}{-}$ (where *ν* is the kinematic viscosity of the fluid), relative to the particle size is important in assessing the extent to which the boundary layer will slow the impinging particles.

Clark and Burmeister [92] have identified the role of a “squeeze film” as a cushion between an approaching particle and a surface, irrespective of particle size and initial velocity of approach. They suggested that the extrusion of the intervening layer may even prevent impact entirely at low Reynolds numbers, a suggestion which was confirmed later by Wong and Clark [93] who showed that, for 50 μm glass beads in a flow at 6 ms^{-1}, impact is prevented altogether. More recently, Clark [64] has noted that knowledge of the flow conditions close to the surface in erosion testers, such as the slurry pot, is “not very sound”, but that the impact velocity of particles, deduced from individual crater dimensions, can be 50% or less of the free stream velocity of the fluid. Much of this difference could be explained by potential flow, taking into account the distribution of impact angles and consequent components of the velocity normal to the target, and the rest was attributed to the retardation effect of the squeeze film, with small (<100μm) particles in dense slurries being most susceptible. Not only may particles approaching the target surface at low Reynolds number be unable to penetrate the squeeze film on rebound or approach and, in more concentrated slurries, a layer of particles can become trapped at the surface offering the target some protection from the effect of impact by further approaching particles.

Turenne and Fiset [94] solved numerically the differential equations for particle movement in the flow field near the surface for a slurry jet impinging a surface with normal incidence. By curve-fitting their numerical results, they produced parametric equations for particle trajectories in terms of the final radial position of the particle on the surface, r, the incident speed V, and the impact angle θ as a function of initial location of the particle in the jet, r_i, the initial velocity (jet exit velocity) V_j, and the particle size d:

(2.15)

Turenne and Fiset noted that the predominant variable affecting the impact parameters is the particle size. Due to their higher inertia, the trajectories of larger particles are deflected less, resulting in an impact angle closer to the original jet direction and the impact velocity is also a higher proportion of the original jet velocity.

2.3 Acoustic emission (AE) technology

All solid materials exhibit some degree of strain under external forces and will spring back when released. If this spring back is rapid, such as might occur during incremental crack propagation or even the sudden movement of dislocations in plastic deformation the recoil can generate an elastic wave. Such rapid releases of elastic energy caused, for example, by deformation or damage within or on the surface of a material and the associated stress waves (essentially propagating elastic strains), are normally referred to as acoustic emission (AE) [95]. A generating event (source) produces an elastic wave which propagates in all directions in the body and on the surface and can be detected by locating sensors at appropriate positions on the surface of the object to be monitored, as shown schematically in **Figure 2.21**. Sources of AE in rotating fluid-handling machinery include impacts, fatigue, friction, turbulence, cavitation and leakage [96].

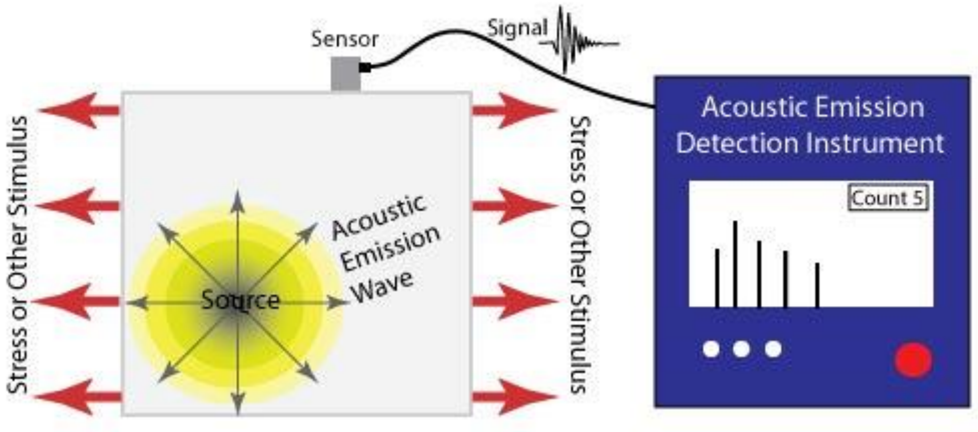

Figure 2.21: Working principle of AE technique [95].

2.3.1 Characteristics of “hit-based” AE

In the current work, the primary interest is in the AE generated by impacting particles, the monitoring principle being that each particle impact will act as a generating event, and the cumulative effect of a number of these events can be recorded using AE sensors. AE is unlike other non destructive methods in many regards [96]:

- AE offers the advantage of earlier defect/failure detection due to the increased sensitivity to the events leading to failure.
- Instead of supplying the energy to the object under examination, AE simply listens to the energy released from the object.
- AE is sensitive to the degradative processes, for example, defect growth or changes in the material, rather than to the static presence of a defect and this is particularly meaningful because only active defects will be detected. It is therefore primarily an in-service monitoring tool as opposed to an out-of-service testing tool.
- AE has the ability to monitor simultaneously the entire structure without taking it out of service. This can offer great cost savings compared to other tests,

although more advanced processing is required to interpret the signal if multiple sources of AE are present or if it is necessary to locate the source.

AE wave types cannot be controlled, and the different wave types travel over different paths and at different speeds according to the shape and properties of the propagation medium and surrounding media [97]. At any point on a surface, AE waves are subject to refraction, scattering, attenuation and reflection from the boundaries, all of which makes interpretation difficult. Whereas it is rarely the case in real systems, AE waves are normally treated as if they were pure modes; the most commonly considered being dilatational (compression) waves, distortional (shear) waves, surface waves (Rayleigh) and plate waves (Lamb).

AE covers a wide frequency range (100 kHz to 1MHz), and recorded AE signals can broadly be categorised into burst, continuous and mixed type (see **Figure 2.22**). In the first type, the signal can be characterized by discrete transients with relatively short decay time and even shorter rise times, this type of signal is observed in unsteady process such as cracking in materials [98]. Continuous emissions are either bursts that occur too closely together to be distinguished or are due to sources that are spread out in time. Examples of the former type of signal might be those associated with plastic deformation in ductile materials and erosion processes in brittle materials [70]. The final type of AE signal is called mixed mode which contains a number of high level bursts above the background continuous emission [99], and are typical of sources which are themselves have some kind of temporal structure, often those where the source is distributed, such as in engines.

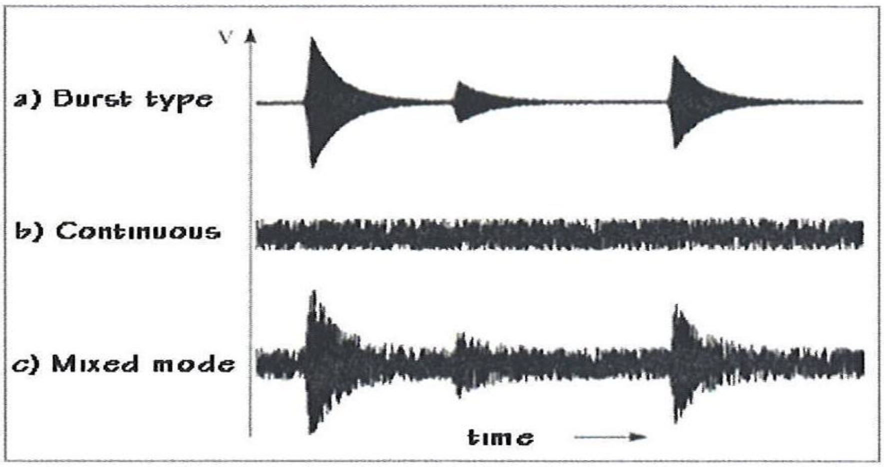

Figure 2.22: AE signal wave types [43]

Typical parameters used to describe time-based AE signal features are shown in **Figure 2.23** and these can be summarised [37]:

- AE energy is calculated from the integral of squared amplitude of signal duration over time.
- AE count is the number of times that burst signal amplitude exceeds the preset threshold.
- RMS AE is the energy rate or the root mean square of voltage, which is generally an indicator of average AE energy over each averaging time.
- Rise time is the time interval between the first threshold crossing and maximum amplitude of the burst signal.
- Signal duration is the time interval between the first and last threshold crossing of the burst signal.

However, these descriptors have evolved from the needs of hit-based inspection systems (aimed at identifying and timing of single events) and they are rarely used as the only means of analysing the more complex time series typical of a monitoring application.

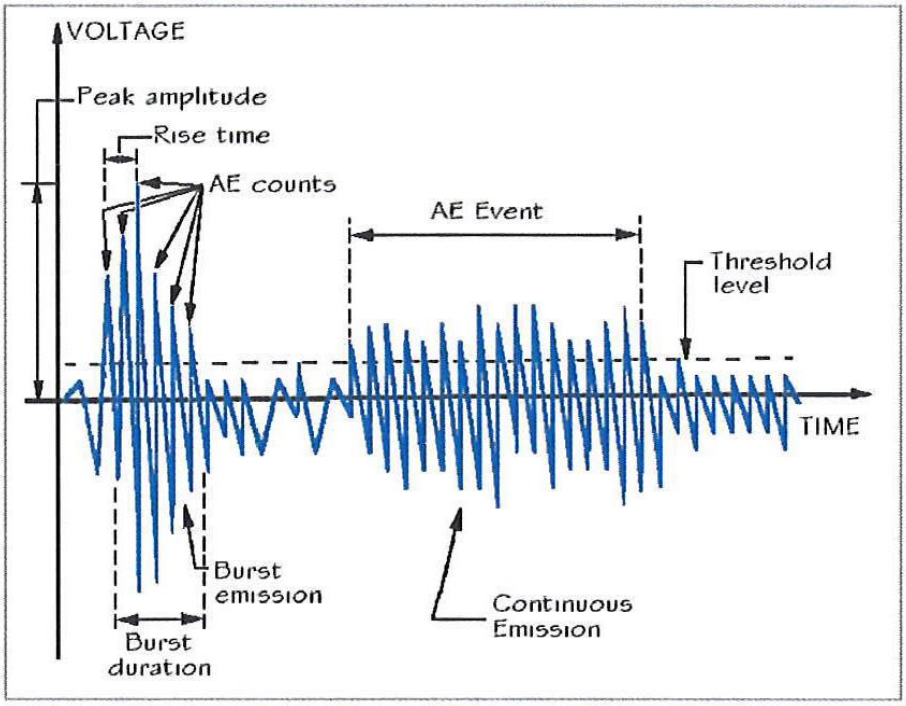

Figure 2.23: Traditional time-based features of AE signals. Adapted from [99]

Signal processing is probably the most important single entity in a condition monitoring system since it is the means of determining the condition of the system from one or more complicated time-series signal. Arguably, AE signals contain too much information, since signals, as acquired, have a bandwidth of 0.1-1MHz. The extraction of a set of diagnostically significant features from such a signal is the role of signal processing and this normally requires to be carried out automatically in a real application. The main aims of signal processing are therefore [100] to:

- Reduce the information to a manageable amount.
- Reveal the signal features which are of interest.
- Minimise the influence of unwanted effects on the signal.

2.3.2 Application of AE as a tool to monitor erosion damage caused by solid particle impacts

Monitoring of particle impact using acoustic emission exploits the fact that, when a hard solid particle strikes a target, a fraction of the incident energy dissipates as elastic waves, which will propagate through the target material according to its shape and elastic properties before being detected by a suitable AE sensor. The characteristics of the observed signal from the sensor will depend not only on the particle impact dynamics, but also upon the propagation of waves into the target medium and the type of sensor used. Because of this, and the very high temporal resolution available from AE, and despite the theoretical observation that little of the energy in particle impact is converted to elastic waves (AE), the potential of AE to monitor erosion phenomena has attracted many investigators, some concentrating on measuring the erosion variables identified in **section 2.2.3**, and others concentrating on monitoring the amount of erosion. It should, however, be noted that AE monitoring is indirect, in that, at best, it will reveal the characteristics of the impacts rather than the effect that these impacts have on removing surface material.

One of the seminal studies of hard particle impact on surfaces using acoustic emission was by Buttle and Scruby [62] in which bronze and glass particles were allowed to fall under gravity in a vacuum onto a specimen onto whose opposite face was mounted an AE sensor of very high fidelity. Using a calibration with a capacitance transducer and pulsed laser, they were able to deconvolve the AE signal to produce force signals for the impacts, and showed that the peak force and impact times were consistent with Hutchings' model [34] for impact time:

, where *A* is a constant, ρ_p, *R* and V_p are the density, radius and impact velocity of the particle, and *f*(*E*) combines the elastic properties of the particles and target: $f\ E\ = \frac{1-\nu_1^2}{E_1} + \frac{1-\nu_2^2}{E_2}$

The peak impact force indicated by the Hutchings model:

, where *B* is a constant, somewhat overestimated the experimental peak forces for some impacts, an observation which was attributed to possible overestimates of velocity, a non-unity coefficient of restitution and non-spherical particles. Nevertheless, Buttle and Scruby concluded that, in the range of impact speeds of 2.5 to 7.1ms^{-1} and particle sizes 50-100µm, particle size could be distinguished using AE provided that individual impacts are separated by at least 1ms.

Boschetto and Quadrini [101] have taken a different approach, dropping a fixed weight of powder of various materials and sizes, and measuring a normalised number of counts, which they found to be simply related to the mean particle diameter. At the other extreme of particle flux, Ivantsiv *et al* [102] have measured the mass flow rates of particles in abrasive jets using AE. Glass beads of approximately 60 µm nominal diameter and aluminium oxide powder of 25 µm equivalent spherical diameter were used as abrasives with particle velocities of around 150ms^{-1} and particle impacts separated by around 30-100µs. They used two approaches to estimate the mass flow rate (controlled to be between 1 and 11 g min^{-1}), the first using a dynamic threshold to count individual impacts and the second using the power spectral density (PSD) of the AE signal. Also working with high particle fluxes (80 g min^{-1} of 18-80 µm equivalent spherical diameter particles), Faisal *et al* [103] showed that the measured AE energy and expected kinetic energy rate in HVOF spraying were well correlated. In both of these pieces of work, it was necessary to mask the surface to limit the number of incident particles. The simple kinematic model for spraying through a slit used by Faisal *et al* [103] assumed that the particle velocity and density was constant across the impinging spot and the particle spay was collimated.

Duclos *et al* [22] carried out a rather more applied study using AE to monitor impacts of streams of particles of various sizes at various concentrations in a water flow loop. By estimating the number of impacts from the particle concentration and flow rate, they showed that the AE energy per particle was approximately proportional to the cube of particle size (i.e. particle mass), although they noted anomalies at higher particle sizes, attributable to particle drop-out according to Stokes' Law. Some authors have reported the possibility of using an AE sensing technique for on-line monitoring of slurry flow properties. Hou *et al* [23] mounted an AE sensor on the external wall of a small diameter pipeline conveying dense slurries of fine silica particles with an average particle size of 13 μm. Based on the acoustic noise produced by the fluid flowing inside the pipeline and using a stepwise regression analysis technique, they were able to derive quantitative relationships between the physical properties of the flow, such as solid concentration, mass flow rate and volume flow rate, and the statistical and spectral characteristics of the recorded AE. They also observed that the frequency in the power density spectrum of the signal increased with increasing flow rate. However, the validity of this empirical regression approach depends upon the mechanical flow properties of the two-component mixture, and is unlikely to be applicable on all other configurations where different components and materials might be involved.

Ferrer *et al* [20, 21] attempted to characterize and understand the mechanical damage during the abrasion-corrosion process with the aid of a combination of AE measurement and an electrochemical device used for corrosion potential measurements. A slurry jet impingement rig was used with the potential of varying fluid flow rate (1-16 ms^{-1}), concentration (1-8 wt.%), and angle of impact (30°-90°) with an AE sensor coupled on the rear surface of the 304L stainless steel target. Two different methods were studied. For the single impact method, where glass beads of diameter 720 μm were introduced into the suspension one by one, they observed that the acoustic energy due to the impact is proportional to the incident kinetic energy. The coefficient of proportionality was found to increase with the impact angle, and this observation was attributed to the hydrodynamic boundary layer that slows the particles at low impact angle as well as lowering the amount of elastic energy transmitted to the target. They also observed that the amplitude and the frequency of the AE bursts increase with the velocity of the fluid (which was assumed to be the same as the velocity of the particles). When the particle velocity was greater than 10 ms^{-1}, new bursts characterized by low amplitude and low frequency parameters were observed. These new bursts were attributed to bubbles generated in different locations on the test loop and it was concluded that AE was capable of separating easily the impact of particles from the collapse of bubbles, an observation confirmed later by Duclos *et al* [22], who reported that acoustic energy due to air bubbles is much lower than that for particle impacts. Both sets of author concur that bubble collapse is unlikely to constitute a significant uncontrolled source of acoustic emission in systems where abrasion and erosion need to be monitored. For the multi-impact method, where defined quantities of SiC particles of size 125 μm were introduced into the suspension, Ferrer *et al* [20] obtained a simple relationship between the weight loss measured at the end of the test (2 hours) and cumulated acoustic energy measured during each test. On this basis, they claimed that acoustic energy may used to quantify the mechanical damage due to abrasion-corrosion processes, whatever the flow rate and the concentration of particles, although clearly some kind of calibration would be required.

Oltra *et al* [73] used AE to monitor combined abrasion and corrosion of stainless steel plates with a slurry jet impinging normal to one surface and an AE sensor fixed on the other. They measured the relative amounts of erosion and corrosion, and showed that the mechanical wear (measured as a mass loss after the 1 hour erosion test) was proportional to the mean value of RMS AE signal for the duration of the test. However, in parallel experiments with individual impacts using spherical glass beads of various diameters (from 1 to 2.5 mm) and SiC particles of various sizes (from 1 to 2.8 mm), they observed that the acoustic emission was proportional to the kinetic energy of the particle impact and not to the mechanical damage, measured as the volume of the wear crater which was determined after averaging the mass loss due to several impacts.

Burstein and Sasaki [24], as well as concurring with the observation [73] that the wear rate by particle abrasion is correlated to the RMS AE signal, further indicated that using either the maximum amplitude of individual AE events or the RMS AE value was an acceptable measure of the magnitude (wear induced) of the impact in slurry handling after a clear linear correlation between RMS AE signal and maximum amplitude of individual AE events was found. Using a slurry jet impingement rig to study the effect of impact angle on slurry erosion-corrosion of a stainless steel target, they examined the correlation between the maximum amplitude of AE events and the electrochemical transient caused by the impact of an individual erosive particle (400-650 μm rounded silica sand particles). A high degree of scatter was observed in correlations between current rise and AE amplitude although it was observed that each sharp rise in the electrochemical current transient under particle impact was accompanied by an AE event. The correlation was found to depend on impact angle and less scatter was found at oblique angles than at normal incidence. The sharp current rises were ascribed to the rupture or removal of oxide film on the surface by the impact of abrasive particles. To simulate erosion of boiler tubes, Zhang *et al* [25] directed an air stream with particles <500 μm onto the surface of a tube while measuring the AE energy. Using dimensional analysis, they established a relationship between AE energy and the erosion wear, including erosion parameters: $\zeta = \frac{\rho_p}{H}\frac{f}{g}E$, where ζ is the erosion wear after a given time, E is the acoustic emission energy, ρ_p is the particle density, H is the hardness of the tube material, and f and g are dimensional functions of $\left(\frac{C}{\rho_p}, \frac{d_p}{\sqrt{H/\rho_p}}, \frac{V}{\sqrt{H/\rho_p}}, \theta\right)$ where c is the particle concentration, d_p is average particle diameter, V is particle velocity and θ is the particle impingement angle. Zhang *et al* observed that the measured AE indicated that low collision angles dissipate less energy than higher collision angles, an observation which is consistent with [20].

AE has also been proposed as a promising tool for on line monitoring of material removal involved in the abrasive water jet (AWJ) drilling process. Mohan *et al* [104] have investigated the ability of the AE technique to detect the amount of energy dissipated in the workpiece during such a process. A simple physical model to determine the absorbed jet energy was developed and correlated to the measured energy of the AE signals at different water pressures. A logarithmic relationship was found between the calculated absorbed energy and the measured AE energy which implies the possibility of using AE as an indicator of energy dissipated during AWJ machining. In related work, Kovacevic *et al* [70] used AE to study the material removal mechanisms involved in the AWJ drilling process for three different materials, magnesia chromite, sintered magnesia, and bauxite. The time domain AE signals corresponding to the first material, which is characterized by a lower Young's modulus and lower cold compressive strength as well as the presence of hard inclusions in a much softer matrix, were of continuous type representing a material removal mechanism due to intergranular erosion or microcracking. The material removal in a highly brittle material (the second material) was primarily due to continuous propagation of a microcracking network as was indicated by dense continuous AE. The time domain AE signals for the last material were of burst type which indicated that the material removal mechanism is of the transgranular fracture type. Moreover, they correlated RMS AE signals with drilling depth to investigate the feasibility of using AE to monitor the AWJ drilling depth. Plots of RMS AE against drilling depth for the three materials showed that RMS AE reduces with increase in drilling depth. This reduction was attributed to the effect of back flow of the jet which reduces the particle velocity in addition to the damping effect on the AE signal caused by AWJ debris present in the small diameter hole.

In another area of abrasion study, Momber *et al* [72] employed the AE technique for on line monitoring of hydro-abrasive erosion (HAE) of pre-cracked multiphase materials exemplified by five types of concrete. They investigated the effect of a range of erosion parameters such as abrasive particle velocity, local exposure time, and abrasive mass flow rate on the AE signals. They observed a higher amplitude of AE signal at higher impact velocities and attributed this to the presence of a more powerful material removal process, whereas, in contrast, the influence of the abrasive mass flow rate was not very significant. In addition, they found that material removal which is dominated by intergranular fracture is characterized by continuous AE signals, while material removal dominated by transgranular fracture is characterized by burst emission due to the sudden energy release during inclusion fracture. This observation is consistent with other work [70], and confirms the suggestion that AE is capable of revealing different material removal mechanisms occurring in materials when subject to HAE.

AE has also been used to monitor sliding wear in various types of laboratory test. Boness and McBride [105], using a ball-on-cylinder test apparatus, where a stationary ball is loaded against a rotating cylinder, acquired AE signals from a sensor coupled acoustically to the ball housing. They obtained an empirical relationship between RMS AE and the volume of wear removed from the test ball. They also studied the effect of using different lubricants in the sliding contact on both wear and acoustic emission. They indicated that RMS AE is quite sensitive to the type of lubricant used (for example, RMS AE signals were larger for light paraffin, followed by heavy paraffin then smallest for SAE 30 oil) and were able to characterise the abrasive wear involved in lubricated sliding contacts. A similar empirical relationship between material removal and RMS AE was verified later by Matsuoka *et al* [106]. Another study concerning sliding wear was carried out by Mechefsek and Sun [107], who used a similar experimental rig to Boness and McBride in an attempt to distinguish between effective and poor boundary lubrication. In the time domain, they observed that the AE counts were small when the wear rate was mild (effective lubrication) and large when the wear rate was severe (poor lubrication). They suggested using either AE peak level or RMS AE values to represent the wear surface strain rate. This is in agreement with the work of Burstein and Sasaki [24].

2.4 Identification of thesis topic

It is clear from the foregoing review that AE has been used successfully as a means of monitoring erosion caused by hard particle impact on a target material. However, different investigators have made measurements under varying geometrical and dynamic conditions which in turn lead to results which are often simply correlations and are not precisely comparable with each other and, indeed, are divergent in some cases. No model is available so far to link either the material removal or the incident kinetic energy with AE signals for practical applications. Also, most of the work that has been done (with a few exceptions) on identifying AE energy with impact energy carries with it an inherent calibration problem in a system where energy might be lost by propagation and multiple sources with different propagation paths might be present. The approach to be taken here, therefore, is to use a standard measurement "cell" consisting of a target and sensor and to carry out a set of staged experiments where control of the impact conditions is gradually ceded in the interest of practical applicability, thus bridging the gap between controlled impact experiments with one or few impacts to experiments in realistic flow conditions with multiple overlapping impacts and noise from the carrier fluid.

Chapter 3

Experimental method

This chapter describes the solid particle types and specimen details, AE measurement system, and all the experimental procedures and arrangements for this study including calibration tests.

First, the materials, AE monitoring apparatus and signal processing techniques are described. Next, the calibration of the AE sensor using simulated sources on a steel block and on the target specimen along with the calibration of the specimen for its AE propagation characteristics are presented. Finally, the details of systematic experimental procedures for the three types of AE monitoring experiments are presented; free-fall and air-assisted particle impacts, slurry impact using a slurry jet impingement rig, and particle impacts in a flow loop bend.

3.1 Materials, instrumentation and signal processing

The experiments essentially consisted of monitoring particles impinging on a steel surface and, as such, used a common set of materials and equipment.

3.1.1 Particle types and target plate details

The free-fall and air-assisted particle impact experiments used the widest range of particle types; steel balls, solid spherical glass beads, and angular silica sand. The sizes and fractions used are listed in **Table 3.1**. Most of the experiments were performed with sieved samples of glass beads and silica sand, the sieving having been carried out to British Standard 410, and size distributions for air-assisted multiple particle impact experiments are given in **Table 3.2.** The distribution functions were measured using a Malvern particle size analyser, an example distribution being shown in **Figure 3.1**. These distributions were assumed to be Gaussian and the mean and standard deviation were obtained by curve fitting to the Malvern data.

For the slurry jet impingement and flow loop experiments, silica sand sieved fractions were separated with dry sieves from commercial bulk silica sand (from Hepworth

Minerals and Chemicals Ltd, UK). The fractions used are listed in **Table 3.3**. The geometry of the silica sand was examined using an optical microscope (Nikon, with N50 monochrome camera) and found to be angular with semi sharp-semi round corners, as shown in **Figure 3.2**.

	Single particle impacts		Multiple particle impacts	
Free-fall experiments	Particle type	Particle size fraction µm	Particle type	Particle size fraction µm
	silica sand	125-212	**silica sand**	125-180
		212-300		180-212
		300-425		212-250
		425-500		250-300
		500-600		300-425
	Single particle impacts			
	Particle type	Particle diameter mm	Particle type	Particle diameter mm
	steel balls	1	**glass beads**	0.9
		1.5		1.97
		2		2
		2.5		3.5
		3.2		4
		4		6
Air-assisted experiments	Single particle impacts		Multiple particle impacts	
	Particle type	Particle size fraction µm	Particle type	Particle size fraction µm
	silica sand	125-180	**silica sand**	
		212-250		125-180
		300-425		212-250
		500-600		300-425
	glass beads	125-180	**glass beads**	
		212-250		
		300-425		500-600
		500-600		600-710
		600-710		710-850
		710-850		
		850-1000		

Table 3.1: Particle types and sizes used in free-fall and air-assisted experiments for single and multiple particle impacts.

Particle type	Particle size fraction (µm)	Size distribution function
silica sand	125-180	$\frac{1}{205}\exp\left[-\frac{(d-175)^2}{13448}\right]$
	212-250	$\frac{1}{152.5}\exp\left[-\frac{(d-252)^2}{7442}\right]$
	300-425	$\frac{1}{255}\exp\left[-\frac{(d-320)^2}{20808}\right]$
glass beads	500-600	$\frac{1}{135}\exp\left[-\frac{(d-586)^2}{5832}\right]$
	600-710	$\frac{1}{2075}\exp\left[-\frac{(d-668)^2}{13778}\right]$
	710-850	$\frac{1}{352.5}\exp\left[-\frac{(d-776)^2}{39762}\right]$

Table 3.2: Size distribution functions for air-assisted particle impact experiments.

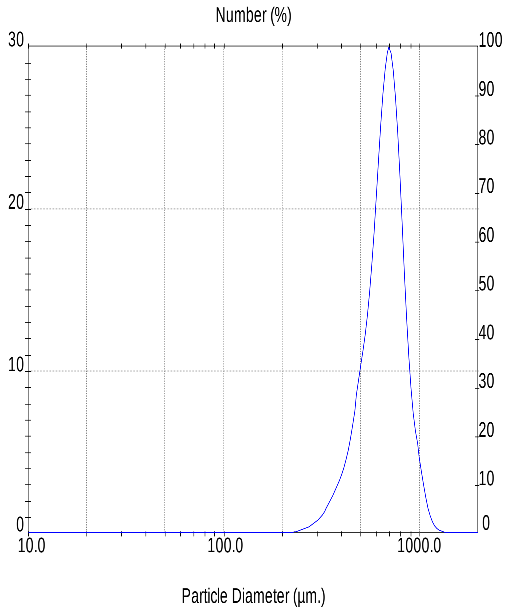

Figure 3.1: Measured particle size distribution for glass beads in size range 710-850µm.

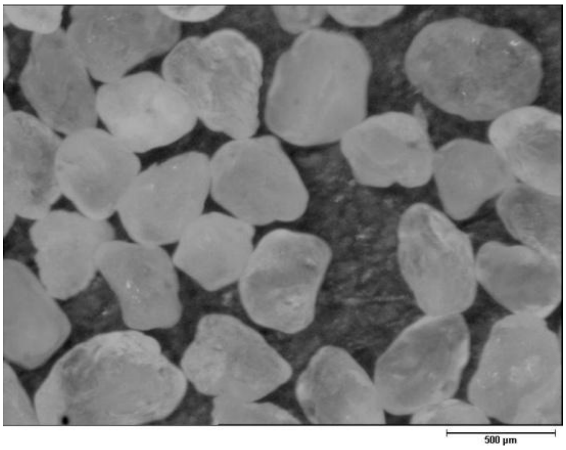

Figure 3.2: Silica sand erodent particles of size fraction 300-425 µm.

	Particle type	Particle size fraction µm
slurry impact experiments	silica sand	125-180 212-250 300-425
Flow loop experiments		212-250 300-425 500-600 600-710

Table 3.3: Particle types and fraction sizes used in slurry impact and flow loop experiments.

The target material was carbon steel, on which all measurements reported in this study have been made. For most of the tests, a specially-designed target was made, consisting of a circular plate of diameter 75 mm and thickness 7 mm, mounted into a sample holder as shown in **Figure 3.3**. A purpose-designed clamp with screws was designed to hold the sensor onto the centre of the rear specimen surface. Great care was taken to isolate the target material from the surrounding sample holder material both to avoid noise and to provide reproducible conditions over a range of experiments. For the flow loop experiments, a sharp 90 degree bend made from 5 mm bore carbon steel was machined and used as a target (see **Section 3.3.3**).

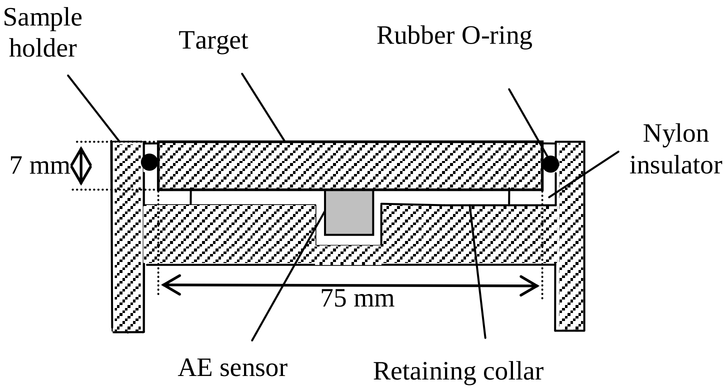

Figure 3.3: Sectional view of target plate in sample holder

3.1.2 AE apparatus

The AE acquisition system is shown schematically in **Figure 3.4**. The system comprised a target, an AE sensor, a pre-amplifier, a signal conditioning unit, a connector block, a data acquisition card and a computer with LabVIEW software for controlling the acquisition and storage of data in the PC as shown in **Figure 3.5**.

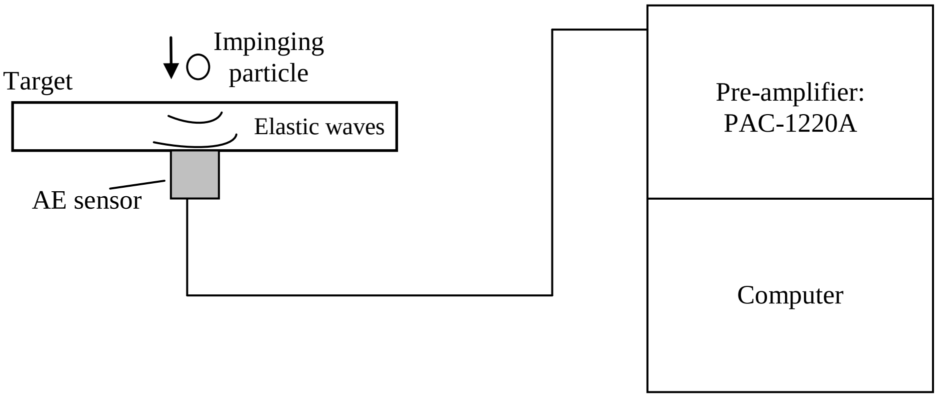

Figure 3.4: Schematic view of the AE acquisition system

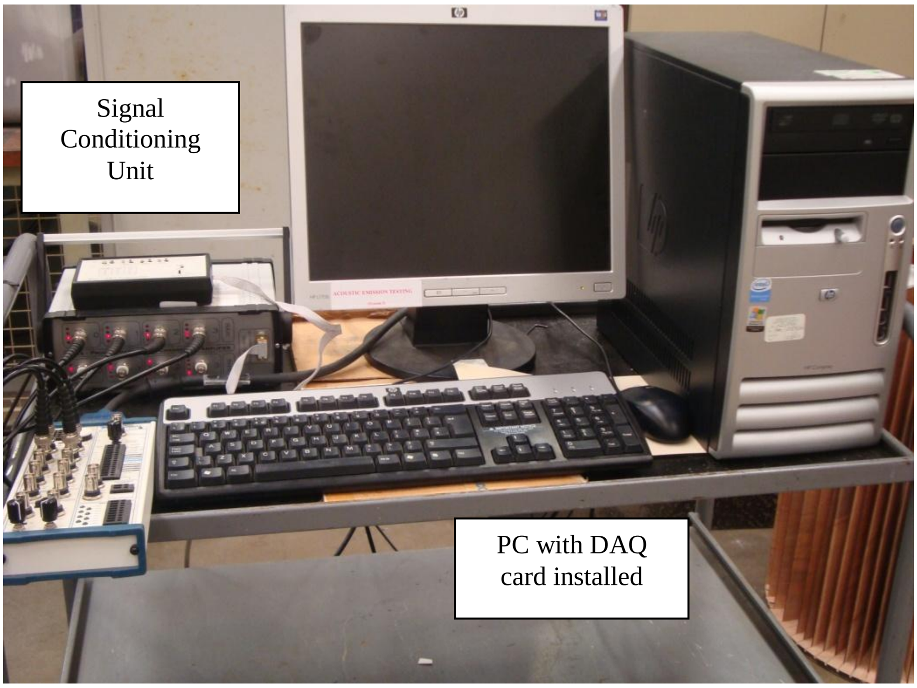

Figure 3.5: The AE acquisition system

The AE sensor, which was used for all experiments, was a commercially available "broadband" sensor of type Physical Acoustics (PAC Micro 80 D-93), based on lead zirconate titanate (PZT). The sensor was 10 mm in diameter and 12 mm in length, and is not truly broadband but produces a relatively flat frequency response across the range (0.1 to 1 MHz) and operates in a temperature range of -65 to 177 ^{o}C. The sensor was chosen because of its wide use in other research on machinery monitoring and its relative robustness. In order to obtain a good transmission between the test object and the AE sensor, silicone high vacuum grease was applied to the sensor face before mounting onto the specimen to fill any air gaps caused by surface roughness which might otherwise impair wave transmission. Before every test, the sensor was checked by performing a pencil lead break test to ensure proper connection and attachment of the sensor.

A preamplifier shown in **Figure 3.6a**, was used to amplify the AE signal to a level that can be transmitted and read by an ADC of type PAC model 2/4/6, having a switchable gain (20/40/60 dB) and internal band pass filter from 0.1 to 1.2 MHz to ensure that electronic noise outside the frequency range of interest is kept to a minimum. The preamplifier was powered by a +28 V power supply and used a single BNC connection for both power and signal. A programmable 4-channel signal conditioning unit (SCU) and a gain programmer (shown in **Figure 3.6b)** of in-house manufacture were used to power the AE sensors and pre-amplifiers as well as to adjust the gain level, if necessary, to ensure that all relevant parts of the signal could be examined.

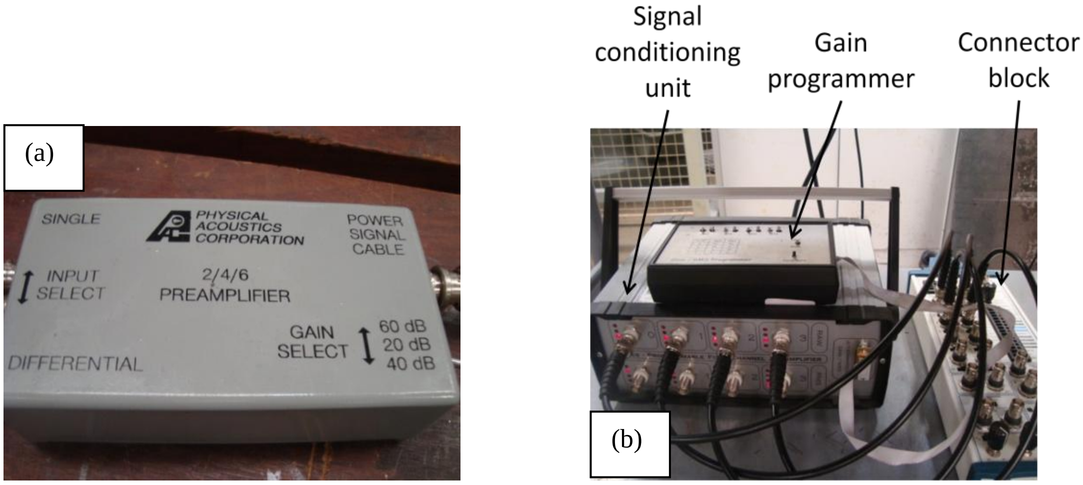

Figure 3.6: (a) Pre-amplifier, (b) Signal conditioning unit, connector block and gain programmer

Different levels of amplification were used both in the preamplifier and the gain programmer, according to experimental conditions. Prior to any signal processing, all amplifications due to different gains were normalized using a code in MATLAB.

A National Instruments BNC-2120 connector block (**Figure 3.6b)** was used to carry signals from the sensor to the data acquisition system. This was a shielded connector block with signal-labelled BNC connectors and included a LED to check the functioning of the hardware.

Since the acquisition of raw AE signals in the bandwidth 0.1 to 1MHz requires a high sampling rate, a 12-bit resolution National Instruments (NI), PCI-6115 data acquisition card (DAQ) was used, and assembled into an in-house built desktop PC as shown in **Figure 3.5**. The board allowed raw AE to be sampled and stored simultaneously at up to 10 M Samples/s for up to four channels (i.e. 2.5 M samples/s/channel) with a total onboard memory of 32 MB. The board supports only a differential input configuration and has a maximum voltage protection of 42 V. LabVIEW software from National Instruments was used to obtain the raw signals from the PCI-6115 board along with LabVIEW code [108] to control sampling frequency, number of acquired samples per channel, number of records, input range, pre-trigger data, trigger channel and trigger level. Most of the data in this study were acquired at 2.5 M Samples/s for different record lengths.

3.1.3 AE signal processing techniques

Once generated, AE waves radiate in all directions, propagating throughout the material in a variety of forms namely; compression, shear, Lamb and Rayleigh waves. Since the wave from a point source has a fixed amount of energy, the wave amplitude will decrease with distance. According to Pollock [109], this phenomenon, known as attenuation can be attributed to four reasons; geometric spreading of the wavefront, internal friction, dissipation of energy into adjacent media and velocity dispersion. Further signal distortion can occur when material boundaries are encountered where wave reflection, refraction, transmission and mode conversions can all occur. In reality, this means that AE waveforms are complex and using them to characterise the source can be difficult as AE signal waveform (amplitude-time) is affected by characteristics of the source, the path taken from the source to the sensor, the sensor characteristics and the AE measuring system. Therefore, signal processing is probably the most important single entity in a condition monitoring system whose aim is to determine the condition of a system under test. The aim can be translated as the need to extract a set of diagnostically significant features from the AE waveform.

For this particular application, there are multiple random sources arriving at an area quite close to the sensor, so some of the more sophisticated methods associated with source location and propagation are not needed. However, the target plate is thin and considerable ringing in the target can be expected.

3.1.3.1 Time domain analysis

Time domain analysis involves extracting time features from raw AE time series signals, which themselves can be categorised as continuous type or burst type. For AE burst signals, where the amplitude usually rises rapidly to a maximum value and decays nearly exponentially to the background noise level, a number of conventional features have been developed to describe the AE burst signal, and these were summarised in **Section 2.3.1**.

For the purpose of making an assessment of the correlation between particle incident energy and AE energy for single particle impact experiments, the AE impact energy *E* was calculated from the raw signal by integrating over the entire time record *t* above a threshold level of 10% of the maximum peak height, (measured as an amplified voltage, *V*):

$$E = \int_0^t V^2(t)dt \tag{3.1}$$

In practice, even at 2.5 MHz sampling rate, the AE associated with multiple particle impact events may well overlap. In order to simplify the signal processing for peak searching, each record was divided into intervals and then the root mean square RMS for each interval was calculated. It should be noted here that other time domain analysis using different thresholding techniques are described later.

3.1.3.2 Frequency domain analysis

Frequency domain analysis offers further options for investigation of AE signals. It involves obtaining signal spectral characteristics to estimate the distribution of the signal energy in the frequency domain. In general, frequency analysis involves the decomposition of time-series data into the frequency domain using a Fast Fourier Transform (FFT) algorithm [110] or Welch's Power Spectral Density PSD estimate [111]. Frequency analysis is sometimes used to filter out noise from a signal in cases where AE sources are masked by the noise or the frequency structure may be used as a diagnostic indicator itself. In the first of these, if the required filter is carefully identified and constructed, then this can allow removal of noise in narrow frequency bands and accordingly enhance signal-to-noise ratios, provided, of course, that the noise has a different frequency structure to the signal.

Another application of the FFT which is of particular use is called demodulated resonance analysis [112]. The technique involves averaging the signal using a sliding root mean square RMS to reveal lower frequencies in the envelope of the signal, where the AE wave acts as a carrier frequency for the lower frequency information, **Figure 3.7**. Again, the structure of the demodulated spectrum can itself be used as a diagnostic indicator, or can be used to identify, and remove, noise.

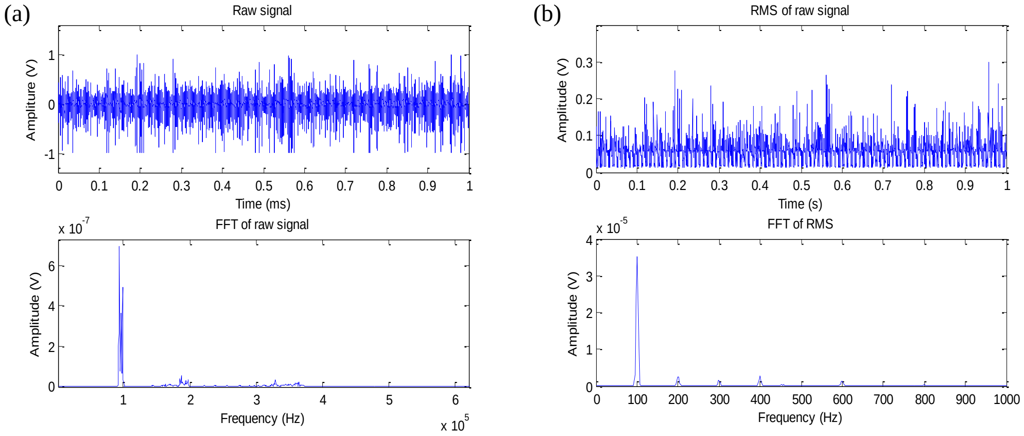

Figure 3.7: Steps of demodulation frequency analysis, (a) raw AE signal, (b) RMS of the AE signal, using averaging time of 0.2 ms

3.2 Calibration tests

The calibration tests were carried out to determine AE propagation characteristics in the target and to assess the repeatability and functionality of the AE system. First, the simulated AE source is described, and then, the three calibration tests for the sensor in different installations are presented.

All AE signals associated with the calibration tests were acquired at 2.5 MHz for a record length of 20 ms, and a total of ten lead breaks were performed at each location. The total energy in each record was obtained using the method described in **Section 3.1.3.1**.

3.2.1 Simulated source for calibration tests

A pencil lead break test is a well established procedure for generating simulated AE sources. Therefore, a commercial mechanical pencil with an in-house machined guide ring was used to generate simulated AE sources by breaking a 0.5 mm diameter and 2-3 mm length 2H pencil lead, as recommended by ASTM standards (E976-99) [113]. The so-called Hsu-Nielson source along with its guide ring is shown in **Figure 3.8.** The guide ring made it possible to maintain the same orientation of the pencil for all tests and hence break the lead in a consistent way.

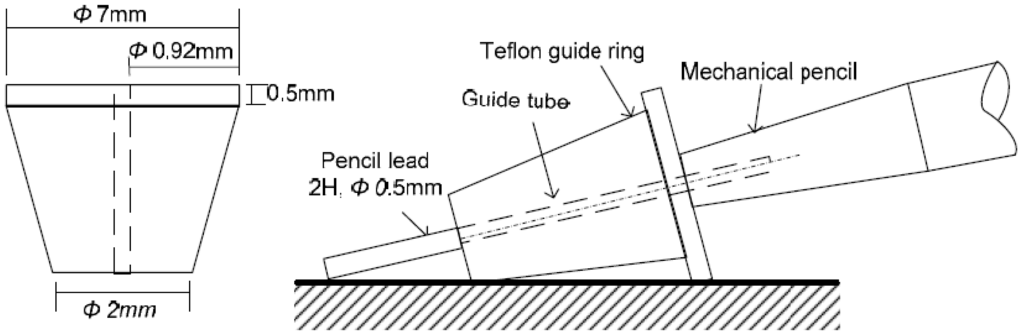

Figure 3.8: Hsu-Nielsen source and guide ring [113]

3.2.2 Calibration tests on steel cylinder

Using a large steel block with a pencil lead break source can provide a reference calibration for characterizing a sensor. So, AE signals were acquired at four positions separated circumferentially by 90^o on a large cylindrical steel block of dimension 300 mm diameter and 200 mm height as shown in **Figure 3.9**. The AE sensor was placed on the surface of the block at the same radial distance (120 mm) from the source at the centre of the top surface, and was installed and de-mounted 5 times at each position with records of 10 pencil-lead breaks being acquired each time, so that 50 breaks were recorded for each position (indicated **P** in the Figure). Then, the sensor was moved to another position and the entire process was repeated.

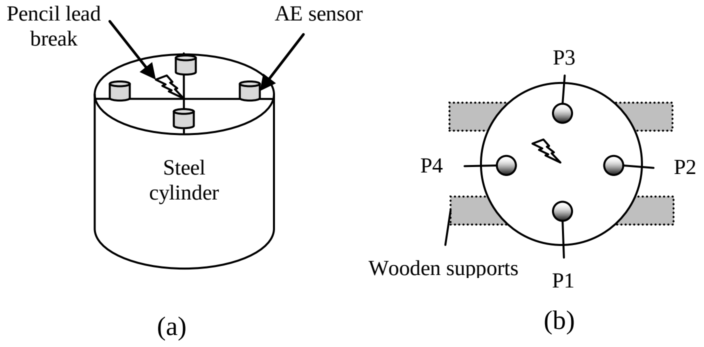

(a) (b)

Figure 3.9: Sensor calibration set-up (a) schematic view of steel cylinder arrangement, (b) plan view of sensor positions relative to the cylinder and supports

Figure 3.10 shows the AE energy recorded for all of the 50 pencil-lead breaks at each of the four positions, each point showing the average and the variation over the 50 lead breaks. As can be seen, P1 and P3 show similar (lower) values with less scatter in recorded AE energy than P2 and P4. This effect is probably due to the configuration with the wooden support underneath P1 and P3 providing a leakage path.

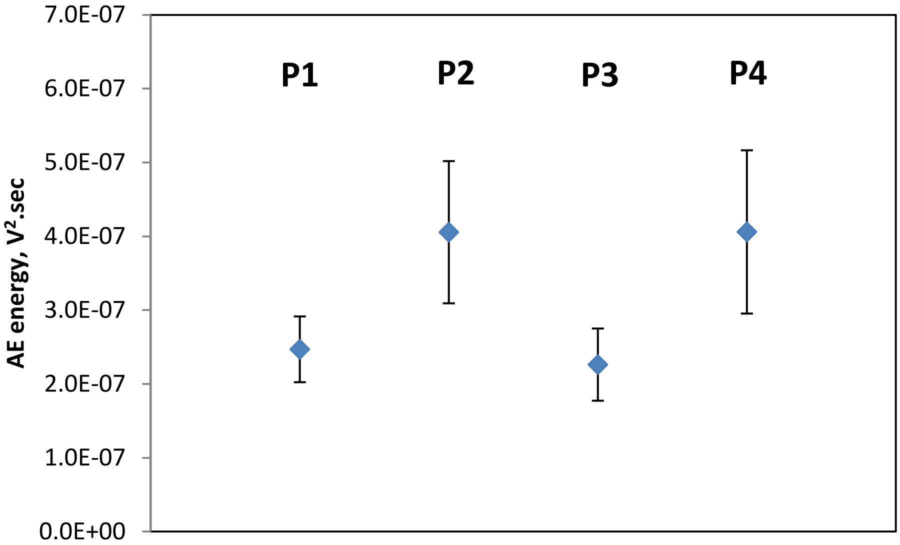

Figure 3.10: AE energy recorded at the four calibration positions on the steel cylinder

Figure 3.11 shows the energy distribution as average, minimum, and maximum AE energy recorded, for the five independent trials in which the sensor was removed and replaced at each of the four positions. As can be seen, the energy recorded for a given installation varies considerably and this can be attributed to the variation of the pencil-lead break (within group variation). In addition, the energy recorded between installations at the same position is different and this is attributed to changes in coupling conditions and magnetic clamp tightening force. In order to analyse the variance between a given installation (the effect of de-mounting the sensor) and among installations (the effect of lead breaks) quantitatively, the data for each placement at each position was grouped and ANOVA testing was carried out. The indicator F_{value} was compared with F_{crit} (2.57 for the degrees of freedom involved and at the 95% confidence level) and, as can be seen in **Table 3.4**, F_{value} is always greater than F_{crit} indicating that the variation due to removal and replacement of the sensor is more important than the variation in pencil lead breaks at all positions. In addition, the data for each position was grouped to analyse the variance between positions and among positions which enables the comparison between the effect of position and the effect of lead break and sensor replacement. This time F_{value} was 74, much greater than F_{crit} indicating that the effect of changing position is more important than the effect of pencil lead break and sensor replacement.

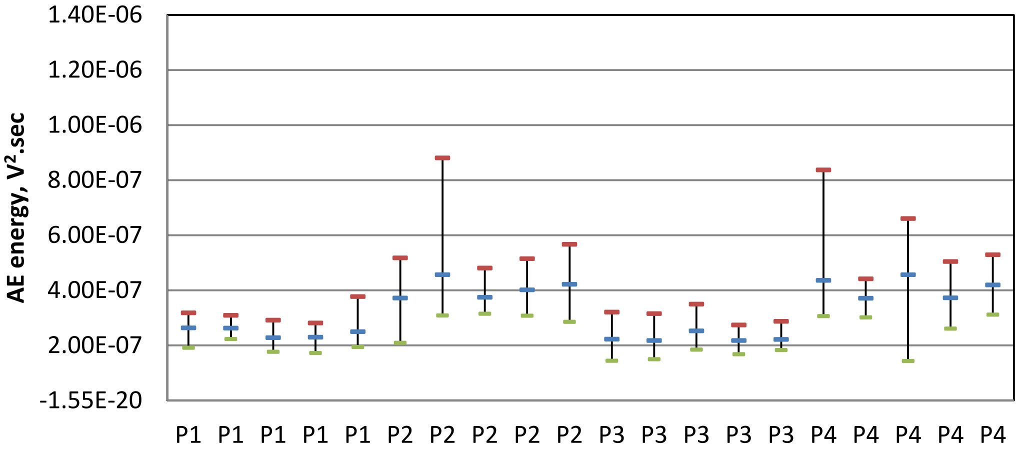

Figure 3.11: Recorded AE energy for simulated sources at four positions (results of five independent tests between which the sensor was removed and replaced)

Position	F_{value}	F_{critc}
1	4.56	2.57
2	3.38	2.57
3	5.93	2.57
4	3.04	2.57

Table 3.4: Summary of ANOVA results comparing the effect of demounting the sensor with the effect of pencil lead breaks at each position

3.2.3 Calibration tests on target

Since the target was relatively small, it was necessary to obtain an indication of the type of propagation behaviour shown by the wave generated from a simulated source, as well as understanding any time or frequency domain characteristics introduced by the target.

The AE sensor was placed at the rear surface of the target on its epicentre, as it is placed for all of the experiments carried out during this study, and AE was recorded with the simulated source placed at four different positions on the face of the target as shown in

Figure 3.12. Two independent tests were carried out, acquiring ten pencil leads at each of the four positions, after which the sensor was removed and replaced on the target plate, giving a total of 20 AE records at each position.

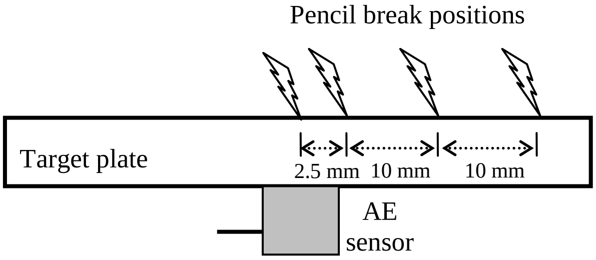

Figure 3.12: Schematic view of the target calibration arrangement

Figure 3.13 summarises the recorded AE energy for the pencil lead breaks at all positions represented by average points and the range for the ten lead breaks at each position for each test. It is clear that significant change in recorded AE energy occurs as the source was moved away from the plate centre. It might be noted that the variation in AE energy at each position due to the variation of the pencil-lead break was smaller than the variation due to sensor removal and repositioning as was found in the calibration tests.

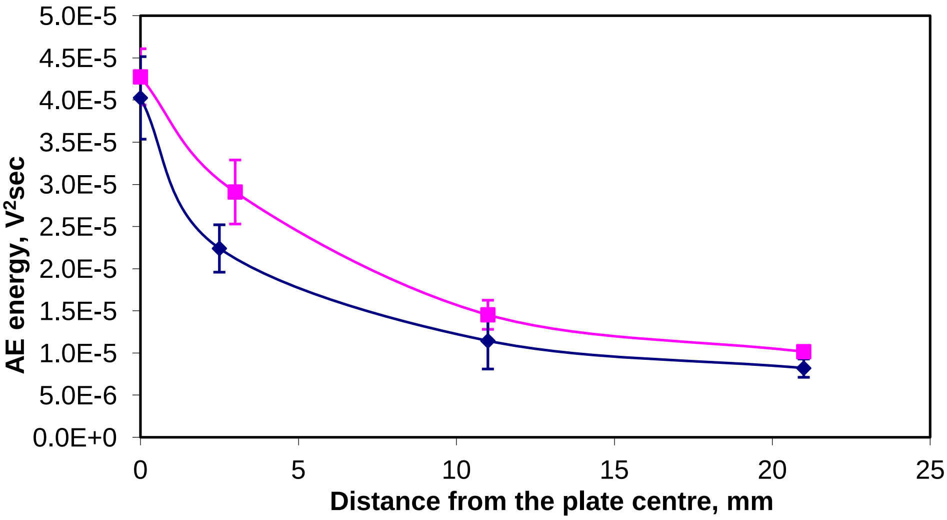

Figure 3.13: Recorded AE energy for simulated sources across the target diameter (results of two independent experiments between which the sensor was removed and replaced)

Because the experiments involve re-installing the sensor at different times, it was necessary to establish the repeatability of AE energy measurement and quantify the effect of sensor remounting at different installations. Therefore, at a fixed position (centre of the target plate), 5 pencil lead breaks were recorded in each of ten independent batches after each of which the sensor was removed and replaced in the same position. As can be seen in **Figure 3.14**, the energy recorded between installations is different and this is might be attributed to changes in coupling conditions and clamp tightening force.

As with the steel cylinder calibration tests, the data for each installation was grouped to carry out an ANOVA test. The F_{value} of 4.1 was greater than F_{crit} (2.1 for the degrees of freedom involved and at the 95% confidence level), indicating that the variance associated with de-mounting the sensor is more significant than that of the pencil lead break, confirming the finding with the steel cylinder. Therefore, the sensitivity variation for a given installation (approximately 15%) needs to be taken into account when comparing measurements made at different times where the sensor has been removed and re-mounted again.

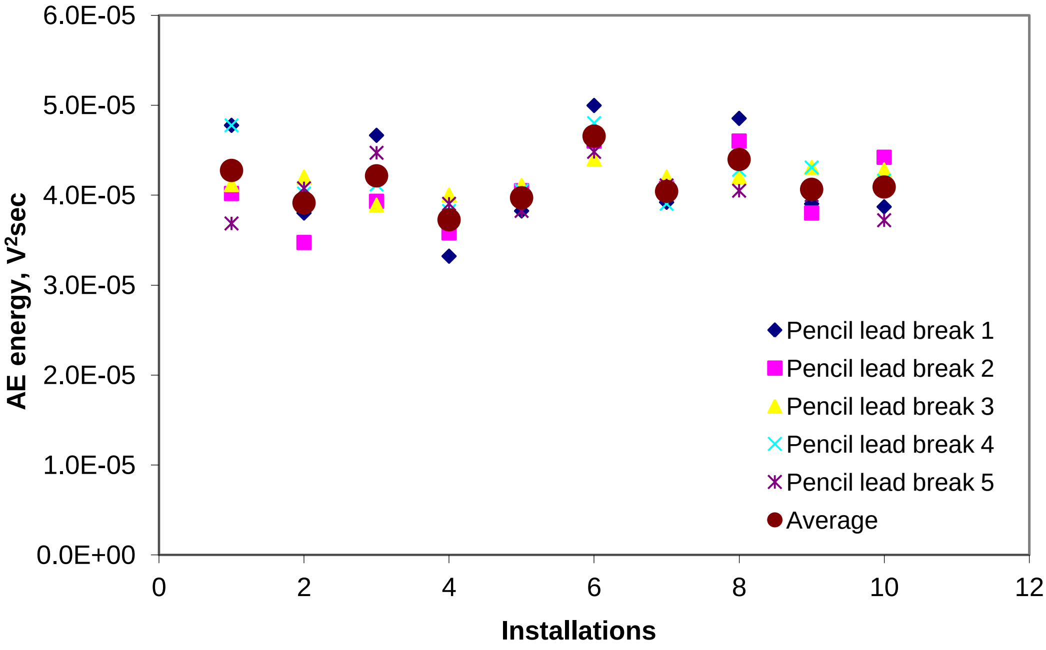

Figure 3.14: Testing of repeatability of recorded AE energy using H-N source

Figure 3.15a shows the time-domain of a typical raw AE signal due to a pencil lead break at the centre of the target plate, whereas, using the same sensor, a typical raw AE signal due to a pencil lead break on the face of the steel cylinder is shown in **Figure 3.16a**. To compare these signals **Figure 3.16b** shows part of the record from

Figure 3.16a expanded to a length similar to that shown in **Figure 3.15a**. Cleraly both test objects exhibit considerable ringing with the target plate decaying more rapidly than the cylindrical block. In order to understand the causes of the ringing, **Figure 3.15b** and **Figure 3.16c** show magnified segments of the records depicted in **Figure 3.15a** and **Figure 3.16b,** respectively. As can be seen, the AE signal in the target plate is of higher intensity than that in the steel block. **Figure 3.16c** also shows two clear wave reflections whose return times are consistent with a Rayleigh surface wave reflecting from the edges of the cylinder nearest to and diametrically opposite to the sensor, while reflection from the bottom of the cylinder is not clearly observable above the background. In the target plate, the return time of a compression wave reflected at both surfaces is observable, but this time is so short as to be within the period of the AE waves themselves. These signals indicate a strong influence of the carrier structure on the AE recorded. Therefore, in order to quantify the effect of the target thickness on AE energy, **Figure 3.17** shows the variation in AE energy for pencil lead breaks on the face of the target plate and on the face of the steel cylinder, where each point represents the average, maximum, and minimum of 10 AE records. The high energy recorded for the target plate is therefore associated with many reflections from the faces and little absorption at each reflection.

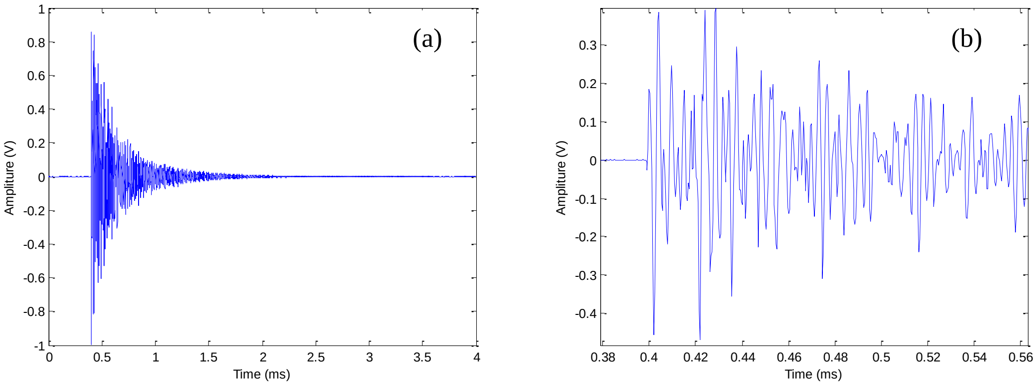

Figure 3.15: Typical raw AE signal for a pencil lead break on the face of the target plate: (a) a full record, (b) a magnified view of (a)

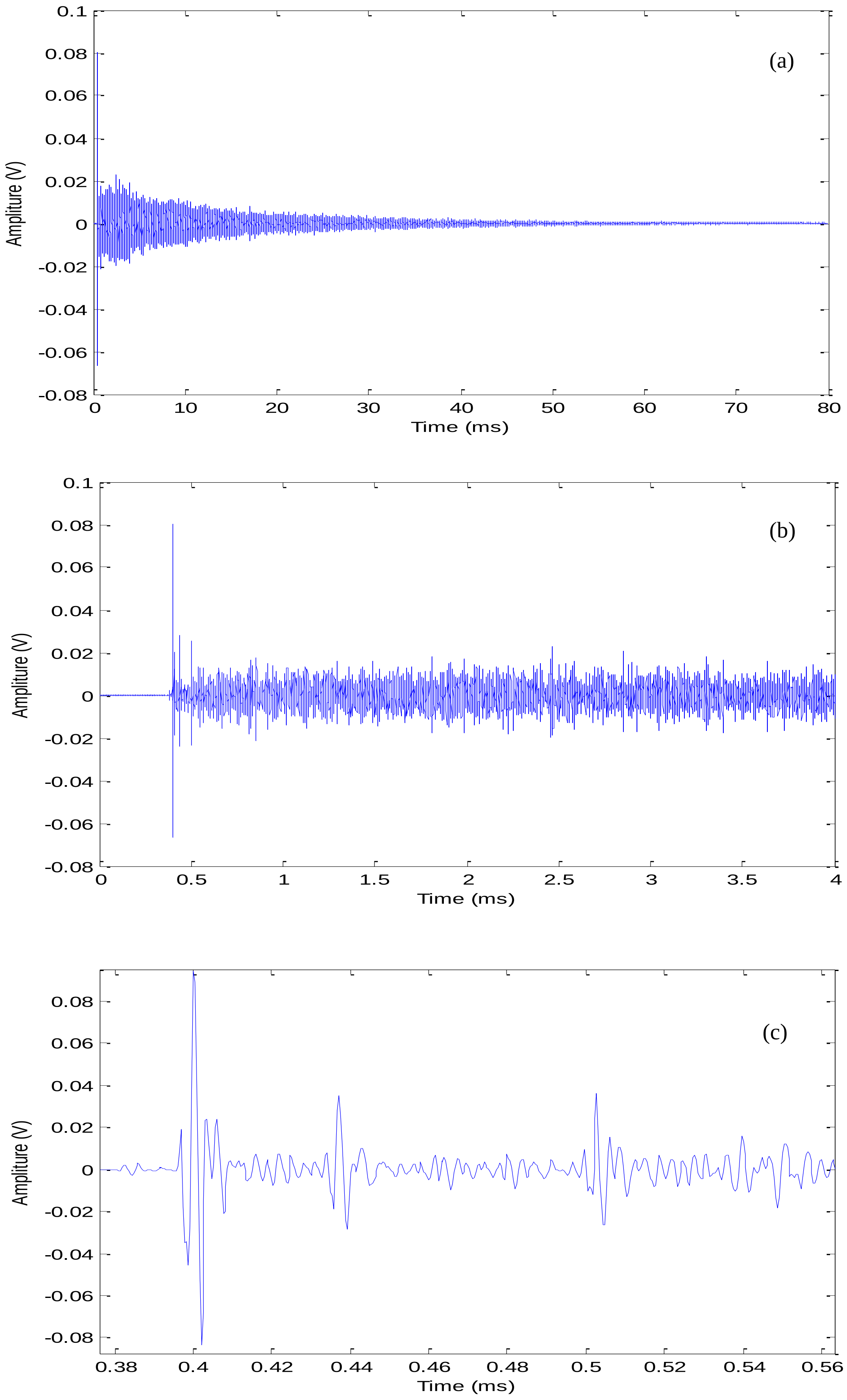

Figure 3.16: Typical raw AE signal for a pencil lead break on the face of the steel cylinder: (a) a full record, (b) a magnified view of (a), (c) a magnified view of (b)

The decay time was obtained from the AE records as the time between the first and final appearance of the AE above a threshold level of 15% above the continuous background level. **Figure 3.18** shows the variation in AE decay time for pencil lead breaks on the face of the target and on the face of the steel cylinder, where each point again represents the average, maximum and minimum of 10 AE records. As can be seen, the decay time for the target plate is much shorter than that for the steel cylinder, most likely because there are many more reflections per unit time for the target plate but also possibly due to differences in the reflections coefficients for Rayleigh and compression waves.

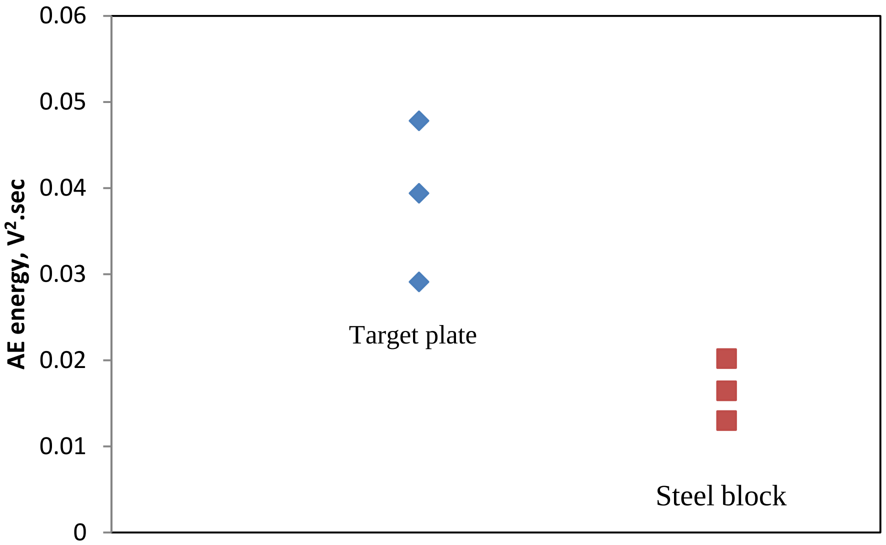

Figure 3.17: AE energy for a pencil lead break on the face of the target plate and on the face of the steel cylinder

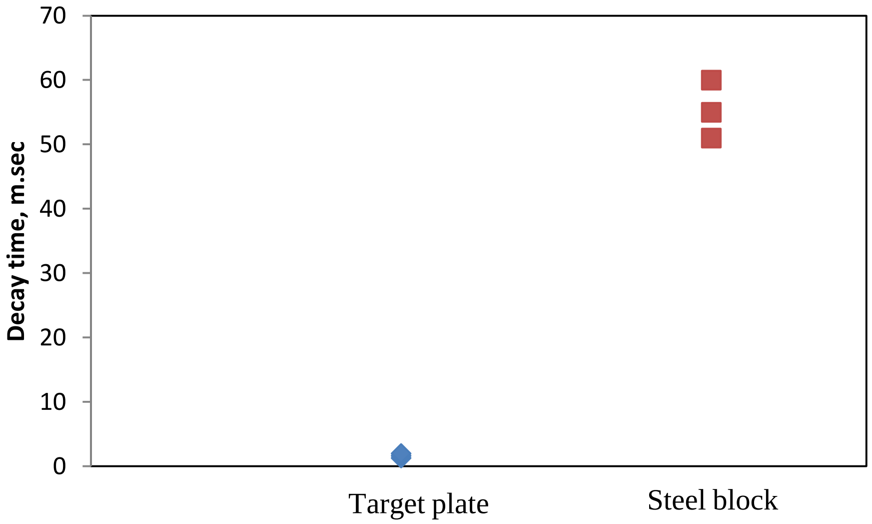

Figure 3.18: AE decay time for a pencil lead break on the face of the target plate and on the face of the steel cylinder

Figure 3.19a shows a typical frequency domain plot of a raw AE signal due to a pencil lead break at the centre of the target plate whereas, using the same sensor and source, **Figure 3.19b** shows a typical frequency domain plot for the steel cylinder. As can be seen, the spectrum for the target plate shows that most of the power is focused in one very narrow band centred on a frequency of around 280 kHz, and the proportion of energy in this band was checked for the 10 AE records and was found to vary from 45% to 60%, against 56% in **Figure 3.19a**. This frequency corresponds to the frequency with which a compression wave would return having traversed twice the target plate thickness (14 mm), at a speed in the published range for compression waves in steel (3000-5000 ms^{-1}) [108], i.e. a frequency range of (210-350 kHz). **Figure 3.19b** shows two dominant spectral peaks; a band centred on a frequency of around 160 kHz and a band centred on a frequency of around 240 kHz. Again, the proportion of energy in these two bands was checked for 10 AE records and was found to vary from 17% to 25% for the first band and from 15% to 20% for the second band, while the example in **Figure 3.19b** is 23% and 18%, respectively. The frequencies corresponding to surface wave reflections are more difficult to estimate, but the return time from the near edge taking a surface wave speed of 3000 ms^{-1} [108] and twice the sensor-edge distance of 6 cm gives a frequency of 50 kHz, while the frequency corresponding to reflection from the far edge (approximately 1.5 diameters of the cylinder) was calculated to be around 7 kHz. Although these low frequencies are absent from the raw AE spectrum, the observed bands are close to low multiples of the 50kHz frequency. In summary, the spectral analysis confirms reasonably well the preliminary observations about the ringing in the two structures concerned, especially given that the frequencies involved are distorted somewhat by the characteristics of the sensor (as shown in the calibration certificate, *Appendix A*).

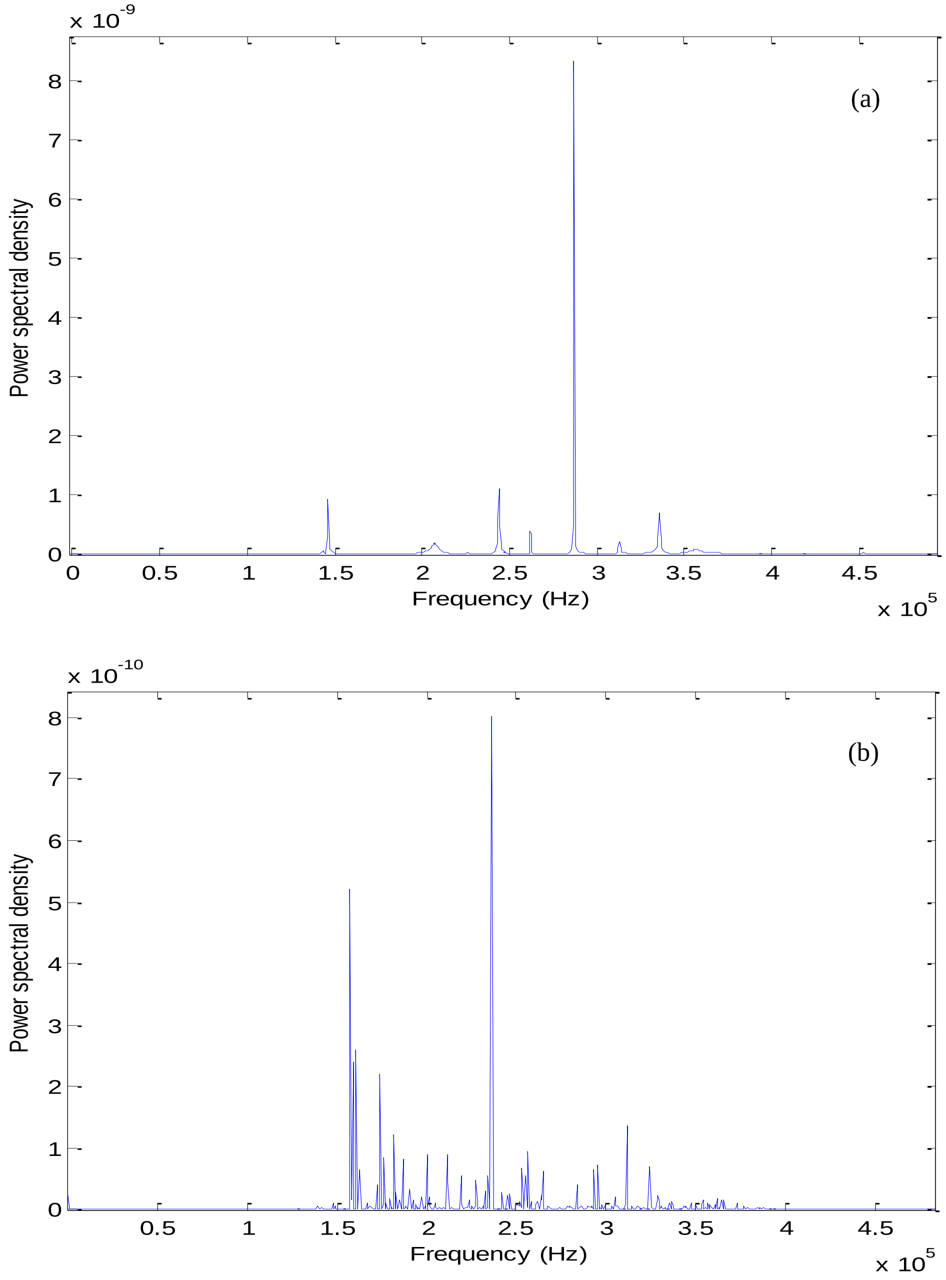

Figure 3.19: Typical raw AE frequency domain for a pencil lead break: (a) on the face of the target plate, (b) on the face of the steel cylinder

3.3 Particle impact tests

Since the primary cause of erosion is the energy transmitted from impinging particles to the target, three distinct types of experiments were carried out to monitor AE from particle impact; airborne particle impacts (both free-fall and air-assisted), slurry impact using a slurry jet impingement rig, and particle impacts in a flow loop. These experiments were designed to progress from idealised experiments in which control over particles was relatively good to more realistic experiments with limited control over individual particles as the behaviour of the flow near the surface has a major influence on particle motion. The rationale behind each of the experiments is described below.

3.3.1 Free fall and airborne particle impact tests

These measurements were aimed at detecting the amount of energy dissipated in a carbon steel target during airborne particle impact in a situation where the kinetic energy of the particles was under relatively close control. The second important aim was to use single particles (or relatively small numbers of particles) in order that a model for single-particle impact AE energy could be obtained as an aid to analysing further experiments. Three experimental arrangements were used to investigate three impact regimes; low velocity-low mass (impact speeds of 1.5 ms^{-1} to 3 ms^{-1} and masses of 4.9×10^{-6} to 2.3×10^{-4} g), low velocity-high mass (sphere masses of 0.001 to 2 g), and high velocity-low mass (impact speeds of 4 to 16 ms^{-1}). Within each of these regimes, both single-particle and multiple-particle impacts were studied in order to investigate the effect of overlapping events and determine the time and kinetic energy resolution of the target-sensor arrangement. Two variables, particle diameter and particle impact speed, both of which affect the energy dissipated into the material were investigated and correlated with AE energy. The essential experimental approach was to control, as far as possible, the impact of individual particles, and groups of particles, impinging normal to the carbon steel target, whilst monitoring the AE.

Single and multiple particle impacts were conducted either at “low velocity”, where particles were dropped under gravity (dropping distances of 10 cm, 20 cm, 30 cm and 40 cm) or at “high velocity” where particles were entrained into an air stream. Slightly different arrangements were made for particle handling for single and multiple impacts, respectively.

Figures 3.20 (a) and (b) show the two arrangements for individual particle free-fall impact, both of which used glass guide tubes of lengths from 100mm to 400mm in order to provide different impact speeds. For larger particles individual steel balls or glass beads of sizes specified in **Table 3.1** were positioned at the top of a glass tube using tweezers and released to drop onto the target, **Figure 3.20a**. For smaller (sieved) particles a small quantity of the appropriate size fractions (listed in **Table 3.1)** was placed on a vibrating tray with a slight slope so that particles fell into the guide tube individually, **Figure 3.20b**.

Preliminary tests using pencil lead breaks as a simulated AE source at different positions on the face of the target showed significant changes in recorded AE energy as the source was moved away from the plate centre, as can be seen in **Figure 3.13**. Therefore, different glass guide tube diameters were employed in order to restrict the impact area whilst not interfering with the fall of the particles. The largest diameter used was 10 mm so that the maximum expected variation in energy due to the position of the impact was around 40%.

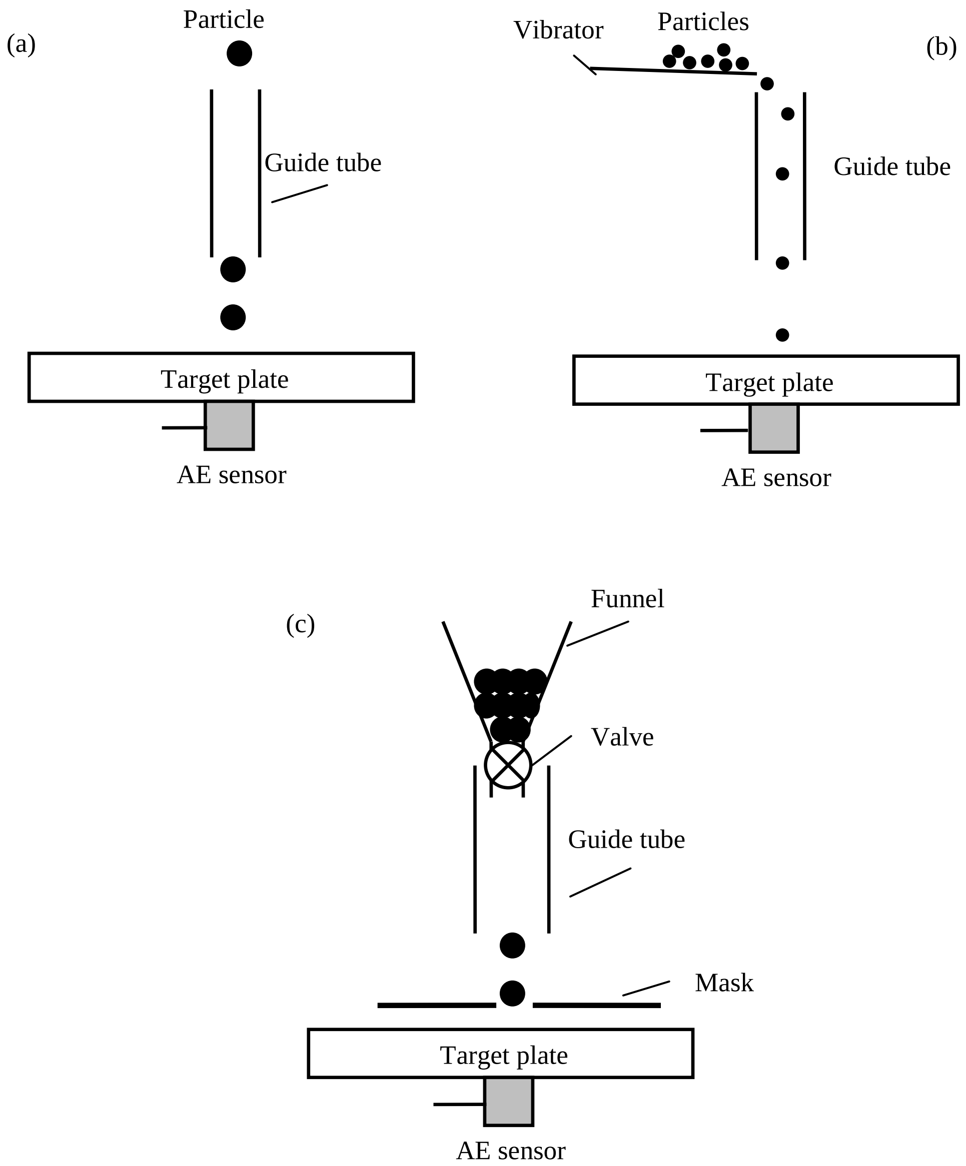

Figure 3.20: Free fall impingement arrangements: (a) individual large particles, (b) individual small particles using vibrating ramp, (c) multiple small particles

For multiple impact experiments small quantities (approximately 5g) of the silica sand fractions specified in **Table 3.1** were loaded into a funnel which was placed above the guide tube as shown in **Figure 3.20c**. Opening a valve in the funnel allowed the particles to drop into the guide tube at a relatively reproducible rate depending on the particle size (approximately 0.23 gs^{-1}). In order to limit the number of particles hitting the target surface in a given time (and hence reduce the likelihood of overlapping signals) and also to focus the stream on the area opposite the sensor, a mask plate with a 4 mm diameter hole concentric with the sensor was fixed above the target plate. All particles passing through the mask hole were collected for each experiment in order to determine approximately the number of particles generating the signal. All single and multiple impact experiments were repeated ten times.

The AE sensor was mounted on the centre of the rear surface as shown in **Figure 3.20** and coupled by means of vacuum grease. The pre-amplified data were acquired at 2.5 MHz for record lengths which depended on the particle size, and which were determined on the basis of some preliminary drops in order to avoid picking up signals due to return after rebound.

For the free-fall impact system, the smaller particles were significantly affected by viscous drag and some did not reach their terminal velocity during the free-fall. Therefore, it was necessary to estimate the velocity using an equation of motion:

$$\frac{\pi D^3}{6}\rho_p\frac{dV_p}{dt}=\frac{\pi D^3}{6}\rho_p g-\frac{1}{2}\rho A_p C_d V_p^2 \qquad (3.2)$$

where the terms on the right hand side represent the weight and viscous drag, respectively, and ρ_p and ρ are the particle and fluid densities, respectively, A_p is the particle projected area and C_d the drag coefficient, which depends on Reynolds number, and was taken from Brucato *et al.* [114]: $C_d=\frac{24}{\mathrm{Re}}\left(1+1.25\mathrm{Re}^{0.75}\right)$. Because **Equation 3.2** is non-linear, it was necessary to solve this numerically, which was done using a Runge-Kutta iteration, and assuming the particles to be spherical, to yield the particle impact velocities shown in **Table 3.5**.

Dropping distance (cm)	**Particle fraction* (μm)**									
	125-212	212-300	300-425	425-500	500-600	125-180	180-212	212-250	250-300	300-425
10	0.995	1.1	1.3	1.35	1.33					
20	1.1	1.5	1.65	1.78	1.8	1.06	1.3	1.44	1.56	1.7
30	1.2	1.7	1.9	2.1	2.17	1.1	1.4	1.6	1.76	2
40						1.19	1.48	1.7	1.91	2.17
	Steel sphere diameter (mm)					**Glass Bead diameter (mm)**				
	1	1.5	2.5	3.2	4	0.9	2	3.5	4.1	6
10	1.395	1.396	1.399	1.4	1.401	1.367	1.393	1.396	1.397	1.4
20	1.96	1.965	1.973	1.975	1.977	1.902	1.956	1.97	1.973	1.973
30	2.39	2.4	2.413	2.417	2.42	2.298	2.382	2.404	2.41	2.414

* Values calculated for mean size in the range.

Table 3.5: Free-fall particle impact velocity (ms^{-1}), estimated from **Equation 3.2**

The air-assisted impingement arrangement (**Figure 3.21**) consisted of an air compressor, a pressure regulator to adjust the air pressure, a pressure gauge to read the pressure drop across the nozzle, and a needle valve and rotameter to measure and control the air flow rate. As before, for single particle impacts, individual glass beads or silica particles from the fractions specified in **Table 3.1** were introduced into a guide tube. Then the particles were accelerated by the air flow down the guide tube. For multiple impact experiments, the particle fractions listed in **Table 3.1** were, as before, loaded into a funnel and, once the valve was opened, could roll down through the feed tube to be drawn into the gas stream and then accelerated down towards the target. The cylindrical nozzle/guide tube was of internal diameter 12 mm and length 300 mm, and the nozzle exit plane was held parallel to the target plate to ensure that the particle stream axis was normal to the plate. Again, a steel mask with a 4 mm diameter hole concentric with the sensor was fixed above the target plate in order to limit the number of particles hitting the target surface in a given time and also to limit the stream to a relatively small area of the target. The distance between the guide tube exit and the mask was 20 mm, and the distance between the mask and the target was 30 mm. Particles which passed through the mask and struck the surface of the target were collected using a circumferential mesh trap and weighed using a digital microbalance to give an estimate of the number of particles landing on the surface for a given 5-second run.

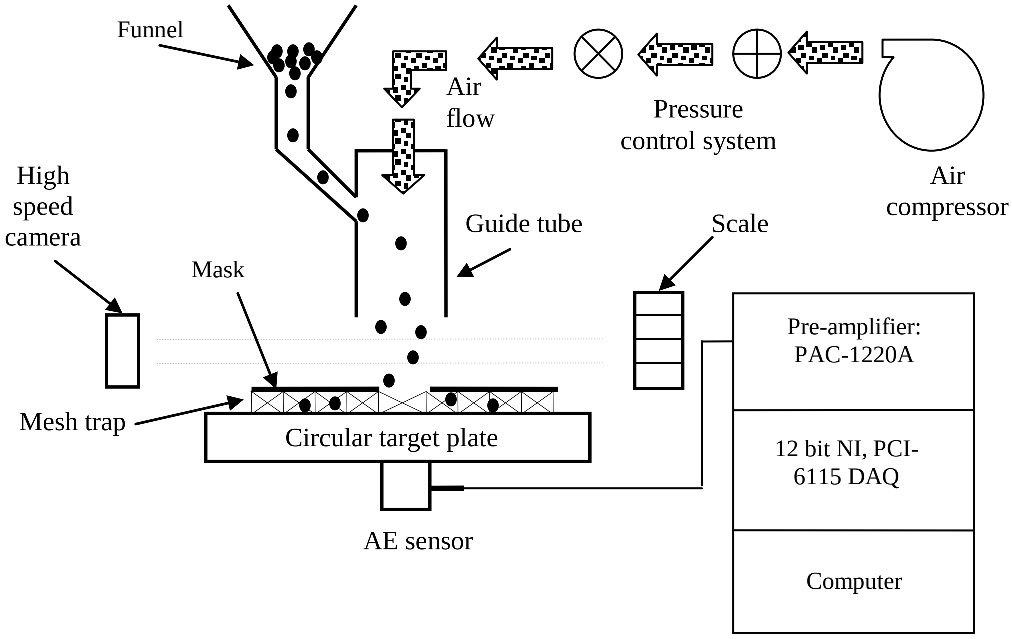

Figure 3.21: Air-assisted particle impact test arrangement

As before, the AE sensor was mounted and coupled by means of vacuum grease to the opposite surface of the target plate directly under the impingement area as shown in **Figure 3.21**. The pre-amplified data were acquired at 1 MS/second for a record length of 5 seconds. Preliminary tests were performed in which the specimen was exposed to the air stream from the nozzle alone without any particles. No detectable AE signal was observed indicating that the AE signals were caused by the effect of particle impacts rather than the effect of the accompanying air stream.

Stevenson and Hutchings [57] have provided an empirical power-law model for the velocity of particles entrained in an air stream confined to a nozzle:

$$V_p^{\ 2} \propto \frac{P_n}{d_p^{0.57} \rho_p^{\ 1.08}} \tag{3.3}$$

where P_n is the pressure drop along the nozzle, d_p is the particle diameter and ρ_p is the particle material density. In order to calibrate the rig for air-assisted impact, the impact velocities of glass beads in the size ranges 500-600 μm and 850-1000 μm were measured photographically with the aid of a high speed camera and scale as shown in **Figure 3.21**. **Figure 3.22** shows that the measured data fit the Stevenson-Hutchings model to within the experimental error.

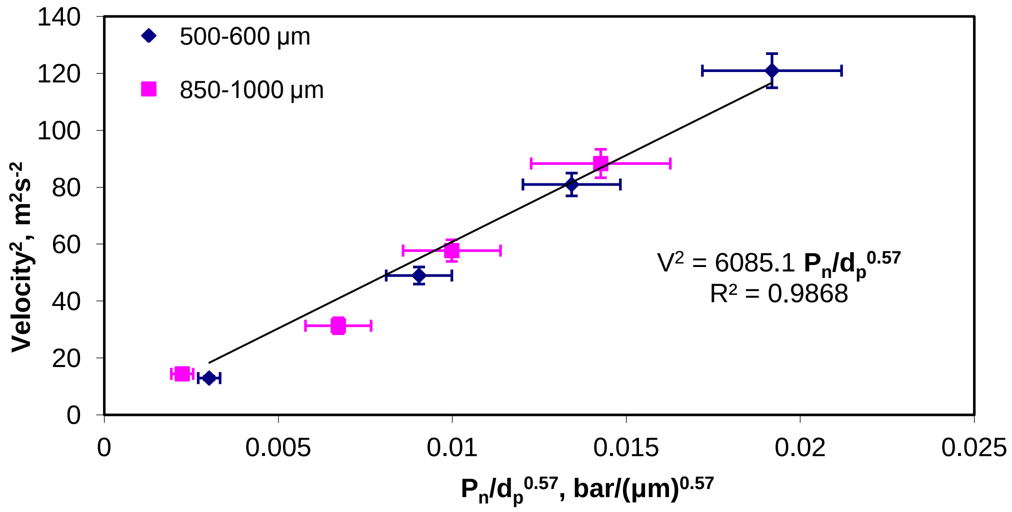

Figure 3.22: Variation of particle velocity with nozzle pressure drop for two particle size ranges

In order to obtain a semi-empirical model to correlate the particle velocity with air speed another model, suggested by Heuer *et al* [115], was used for pressure drop, ΔP, along a tube with turbulent air velocity, U:

$$\Delta P = \lambda \frac{l_{tube}\rho_{air}}{d_{tube}2}U^2 \qquad (3.4)$$

where λ is the tube skin friction coefficient, l_{tube} is the length of the tube, d_{tube} is the internal diameter of the tube and ρ_{air} is the density of the air.

Combining **Equations 3.3** and **3.4**, taking into consideration that the tube characteristics are constants, yields a relationship between particle velocity and air speed along the tube: $V_p{}^2 \propto \frac{U^2}{d_p^{0.57}}$

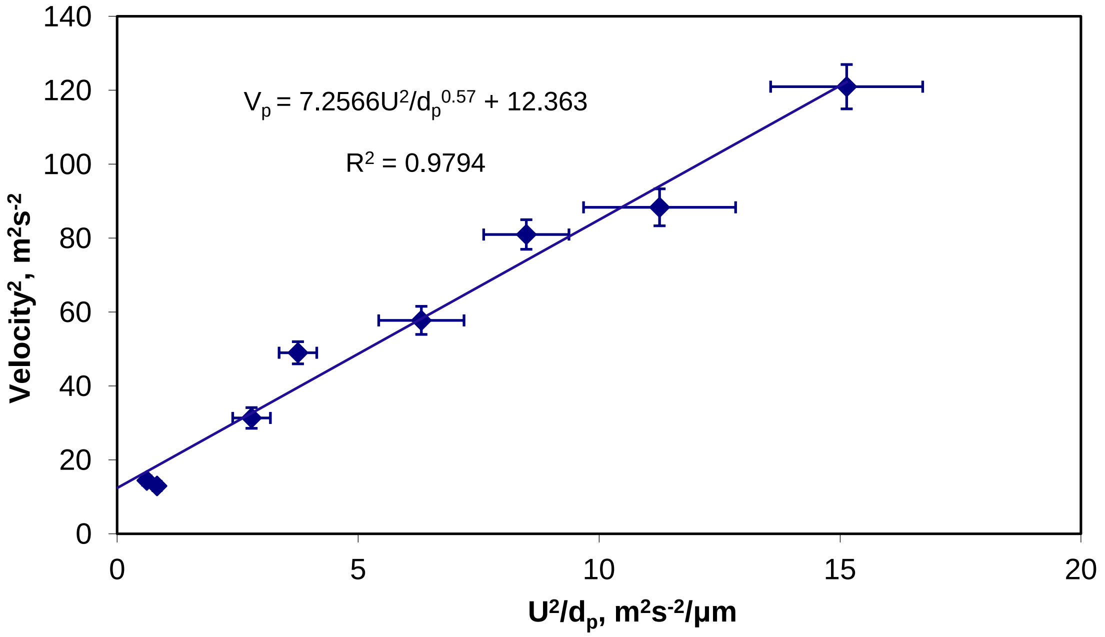

Figure 3.23: Dependence of particle velocity on air speed and particle diameter

Figure 3.23 shows that the particle velocity can be described by the relationship:

$$\frac{\quad}{\quad} \tag{3.5}$$

where d_p is the particle diameter in microns and U is the air velocity in ms^{-1}. This semi-empirical relationship was used to assess the nominal particle velocity for all of the air-assisted impact experiments.

3.3.1.1 Statistical distribution model

Experiments were performed with sieved (to British Standard 410) samples of solid spherical glass beads and angular silica sand whose size distributions are given in Table **3.6.** The nominal particle velocity, V_p, was controlled by adjusting the air velocity and was determined using **Equation 3.5**. For each combination of size fraction and impact speed, five runs were carried out giving a total of 120 5-second records of full bandwidth AE. The particle arrival rate shown in **Table 3.6** was determined by weighing the particles recovered from the mesh trap, dividing by the average mass of a particle and then dividing by the length of the record which contained AE events, found by inspection of the individual records. Ten single impacts were also recorded for each size range and each velocity, the limited number being dictated by the painstaking nature of these experiments. Accordingly, the single particle records were used as a cross-check, rather than as a primary data source.

A simple auxiliary experiment was also performed by dropping individual glass beads of sizes listed in **Table 3.1** from various heights onto the target. By using a high-speed camera assess the particle speeds before and after impact, V_{p1} and V_{p2}, it was possible to obtain an average value of the coefficient of restitution $e = \frac{V_{p2}}{V_{p1}} \approx 0.65$.

Particle type	**Particle size fraction (µm)**	**Size distribution function**	**Nominal velocity (ms^{-1})**	**Average arrival rate (s^{-1})**
silica sand	125-180	$\frac{1}{205}\exp\left[-\frac{(d-175)^2}{13448}\right]$	4.9	4238
			8.3	4238
			11.8	2928
			15.5	3140
	212-250	$\frac{1}{122}\exp\left[-\frac{(d-252)^2}{7442}\right]$	4.7	910
			7.5	803
			10.6	770
			13.8	653
	300-425	$\frac{1}{255}\exp\left[-\frac{(d-320)^2}{70808}\right]$	4.4	151
			6.8	162
			9.5	180
			12.3	231
glass beads	500-600	$\frac{1}{135}\exp\left[-\frac{(d-586)^2}{5832}\right]$	4.3	73
			6.3	70
			8.6	84
			11	110
	600-710	$\frac{1}{2075}\exp\left[-\frac{(d-668)^2}{13778}\right]$	4.2	54
			6	49
			8.2	69
			10.5	69
	710-850	$\frac{1}{3525}\exp\left[-\frac{(d-776)^2}{39762}\right]$	4.1	27
			5.8	35
			7.9	29
			10.1	47

Table 3.6: Summary of particle and particle stream conditions

3.3.2 Slurry impingement tests

In this set of relatively controlled impingement experiments, the carrier fluid was changed to a liquid in order to assess the extent to which the findings with air-borne particles could be carried over to this medium. The experimental set-up consisted of a slurry impingement rig and AE system with a carbon steel target assembly identical to that used for the air jet tests. The test rig was designed to project a jet of slurry with a controlled range of nozzle exit velocities at the target surface. The flow loop used for performing the experiments consisted of a positive displacement pump, standard 25 mm diameter PVC piping, a 50 litre conical tank and choke valves. A schematic diagram of the experimental set up is shown in **Figure 3.24**.

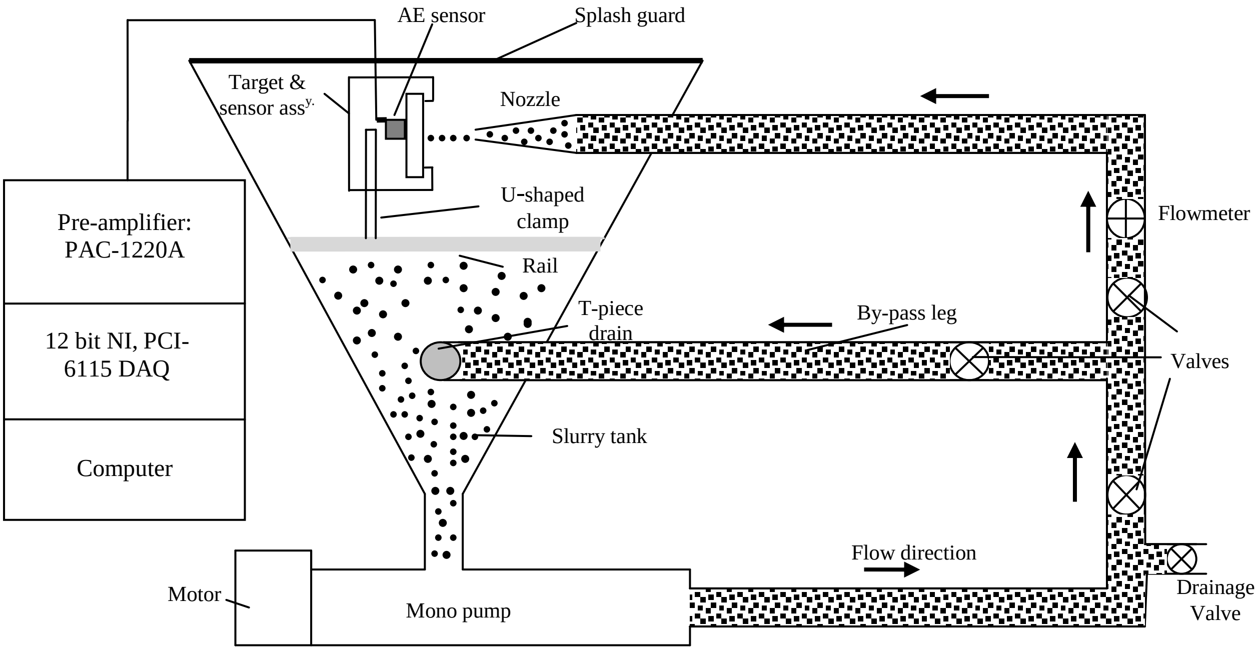

Figure 3.24: Schematic diagram of slurry impingement rig

Figure 3.25: Tee joint inside the tank used for mixing

The solid particles were thoroughly mixed with tap water in the slurry tank. In order to ensure a uniform distribution of solids inside the tank, a T-piece joint was attached to a by–pass leg incorporating end caps which had been drilled at 45^o (as shown in **Figure 3.25**) to encourage vortices and swirls to be created in the tank in order to generate enough turbulence and sufficient mixing. The mixture flowed through the tank and entered the pump through a connection at the bottom of the slurry tank. A Mono pump, model C22BC10RMB, driven by a 1.1 kW geared motor to give an output speed of 587 rpm, was used to circulate the mixture through the flow loop. The action of pumping liquid through the by-pass leg whilst adding the particle charge to the slurry tank provided pre-mixing at the start of an experimental run. Once the solids were fully suspended, the flow could be diverted through the nozzle by partly closing the by-pass and opening a main valve positioned before a flow meter. The flow meter was equipped with a thermal dispersion flow sensor which included a heated element cooled at a rate which varies with the flow rate. This kind of flow meter was chosen because it has no moving parts exposed to the slurry flow thus reducing the potential for wear to occur and the opportunity for blockage. The slurry stream was projected towards the specimen through a 5 mm-diameter nozzle with a 30 mm stand-off distance. After impingement, the slurry falls back into the tank which was provided with a plastic splash cover.

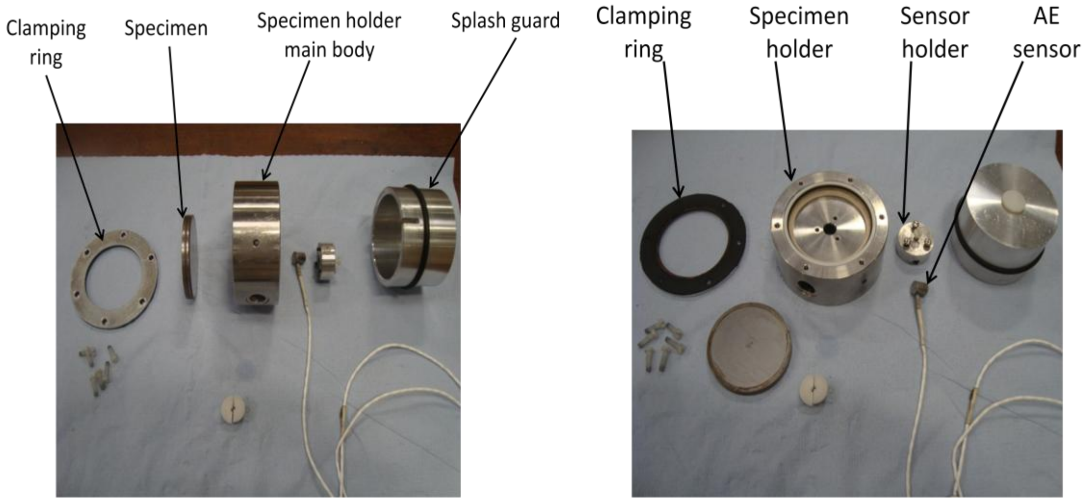

Figure 3.26: Two views of target plate and sensor arrangement for slurry impingement tests.

The specimen was held into a stainless steel specimen holder main body and held with an aluminium clamping ring against a combination of nylon and a rubber O-ring to seal the target plate and isolate it from the surrounding holder. The sensor was placed onto a rubber pad inside the sensor holder, and a nylon screw used to compress the rubber to ensure an appropriate contact with the specimen, the assembly being clamped to the back of the internal main body as shown in **Figure 3.26**. To avoid fluid reaching the sensor, an aluminium splash guard was used to enclose the sensor assembly so that only the front surface of the specimen was exposed to the impinging slurry.

The specimen holder was mounted onto a U-shaped clamp which was slotted to allow the slurry stream to impact the centre of the target at any pre-set impact angle between 0^o and 90^o, defined as the angle between the plane of the target and the direction of the slurry flow. The U-shaped clamp was attached to a rail which was bolted inside the slurry tank and slotted to allow the impact distance to be adjusted as shown in **Figure 3.27**.

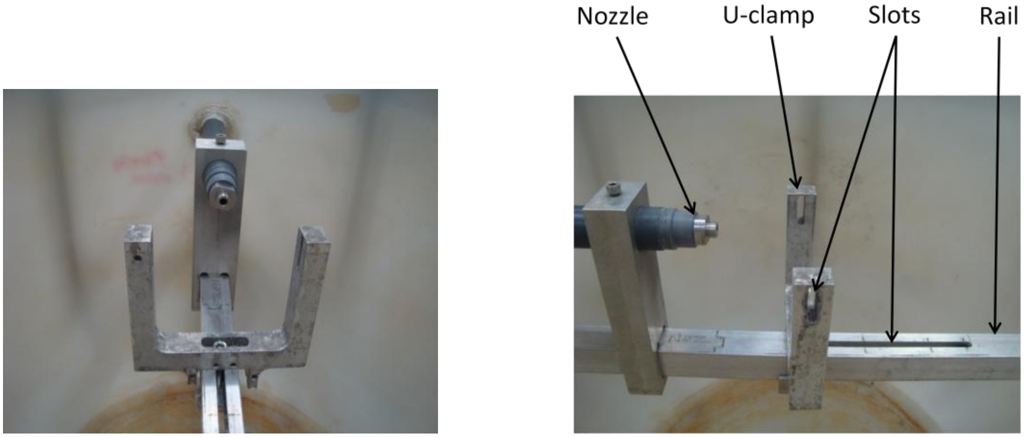

Figure 3.27: Two views for the specimen holder position inside the tank

Before each test, the sensitivity of the sensor was checked using pencil lead breaks to ensure proper connection and attachment of the sensor and, following each set of experiments where the particle size fraction needed to be changed, the test rig was drained and flushed repeatedly to remove all suspended particles.

Five 1-second records were acquired at each of three different size ranges, with each of three different impingement angles, three nominal concentrations and four nozzle exit velocities as summarised in **Table 3.7**. The mean particle masses for the graded particles were 4.8, 16.8 and 64.5 µg determined from the average diameter for each size fraction and the density of silica (2600 kg.m^{-3}), assuming the particles to be spherical. The nominal concentration of the particles in the suspension was based on the amount added to the rig, but, for each combination of size fraction, nominal concentration, and jet exit velocity, the sand content of the mixture emerging from the impingement nozzle was measured by sampling the slurry jet flow at the nozzle exit. Ten samples were taken, dried in an electronic oven, and weighed to measure their sand contents, the average of these ten samples being used as the measured concentration. The launch frequency, total number of particles launched from the nozzle per second, shown in **Table 3.7** was determined by multiplying the volumetric flow rate (m^{3}s^{-1}) by the average measured concentration (kg.m^{-3}) and dividing by the average mass of a particle (kg).

The entrainment of air into the jet and the subsequent collapse of air pockets on the target surface might generate significant AE, and so it was necessary to carry out control measurements with particle-free water to identify the background noise characteristics. Also, because the nature of the experiments might involve the removal and replacement of the sensor, it was again necessary to assess the variability associated with sensor coupling to the target. Accordingly, a series of three independent experiments were carried out between which the sensor was removed and replaced. In each experiment, five 1 second AE records were taken at each of the jet exit velocities shown in **Table 3.7**. **Figure 3.28** shows the recorded AE energy at each of the four speeds for each of the three experiments. As can be seen, the variation between records for a given speed and installation is negligible, while the variation between installations is slightly larger although still small in comparison with the variation with speed. The best fit power equation is also shown for each installation and, as can be seen, the exponent is about 2.5, although the fit is not particularly satisfactory, the slope increasing more rapidly at the highest speed than indicated by this exponent.

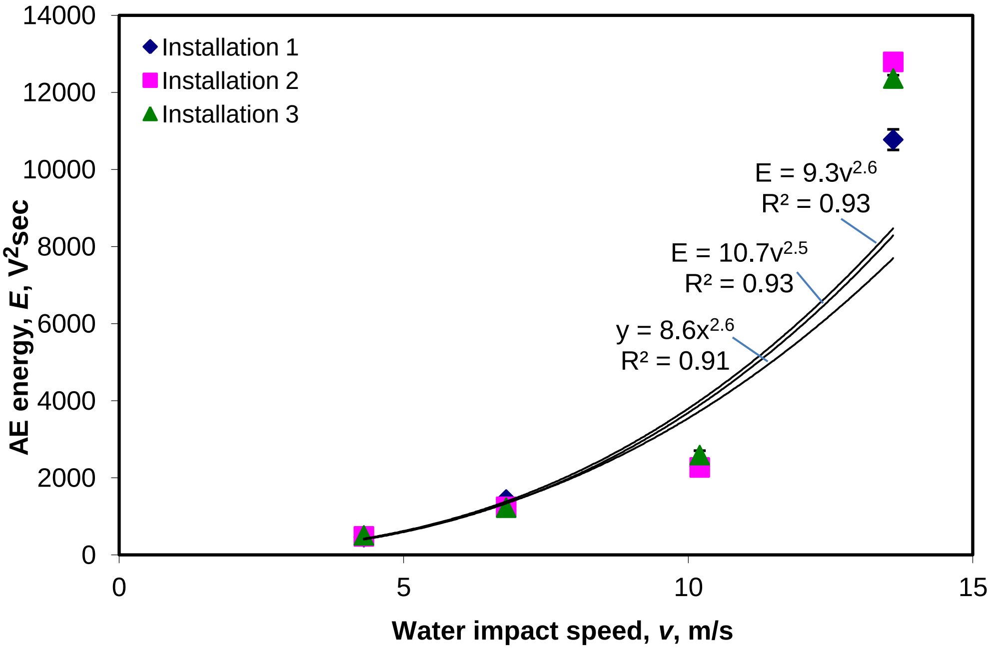

Figure 3.28: Recorded AE energy for pure water jet impingement in slurry impact rig

Particle size range (µm)	Nominal concentration (kg/m^3)	Jet exit velocity (m/s)	Average measured concentration (kg/m^3)	Average launch frequency (particles/second)×10^3
125-180	10	4.2	1.6 ±0.6	27 ±41%
		6.8	5.5 ±0.8	153 ±14%
		10.2	6.1 ±1.7	254 ±29%
		12.7	1.8 ±0.7	94 ±41%
	25	4.2	11.2 ±3.5	193 ±31%
		6.8	19.5 ±1.9	543 ±9.5%
		10.2	19.8 ±0.5	791 ±3.6%
		12.7	9.6 ±1.6	490 ±17%
	50	4.2	42.5 ±2.5	736 ±6.6%
		6.8	52.5 ±4.1	1454 ±6.9%
		10.2	57.3 ±5.7	2380 ±11%
		12.7	47.2 ±2.7	2451 ±7.1%
212-250	10	4.2	1.8 ±1.4	9.2 ±76%
		6.8	6.2 ±2.1	49 ±34%
		10.2	6.2 ±2.8	74 ±44%
		12.7	5.9 ±2.6	88 ±47%
	25	4.2	10.1 ±2.9	50 ±27%
		6.8	16.4 ±0.6	130 ±8.4%
		10.2	18.4 ±1.9	220 ±11%
		12.7	14.3 ±5.2	214 ±35%
	50	4.2	42.7 ±2.3	212 ±10%
		6.8	51.3 ±2.7	408 ±5.4%
		10.2	52.9 ±6.5	631 ±16%
		12.7	54.5 ±5.6	812 ±11%
300-425	10	4.2	1.5 ±1.1	1.9 ±66%
		6.8	8.7 ±3.3	17 ±41%
		10.2	7.9 ±2.9	24 ±49%
		12.7	4.7 ±2.2	18 ±46%
	25	4.2	10.2 ±3.3	13 ±31%
		6.8	17.2 ±2.9	35 ±15%
		10.2	19.0 ±2.9	58 ±15%
		12.7	14.5 ±3.5	55 ±24%
	50	4.2	44.0 ±3.9	564 ±9.1%
		6.8	52.5 ±4.5	107 ±8.6%
		10.2	56.5 ±3.4	173 ±11.5%
		12.7	48.5 ±6.5	186 ±11.3%

Table 3.7: Summary of measured and derived impingement conditions in slurry impact rig

3.3.3 Flow loop impingement tests

In the final series of tests, and in order to simulate realistic flow conditions, the slurry jet impingement tester described in **Section 3.3.2** was modified to make a flow loop. The purpose of this relatively uncontrolled impingement experiment was to assess any further adjustments that need to be made in the processing to use AE as a semi-quantitative diagnostic indicator for particle impingement in real process flows. **Figure 3.29** shows a schematic view of the flow loop experimental apparatus along with the AE measurement system. The test rig again consists of a large plastic conical tank from which the liquid (with or without sand) was drawn using the mono pump. This pump circulated the liquid or slurry through a PVC pipe loop, and was operated and controlled in essentially the same way as that described in **Section 3.3.2**.

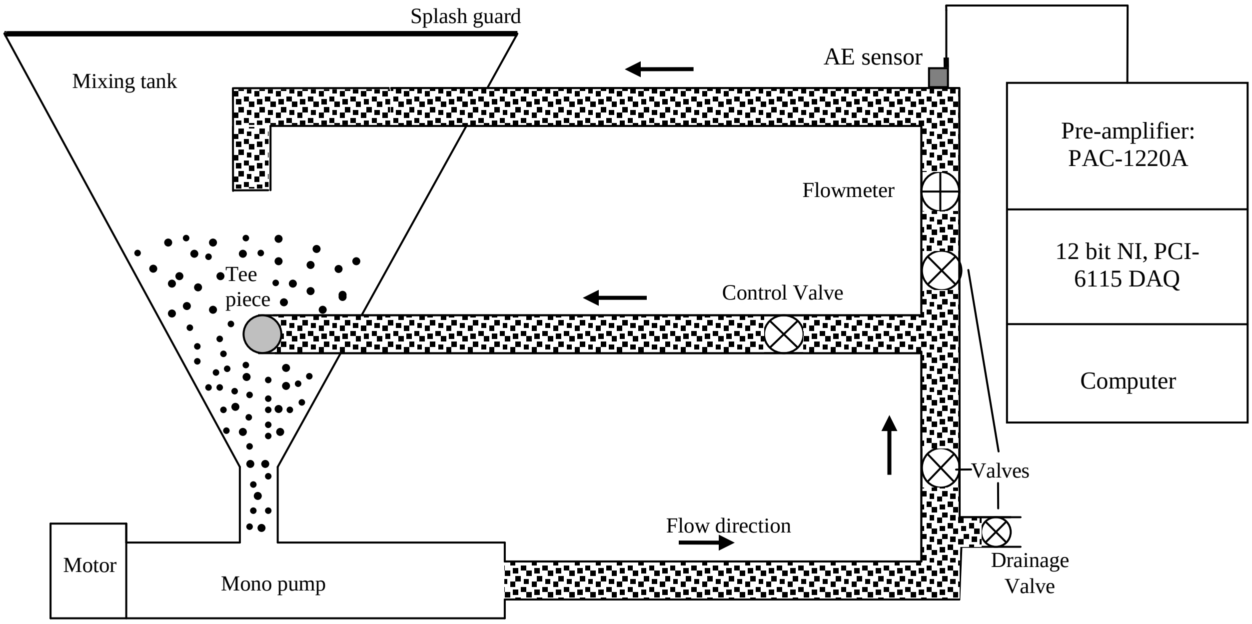

Figure 3.29: Sketch of the experimental flow loop with AE measurement system

A sharp 90 degree bend made from 5 mm bore carbon steel (**Figure 3.30**) was inserted into the 23 mm bore PVC pipeline system, a sharp bend having been selected in order to localize the impingement area and minimize the impact angle range. The pipe wall opposite to the stream was milled flat in order to have a plane area to mount the AE sensor and the bend was machined to give an internal bore of 5 mm with a conical transition, giving 7 mm wall thickness at the site where the sensor was mounted. The length of the target section was 75 mm giving an overall impingement area similar to the other studies. The AE sensor was mounted using the magnetic clamp and coupled by means of vacuum grease to the opposite surface of the bend directly above the impingement area as shown in **Figure 3.30**. As with the slurry impingement tests, the pre-amplified data were acquired at 2.5 MS/second for a record length of 1 second. Prior to testing, the sensitivity of the sensor was checked by performing a pencil lead break test at the bend to check the functioning of the AE detection system and to confirm the quality of sensor coupling.

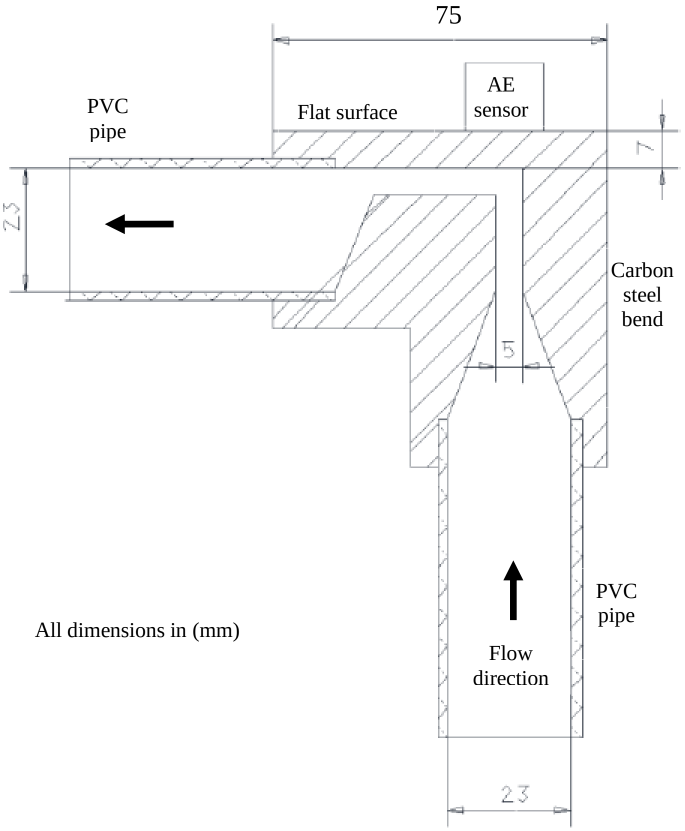

Figure 3.30: Sectional view of carbon steel bend test section

Silica sand slurry was made from 10 litres of clean water and a predetermined mass of different particle size fractions in order to obtain the required concentration. Four different particle size ranges were used and, for each particle size range, an impingement run was carried out with a total of three levels of solid concentration (1, 2.5, and 5wt%) and four different flow velocities (4.2, 6.8, 10.2, and 12.7 ms^{-1}). The AE energy measured was based on at least ten repeat records making a total of 120 AE records for each particle size range tested. Following each set of experiments, the rig was drained and cleaned.

As with the slurry impingement tests, the AE signals were acquired at full bandwidth so that spectral analysis could be carried out on the raw signal and also time domain characteristics could be examined up to the waveform resolution.

The average particle impact rate and the total number of particles expected to strike the bend per second are shown in **Table 3.7** for size fractions 212-250 um and 300-425 um while **Table 3.8** shows particle impact rate for the larger size fractions (500-600 μm and 600-710 μm) assuming similar average concentrations to those for the 300-425 μm size range. Again, average particle impact rate was determined by multiplying the volumetric flow rate (m^3s^{-1}) by the average measured concentration ($kg.m^{-3}$) and dividing by the average mass of a particle (kg).

As with the slurry impingement tests, it was necessary to identify the background noise AE energy associated with particle-free water impact as well as to assess the variability in AE energy that due to the sensor removal and replacement. Again, a series of three experiments were carried out between which the sensor was demounted and reinstalled on the surface of the target section. In each experiment, ten-1 second AE records were taken at each of the flow speeds shown in **Table 3.8**. **Figure 3.31** shows the recorded AE energy at each of the four speeds for each of the three experiments where each point represents the average of ten AE energy values along with its standard deviation. As can be seen, the variation in the energy recorded at each installation (within group variation) is small, while the variation between installations is slightly bigger due to changes when the sensor was re-mounted.

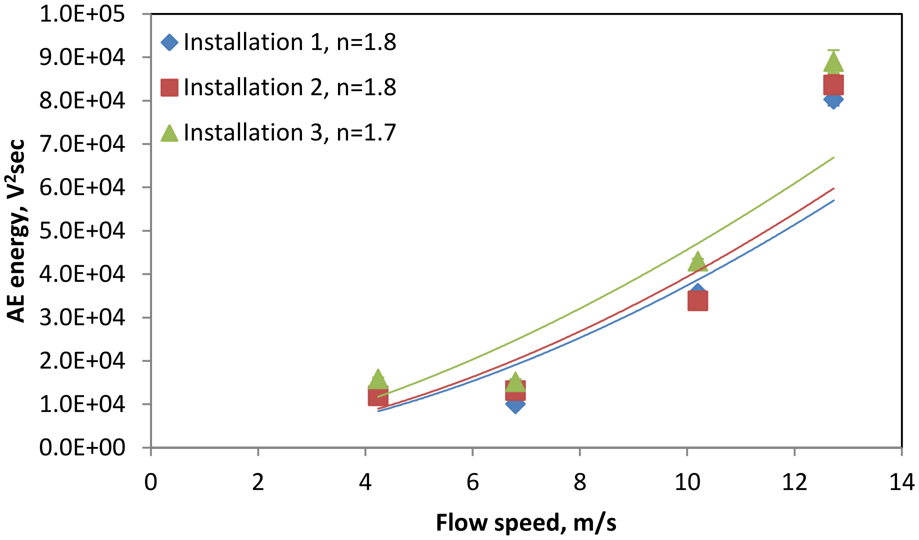

Figure 3.31: Recorded AE energy for pure water impingement in flow loop

Particle size range (μm)	Nominal concentration (kg/m^3)	Flow speed (m/s)	Average assumed concentration (kg/m^3)	Average particle impact rate (particles/second)
500-600	10	4.2	1.5 ±1.1	568 ±66%
		6.8	8.7 ±3.3	5200 ±41%
		10.2	7.9 ±2.9	7200 ±49%
		12.7	4.7 ±2.2	5300 ±46%
	25	4.2	10.2 ±3.3	3800 ±31%
		6.8	17.2 ±2.9	10400 ±15%
		10.2	19.0 ±2.9	17200 ±15%
		12.7	14.5 ±3.5	16400 ±24%
	50	4.2	44.0 ±3.9	16600 ±9.1%
		6.8	52.5 ±4.5	31800 ±8.6%
		10.2	56.5 ±3.4	51300 ±11.5%
		12.7	48.5 ±6.5	55100 ±11.3%
600-710	10	4.2	1.5 ±1.1	330 ±66%
		6.8	8.7 ±3.3	3000 ±41%
		10.2	7.9 ±2.9	4100 ±49%
		12.7	4.7 ±2.2	3000 ±46%
	25	4.2	10.2 ±3.3	2200 ±31%
		6.8	17.2 ±2.9	6000 ±15%
		10.2	19.0 ±2.9	10000 ±15%
		12.7	14.5 ±3.5	9500 ±24%
	50	4.2	44.0 ±3.9	9600 ±9.1%
		6.8	52.5 ±4.5	18400 ±8.6%
		10.2	56.5 ±3.4	29700 ±11.5%
		12.7	48.5 ±6.5	31900 ±11.3%

Table 3.8: Summary of derived impingement conditions for flow loop experiments

Chapter 4

Experimental Results

This chapter is arranged into two main sections. The first section summarises the results of the experimental arrangements which were used to investigate airborne impacts in three regimes; low velocity-low mass, low velocity-high mass, and high velocity-low mass. Within each of these regimes, both single-particle and multiple-particle impact results are presented. The second section presents the results of the slurry impingement tests to investigate the influence of particle size, free stream speed, nominal particle impact angle, and nominal particle concentration on the carbon steel target. The third section examines the effect of the same variables (except the nominal impact angle) on AE energy dissipated in the carbon steel bend in the flow loop.

It should be noted here that the AE impact energy E was calculated from the raw AE signal by integrating over the entire time record above a threshold level of 10% of the maximum peak height.

4.1 Airborne particle impact test

The purpose of this set of experiments was to establish whether, over a wide range of impact conditions, a known incident particle kinetic energy gave rise to a predictable AE energy, i.e. if the proportion of the incident energy converted to AE is constant or not, in an arrangement using sensors and a target which might realistically be applied industrially. Two particle mass ranges and two velocity ranges were identified and three regimes of impact were used: low velocity-low mass (impact speeds of 1.5 ms^{-1} - 3 ms^{-1} and masses of 4.9×10^{-6} - 2.3×10^{-4} g), low velocity-high mass (sphere masses of 0.001 to 2 g), and high velocity-low mass (impact speeds of 4 to 16 ms^{-1}). In addition, low mass experiments were carried with individual particles and particle streams, but particle streams were not necessary for the high mass particles.

4.1.1 Low velocity-low mass impacts

Figure 4.1 shows the measured AE energy normalized by particle mass for the individual impacts against the estimated particle velocity and **Figure 4.2** shows the relationship between measured AE energy normalized by particle velocity and mean particle diameter for the low mass particles. It is clear from these figures that the measured AE energy in this region is only weakly dependent on the estimated impact velocity, whereas the relationship with diameter is much stronger, as can be seen in **Figure 4.2**. It might be noted that the error in the measurements is largely due to the range in particle size within a fraction, which affects the estimated velocity, the size and, to a great extent, the mass.

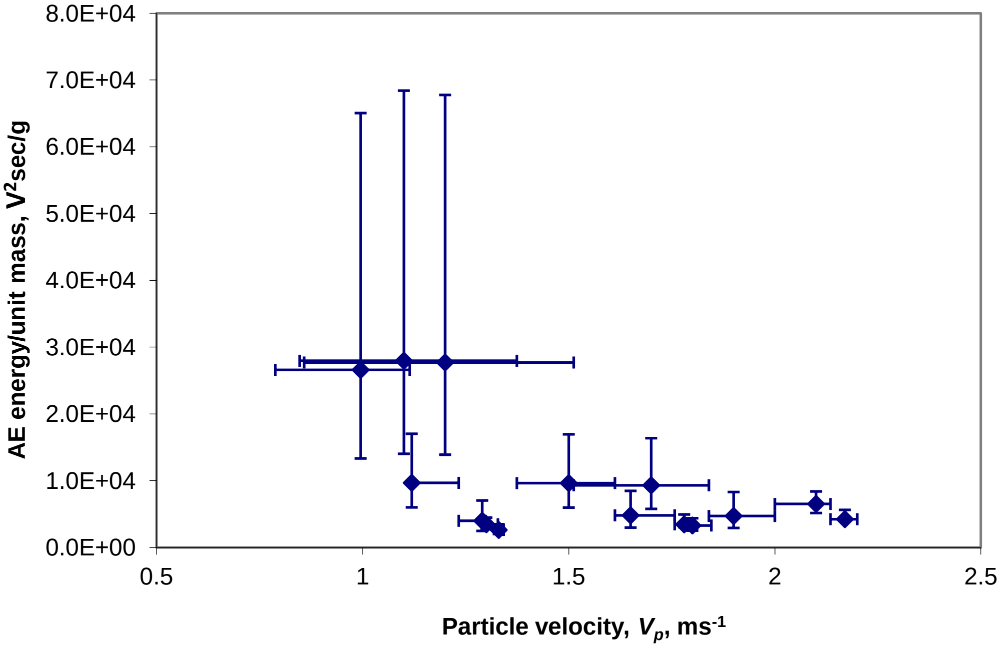

Figure 4.1: AE energy per unit mass of particle versus particle velocity for low velocity – low mass individual impacts

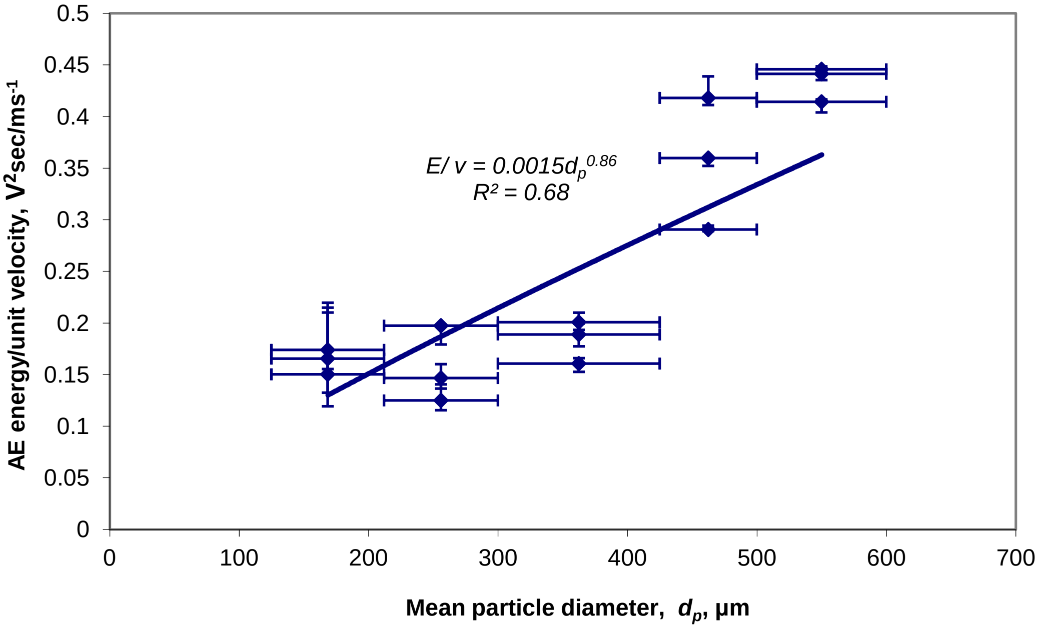

Figure 4.2: AE energy per unit velocity versus mean particle diameter for low velocity – low mass individual impacts

Figures 4.3 and **4.4** show the corresponding plots for multiple impacts, respectively, the effect of estimated particle velocity on the measured AE energy per particle per unit mass and the effect of mean particle diameter on the measured AE energy per particle per unit velocity. Comparing **Figures 4.1** and **4.3**, it is clear that the scatter is much reduced due to the averaging effect of multiple impacts, although the range of measured energy is similar, suggesting that, at the impact rates used (a few hundreds per second for bigger fractions and a few thousands per second for smaller fractions) the effects of individual particles are additive. The multiple impact data exhibit a much clearer trend of energy per unit mass with velocity with a power law exponent of around 2. Comparing **Figures 4.2** and **4.4**, a much stronger trend of energy per unit velocity with diameter also emerges, this time with an exponent of around 4. Given that the range of particle sizes is much smaller than in the single particle experiments, it is clear that the values of the energy per particle per unit velocity are much higher (by a factor of about 2) in the multiple particle experiments. This observation has, of course, to be conditioned by the fact that the normalisation per unit mass and unit velocity are interdependent.

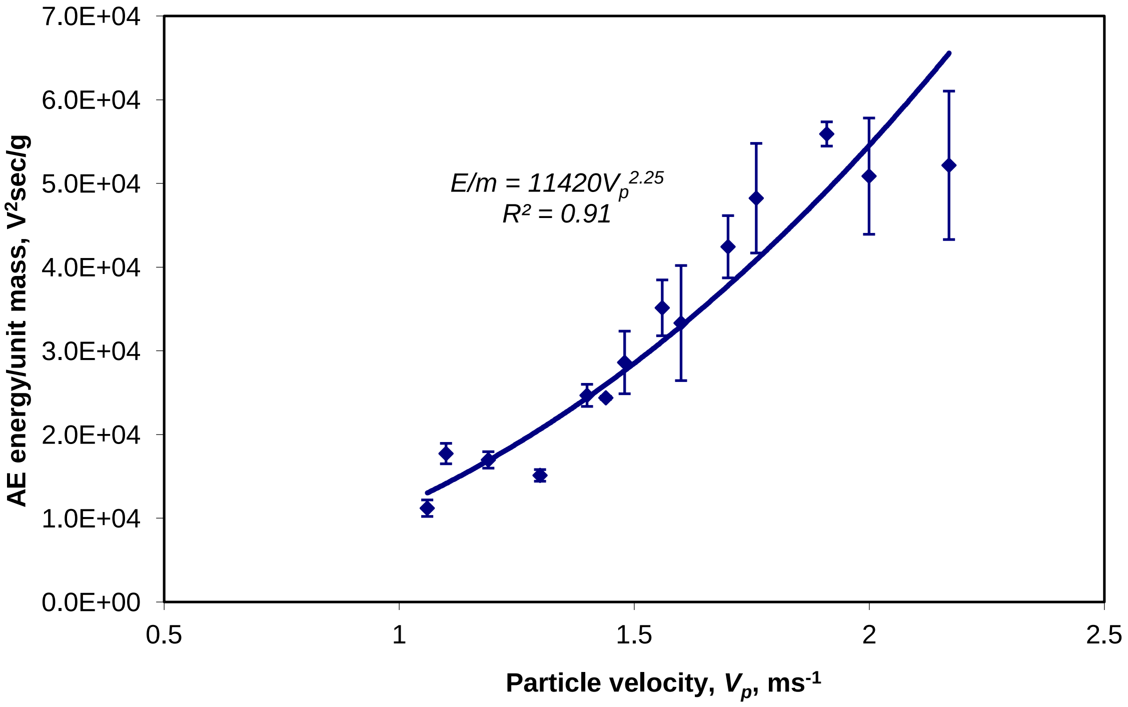

Figure 4.3: AE energy per particle per unit mass versus particle velocity for low velocity – low mass particle streams

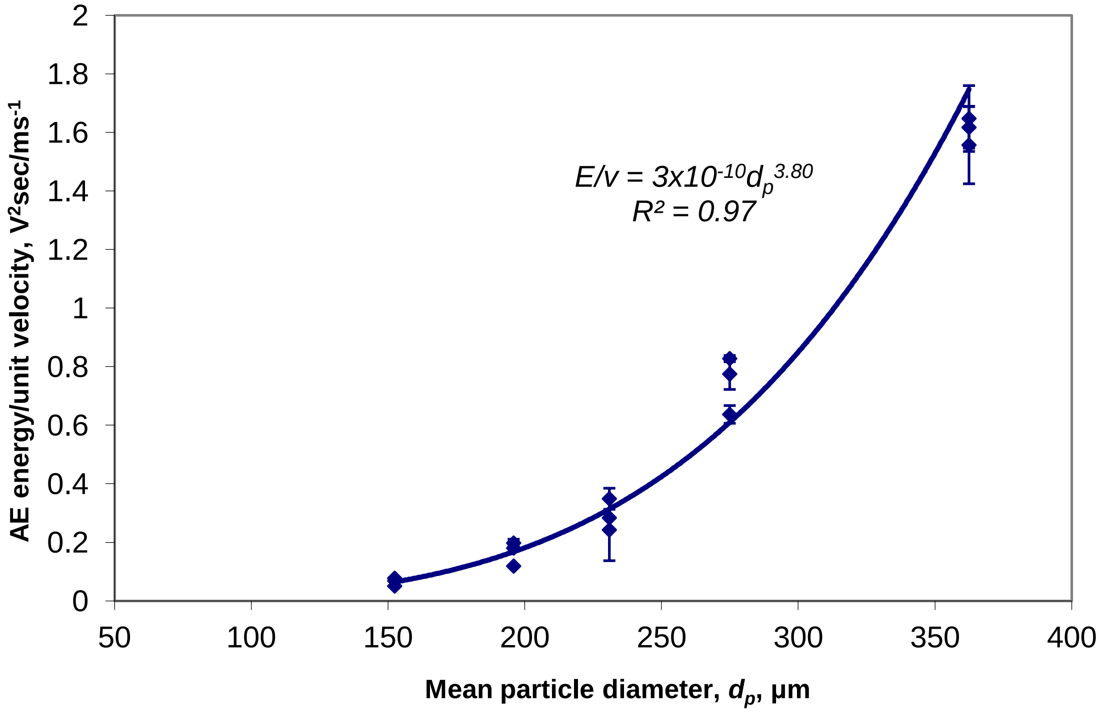

Figure 4.4: AE energy per particle per unit velocity versus mean particle diameter for low speed – low mass particle streams

4.1.2 Low velocity-high mass impacts

The AE energy per unit mass for high mass impacts is plotted against particle velocity in **Figure 4.5**, and the energy per unit velocity against particle diameter in **Figure 4.6**. It is clear from **Figure 4.6** that the smaller particles (up to 2 mm, circled in **Figures 4.5** and **4.6**) behave differently to the larger ones with the smaller ones essentially continuing the trends seen in **Figures 4.2** and **4.4**. The difference in energy between **Figures 4.2, 4.4** and **4.6** would tend to suggest that the diameter exponent is more like the value of 4 seen in **Figure 4.4** than the approximately linear dependence seen in **Figure 4.2**. For the larger particles, the AE energy per unit velocity stops increasing with diameter and, indeed, begins to decrease, suggesting that another energy transfer mechanism may be coming into play.

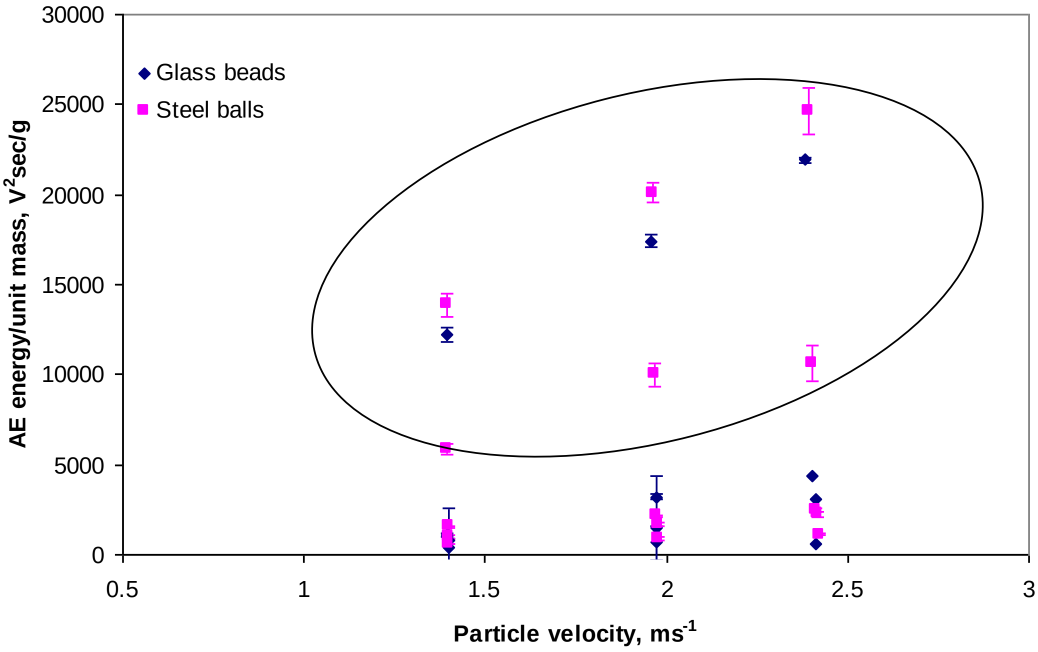

Figure 4.5: AE energy per unit mass of particle versus particle velocity for low velocity – high mass individual impacts

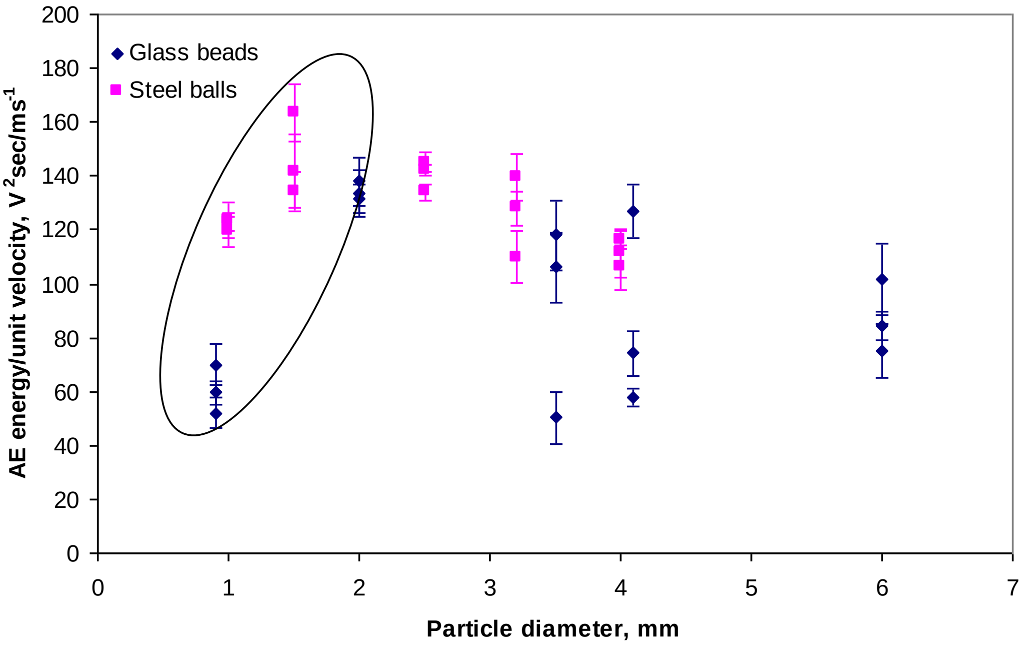

Figure 4.6: AE energy per unit velocity of particle versus particle diameter for low velocity – high mass individual impacts

4.1.3 High velocity-low mass impacts

Figure 4.7 shows the measured AE energy normalized by particle mass against incident particle velocity for high velocity single impacts, where the velocities were estimated using the semi-empirical calibration (**Equation 3.5**) and the average and range of the ten repeat AE energies are shown. For clarity, the diameter used to calculate the mass is simply the mean, unlike the presentation in **Figure 4.1** where the range of diameter is used to show the potential error in the mass. As can be seen, there is a general increase in AE energy per unit mass with a velocity exponent of around 1.5, similar to **Figure 4.3**. The correlations for the two types of particle are not substantially different, although the scatter and the general level of energy are both slightly higher for the glass beads than for the sand.

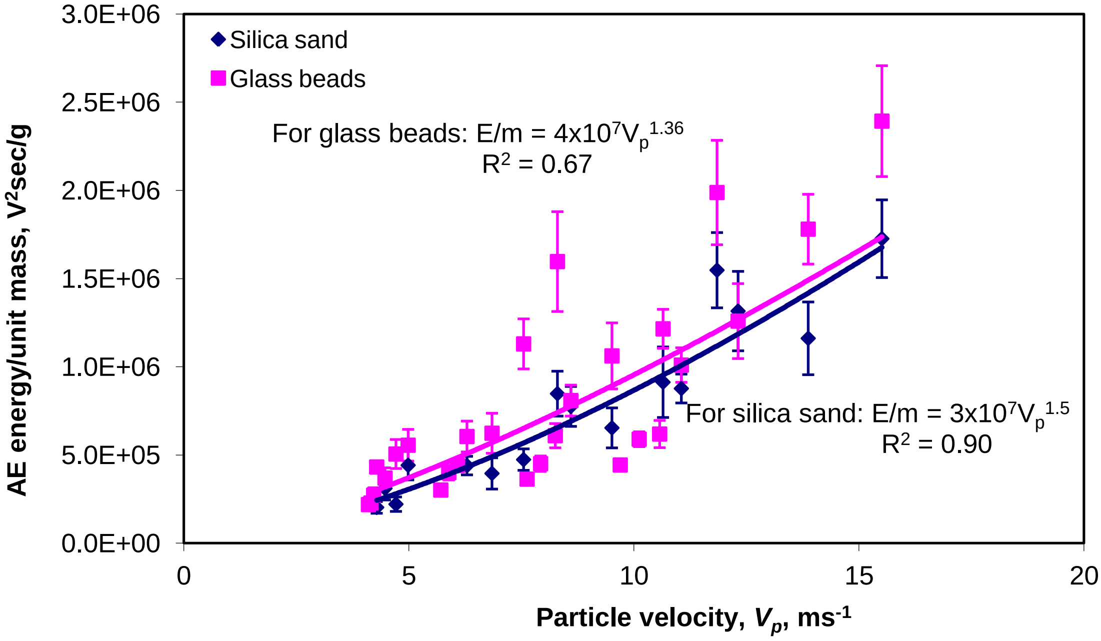

Figure 4.7: AE energy per unit mass of particle versus particle velocity for high velocity – low mass single impacts

Figure 4.8 shows the corresponding diameter correlation for the high-velocity – low mass single impacts and, again, the sand and glass bead exponents are similar, at around 2.5, but somewhat lower than the one indicated in **Figure 4.4**.

Figures 4.9, and 4.10 show, respectively, the velocity and diameter correlations for the high velocity – low mass impacts. The exponents are in general accord, although a little lower than those for single impacts but the general level is consistently lower for multiple impacts.

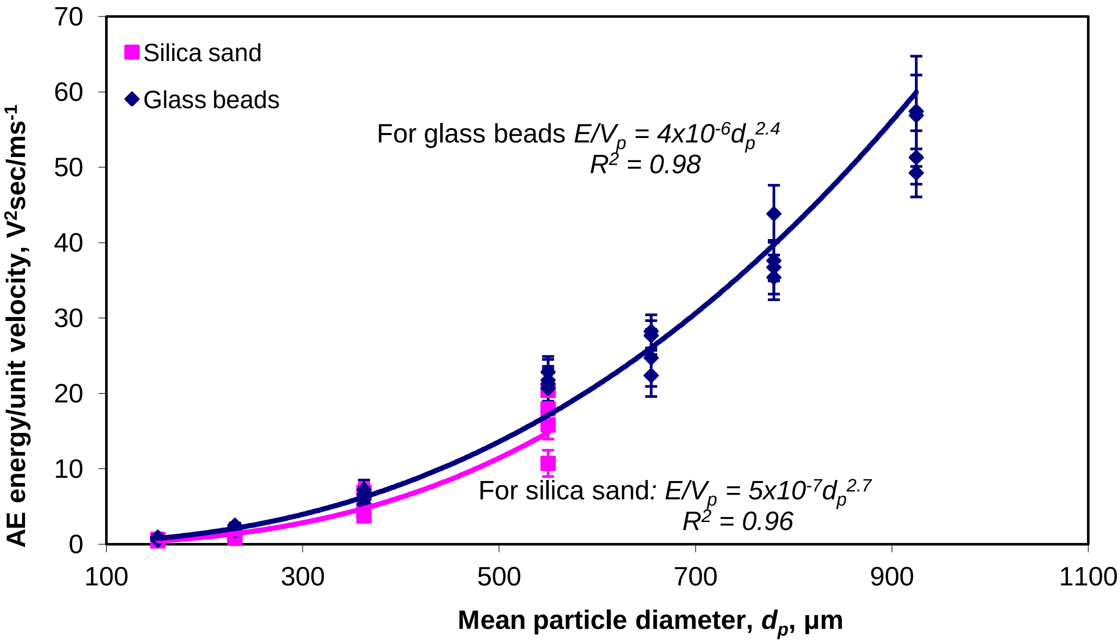

Figure 4.8: AE energy per unit velocity versus particle diameter for high velocity – low mass single impacts

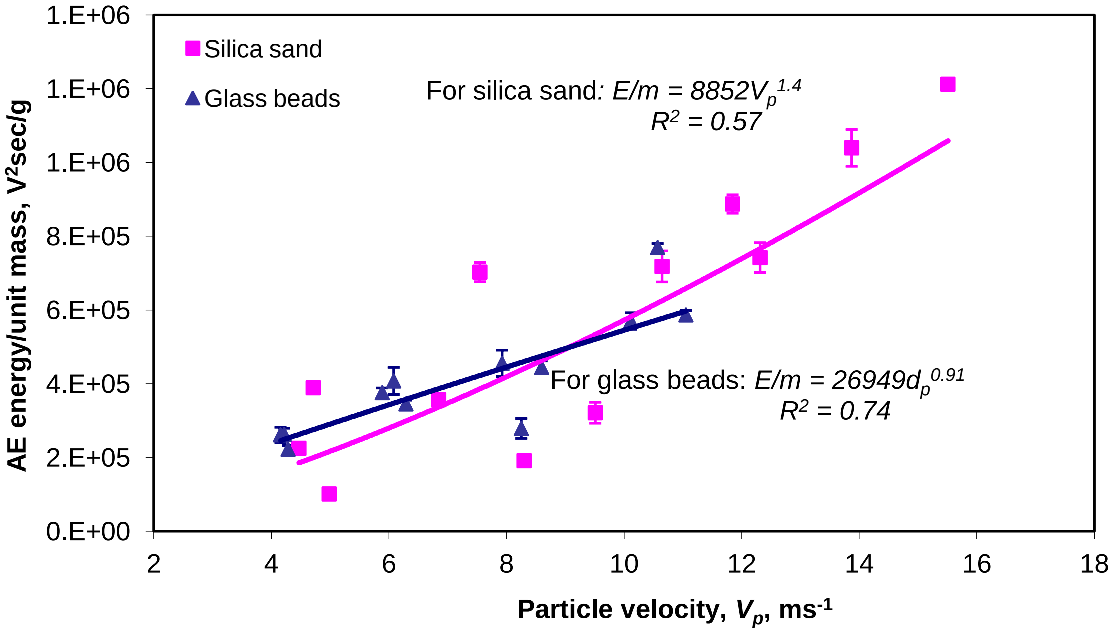

Figure 4.9: AE energy per particle per unit mass versus particle velocity for high velocity – low mass multiple impacts

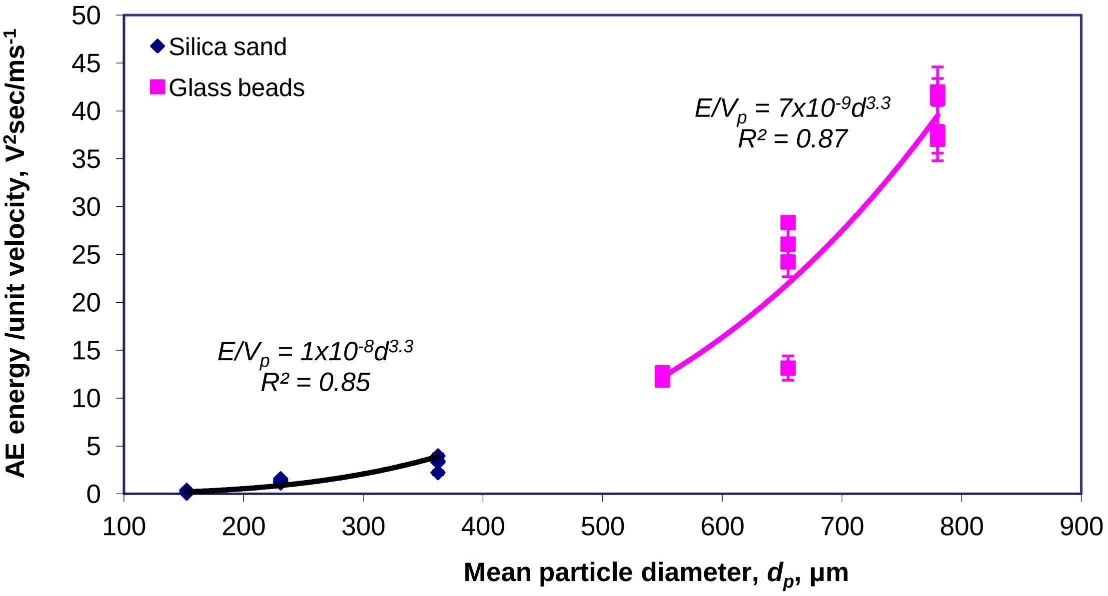

Figure 4.10: AE energy per particle per unit velocity versus diameter for high velocity – low mass multiple impacts

4.2 Slurry jet impingement test

The aim of this set of relatively controlled slurry impingement experiments was to assess the extent to which the previous findings, with air-borne particles, can be applied with this medium. Thus, the purpose of this section is to examine, over a wide range of impact conditions, the relationship between measured AE energy and slurry jet impingement parameters.

Figure 4.11 shows examples of 1-second records of raw AE at the two extremes of flow speed, (i) and (ii), without particles (a) and with the highest size fraction of particles (b). It is clear that particles give rise to a substantial increase in AE, although the magnified views (c) do not seem to show events at the frequency expected from the launch rates given in **Table 3.7**. Furthermore, even at this reduced event rate, the higher concentration and flow speed gives an AE signal which seems to contain a substantial amount of particle overlap.

For each experimental condition, the measured AE impact energy was calculated from the raw signal (measured as an amplified voltage, *V*) by integrating over the entire record using **Equation 3.1**.

At least five repeat 1-second records were analysed for each condition and the average value is used in the following general analysis to establish the effects of flow speed, particle size, impact angle and concentration, against the normal expectation that energy will depend on the square of both the impact speed and the sine of the impact angle, the cube of the particle diameter (i.e. the particle mass) and be linear with concentration, if expressed as mass per unit volume of water.

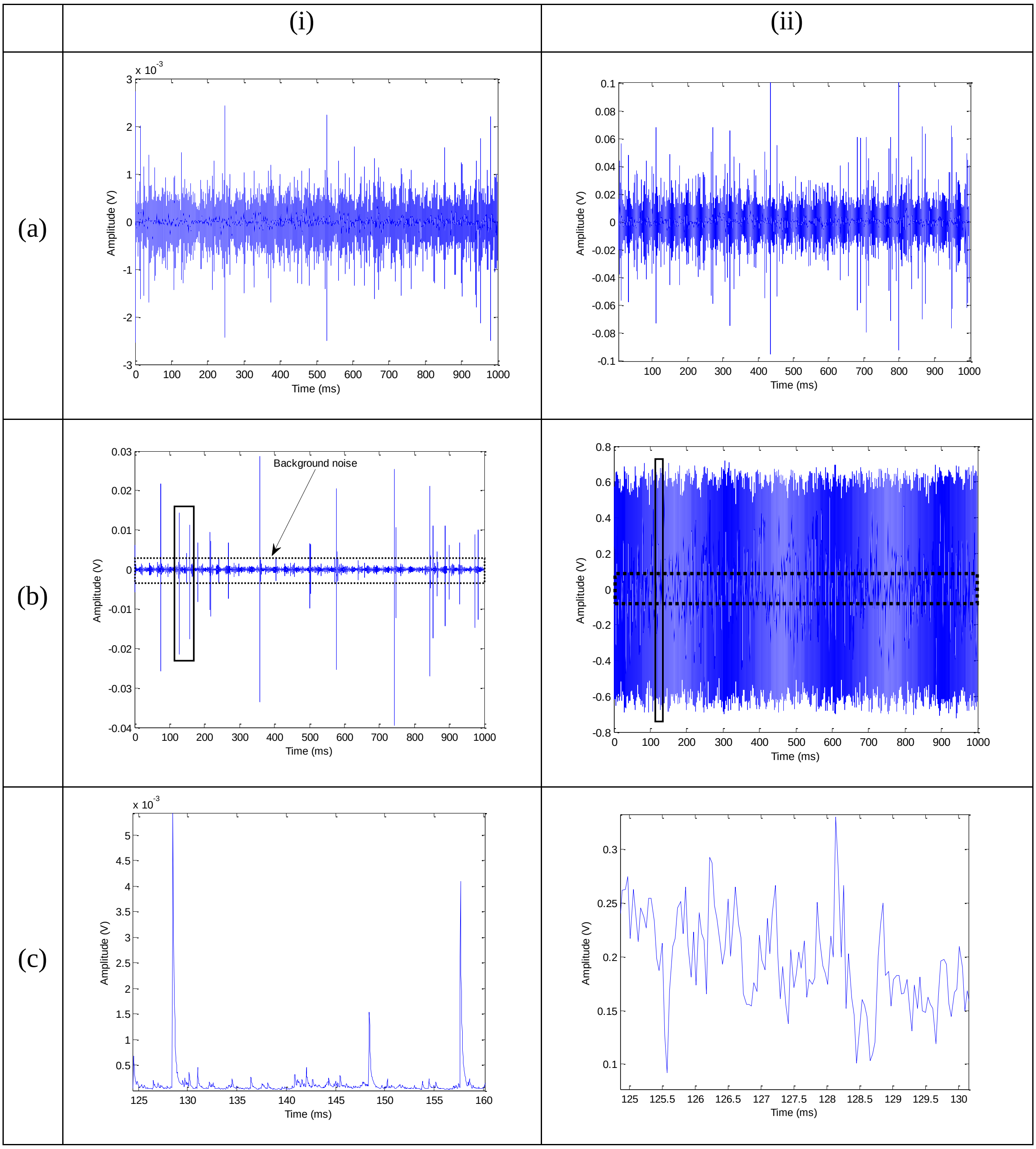

Figure 4.11: Typical 1-second AE records for (a) water and (b) slurry with 300-425 µm sand, at (i) a flow speed of 4.2m/s and a nominal particle concentration of 10kg/m^3 and (ii) a flow speed of 12.7m/s and a nominal particle concentration of 50kg/m^3 Graphs (c) show the RMS AE signal magnified to reveal events, with record c(i) corresponding to around 70 particle launches and record c(ii) corresponding to around 1000 particle launches.

Figures 4.12 and **4.13** show examples of the effect of flow speed (jet exit velocity, V_j) on the measured AE energy for a given concentration and particle size, respectively, at normal incidence. As can be seen, the energy varies with approximately the second power of flow speed, and this power dependence increases slightly with decreasing concentration (at the particle size chosen) and appears also to decrease slightly with decreasing particle size (at the concentration chosen). **Table 4.1** shows the best fit power index for all of the measurements along with the associated R^2 values. The weighted average exponent calculated from $\bar{n} = \frac{\sum n_i R_i^2}{\sum R_i^2}$ was found to be 2.7, which is in reasonable agreement with other studies which report this index to lie in the range of 1.5-3 depending on the slurry properties and mechanical properties of the material under investigation [89]. It is also evident from **Table 4.1** that exponents higher than 2 are associated with the lower concentrations where the signal:noise might be expected to be low.

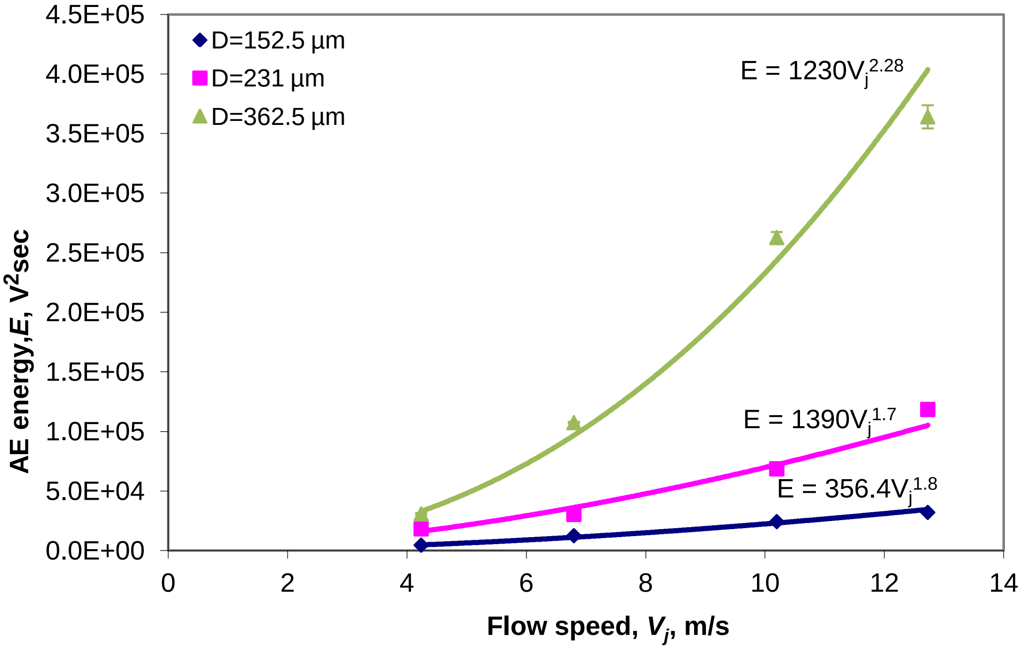

Figure 4.12: Effect of flow speed on AE energy for the three particle sizes at a concentration of 5kg/m^3 impinging at normal incidence

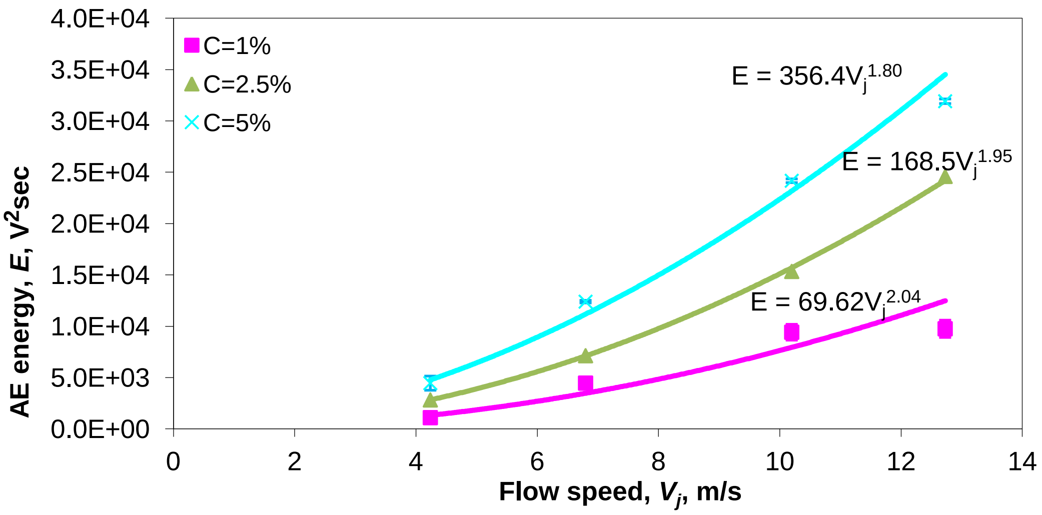

Figure 4.13: Effect of flow speed on AE energy for the three concentrations for particles in size range 125-180 µm impinging at normal incidence

Particle size range (µm)	Nominal impact angle θ (°)	Nominal concentration (kg/m^3)	Flow speed exponent (n)	Curve fitting R^2 value (%)
125-180	**90**	**1**	**2.0**	**94**
		2.5	**1.95**	**99**
		5	**1.8**	**98**
	60	1	3.1	78
		2.5	2.3	98
		5	1.3	99
	30	1	3.3	95
		2.5	3.3	94
		5	1.3	95
212-250	**90**	1	4.4	89
		2.5	2.2	99
		5	**1.7**	**97**
	60	1	4.3	81
		2.5	1.8	99
		5	1.8	99
	30	1	4	96
		2.5	2	99
		5	1.9	98
300-425	**90**	1	5	81
		2.5	5	91
		5	**2.2**	**99**
	60	1	5.2	93
		2.5	2	98
		5	1.8	99
	30	1	4.2	76
		2.5	2.2	99
		5	1.7	98

Table 4.1: Exponent of flow speed dependence of measured AE energy for all experiments. (Data in bold font are plotted in **Figures 4.12 and 4.13**)

Figures 4.14-4.16 show the effect of mean particle diameter on the measured AE energy for the range of flow speed and nominal concentration studied at normal impingement angle. Generally, the power exponent is between 2 and 3, except in the cases (low speed and lower concentrations) where there is very little particle signal (above the water "noise") and where changes are difficult to discern at all. As with the flow speed exponent, the diameter exponent tends towards the expected value of 3 at higher concentrations whereas, at the lower speeds and concentrations, the exponent tends towards 2 (in cases where a change can be discerned). **Table 4.2** shows the parameters for the remaining experiments where similar trends can be seen, leading to a weighted mean exponent of 2.1.

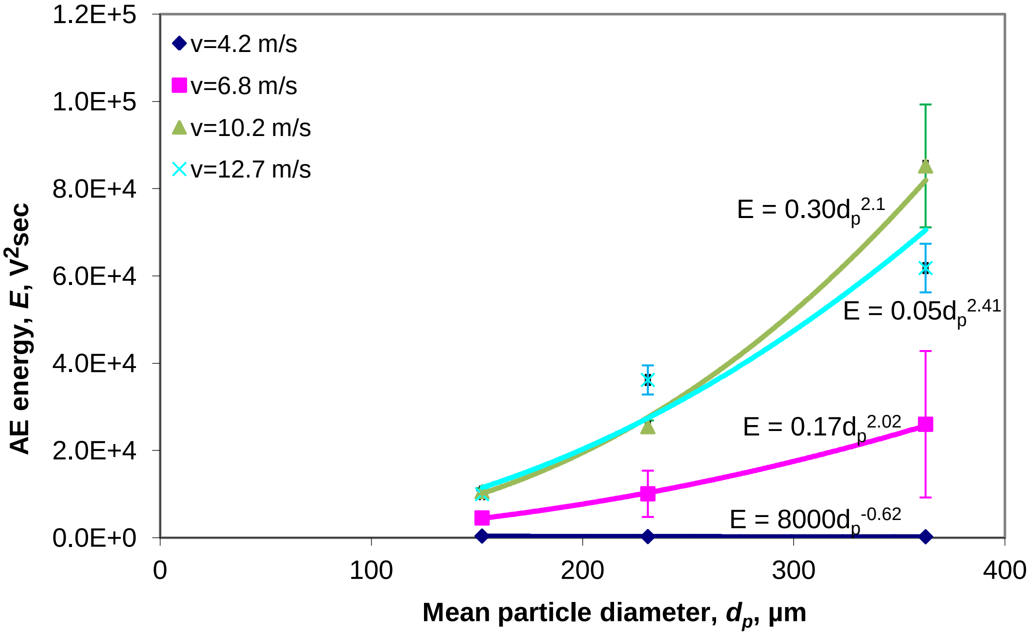

Figure 4.14: Effect of mean particle diameter on AE energy for normal impact at the four nozzle exit velocities with a 1% slurry

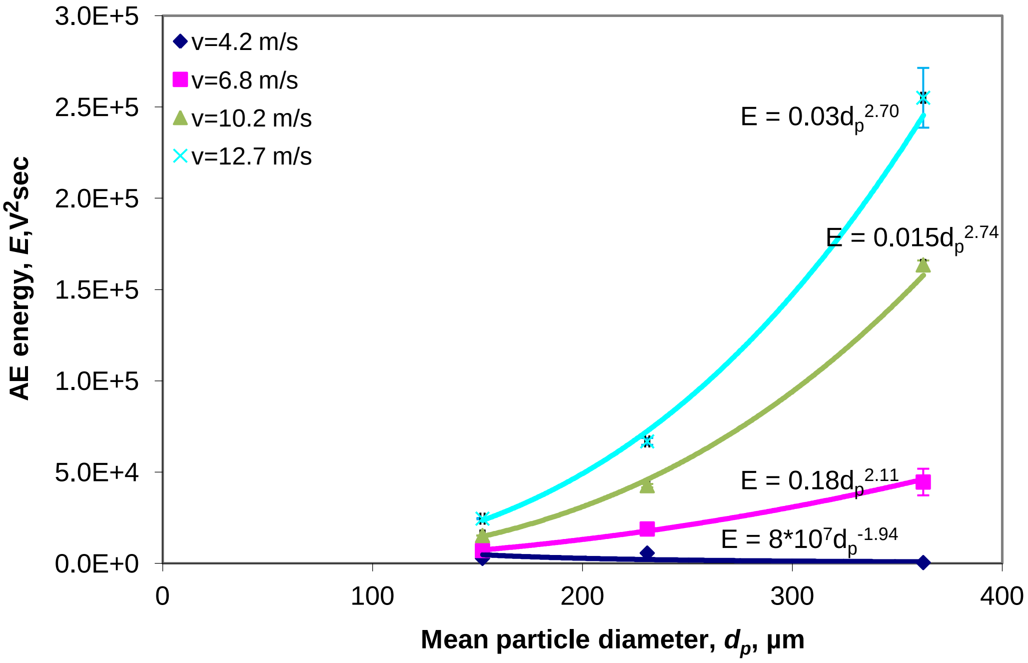

Figure 4.15: Effect of mean particle diameter on AE energy for normal impact at the four nozzle exit velocities with a 2.5% slurry

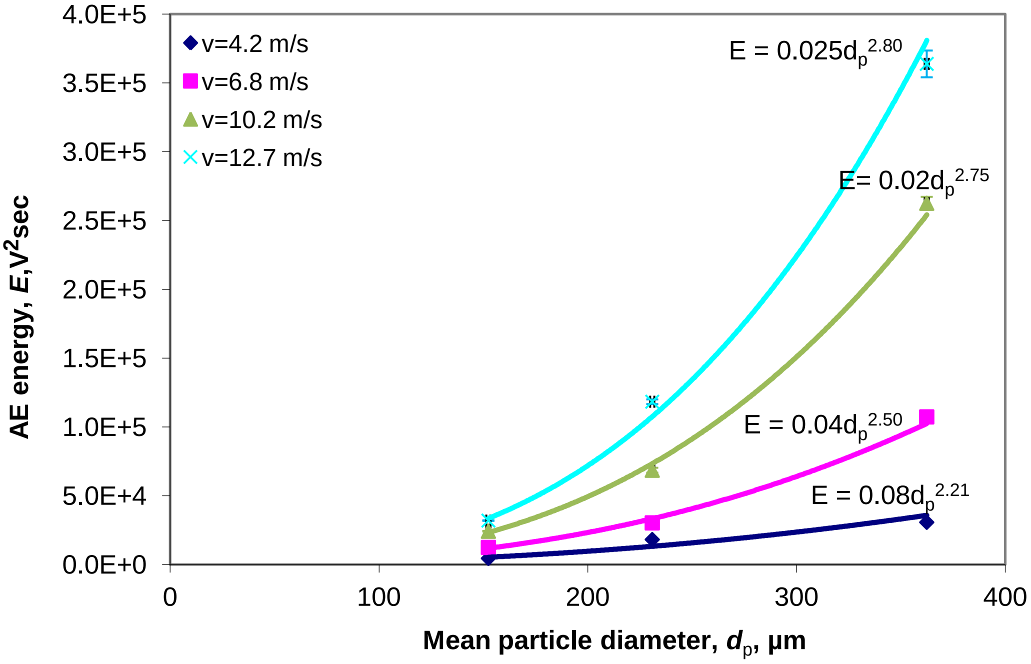

Figure 4.16: Effect of mean particle diameter on AE energy for normal impact at the four nozzle exit velocities with a 5% slurry

Nominal impact angle θ (°)	Nominal concentration (kg/m^3)	Jet exit velocity (m/s)	Particle diameter exponent (Φ)	Curve fitting R^2 value (%)
90	**1**	**4.2**	**-**	**-**
		6.8	**2**	**99**
		10.2	**2**	**99**
		12.7	**2.4**	**93**
	2.5	**4.2**	**-**	**-**
		6.8	**2.1**	**99**
		10.2	**2.7**	**99**
		12.7	**2.7**	**99**
	5	**4.2**	**2.2**	**92**
		6.8	**2.4**	**99**
		10.2	**2.7**	**99**
		12.7	**2.8**	**99**
60	1	4.2	0.3	12
		6.8	0.5	76
		10.2	2.5	98
		12.7	2.8	98
	2.5	4.2	2.4	88
		6.8	2.2	99
		10.2	2.2	100
		12.7	2.1	97
	5	4.2	1.6	99
		6.8	1.9	100
		10.2	2.4	99
		12.7	2.2	97
30	1	4.2	-	-
		6.8	2	56
		10.2	0.7	97
		12.7	1.6	99
	2.5	4.2	3	91
		6.8	2	99
		10.2	1.7	98
		12.7	2	99
	5	4.2	2	97
		6.8	2.2	95
		10.2	2.3	88
		12.7	2.3	88

Table 4.2: Exponent of particle size dependence of measured AE energy for all experiments. (Data in bold font are plotted in **Figures 4.14-4.16**)

Figures 4.17 and **4.18** show the variation of the measured AE energy with nominal solid concentration for the two smaller particle size fractions and for the largest size fraction, respectively. Again, for the larger particle sizes and flow speeds, the exponent tends towards the expected value of unity. **Table 4.3** summarises all of the results for the concentration exponent and led to a weighted average of 1.1.

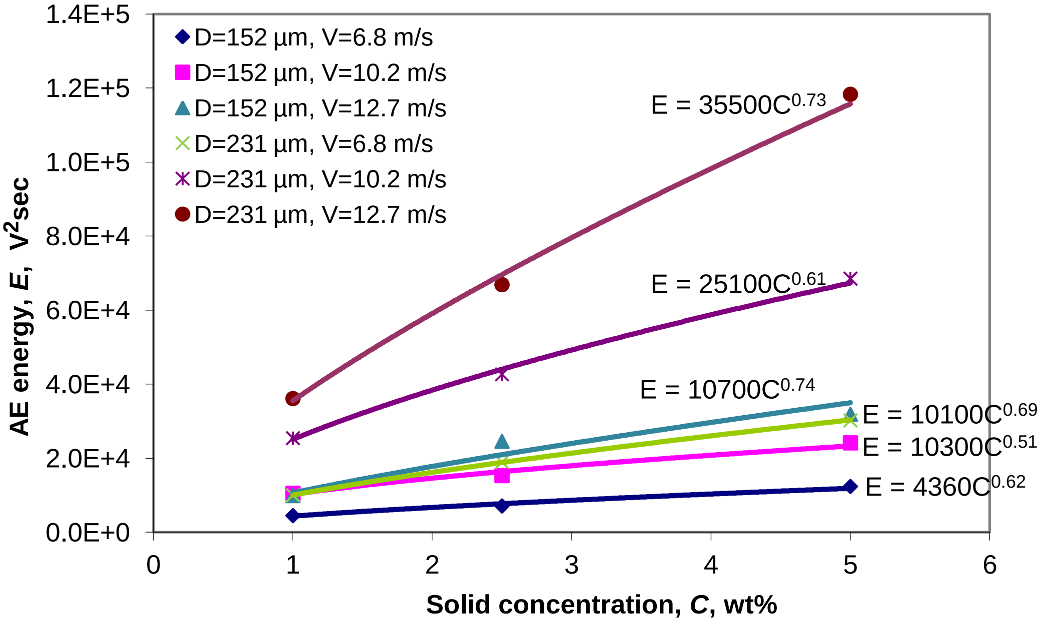

Figure 4.17: Effect of nominal solid concentration AE energy for normal incidence for the smaller particle sizes

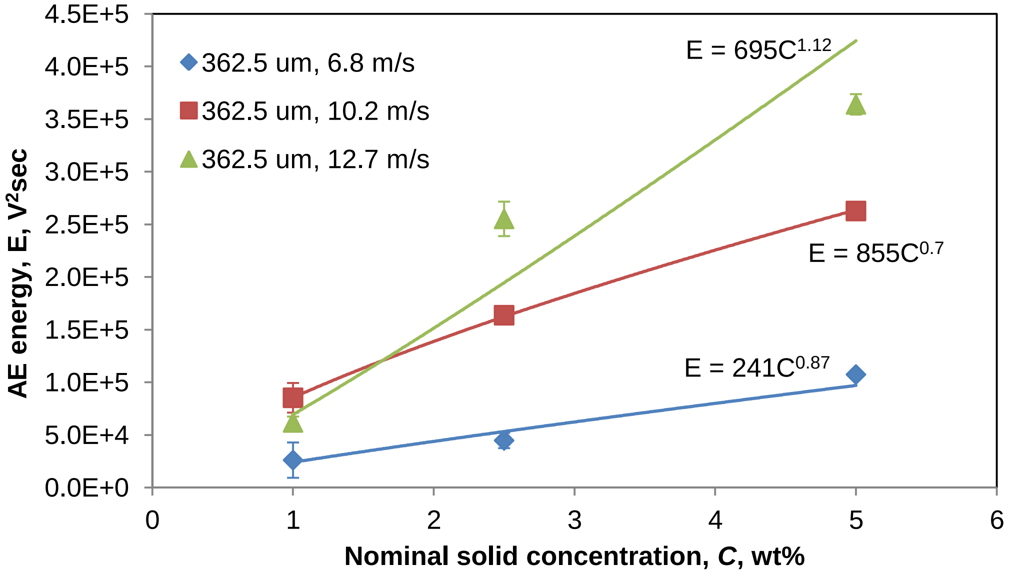

Figure 4.18: Effect of nominal solid concentration AE energy for normal incidence for the smaller particle sizes

Particle size range (μm)	Nominal impact angle θ (°)	Jet exit velocity (m/s)	Solid concentration exponent (β)	Curve fitting R^2 value (%)
125-180	**90**	4.2	1.5	0.92
		6.8	**0.6**	**0.98**
		10.2	**0.5**	**0.98**
		12.7	**0.73**	**0.94**
	60	4.2	2	0.99
		6.8	0.4	0.66
		10.2	0.5	0.97
		12.7	0.7	0.99
	30	4.2	1.6	0.79
		6.8	0.6	0.99
		10.2	0.3	0.86
		12.7	0.5	0.99
212-250	**90**	4.2	2.7	0.96
		6.8	**0.7**	**0.99**
		10.2	**0.6**	**0.99**
		12.7	**0.7**	**0.99**
	60	4.2	2.7	0.86
		6.8	0.6	0.99
		10.2	0.6	0.99
		12.7	0.9	0.98
	30	4.2	2.5	0.98
		6.8	1.6	0.98
		10.2	0.9	0.90
		12.7	1.2	0.98
300-425	**90**	4.2	2.9	0.83
		6.8	**0.9**	**0.95**
		10.2	**0.7**	**0.99**
		12.7	**1.1**	**0.93**
	60	4.2	2.8	0.91
		6.8	1.1	0.95
		10.2	0.3	0.86
		12.7	0.5	0.99
	30	4.2	3	0.95
		6.8	0.7	1.00
		10.2	0.6	0.98
		12.7	1.2	0.95

Table 4.3: Exponent of particle concentration dependence of measured AE energy for all experiments. (Data in bold font are plotted in **Figures 4.17 and 4.18**)

Finally, **Figure 4.19** shows the effect of the sine of the impact angle on the measured AE energy, at the highest concentration and the largest size tested and **Table 4.4** summarises the exponents for all experiments. As can be seen the power index occasionally approaches the expected value of 2, but there is a considerable variation with no consistent pattern and the weighted average is around 1.

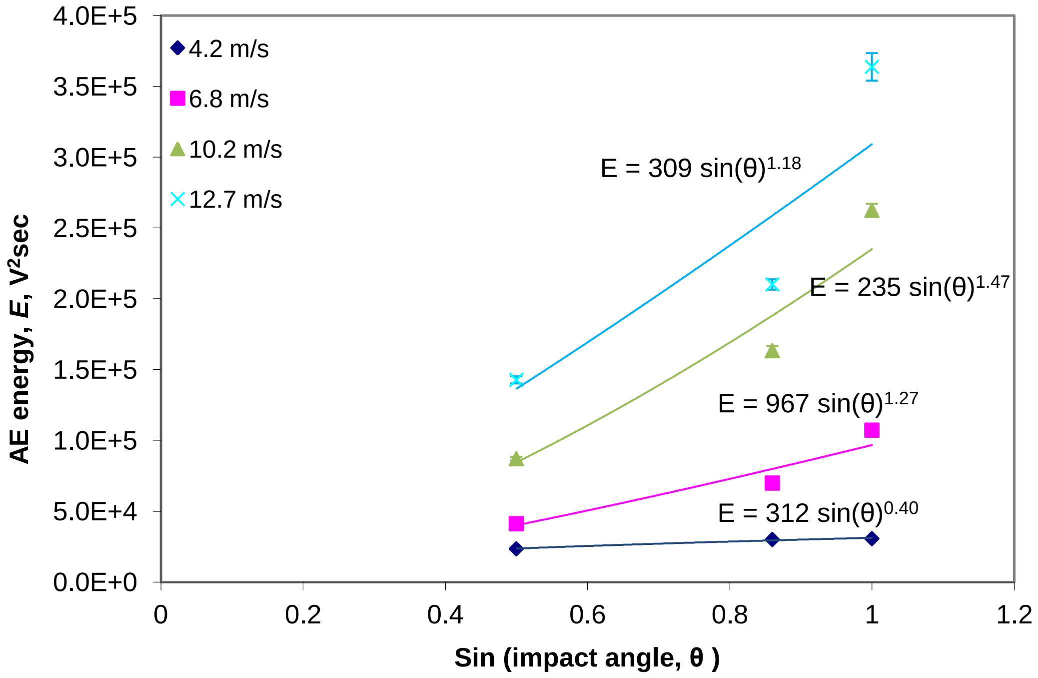

Figure 4.19: The effect of the sine of the impact angle on AE energy, for a 5% slurry for the largest particle size tested

Particle size range (µm)	Nominal concentration (kg/m3)	Jet exit velocity (m/s)	Sin (impact angle) exponent (*q*)	Curve fitting R^2 value (%)
125-180	1	4.2	0.4	57
		6.8	1.1	62
		10.2	0.4	96
		12.7	0.1	29
	2.5	4.2	2.8	99
		6.8	0.77	98
		10.2	0.55	87
		12.7	0.65	94
	5	4.2	0.3	17
		6.8	1	90
		10.2	1.1	99
		12.7	0.72	96
212-250	1	4.2	0.1	8
		6.8	2.9	93
		10.2	1	99
		12.7	1.4	94
	2.5	4.2	1	55
		6.8	1	95
		10.2	1.2	97
		12.7	1.1	96
	5	4.2	0.5	68
		6.8	0.5	98
		10.2	0.22	87
		12.7	0.3	72
300-425	1	4.2	0.37	18
		6.8	0.5	21
		10.2	1.6	88
		12.7	2	82
	2.5	4.2	0	25
		6.8	0.9	93
		10.2	1.7	98
		12.7	1.4	82
	5	**4.2**	**0.4**	**97**
		6.8	**1.3**	**93**
		10.2	**1.5**	**94**
		12.7	**1.2**	**83**

Table 4.4: Power index for sin (nominal impact angle) dependence on the measured AE energy for all experiments. (Bold text data are shown in **Figure 4.19**)

4.3 Flow loop test

As with the slurry jet impingement experiments, the aim of this set of experiments was to investigate, over a wide range of impact conditions, the dependence of the measured AE energy associated with particle impacts upon the slurry impingement parameters this time in a way in which it might be deployed in practice. As with the slurry jet impingement experiments and for each experimental condition specified in **Table 3.8**, the measured AE impact energy was calculated from **Equation 3.1.** At least ten repeat 1-second records were analysed for each condition and the average value is used in the following general analysis to establish the effects of flow speed, particle size, and concentration. As before, the normal expectation is that energy will depend on the square of the impact speed, the cube of the particle diameter (i.e. the particle mass) and be linear with concentration expressed as mass per unit volume of water.

Figures 4.20 to 4.23 show the effect of the flow speed (*v*) on the measured AE energy for a given particle size and all concentrations. As can be seen, the measured AE energy generally increases with both flow speed and concentration following approximately the second power of flow speed for all particle size ranges except the lowest size fraction where the signal:noise might be expected to be low. The variation of the best fit power index for all experiments along with the respective correlation coefficients are summarised in **Table 4.5** which shows the weighted average exponent to be 2.

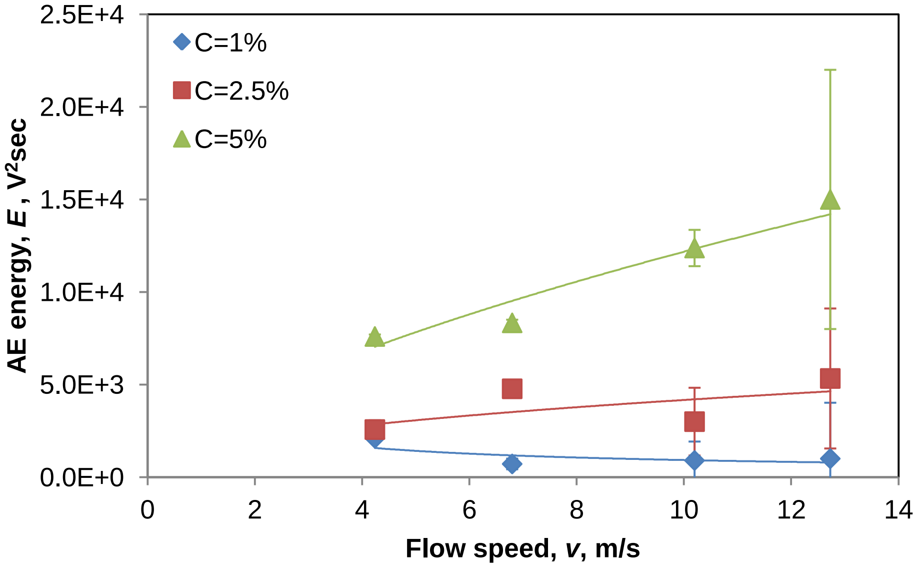

Figure 4.20: Effect of flow speed on the measured AE energy for the three concentrations for particle size range 212-250 µm

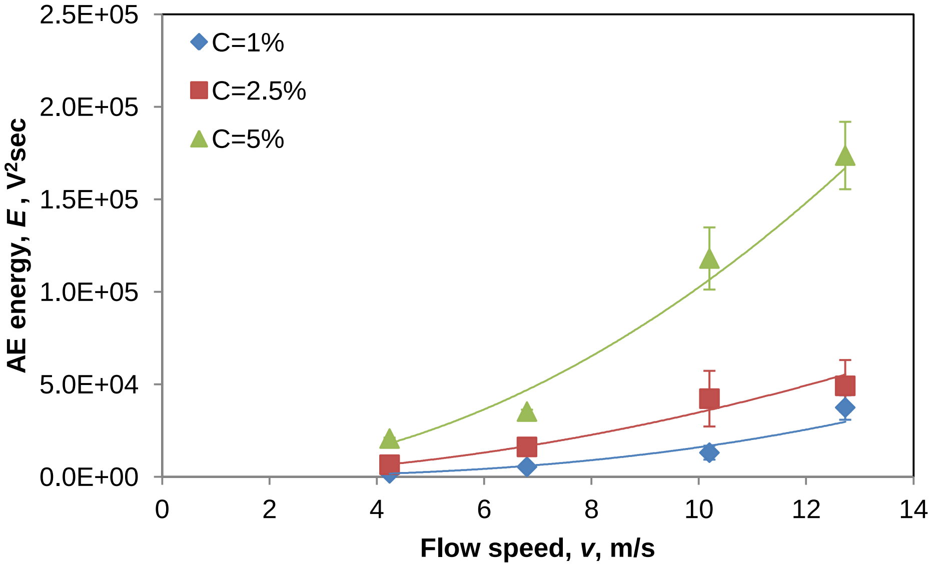

Figure 4.21: Effect of flow speed on the measured AE energy for the three concentrations for particle size range 300-425 µm

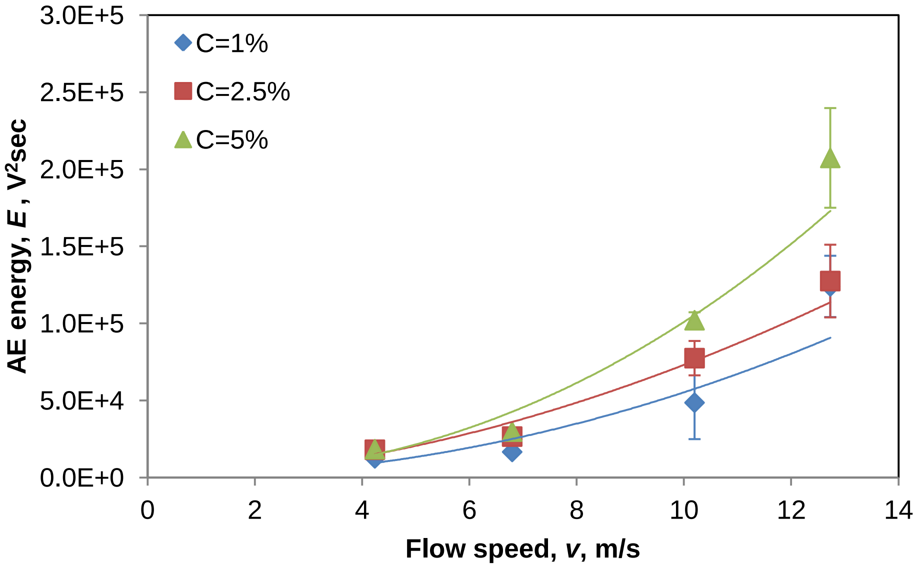

Figure 4.22: Effect of flow speed on the measured AE energy for the three concentrations for particle size range 500-600 µm

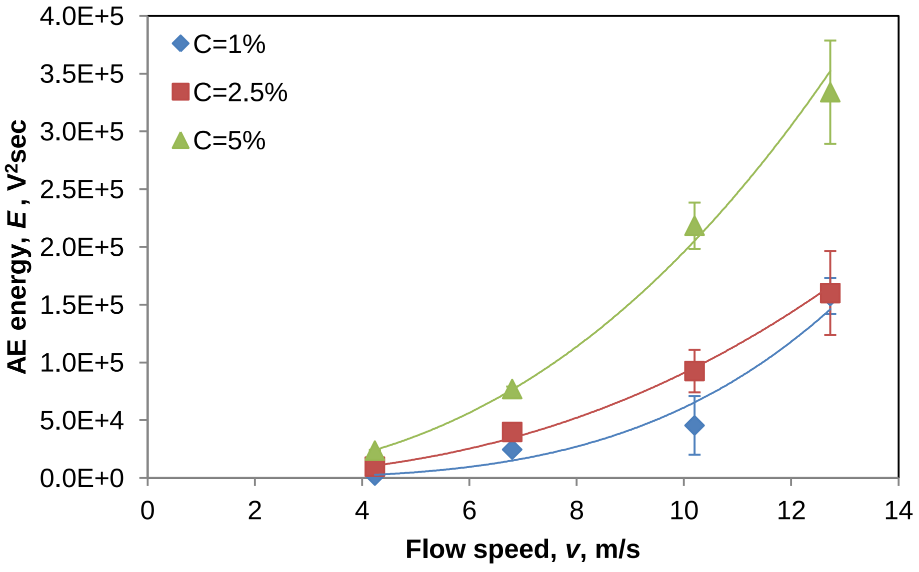

Figure 4.23: Effect of flow speed on the measured AE energy for the three concentrations for particle size range 600-710 µm

Particle size range (µm)	Nominal concentration (kg/m^3)	Flow speed exponent (n)	Curve fitting R^2 value (%)
212-250	1	-	-
	2.5	0.45	36
	5	0.63	91
300-425	1	2.5	97
	2.5	1.9	98
	5	2	96
500-600	1	2	88
	2.5	1.8	94
	5	2.2	94
600-710	1	3.6	95
	2.5	2.5	99
	5	2.4	99

Table 4.5: Exponent of flow speed dependence of measured AE energy and correlation coefficient for all experiments

Figures 4.24 to **4.26** show the effect of mean particle diameter on the measured AE energy for the range of flow speed and nominal concentration studied. Generally, the energy varies with approximately the third power of the mean particle diameter, except in the cases (low speed and lower concentrations) where there is very little particle signal (above the water "noise") and where changes are difficult to discern at all. As for the flow speed exponent the diameter exponent tends towards the expected value of 3 at higher concentrations whereas, at the lower speeds and concentrations, the exponent tends towards 2 (in cases where a change can be discerned). **Table 4.6** lists the best fit power index for all measurements, leading to a weighted mean exponent of 2.6.

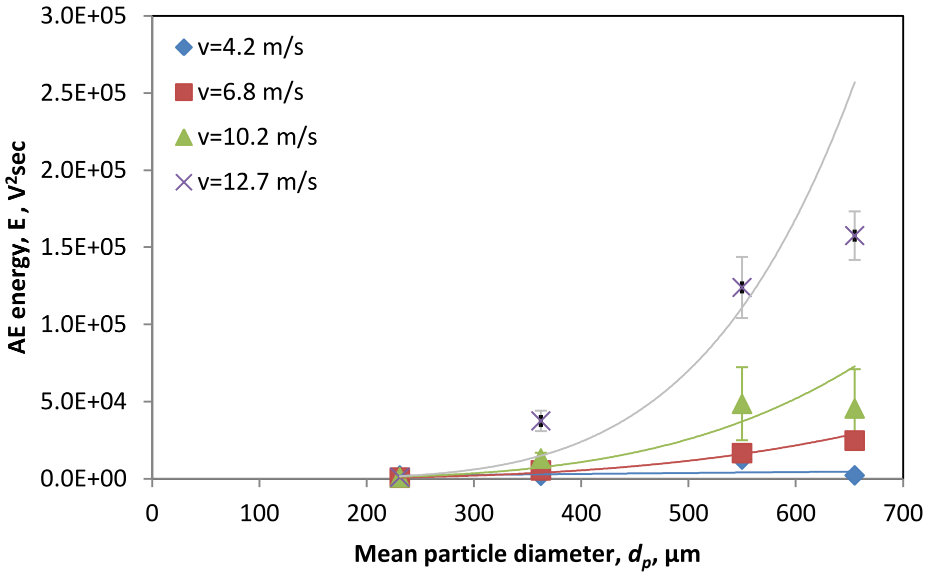

Figure 4.24: Effect of mean particle diameter on the measured AE energy at the four flow speeds with a 1% slurry

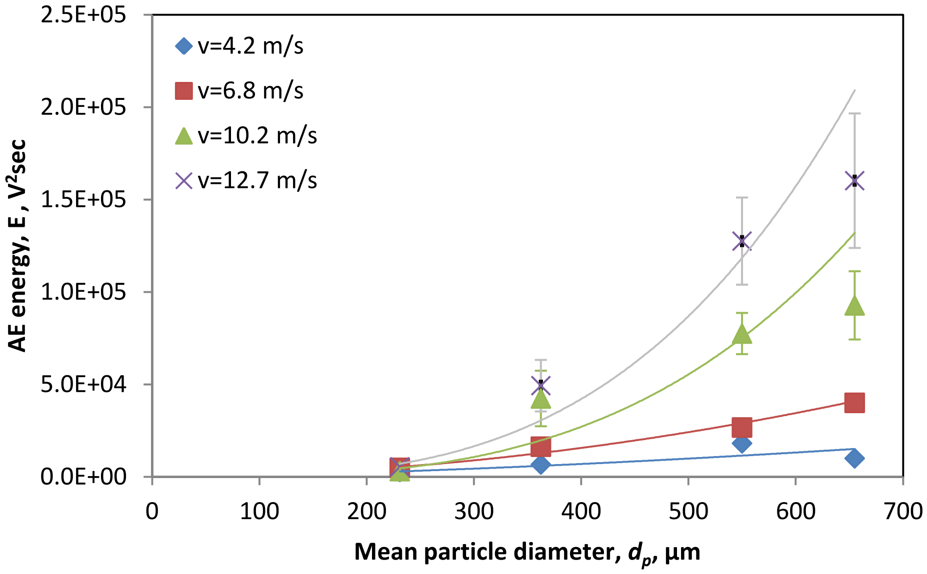

Figure 4.25: Effect of mean particle diameter on the measured AE energy at the four flow speeds with a 2.5% slurry

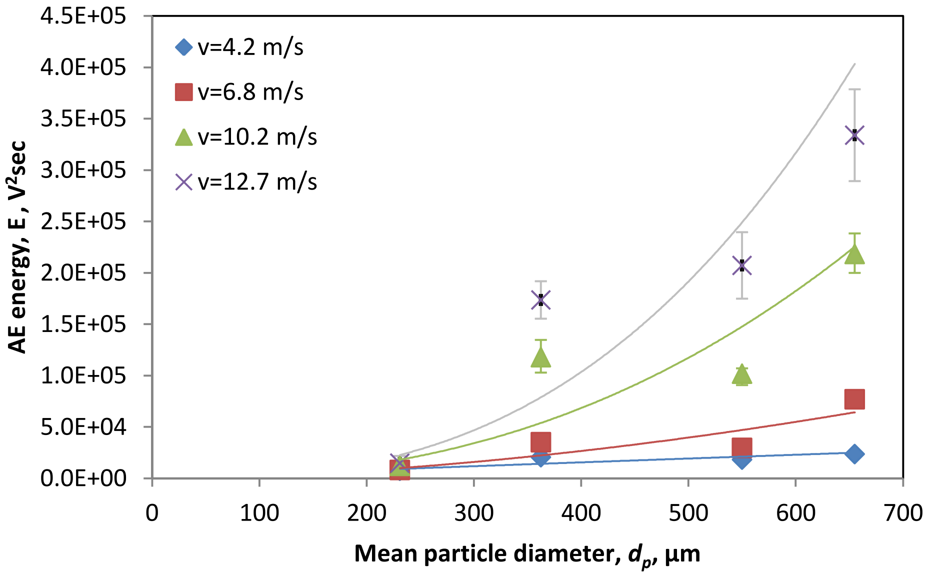

Figure 4.26: Effect of mean particle diameter on the measured AE energy at the four flow speeds with a 5% slurry

Nominal concentration (kg/m^3)	Flow speed (m/s)	Particle diameter exponent (φ)	Curve fitting R^2 value (%)
1	4.2	0.8	17
	6.8	3.3	97
	10.2	3.8	92
	12.7	4.8	91
2.5	4.2	1.5	79
	6.8	2	97
	10.2	3.2	88
	12.7	3.2	94
5	4.2	0.95	74
	6.8	1.8	81
	10.2	2.4	80
	12.7	2.75	85

Table 4.6: Exponent of particle size dependence of measured AE energy for all experiments

Finally, **Figures 4.27 to 4.30** show the effect of nominal solid concentration on the measured AE enrgy for all particle size ranges. The resulting average values of the ten AE records at each condition show a general increase in AE energy with concentration for all particle sizes at all flow speeds, although there is a considerable scatter at higher flow speeds. The nominal concentration exponent tends towards the expected value of unity except in cases of larger particle sizes and flow speeds where a drop out phenomenon might play a significant role. Again, **Table 4.7** summarises the solid concentration exponent along with curve fitting R^2 values and led to a weighted average of 0.95.

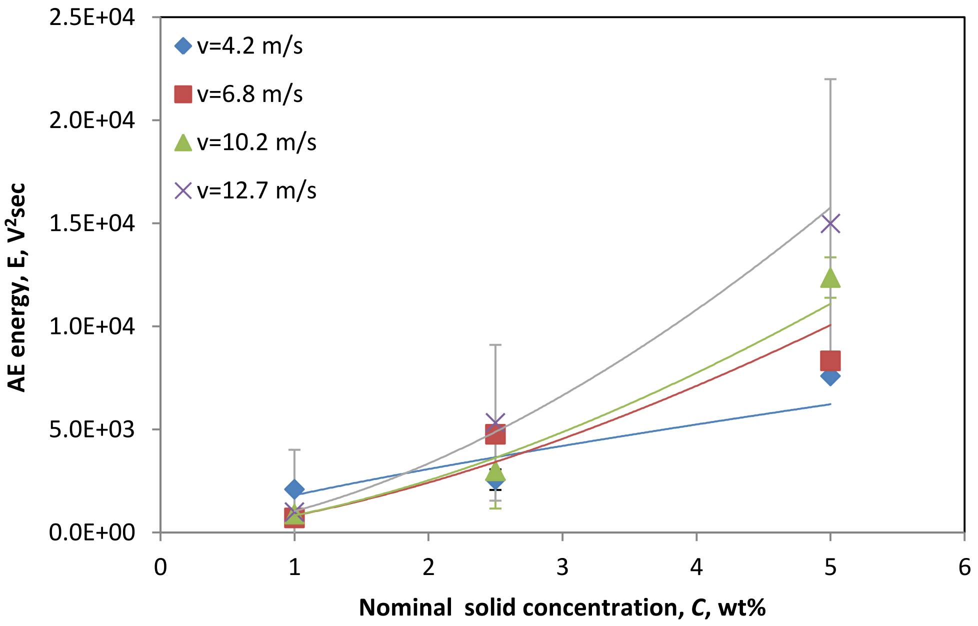

Figure 4.27: Effect of nominal solid concentration on the measured AE energy for the four flow speeds for particle size range 212-250 µm

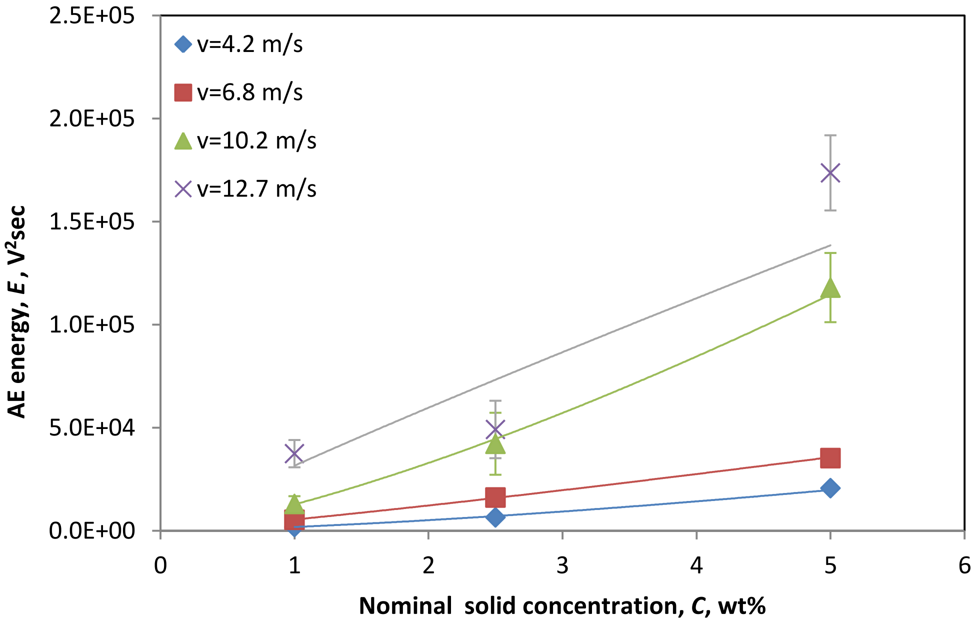

Figure 4.28: Effect of nominal solid concentration on the measured AE energy for the four flow speeds for particle size range 300-425 µm

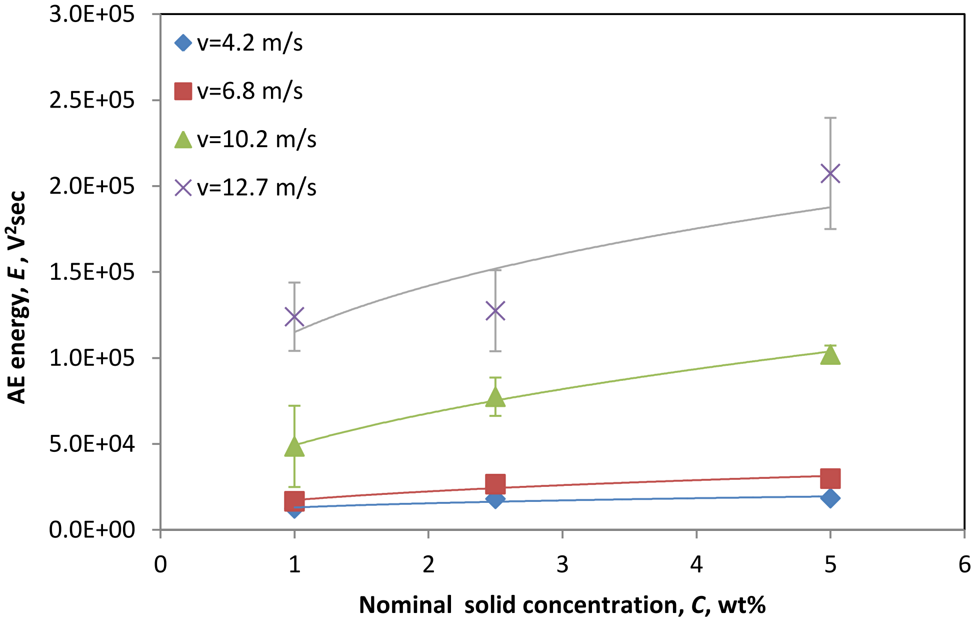

Figure 4.29: Effect of nominal solid concentration on the measured AE energy for the four flow speeds for particle size range 500-600 µm

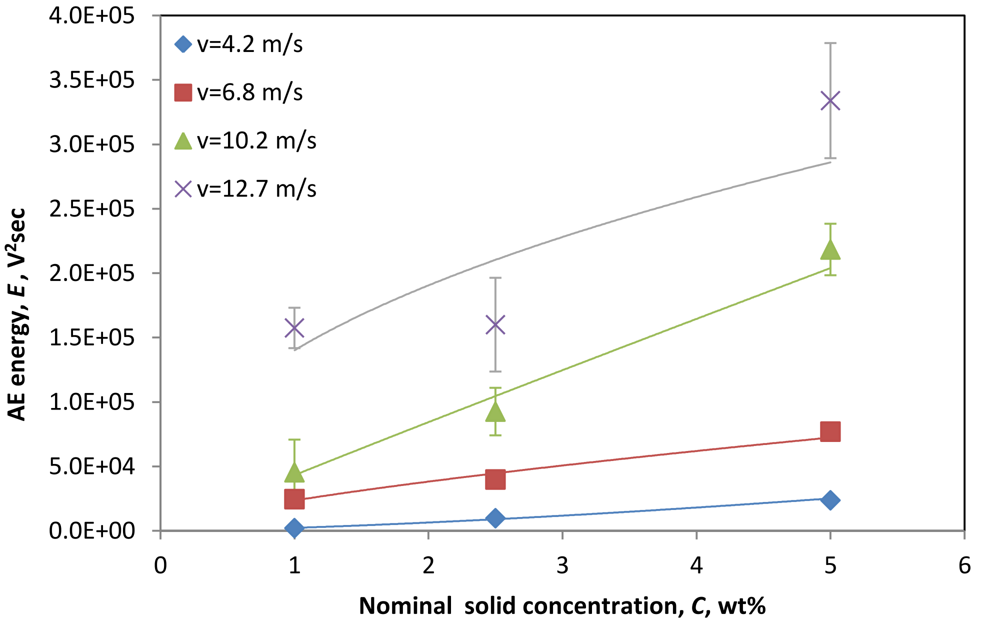

Figure 4.30: Effect of nominal solid concentration on the measured AE energy for the four flow speeds for particle size range 600-710 μm

Particle size range (μm)	Flow speed (m/s)	Solid concentration exponent (β)	Curve fitting R^2 value (%)
212-250	4.2	0.76	80
	6.8	1.5	95
	10.2	1.6	98
	12.7	1.6	99
300-425	4.2	1.4	99
	6.8	1.1	99
	10.2	1.3	99
	12.7	0.9	82
500-600	4.2	0.25	84
	6.8	0.37	93
	10.2	0.46	99
	12.7	0.3	72
600-710	4.2	1.4	99
	6.8	0.7	97
	10.2	1	98
	12.7	0.45	69

Table 4.7: Exponent of particle concentration dependence of measured AE energy for all experiments

Chapter 5

Time series model for particle impacts

This chapter further analyses the results of the measurements in which a particle laden airflow was directed at the target plate. The impingement conditions were chosen to limit the amount of overlap of particle arrival events in order to develop a model of the stream as the cumulation of individual particle arrival events. To this end, some limited experiments were also done with individual particles.

First, the probability distribution of particle impact energy was obtained for a range of particle sizes and impact velocities. Two methods of time series processing were investigated to isolate the individual particle arrivals from the background noise and from particle noise associated with contact of the particles with the target after their first arrival. For the conditions where it was possible to resolve individual impacts, the probability distribution of particle arrival AE energy was determined by the best-fit lognormal probability distribution function. The mean and variance of this function was then calibrated against the known nominal mass and impact speed.

A pulse shape function was devised for the target plate by inspection of the records, backed up by pencil lead tests and this, coupled with the energy distribution functions allowed the records to be simulated knowing the arrival rate and the nominal mass and velocity of the particles. This successful simulation of an AE record was taken as the time series model for any particle arrival and forms the basis of further analysis of the remaining experiments.

5.1 Determination of probability distribution functions

The purpose of this analysis is to develop a model describing the AE time series associated with a particle stream, which accumulates the effect of incident particles, is based on observations of individual impacts, and can be extended to situations where the particle arrivals cannot be resolved. The particle impact energy will depend on the mass and the velocity of the particles arriving at the surface, and may also depend on their angle of incidence. All of these quantities will have a range of values which can be described by probability density functions and these functions will be related to the physical attributes of the flow as well as of the particles themselves.

Figure 5.1a shows a typical example of a 5-second record of raw AE. In order to simplify the signal processing for peak searching, each record was divided into intervals of length 100 points and then the root mean square RMS for each interval was calculated to produce 50 000 points of RMS in a 5-second record, **Figure 5.1b**. This averaging time ensures that there are at least two (re-sampled) samples for each particle arrival at the highest rate observed, although, as will be seen later, it is the ring-down which affects the resolution of particle arrivals.

As can be seen in **Figure 5.1**, the nature of a multiple-particle impact signal is complicated by the particle arrival rate being variable across the record, dictating a time-based processing approach. Given the measured coefficient of restitution, it is possible to estimate the particle speed after impact, V_{p2}, and hence the time, T_r, between first arrival and re-arrival of a rebounding particle, since $V_{p2} = \frac{gT_r}{2}$. These times (0.5 sec for the lowest speed and 2 sec for the highest) are in considerable excess of the time between particle arrivals, even at the lowest arrival rate. However, rebounding particles are unlikely to pass back through the hole, so most rebounding particles will hit the underside of the mask and be reflected back onto the target. Assuming the same coefficient of restitution, the return times are 30 msec for the lowest speed and 8 msec for the highest, compared with the respective times between arrivals of 37 msec and 0.3 msec, respectively, and the re-arrival kinetic energy will be in the order of 20% of the original. Since the air passes through the hole and out through the mesh trap, it will also lift “dead” particles and drive them towards the periphery, further confusing the picture, as saltation will produce some AE noise.

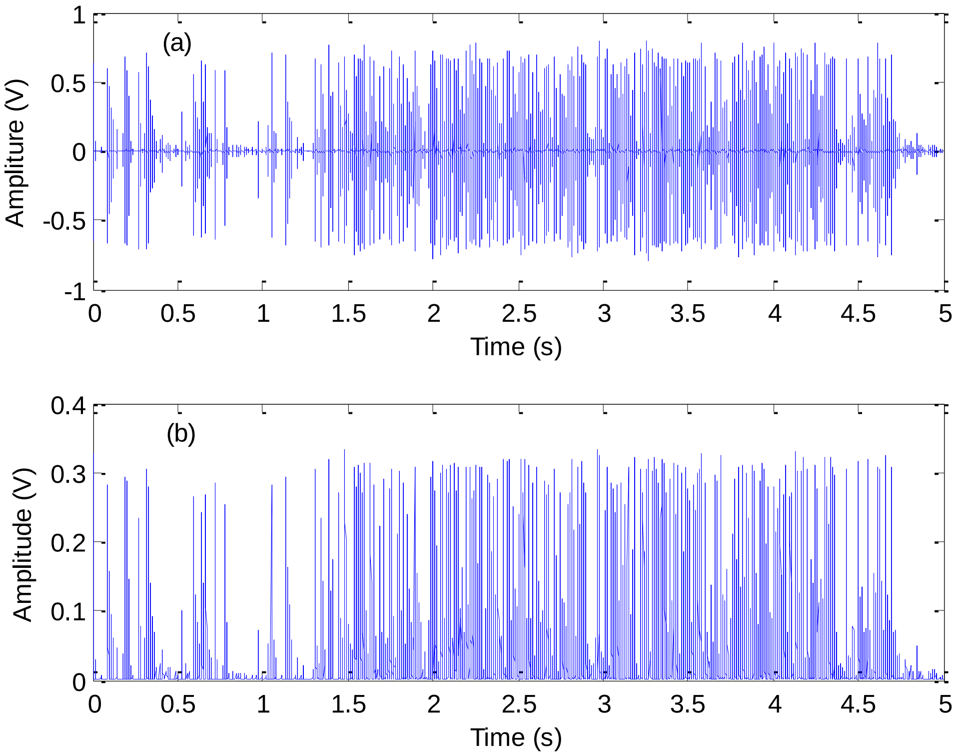

Figure 5.1: Typical 5-second record for particle impacts: (a) raw AE signal, (b) RMS AE signal. 710-850 μm glass beads, impact velocity 10.1 ms^{-1}

Given that the effects of interaction between the particles and between particles and the guide tube walls are unknown and the effects of rebounding and saltating particles constitute mechanical noise expected to be of amplitude less than 20% of first particle arrivals, two approaches were taken to identifying those peaks in the record that are due to first particle arrivals and finding the relevant distribution of AE energy, one using a dynamic amplitude threshold to identify significant AE peaks and the other using a fixed threshold, but truncating the particle energy distribution function to match the estimated number of arrivals.

5.1.1 Dynamic threshold method

Figure 5.2 shows a magnified segment of the record depicted in **Figure 5.1** in both raw and averaged forms. At the estimated average particle arrival rate of 50 particles per second (**Table 3.6**), only around 2 particles would be expected in the time interval shown, so, even allowing for some unevenness of arrival rate, it would seem likely that some events are secondary, possible sources being rebounding, rolling and saltation after arrival.

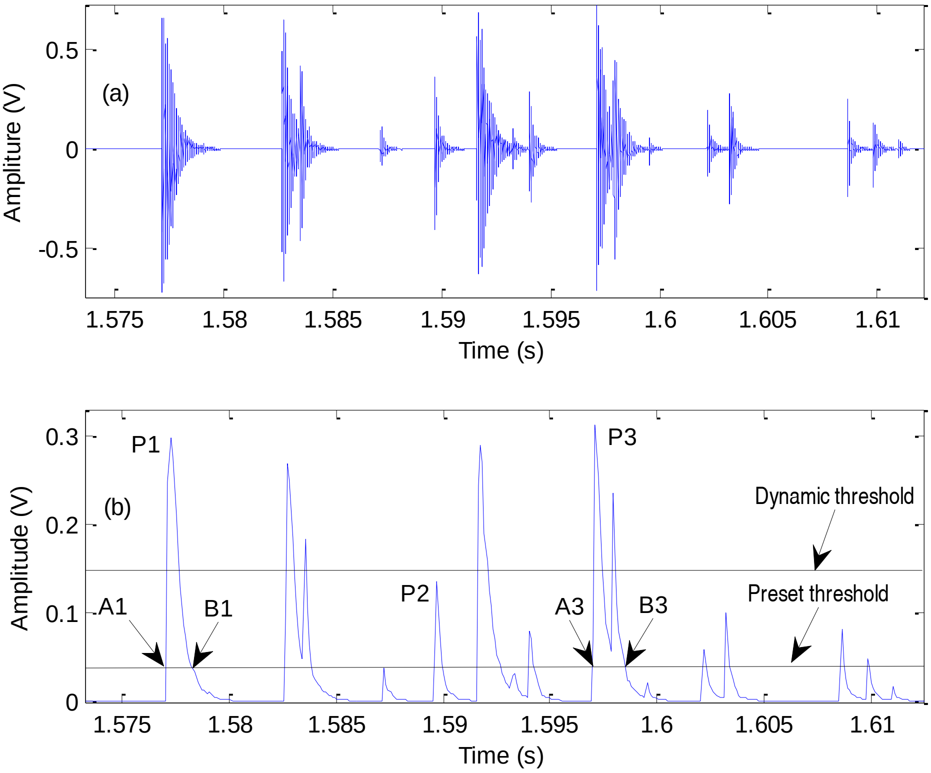

Figure 5.2: Magnified view of (a) raw and (b) RMS AE signal shown in **Figure 5.1**, illustrating dynamic threshold method

The dynamic threshold Matlab algorithm incorporated two rules, the first one to identify the most significant peaks on the assumption that these correspond to the first particle arrivals, and the second one to compute the energies of those peaks.

In the first rule, a varying threshold was adjusted in the range 10% to 50% of the maximum peak height in the record, and the number of peaks were counted for each threshold. This rule allowed the threshold to be chosen at which the number of peaks matched the number of particles estimated by weight. In the second rule, a fixed threshold of 10% of the maximum peak height (the same threshold used to analyse single impacts) was applied to the peaks identified by the first rule, in order to obtain an AE energy which could be compared with single impact AE energies. The signal was traversed temporally and when a peak (i.e. $y_{n-1} \le y_n \ge y_{n+1}$) voltage index, y_n, was found to be above the preset threshold, the peak start $\mathbf{A_n}$, end $\mathbf{B_n}$, and peak height $\mathbf{P_n}$ were identified as shown in **Figure 5.2b**. Then, if the peak height exceeded the dynamic threshold, the particle impact energy was computed by integrating the area under the peak:

$$E_{impact} = \int_{A_n}^{B_n} V^2(t)dt \qquad (5.1)$$

The process is illustrated in **Figure 5.2b** for three of the peaks in the record. Peak $\mathbf{P_1}$ was above the dynamic threshold and its energy was found by integrating the signal above threshold between $\mathbf{A_1}$ and $\mathbf{B_1}$. Peak $\mathbf{P_2}$ was below the dynamic threshold and was therefore discounted as a possible rebound peak. Peak $\mathbf{P_3}$ appears to have two overlapping events, but the algorithm treats it as one event integrated between $\mathbf{A_3}$ and $\mathbf{B_3}$ because the trough between the events does not go below the fixed threshold.

Figure 5.3 shows the distribution of AE energy thus obtained from the record shown in **Figure 5.1**, which is one of five obtained under these experimental conditions. The other four runs produced similar distributions.

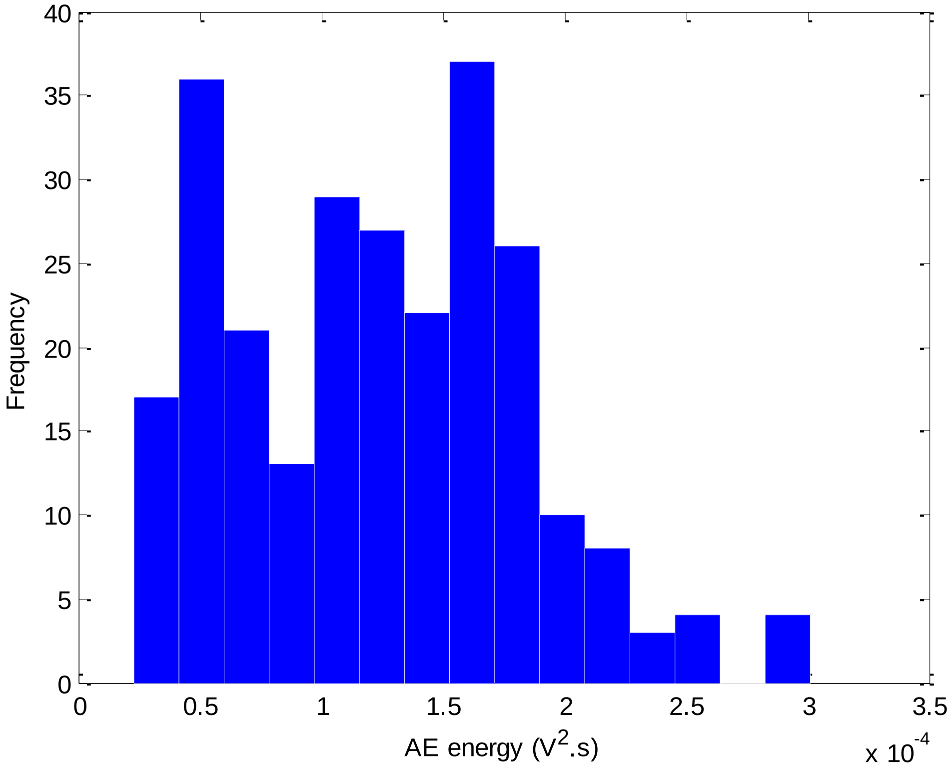

Figure 5.3: Distribution of AE energy attributed to particle impact from record shown in **Figure 5.1** using dynamic threshold approach

Some of the distributions appeared to contain two modes and many had a peak at the low end, so the data were fit with both a bimodal distribution *Y* (the sum of two normal distributions *Y1* and *Y2*) and a monomodal log-normal distribution. A least-squares algorithm implemented in Matlab was used to obtain the best fit to each distribution as shown in **Figure 5.4**.

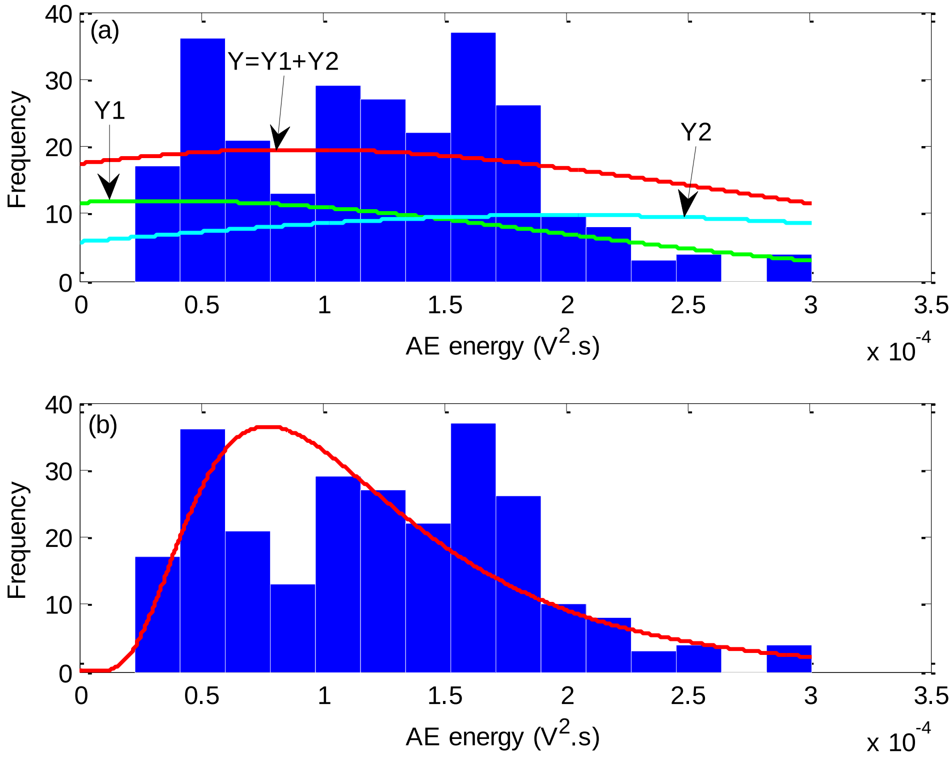

Figure 5.4: Probability function fit to distribution of AE energy attributed to particle impact from record shown in **Figure 5.1** using the dynamic threshold approach: (a) bimodal distribution and (b) log-normal distribution

5.1.2 Truncated distribution method

This approach involved using only a preset threshold, coupled with an overlap detector to obtain the distribution of AE energy attributed to particle impact. All peaks above the preset threshold (10% of maximum peak height) were identified in the averaged time series along with their upward and downward crossings of the threshold. Next, an overlap detector identified, within each peak, any reversal in signal slope, recording times at which these reversals take place. The energy of each peak was obtained as before, except that any overlapping peaks were split into two (or more) at the overlap point. The process is illustrated in **Figure 5.5** for the same time-series segment as **Figure 5.2** using the same peaks. As before, peak **P_1** was above the threshold and its energy was found by integrating the signal between **A_1** and **B_1**. This time, peak **P_2** was also above the preset threshold and its energy was found by integrating the signal between **A**$_2$ and **B**$_2$. Peak **P**$_3$ was found to include two overlapping events, so the energy of the first was integrated between **A**$_3$ and **B**$_3$ and the second, labelled **P**$_4$, was integrated between **A**$_4$ and **B**$_4$. The histogram of energies was then prepared using 15 bins, and events counted from the highest values of energy downwards. In order to obtain an internally consistent number of events, the distribution was truncated at the nearest bin to the number of particles estimated by weighing.

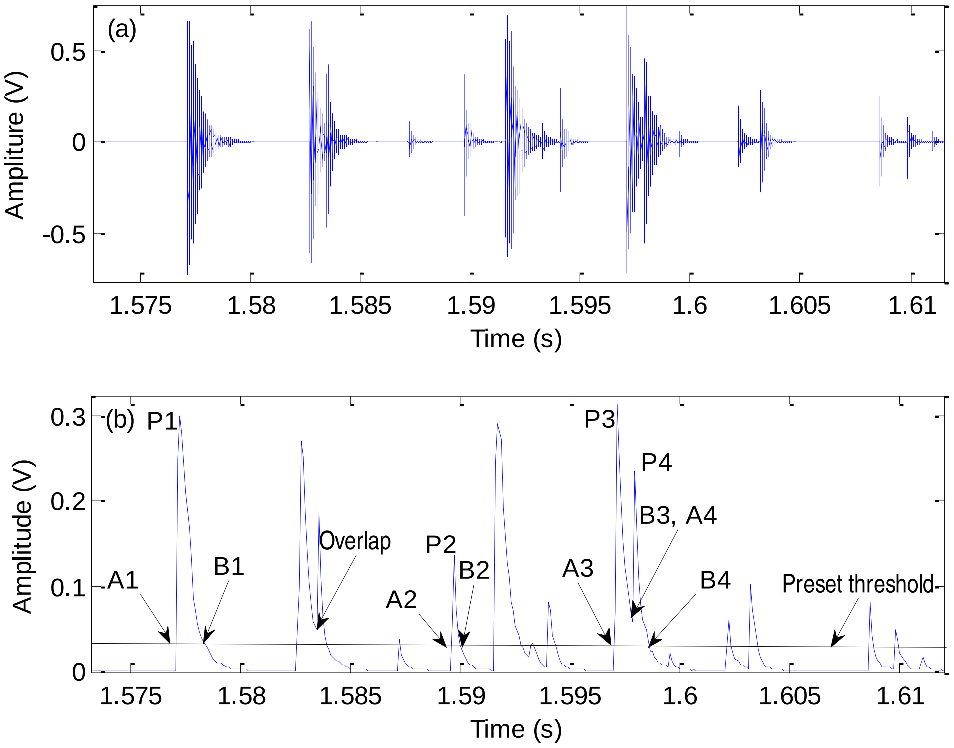

Figure 5.5: Magnified view of (a) raw and (b) RMS AE signal shown in **Figure 5.1**, illustrating truncated distribution method

Figure 5.6 shows the resulting distribution, again with the best-fit bimodal and log-normal distribution functions.

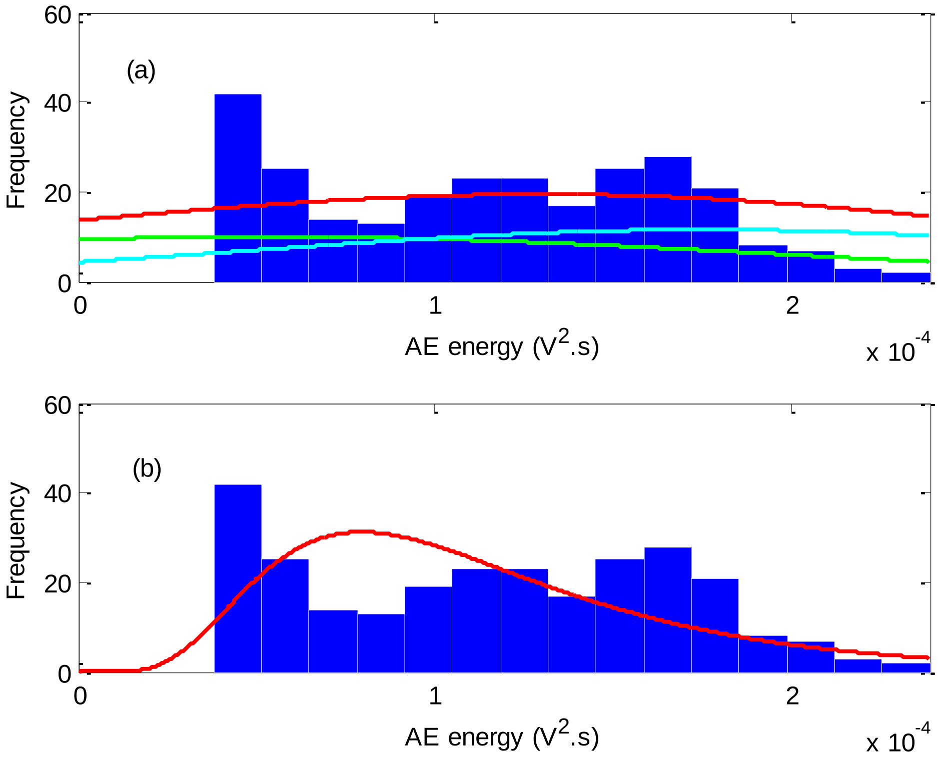

Figure 5.6: Probability function fit to distribution of AE energy attributed to particle impact from record shown in **Figure 5.1** using the truncated distribution approach. (a) bimodal distribution and (b) log-normal distribution

5.2 Development of time series model

Following the approach of Brodie and Rosewell [86], the expected distribution of particle energies can be calculated using the measured particle size distribution functions given in **Table 3.6** and the semi-empirical relationship between particle speed, gas flow speed and particle size **Equation 3.5**. The size distribution was divided into 5-micron sized bins and the incident kinetic energy, $\frac{1}{2}mV_p^2$, calculated for each bin. The resulting distribution matching the conditions for the record illustrated in **Figure 5.1** is shown in **Figure 5.7**. As can be seen, the non-linear relationship for the energy results in a skewing of the expected distribution, giving it a shape more like the lognormal function.

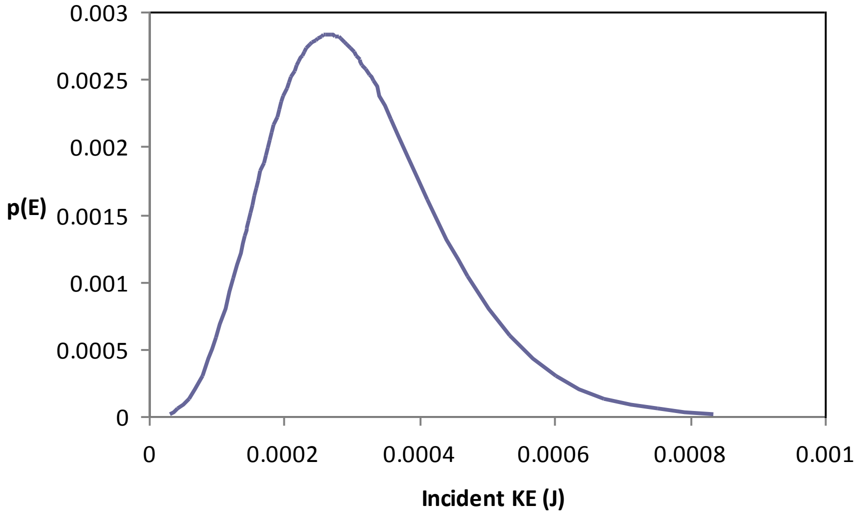

Figure 5.7: Expected distribution of incident particle energy, accounting for particle size distribution only.

The bimodal distribution equations developed by Gomes-Ferreira *et al* [84] cannot directly be used here since they are spatial distributions rather than p.d.f.s. Nevertheless, an estimate of the bimodality due to particle interaction can be obtained from the best-fit values of *c*, the proportion of particles which interact, reported in their simulations carried out for a range of values of β (the dimensionless divergence parameter), coefficient of restitution, and two other dimensionless parameters, the dimensionless particle radius: $r_p* = \frac{r_p}{d}$ and the dimensionless stand-off distance: $d* = \frac{f \times d}{V_p}$, where d is the nozzle stand-off distance (here 50mm), r_p is the particle radius and f is the particle launch rate (here taken to be the same as the particle arrival rate). Values of these dimensionless parameters are shown for the present stream conditions in **Table 5.1**. Taking the highest value (40) of β simulated by Gomes-Ferreira *et al*, representing the most focused stream, and using the results for a coefficient of restitution of unity, the results for the fraction of particles colliding as a function of $d*$ are shown in **Figure 5.8**, for two values of r_p*; 0.01 which covers the larger particles in the present study and 0.005, which covers the smaller. The dimensionless stand-off is the number of particles launched into the stream in the time it takes for a particle to traverse the stand-off distance and so is a measure of the number particles in transit at any given time. Comparison of **Table 5.1** and **Figure 5.8** suggests that the fraction of interacting particles will vary between 0 and about 0.5 over the conditions studied here, although the extrapolation to values of r_p* other than those simulated is uncertain. For the conditions corresponding to the record illustrated in **Figure 5.1** (shaded in **Table 5.1**), it is clear that inter-particle interactions in the stream are rather unlikely and that the noise peaks observed in the record must be due to recirculation of particles caused by the air passing through the cavity between the mask and the target plate. This means that a monomodal distribution is more appropriate for describing first particle arrivals.

Particle size fraction (µm)	**Nominal particle diameter, d_p (µm)**	**Nominal particle velocity, V_p (ms^{-1})**	**Average arrival rate, f (s^{-1})**	**Dimensionless stand-off distance, d^***	**Dimensionless particle radius, r_p^***
125-180	152.5	4.9	4238	132	0.003
		8.3	4238	77.9	
		11.8	2928	37.8	
		15.5	3140	30.9	
212-250	231	4.7	910	44.7	0.005
		7.5	803	24.7	
		10.6	770	16.8	
		13.8	653	10.9	
300-425	362.5	4.4	151	12.4	0.007
		6.8	162	8.64	
		9.5	180	6.87	
		12.3	231	6.81	
500-600	550	4.3	73	9.34	0.011
		6.3	70	6.11	
		8.6	84	5.37	
		11	110	5.50	
600-710	655	4.2	54	8.42	0.013
		6	49	5.35	
		8.2	69	5.51	
		10.5	69	4.30	
710-850	780	4.1	27	5.14	0.016
		5.8	35	4.71	
		7.9	29	2.86	
		10.1	47	3.63	

Table 5.1: Derived particle and particle stream conditions. See text for shaded conditions

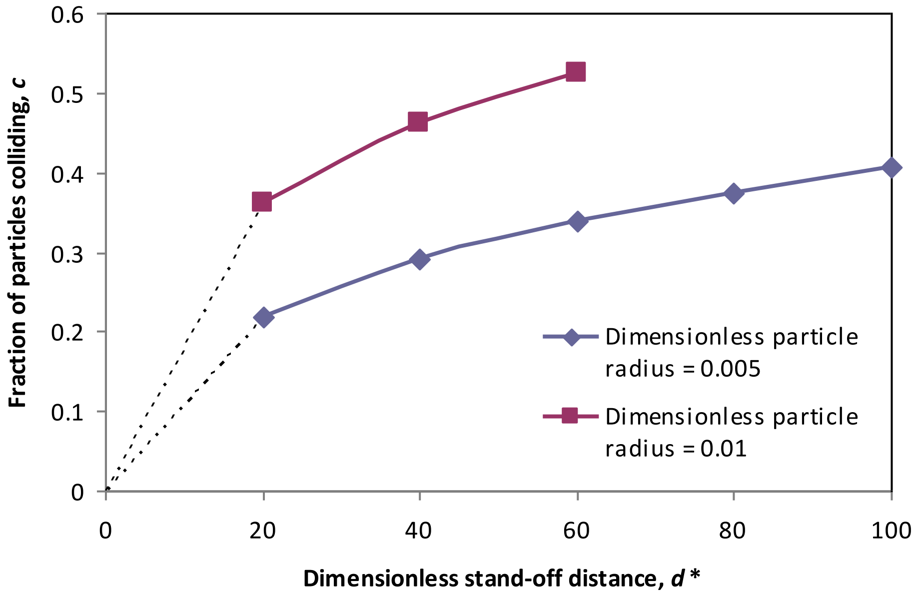

Figure 5.8: Values of fraction of particles colliding derived from the simulations of Gomes-Ferreira *et al* [84]. Dotted and chained lines are manual extrapolations of the simulation results to low particle densities

The two main advantages of using the truncated energy method over the dynamic threshold method are that it can handle the smaller size fractions which produce weaker impact signals, and it can be used to measure the higher arrival rates which create frequent impacts with small time intervals between them. Nevertheless, either method can only distinguish individual impacts if: (a) the peaks corresponding to particle impacts are above the threshold level (here 10% of the maximum peak height), and (b) the time interval between peaks is sufficient for the first peak amplitude to decay sufficiently that a down-crossing can be detected. For the current configuration, this meant that the peaks for the smallest size fraction (125-180 μm) were not distinguishable for either method.

In order to examine the goodness of the bimodal and log-normal fits for each signal processing approach, a comparative measure (error) (CM) was devised, that computes the sum of absolute differences between observed values and fitted values of frequencies multiplied by the corresponding AE energy in each of the *N* classes:

$$CM = \sum_{i=1}^{N} \left(abs\left(f_{i,obs} - f_{i,fit} \right) \times E_i \right)$$

Figure 5.9 shows how the error varies with average particle arrival rate over the three size ranges where it was possible to obtain results using the dynamic threshold approach. The error increases with increase in particle arrival rate, which is to be expected as it becomes more challenging to identify individual particles as the overlap rate increases. Also, the bimodal fit generally gave higher errors as well as a larger variation in error, indicating that it is generally a less good description of the distributions.

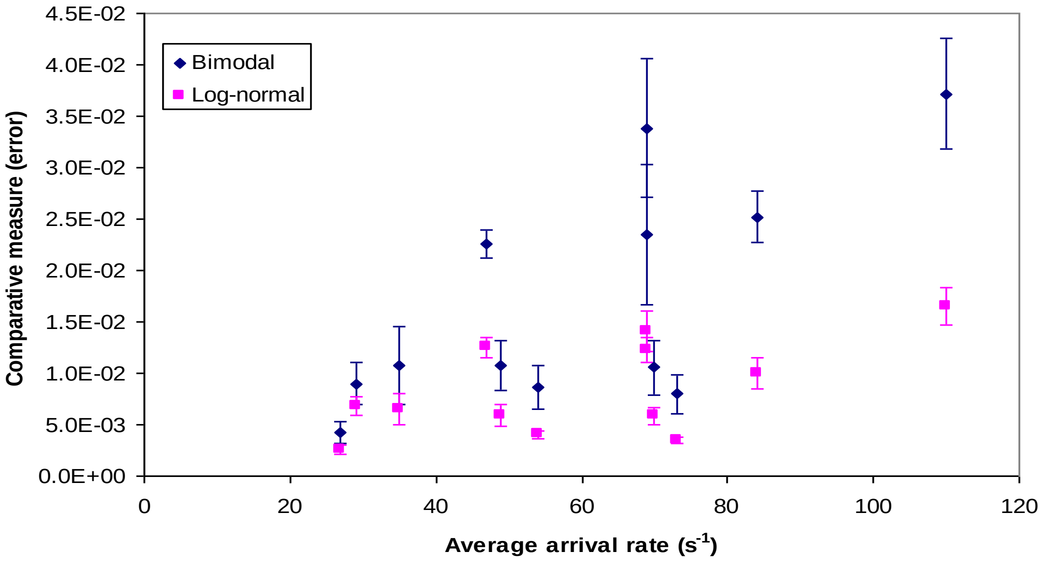

Figure 5.9: Dependence of comparative error upon average particle arrival rate using the dynamic threshold method for the particle size range 850μm to 300 μm

Figures 5.10 and 5.11 show the error using the truncated distribution method over the arrival rates for particle sizes from 850μm to 212 μm and 850μm to 300 μm, respectively. Comparing **Figures 5.10** and **5.11** shows the truncated energy method to give about the same error for bimodal and log-normal distributions, and an overall error about the same as that for log-normal distributions using the dynamic threshold method. At higher arrival rates, the error stops increasing, and the log-normal distribution gives significantly lower error and scatter in error.

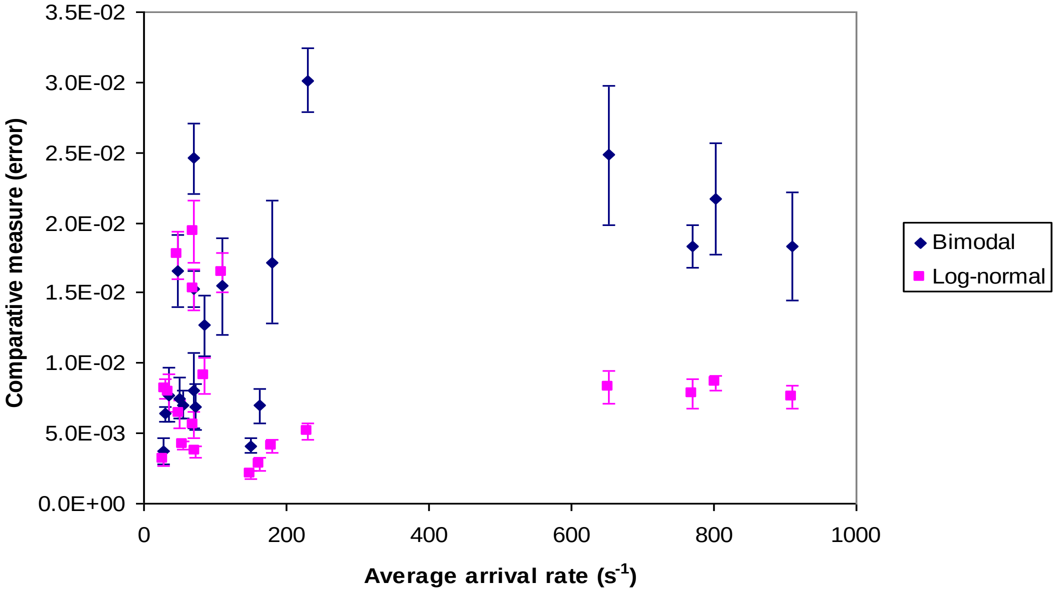

Figure 5.10: Dependence of comparative error upon average particle arrival rate using the truncated energy method for the particle size range 850µm to 212 µm

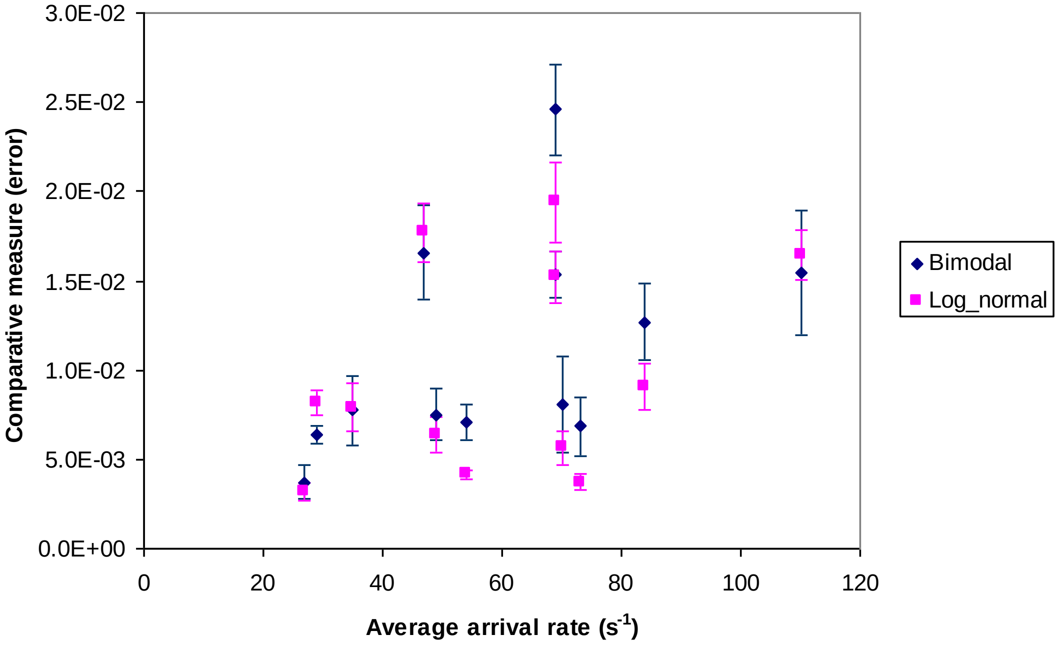

Figure 5.11: Dependence of comparative error upon average particle arrival rate using the truncated energy method for the particle size range 850µm to 300 µm

In summary, the truncated distribution method, coupled with the monomodal fit to the data gives a more robust description of the experimental data, and one which fits with the types of distributions observed in the literature. Accordingly, the rest of the chapter will focus on this approach.

5.2.1 Correlation between truncated distribution and incident impact energy method using log-normal distributions

As can be seen from **Table 5.1**, there are 20 discrete combinations of average particle diameter, d_p, (hence particle mass, m) and nominal particle impact velocity, V_p, excluding the smallest size fraction. The log-normal probability distribution function is given by:

$$P(E) = \frac{1}{\sqrt{2\pi} \times \sqrt{\log\left(\frac{\nu}{M^2}+1\right)} \times E} \exp\left[-\frac{\left(\ln E - \ln\left(\log \frac{M^2}{\sqrt{\nu + M^2}}\right)\right)^2}{2 \times \log\left(\frac{\nu}{M^2}+1\right)}\right] \qquad (5.2)$$

where P is the probability, E is particle impact energy variable, and M and ν are the mean and variance, respectively, of the lognormal distribution.

Figures 5.12 and **5.13** show the best fit mean and variance of the lognormal distribution for each of the 20 combinations (incident energy), the error bars indicating the range of values over the five observations at each incident energy. The best-fit straight line through each of these plots provides a calibration of the distribution functions:

$$M = 1.7621 mV_p^2 + 1\times10^{-5} \quad \text{and} \quad \nu = 7\times10^{-5} mV_p^2 + 2\times10^{-10} \qquad (5.3)$$

where m is particle mass in kg and V_p is particle velocity in ms^{-1}.

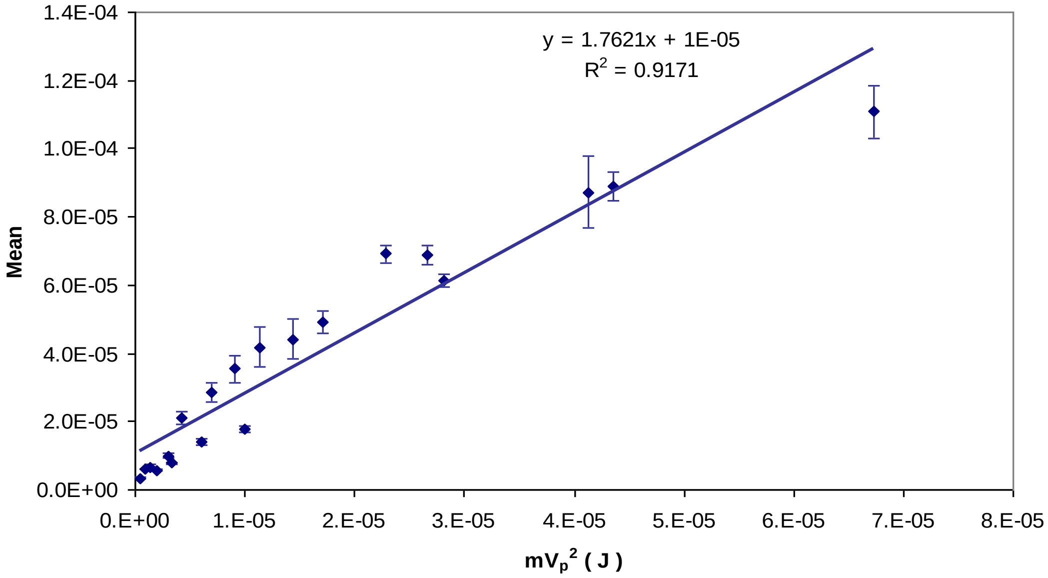

Figure 5.12: Correlation between the mean of the log-normal distribution and nominal incident energy

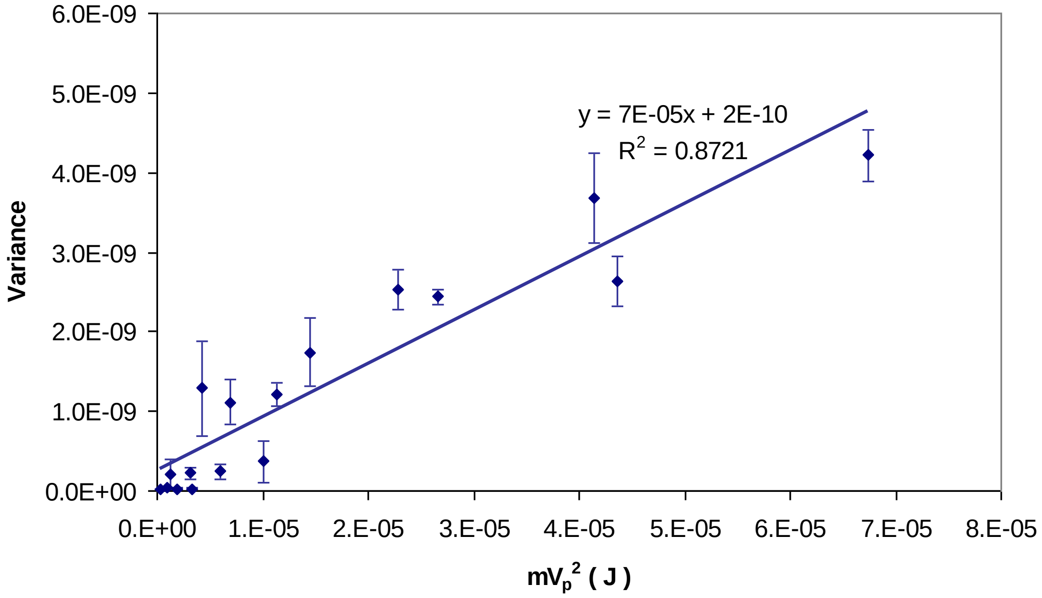

Figure 5.13: Correlation between the variance of the log-normal distribution and nominal incident energy

As a calibration check, **Figure 5.14** illustrates the correlation between the distribution mean (average value of the 5 observations) and the AE energy (average of the ten observations) from the single impact tests. As can be seen, the correlation is excellent, although the slope indicates that the distribution only captures about 85% of the energy recorded in a single impact.

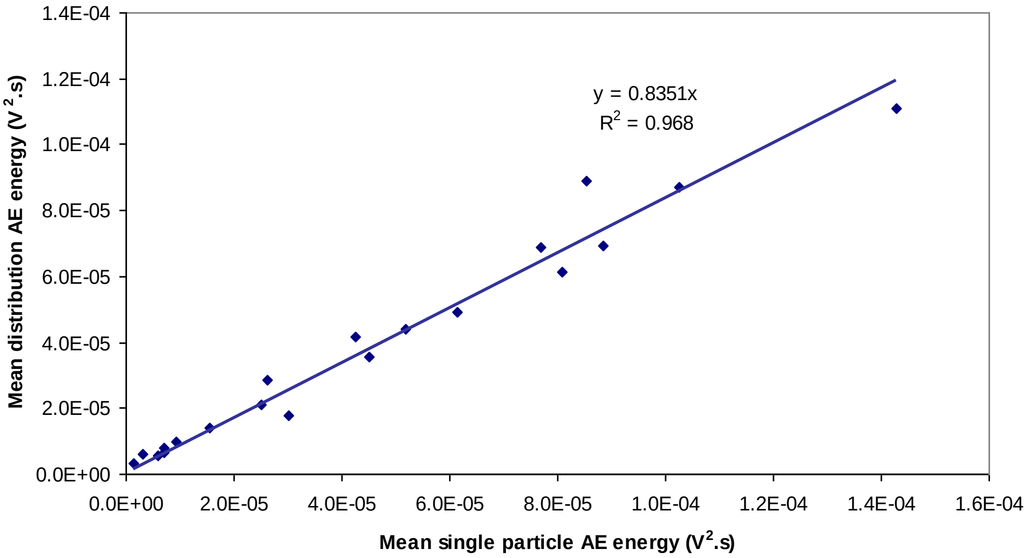

Figure 5.14: Correlation of mean distribution AE energy with mean AE energy for single impacts

The “truncated energy”, all energy not attributed to primary particle impacts (**Equation 5.1**), was calculated for all records as a proportion of the total energy of the record:

$$E_{trunc} = \frac{\int_0^{t_{sig}} \left[V(t)\right]^2 dt - \sum_{impacts} E_{impact}}{\int_0^{t_{sig}} \left[V(t)\right]^2 dt}$$

This energy can be regarded as particle noise, i.e. AE activity associated with rebound and saltation of the particles after primary impact. As can be seen in **Figure 5.15**, this noise generally increases with nominal impact velocity as might be expected for rebounds or from the higher fluid speeds associated with the higher particle speeds. The particle noise also increases with particle size, again as might be expected with the secondary activity of larger particles being more likely to come above the threshold.

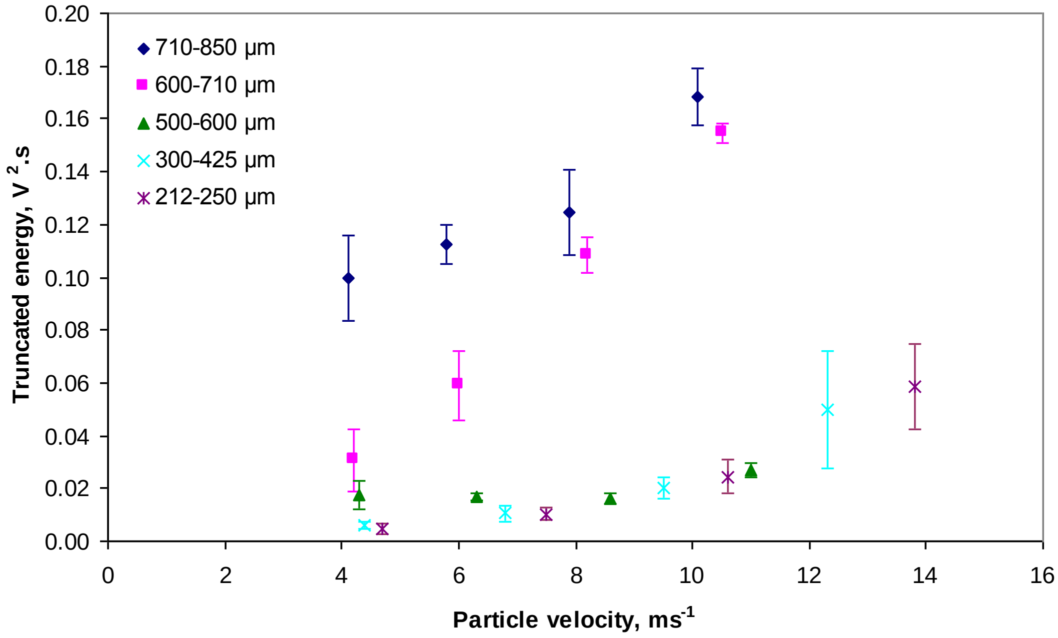

Figure 5.15: Truncated energy versus particle impact speed

5.2.2 Time series simulation

Equations 5.2 and **5.3** form the basis of a time-series model where the pulse energies (**Equation 5.1**) are given by the distribution function:

$$P(E)=\frac{1}{\sqrt{2\pi}\times\sqrt{\log\left(\frac{7\times10^{-5}mV_p^2+2\times10^{-10}}{(1.7621mV_p^2+1\times10^{-5})^2}+1\right)}\times E}$$
$$\times\exp\left[-\frac{\left(\ln E-\ln\left(\log\frac{(1.7621mV_p^2+1\times10^{-5})^2}{\sqrt{(7\times10^{-5}mV_p^2+2\times10^{-10})+(1.7621mV_p^2+1\times10^{-5})^2}}\right)\right)^2}{2\left(\log\left(\frac{7\times10^{-5}mV_p^2+2\times10^{-10}}{(1.7621mV_p^2+1\times10^{-5})^2}+1\right)\right)}\right] \tag{5.4}$$

As can be seen from the RMS AE traces, the pulses can be modelled approximately by an instantaneous rise followed by an exponential decay:

$$V_{peak}=V_{0,peak}e^{-kt} \tag{5.5}$$

Thus, using **Equation 5.1**:

$$E_{impact}=\int_{upcross}^{downcross}V_{0,peak}^2e^{-2kt}dt=\frac{V_{0,peak}^2}{4k^2}\left[e^{-2kt}\right]_{upcross}^{downcross} \tag{5.6}$$

The decay constant, *k*, was found to be approximately 3000 sec^{-1} by inspection of 40 randomly selected pulses and was confirmed by breaking a pencil lead on the surface of the target plate, **Figure 5.16**.

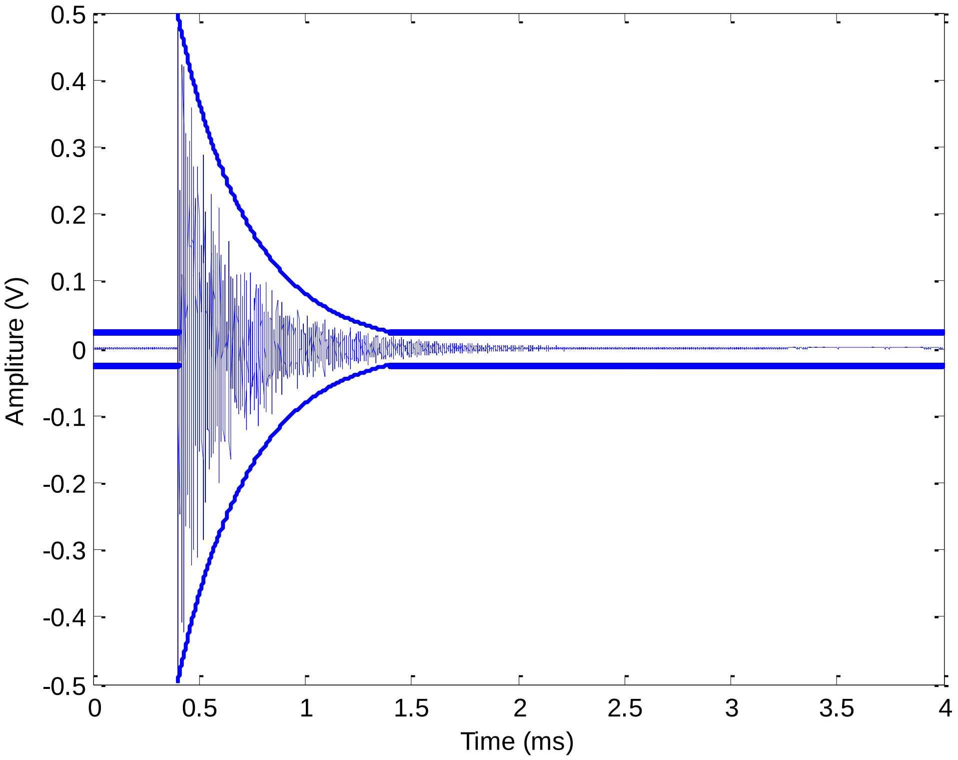

Figure 5.16: Raw AE signal for pencil lead break on the face of the sample. The pulse shape is identified by the solid lines bounding the signal

It might be noted that the decay time is rather long for the target plate. **Figure 5.17** shows the recorded signal for a pencil lead break on a large steel block using the same sensor with the target plate decay curve superimposed, from which it is clear that the long decay time is due to ringing in the target plate. Using information provided in the paper by Ivantsiv *et al* [102], it was possible to estimate the coefficient of decay in their target plate (also shown in **Figure 5.17**), although they do not provide any information on its dimensions.

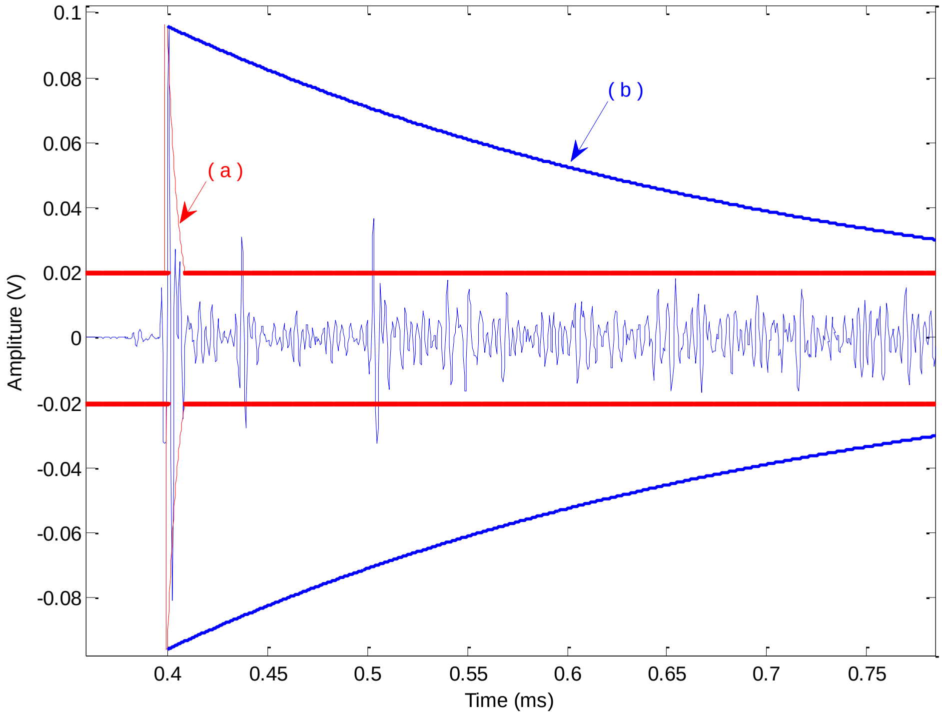

Figure 5.17: Raw AE signal for pencil lead break on the face of a large cylindrical steel block. Curve (a) is the decay curve estimated from Ivantsiv *et al* [102], and Curve (b) is the decay curve for the target plate

The pulse shape function and the energy distribution p.d.f. can be used to simulate the AE signal expected for any value of mass and nominal velocity, provided that the particle arrival rate is known. After truncating the top 1% of the lognormal distribution, it was then divided into 50 equal bins, whose individual integrals were computed and multiplied by the total number of particles and divided by the energy of the bin to obtain the corresponding number of particles in each bin. The AE energy associated with each bin was converted to a voltage using **Equation 5.5** and the corresponding pulses generated from **Equation 5.4** were distributed randomly within a simulated record, assuming no medium-term fluctuation in the mass flow rate. Overlapping was dealt with simply by adding the two pulse functions in a given interval. **Figures 5.18** and **5.19** show two extremes of simulated time series records for a heavily overlapped and a sparse signal respectively, alongside an example measured record with the non-noise peaks labelled. As can be seen, the simulated signals have fewer peaks, since there are no noise peaks, and allow a wider distribution of peak heights. **Figure 5.20** shows simulated and measured time series for one of the cases where it was not possible to identify individual arrivals not only because of the strong degree of overlapping, but also because of the low signal : noise. Also shown in **Figure 5.20** is a simulation of the effect of reducing the amount of ringing in the target plate, indicating how the simulation can be used to design the sensing/acquisition approach and to determine performance limits.

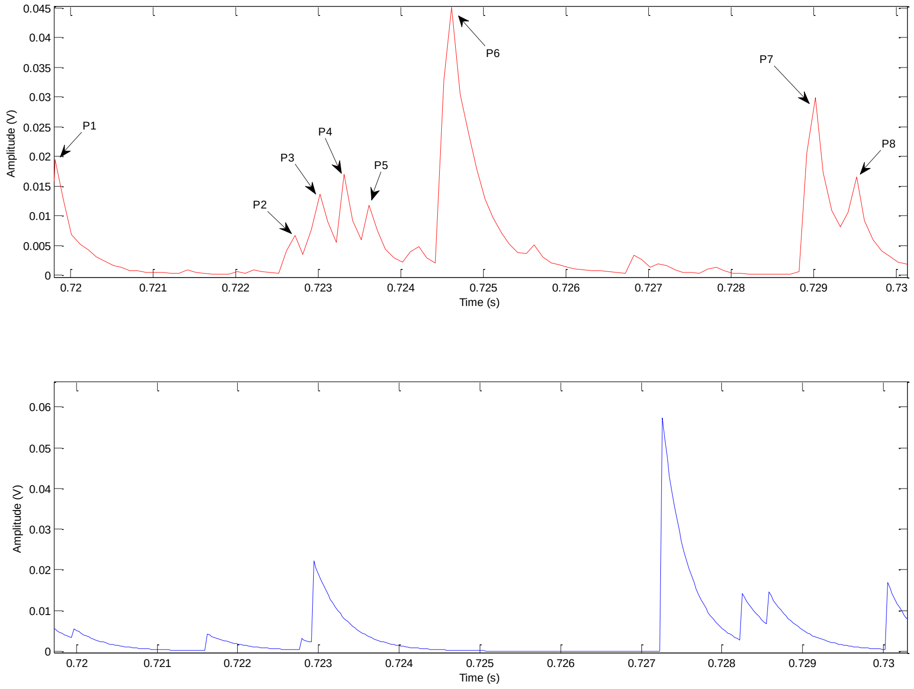

Figure 5.18: Measured (top) and simulated AE records for 212-250µm silica sand with nominal impact velocity of 12.3 ms^{-1}, and particle arrival rate of 900 per second. Peaks that were identified as particle impacts in the measured record are labelled

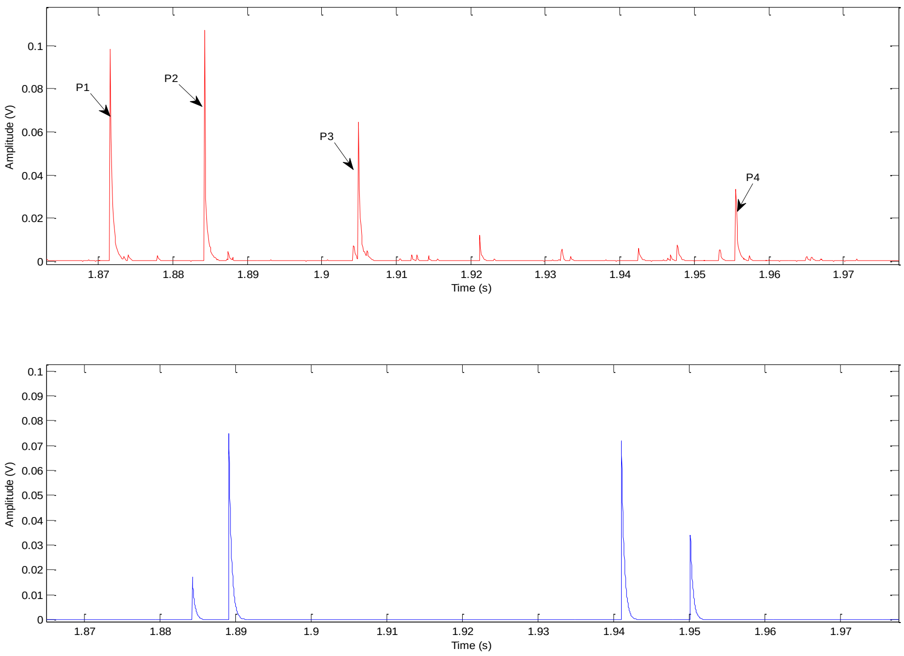

Figure 5.19: Measured (top) and simulated AE records for 710-850μm glass beads with nominal impact velocity of 4 ms^{-1}, and particle arrival rate of 40 per second. Peaks that were identified as particle impacts in the measured record are labelled

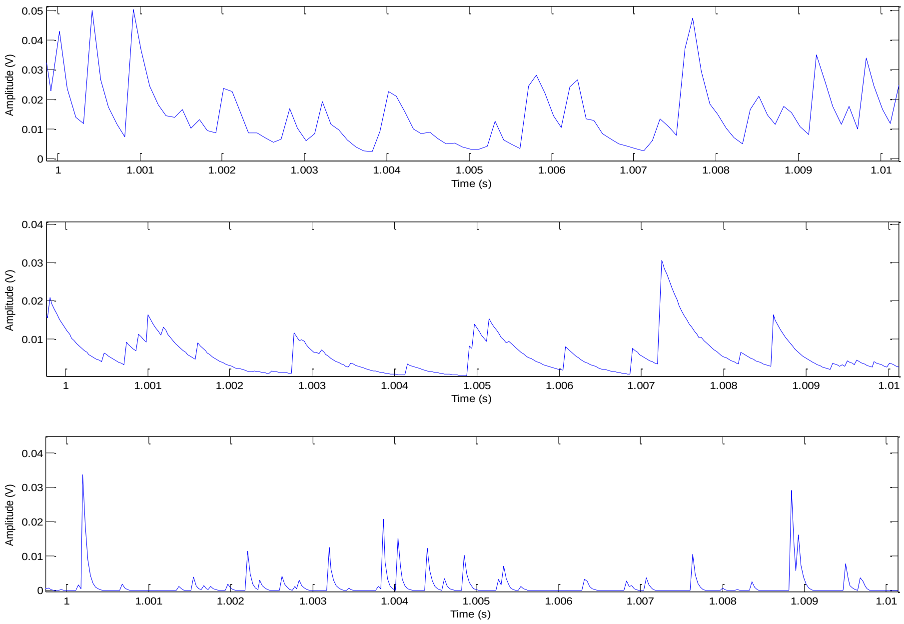

Figure 5.20: Measured (top) and simulated AE records for 125-180 μm silica sand with nominal impact velocity of 15.5 ms^{-1}, and particle arrival rate of 4000 per second Simulations with a decay constant of 3000sec^{-1} (middle) and 30000sec^{-1} (lower)

In order to evaluate the performance of the time series model, the energy of the simulated AE time series signal was correlated to the energy of raw AE signal (including the fraction 125-180 µm). **Figure 5.21**, shows that the average slope is very close to unity, although there is a distinct tendency for small particle sizes to contain about 10% excess energy in the simulation and larger particle sizes to show a 10% deficit. The error for the larger particles is likely to be because of some noise leakage into the correlated distributions whereas the excess for the smaller particles is likely to be due some signal being lost in the noise for the correlated distributions. Overall, the correlation shows that the model can be used to simulate time series where the degree of overlap is such that individual particles cannot be resolved.

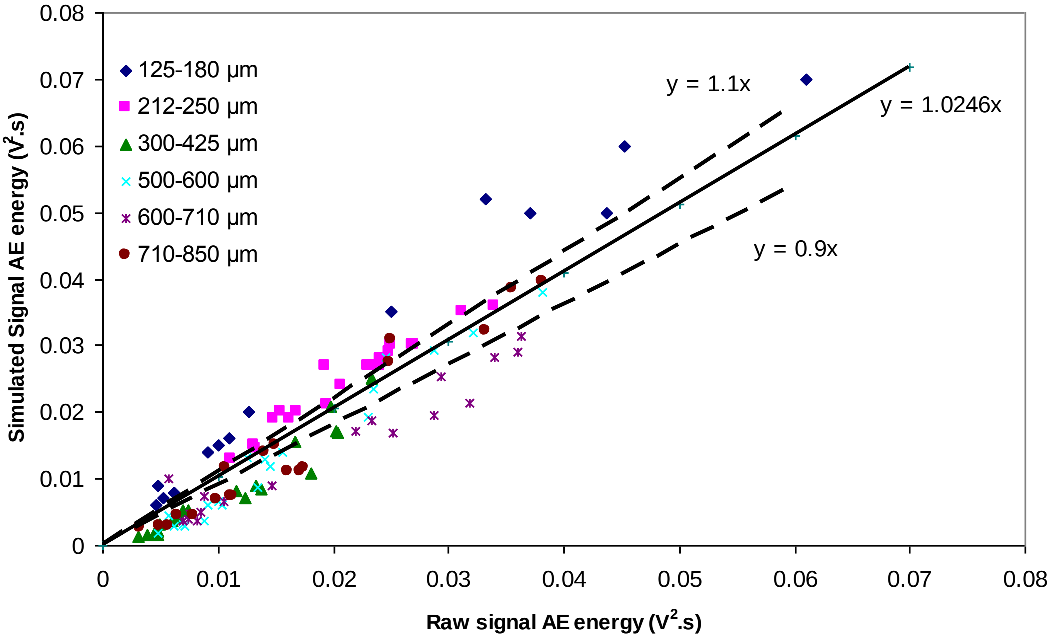

Figure 5.21: AE energy from simulated time series signal versus raw AE energy

Chapter 6

Analysis and Discussion

This chapter uses the findings of **Chapter 5**, in which it was demonstrated that an AE time series could be simulated for dry particle impacts. Using this model, it is then possible to analyse more meaningfully data which include cases where the particles act as an ensemble. The approach is applied first to the remaining dry particle impact data, then to the slurry impingement results and, finally, to the results for the flow loop.

6.1 Airborne particle impact test

The main aim of the dry impact study was to assess whether AE energy could be calibrated for incident particle kinetic energy under a wide range of conditions where particles could be relatively easily controlled. **Figures 6.1** to **6.4** present all of the measured data in a format that allows such an assessment, where the measured energy is divided by particle mass (**Figures 6.1** and **6.2**) and by the square of particle velocity (**Figures 6.3** and **6.4**).

As can be seen in **Figures 6.1** and **6.2**, AE energy per particle per unit mass generally increases with increasing particle velocity across the whole range of mass and velocity studied. However, the measured AE energy per particle per unit mass is higher for individual impacts and shows a stronger dependence on particle velocity than that for multiple impacts at higher velocities but the difference is less evident at lower velocities. As the velocity increases, the number of particle impacts per second increases from a few hundreds to a few thousands, and this may lead to overlapping of the transmission paths, or, indeed, to particle interactions at or near the surface, both of which would reduce the amount of energy being recorded at the sensor for each particle. Closer inspection of **Figure 6.2** also shows that the lower fractions of the low mass range and high mass range (1a *vs* 1b and 3 *vs* 4) for single impacts both exhibit higher energies per unit mass, whereas this is not observed for multiple impacts. For the smaller particles, this might be explained by the difficulty in controlling the number of particles leaving the shaker, where perhaps more than one is recorded on some occasions. The particle streams, where relatively large numbers of particles impinge on the surface, would not be susceptible to this type of error. This explanation does not hold for the high mass particles which are large enough to be individually handled, and here the explanation is more likely to be that the particle momentum is sufficient to cause significant whole body movement of the target (specimen and holder) and hence a different additional energy dissipation mechanism.

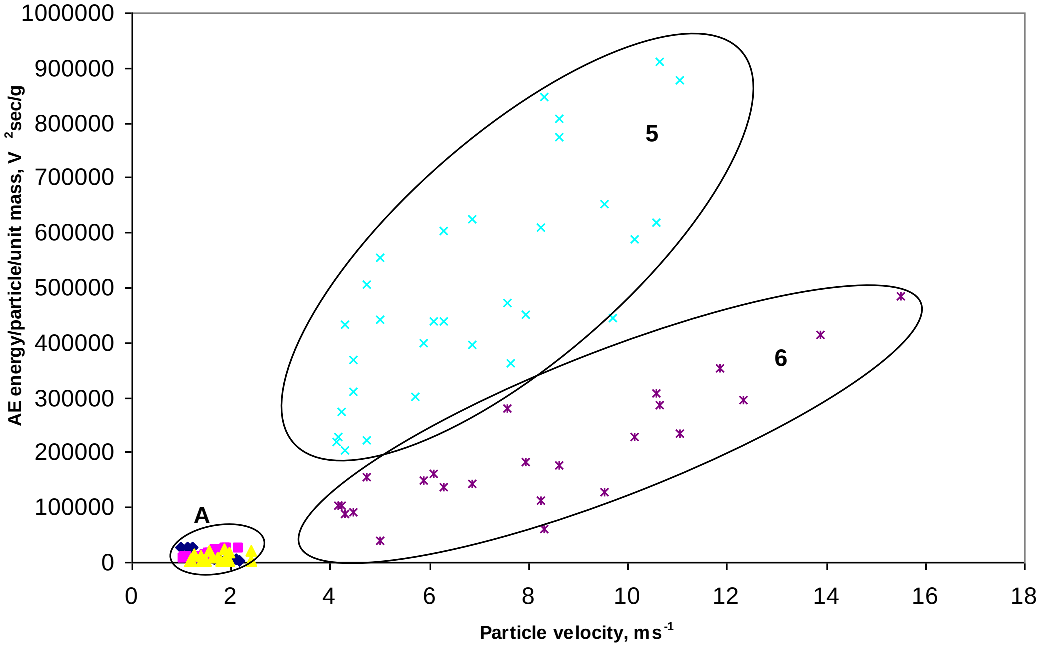

Figure 6.1 AE energy per unit mass versus particle velocity for all regimes investigated: (A) low velocity, (5) high velocity-low mass single impacts, (6) high velocity-low mass multiple impacts

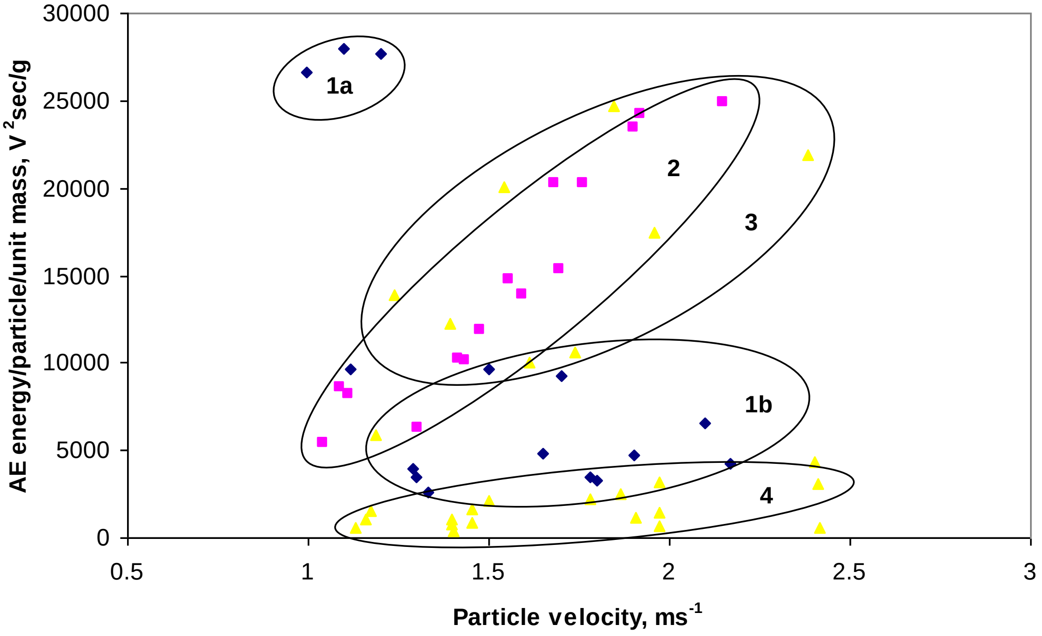

Figure 6.2: AE energy per unit mass versus particle velocity for all low velocity measurements (area A above): (1a) low mass-lower range single impacts, (1b) low mass-higher range single impacts, (2) low mass multiple impacts, (3) high mass-lower range, (4) high mass-higher range

Figure 6.3 shows that AE energy per particle divided by the square of the velocity increases with particle diameter only up to a diameter of about 1.5mm, above which the energy appears to remain constant. **Figure 6.3** also shows that the curvature at diameters less than 1.5mm is positive, ie. a higher order dependence than linear. The AE energy level is again higher for single impacts than for multiple impacts at high velocities (5 *vs* 6) and not at low velocities (2 *vs* 1) attributable, again, to the overlapping effect described above.

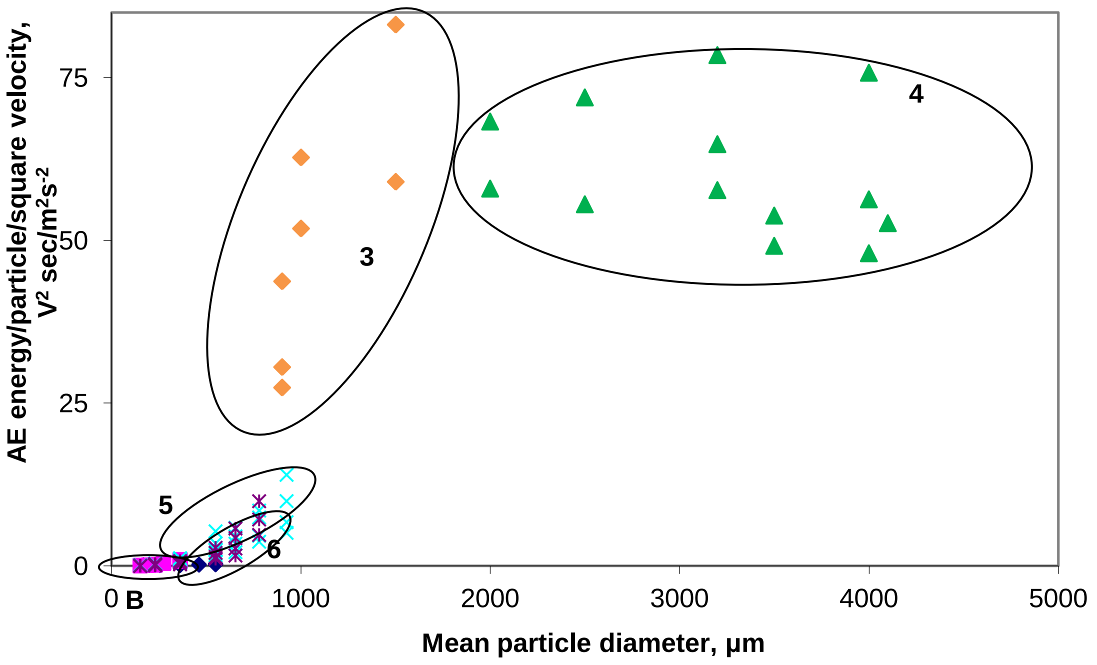

Figure 6.3: AE energy per particle divided by the square of the velocity versus particle diameter for all regimes investigated: (B) low velocity-low mass regime, (3) high mass-lower range, (4) high mass-higher range, (5) high velocity-low mass single impacts, (6) high velocity-low mass multiple impacts

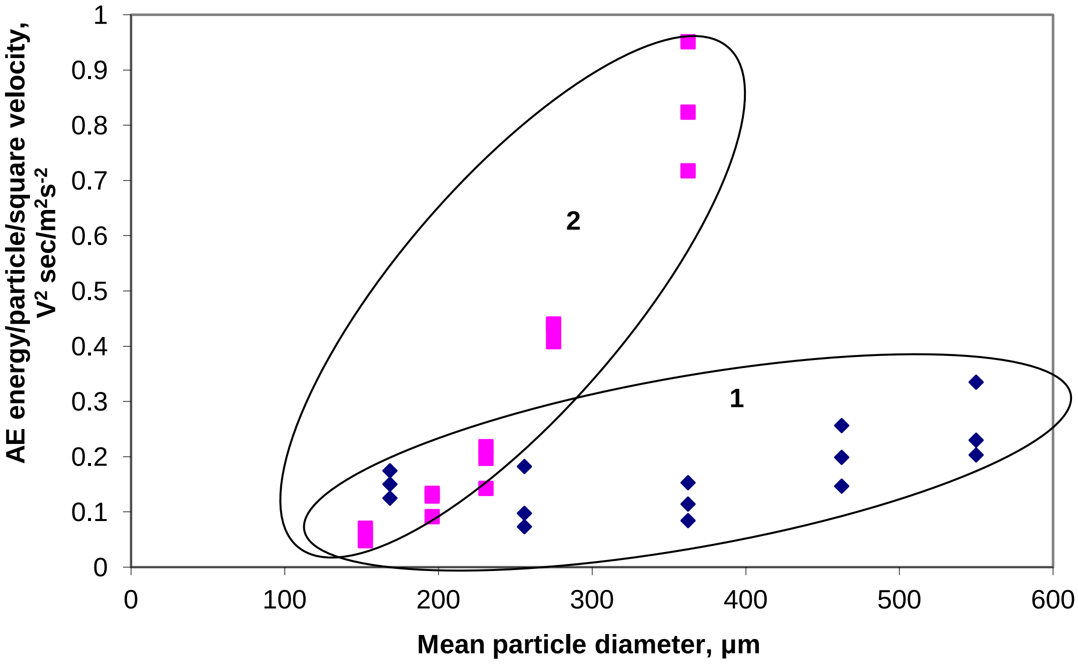

Figure 6.4: AE energy per particle divided by the square of the velocity versus particle diameter for low velocity-low mass regime (area B above): (1) low velocity-low mass single impacts, (2) low velocity-low mass multiple impacts

Since there is a clearly different mechanism of energy dissipation occurring at diameters greater than 1.5mm, these data were excluded when determining the velocity and diameter exponents, and the relevant plots are shown in **Figures 6.5** and **6.6**.

As can be seen from **Figure 6.5**, the velocity exponent is very close to 2 when taking all the data together, although it might be noted that there are two reasonable distinct sets of points, the single impacts, where the exponent is about 2.3 and the multiple impacts where the exponent was around 1.5. This is in accord with the findings of Feng and Ball [13], who observed a diameter exponent of 3 and a velocity exponent which varied between 1.1 and 3.4. It therefore appears that, when the particles approach the surface individually, their impact velocity is reasonably predictable, whereas, if there is a stream, interactions within the stream and at, or near the surface, may well affect the actual impingement velocity (magnitude and direction) for each particle. Deng *et al* [63], for example, have found, for an average velocity of about 20 m/s, that actual particle velocities at the outlet of the acceleration tube varied from 6 m/s up to 30 m/s. Moreover, Shipway and Hutchings [56] have suggested that the particles in the acceleration tube are subject to many impacts between themselves and with the wall of the nozzle as they are accelerated, and that such impacts will tend to reduce the final velocity.

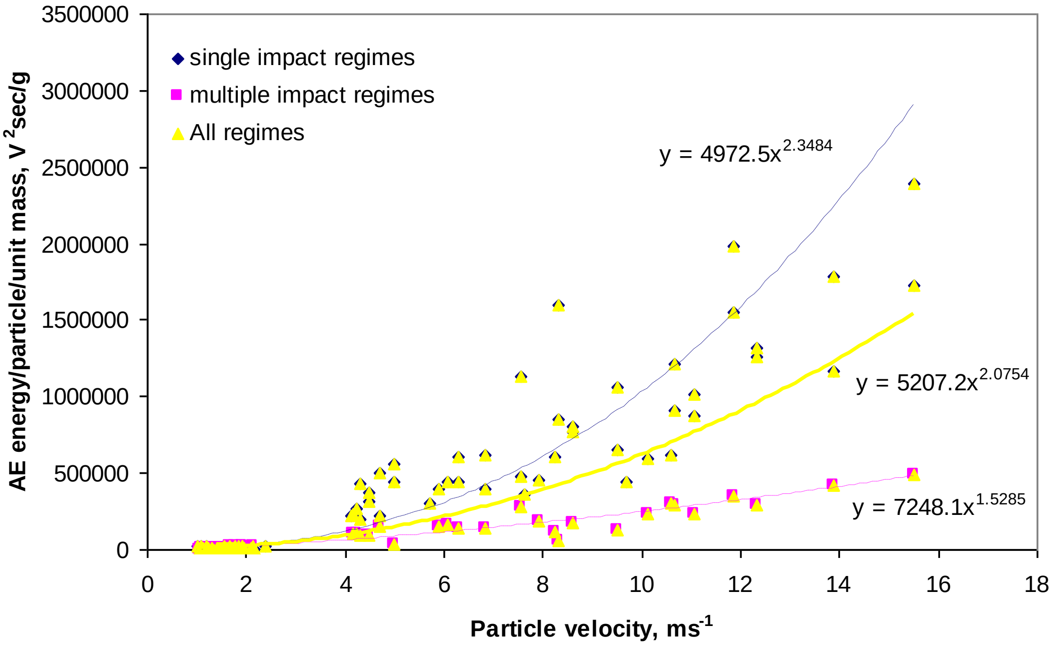

Figure 6.5: The dependence of AE energy per unit mass upon particle velocity

Figure 6.6, shows that, assuming that the velocity exponent is 2, particle diameter exponent is close to 3, which is in agreement with other workers [23, 73]. **Figure 6.6** does reveal, however, that particles of diameter greater than about 1mm lie above the best-fit curve (and therefore contribute to the exponent being a little above 3). This might be an effect of the experimental conditions since these particles are large enough to handle and observe easily, and hence their velocities may be more tightly controlled, and/or because none of these larger particles were used in multiple impact streams.

In summary, this analysis shows that, within the range of experimental error, the natural variations of particle size, and possible effects of overlap and interactions, airborne particle impacts generate AE energy that is approximately proportional to , i.e. the total kinetic energy. Taking account of the variation in particle mass and comparing calculated with observed distributions of AE event energy confirms this approach and justifies the summation even when the events cannot be distinguished. The approach, however, only holds for particle diameters below about 1 mm, after which a different energy dissipation mechanism appears to be operating.

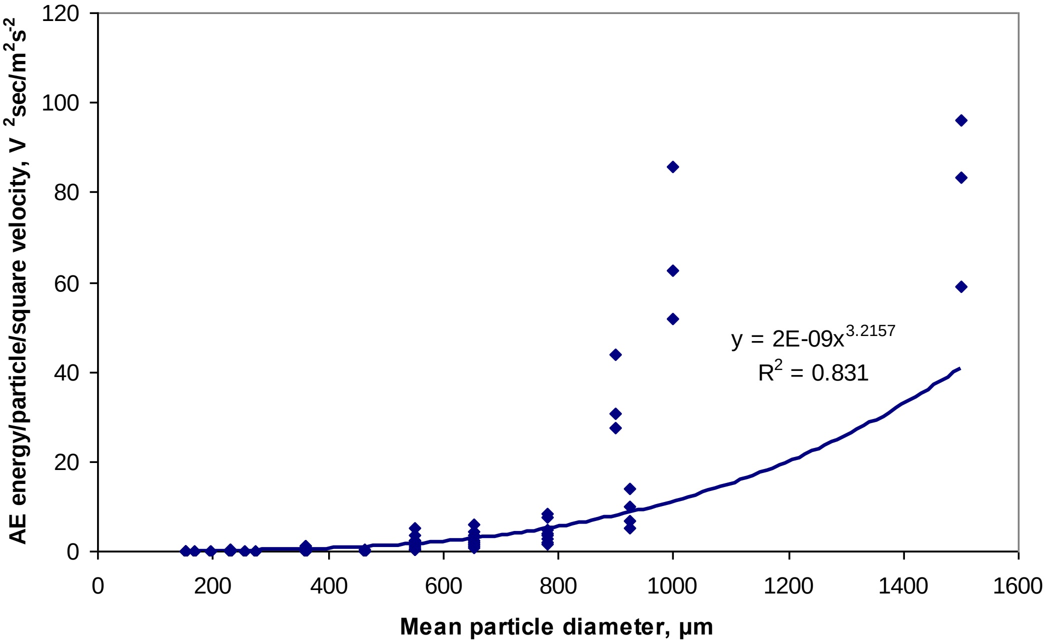

Figure 6.6: Influence of mean particle diameter on AE energy divided by the square of impact velocity

6.2 Slurry jet impingement

The purpose of this section is to extend the applicability of the statistical model described in **Chapter 5** to relatively uncontrolled impingement experiments where the carrier fluid was a liquid as well as to assess the extent to which the previous findings can be applied with this medium. Emphasis is placed on the effect of fluid mechanical phenomena on the motion of particles near the target, applied first to a free jet in the interest of comparison with experiments with a free air jet.

Given that the measured AE energy shows roughly the expected variation with speed, particle density, nominal impact angle and particle size, as shown in **Section 4.2,** it remains to be seen whether the energy measured corresponds to what would be expected from the log-normal distribution function developed in **Chapter 5** to describe the probability distribution of particle arrival AE energy for air-propelled particles using the same target and sensor. The mean of this distribution was found to vary with particle arrival speed, and the correlation between the mean AE energy determined for the dry impacts is reassessed first, based on the smaller particle size ranges (300-425 µm and 212-250 µm) used in the slurry impingement tests. **Figure 6.7** shows the best fit mean along with error bars indicating the range of values over the five observations for each incident energy giving the mean AE energy:

(6.1)

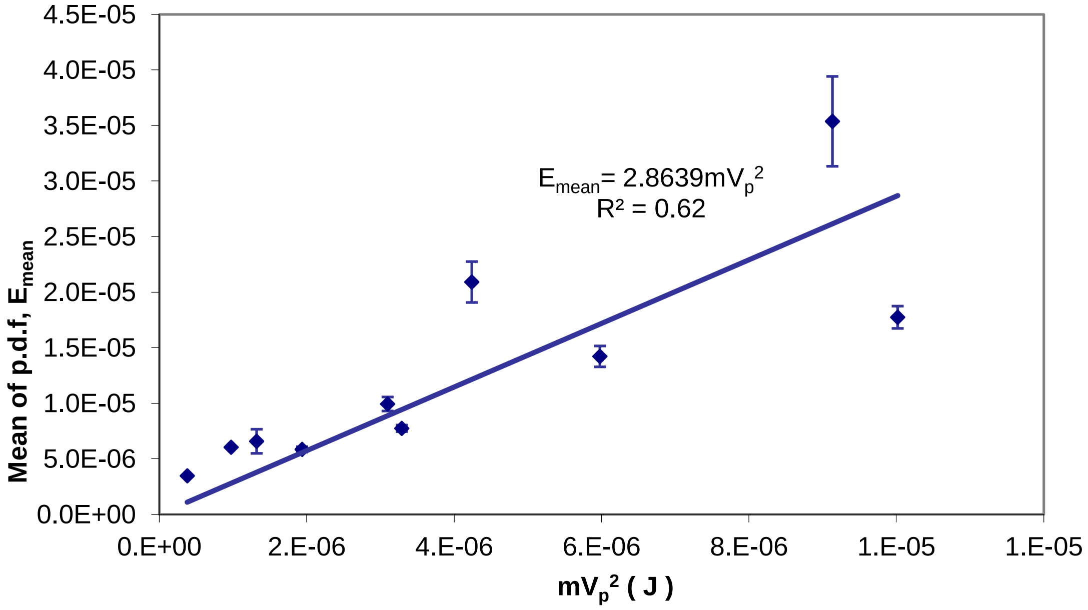

Figure 6.7: Correlation between the mean of the lognormal distribution and nominal incident energy, using data from **Figure 5.12**

The expected AE energy in a population of impacts, $E_{calculated}$, can now be obtained using the average particle arrival rate given in **Table 3.7** and the mean of the energy distribution function:

(6.2)

The measured AE energy associated with the particles, $E_{measured}$, can be estimated by subtracting the background water jet energy E_w from the integral of the signal, E:

(6.3)

where E_w was taken as the average of the three curves shown in **Figure 3.28**.

The nominal impact angle is accounted for by calculating the normal component of the jet exit velocity, and **Figure 6.8** shows the resulting relationship between the measured and calculated energy and, as can be seen, there is a considerable discrepancy between (measured) wet and (calculated) dry impacts with the same jet exit velocity, the dry impacts giving at least a factor 10 higher AE energy. Such a discrepancy in the AE energy could stem from the difference in the carrier medium and its influence on the direction of particles. For particles laden gases, this direction is little affected by the spreading effect of the fluid, because the viscosity of air is very small (1.81×10^{-5} $Kg.m^{-1}sec^{-1}$), leading to a much lower drag force than arises from the viscosity of a water-based carrier (8.9×10^{-4} $Kg.m^{-1}sec^{-1}$). Therefore, the incident particle velocity is important, but there are difficulties in measuring or modelling this.

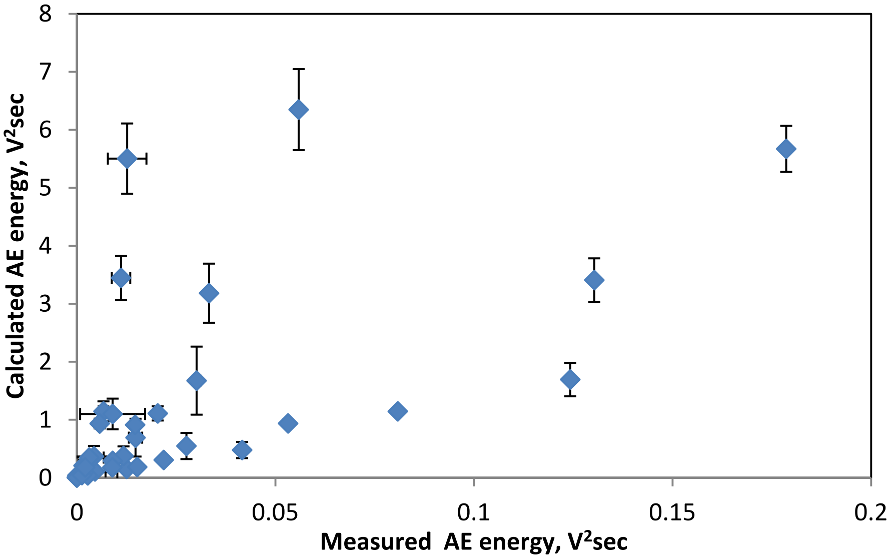

Figure 6.8: Measured and calculated AE energy, assuming the particle arrival speeds given in **Table 3.7**

The most likely reason for the discrepancy in **Figure 6.8** is that the water-driven particles are moving much less rapidly than the jet exit velocity when they strike the target. To deal with this, the empirical model of Turrene and Fiset [94] (**Equation 2.13**) was used to calculate the average arrival speed, using the particle mean diameter, the jet exit velocity, and taking an average value of the initial radial position of the particle (1.25mm). **Table 6.1** shows the calculated arrival speeds for all the conditions studied. In some cases of slowly moving particles the model does not give a positive speed, corresponding to particles that fail to penetrate the squeeze film.

Particle size range (μm)	Jet exit velocity (m/s)	Average calculated arrival speed (m/s)
125-180	4.2	-
	6.8	0.21
	10.2	0.73
	12.7	1.10
212-250	4.2	-
	6.8	0.30
	10.2	0.95
	12.7	1.43
300-425	4.2	0.10
	6.8	0.84
	10.2	1.80
	12.7	2.50

Table 6.1: Calculated particle arrival speed using the model of Turenne and Fiset [94]

Figures 6.9 to **6.11** show the calculated and measured AE energy for each of the three impact angles, sorted for each of the particle sizes, and using the estimated impact speed following Turenne and Fiset. As can be seen, the calculated and measured values are much more compatible, the slope varying from a little below unity to a little above and these are listed in **Table 6.2** along with the average slope for each angle. **Figure 6.12** shows that the average slope is very close to unity when taking all the data together, although there is a distinct tendency for smaller particles to have higher than expected energy and larger particles to have lower than expected. **Table 6.2** also shows the average slope to be very close to unity for nominal impact angles of 60^o and 90^o, but rather less for impingement at 30^o, even when the normal component is taken into account.

The particle size effect might be explained by the fact that the slurry jet is directed horizontally, so that there might be some drop-out relative to the water which would change the angle and also proportion of particles striking the surface, and this would affect larger particles more than smaller ones. Also, streams that are directed in a downward direction will have the vertical (parallel to the target) component of their velocity affected more than the horizontal, and so the lower impingement angles might be expected to have lower normal speeds than expected, and this would be expected to affect the larger particles more.

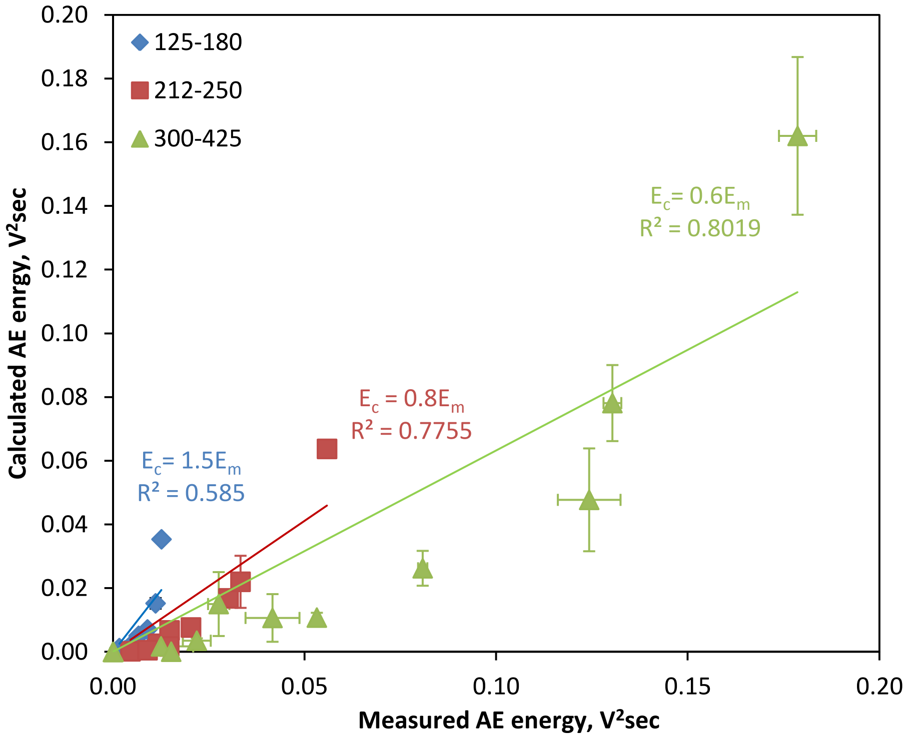

Figure 6.9: Calculated AE energy versus measured AE energy at nominal impact angle 90^o

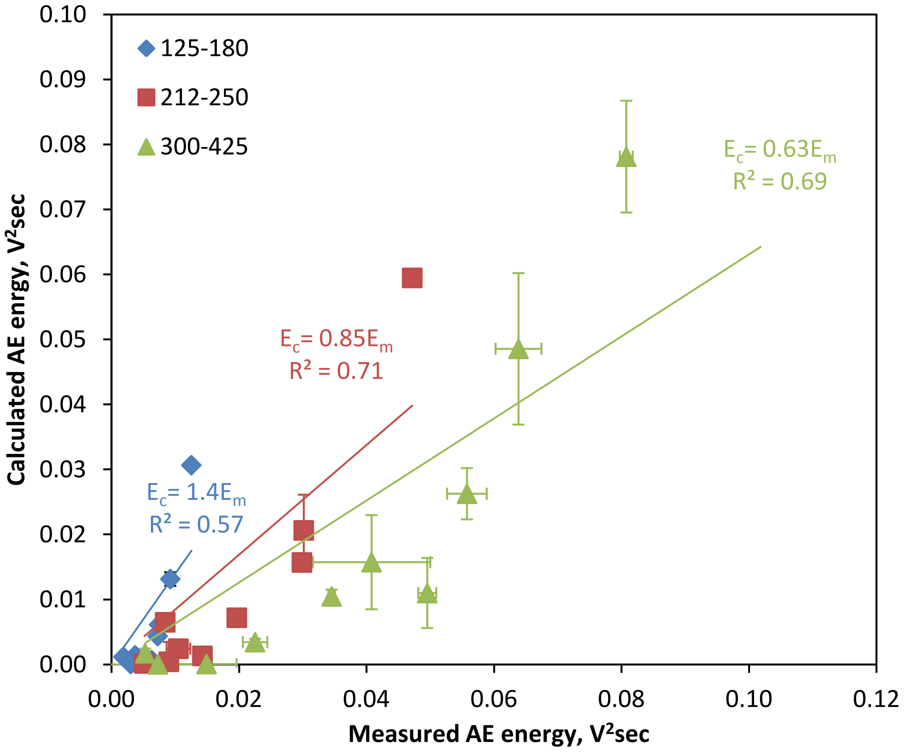

Figure 6.10: Calculated AE energy versus measured AE energy at nominal impact angle 60^o

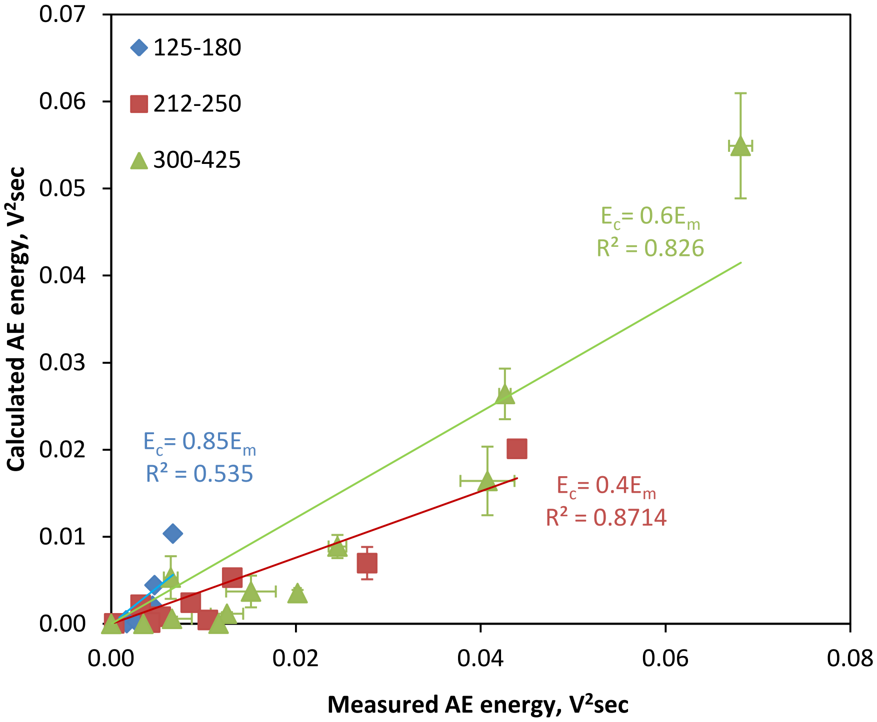

Figure 6.11: Calculated AE energy versus measured AE energy at nominal impact angle 30^{o}

Nominal impact angle (θ^{o})	Particle size range (μm)	Correlation function	Average slope
90	125-180	E_c=1.53 E_m	0.99
	212-250	E_c=0.82 E_m	
	300-425	E_c =0.63 E_m	
60	125-180	E_c =1.39 E_m	0.95
	212-250	E_c =0.85 E_m	
	300-425	E_c=0.63 E_m	
30	125-180	E_c =0.85 E_m	0.61
	212-250	E_c =0.40 E_m	
	300-425	E_c =0.60 E_m	

Table 6.2: summary of correlation functions between calculated and measured AE energy

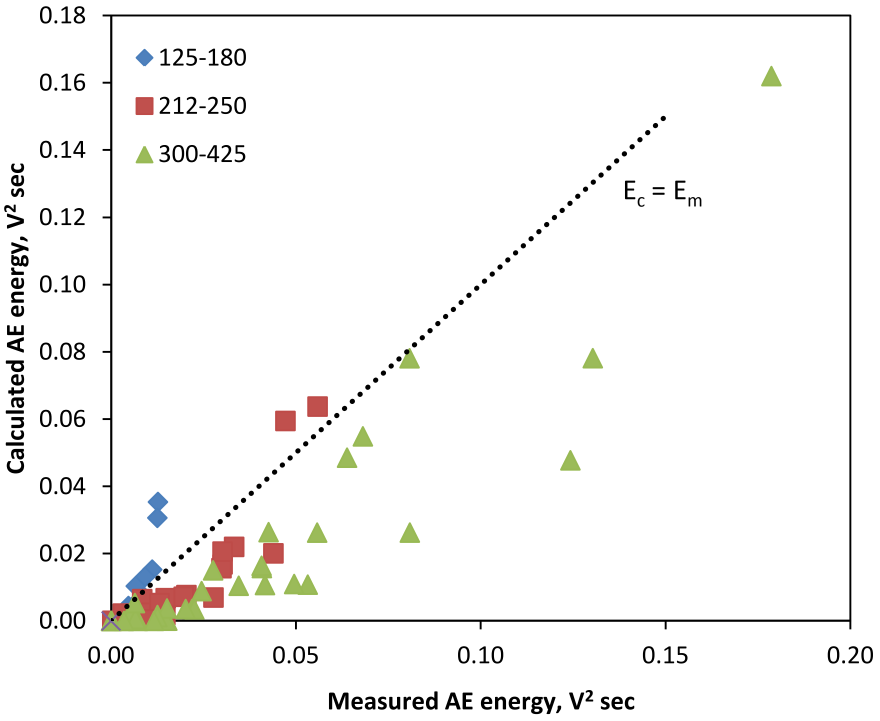

Figure 6.12: Calculated AE energy versus measured AE energy for all nominal impact angles investigated

In summary, the slurry impingement tests have shown that the "calibration" of the target plate carried out using the airborne particles can be used to predict the expected AE energy in slurry impingement tests. Such a prediction requires a re-assessment of particle velocities using a published model and is best for normal or near-normal impingement.

6.3 Impacts during pipe flow

Besides the change in flow conditions from the two free jets discussed in preceding sections, the data acquired from the flow loop can be expected to differ from the previous tests in two important respects. The structure of the bend introduced in the flow loop will involve more contact between the slurry and the surrounding internal surfaces of the bend, and so the target impact area is potentially much larger. Also, AE wave propagation will be more complex than in the target plate, although the greater wall exposed area may well lead to less ringing and hence greater temporal resolution of impact events. Thus, some of the "calibration" achieved in the free jet experiments was expected to be lost, but the confidence gained by applying the time series model to the free jet experiments was expected to allow an assessment of the factors which need to be taken into account in a real implementation.

This section firstly presents a more detailed analysis of the particle-free water AE signals in order to identify the background noise characteristics, and hence develop a model for background water noise which is itself more complex than for the slurry jet. Then, the analysis was focused onto dividing the AE recorded in particle-laden flows into stationary and non-stationary parts and dealing with the non-stationary part where frequency can vary substantially with time.

6.3.1 Analysis for particle-free water

The high AE energy associated with the water impingement signal in the flow loop dictated a different approach to that used in slurry impingement, where it was possible simply to subtract an average energy. In particular, the hydraulic conditions produce a strong pulsatile nature to the particle-free time series which can be seen as a carrier wave for the particle signatures. Dealing with such pulsatile signals requires a demodulated analysis of the signals to make use of the periodicity.

Figure 6.13 shows samples of typical raw AE signals recorded for water impingement along with typical raw AE spectra over the range of flow speeds tested. It is clear that the raw AE signal amplitude, in general, increases with increasing flow speed. The effect of the sensor bandwidth is apparent in the raw frequency spectrum, with most energy being contained in the range 100-400 kHz. The spectra show that most of the power is focused in three bands; one very narrow band centred on a frequency of around 100 kHz and characterised by a spike at the lowest speed whose magnitude decreases rapidly with increasing flow speed, a band at 150 kHz to 200 kHz, and another band at 300 kHz to 400 kHz. It is also clear that, within its bandwidth, the sensor shows a systematic shift in frequency content (power) towards the higher end as the flow speed increases. To quantify these systematic changes in raw AE frequency content, the proportion of the total energy in these three frequency bands was determined, for each of the 20 AE records at each flow speed. **Figure 6.14** shows the variation in AE energy proportion in each band with flow speed where each point represents the average of 20 AE records along with the standard deviation. As can be seen, the first band decreases rapidly with flow speed while the highest frequency increases with speed. Thus, raw AE frequency analysis can potentially offer a means of monitoring flow speed.

<table>
<tr><th></th><th>Raw AE signal</th><th>Frequency spectrum</th></tr>
<tr><td>(a)</td><td>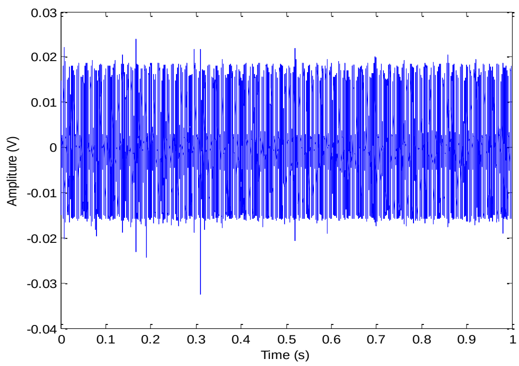
</td><td>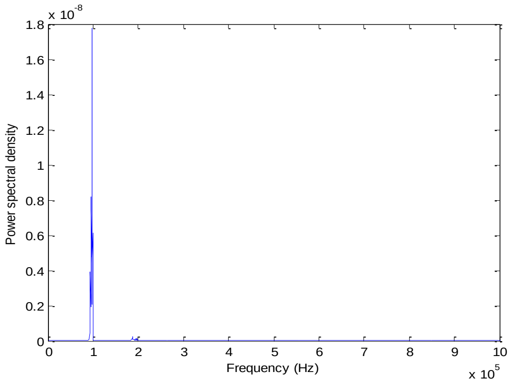
</td></tr>
<tr><td>(b)</td><td>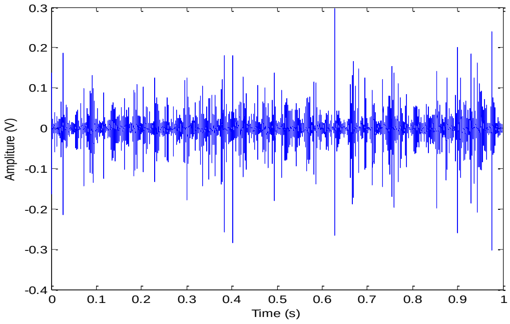
</td><td>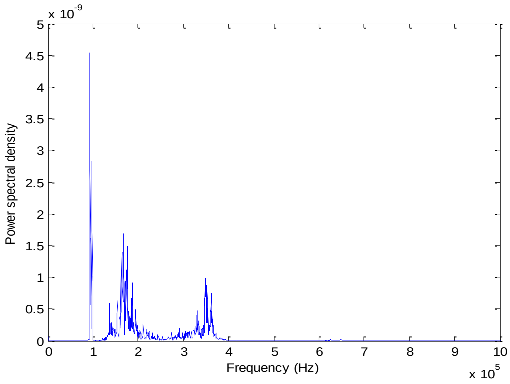
</td></tr>
<tr><td>(c)</td><td>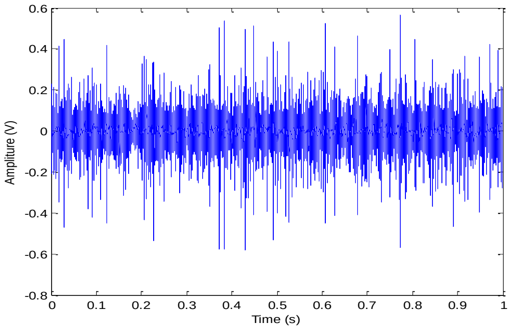
</td><td>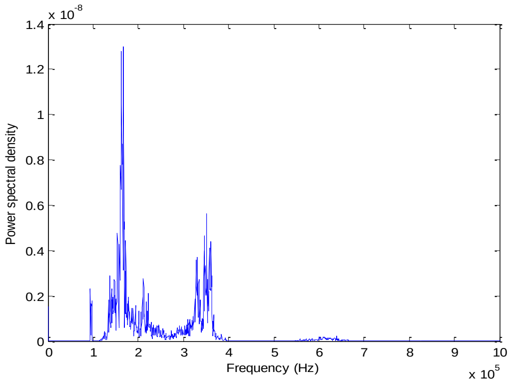
</td></tr>
<tr><td>(d)</td><td>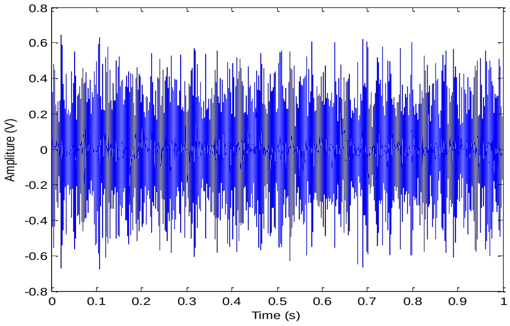
</td><td>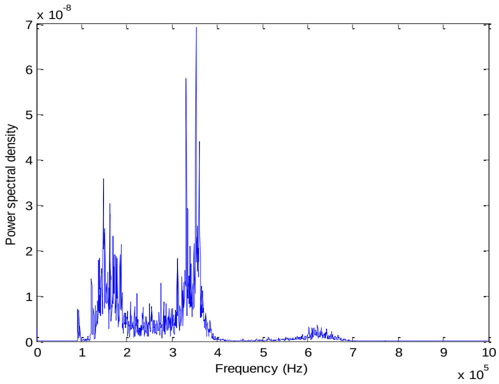
</td></tr>
</table>

Figure 6.13: Typical 1-second raw AE time series for water impingement in the flow loop and their corresponding raw frequency spectra for flow speeds: (a) 4.2 ms^{-1}, (b) 6.8 ms^{-1}, (c) 10.2 ms^{-1}, and (d) 12.7 ms^{-1}

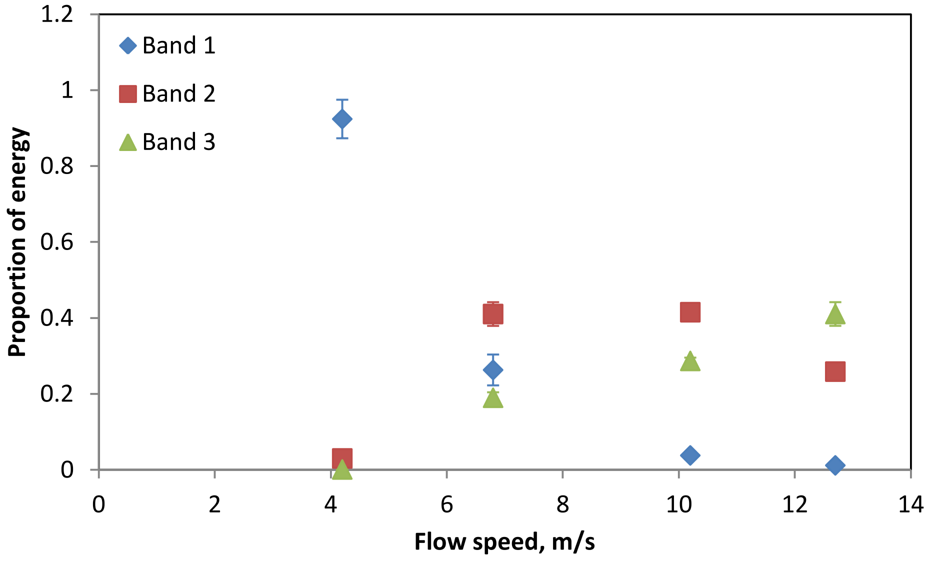

Figure 6.14: Proportion of AE energy in raw frequency bands versus flow speed; Band 1: 100 kHz, Band 2: 150-200 kHz, Band 3: 300-400 kHz

Figure 6.15 shows a magnified 0.1-second segment of the record depicted in **Figure 6.13a** in both raw and averaged forms. These signals suggest a strong influence of fluid pulses on the recorded AE with a pulse period of around 0.01 s, most likely associated with the rotational speed of the pump.

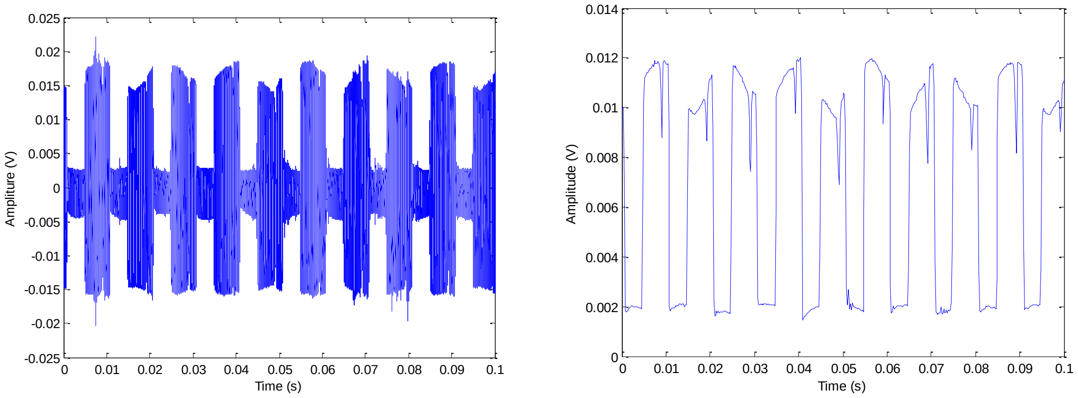
(a) Raw AE signal

(b) RMS AE signal

Figure 6.15: Magnified view of 0.1-second segment of the signal shown in **Figure 6.13a**, (a) raw and (b) RMS AE

To investigate the lower frequency characteristics of the water impingement signals, demodulated frequency analysis was applied to all signals at all flow speeds tested. First, the raw AE signals were averaged with a 0.2 ms averaging time (over 500 points) using a root mean square (RMS) algorithm, making the effective sampling rate 5000 Hz samples per second as shown in **Figure 6.15b**. Then, the RMS AE signal was made bipolar by subtracting the mean value of the record from each point in order to remove the DC component before transforming the signal into the frequency domain. Finally, all spectra were normalized to a unit energy content in order to facilitate comparison.

Figure 6.16 shows typical examples of the resulting normalized RMS AE signals along with the corresponding normalized frequency for water impingement for each of the flow speeds tested. The frequency domain at the lowest flow speed, **Figure 6.16a**, shows spectral peaks occurring at relatively regular frequency intervals which imply the possibility of one fundamental frequency component with other peaks resulting from harmonics. On closer inspection, it was found that two spectral peaks are dominant; 100 Hz at the lowest flow speed and 42 Hz at the highest flow speed, **Figure 6.16d**. Between the two extreme speeds, the energy in the 100 Hz peak decreases with speed while the 42 Hz increases. The spectra at the intermediate speeds show a transition between the two extremes, **Figure 6.16b** showing both spectral peaks and **Figure 6.16c** exhibiting a broad demodulated frequency spectrum.

At first sight, the complexity of what is essentially a noise pattern might make the identification of particle impact signatures a daunting prospect. However, a clear understanding of this pattern assists in separating signal from noise, but also allows the exploration of the potential to use the low frequency as a carrier wave.

	RMS AE signal	Normalized Frequency spectrum
(a)	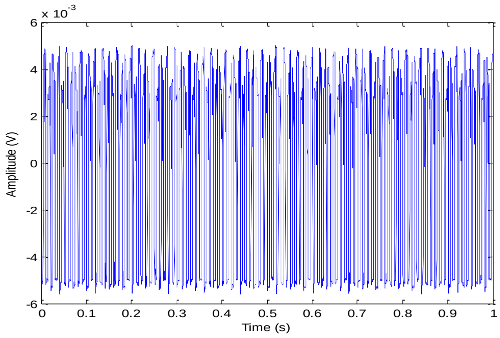	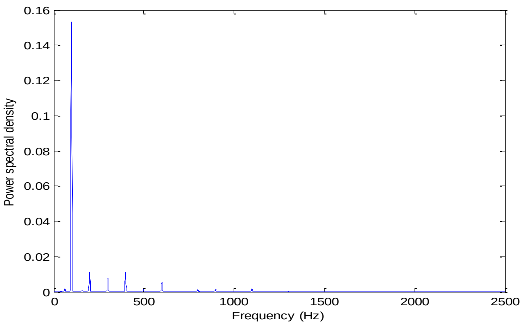
(b)	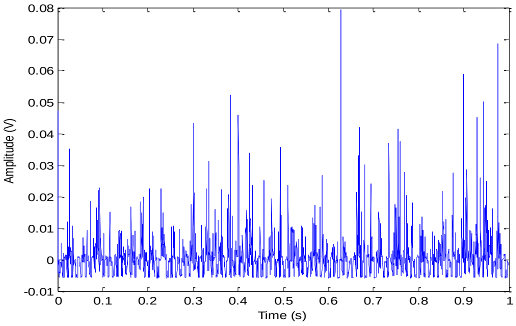	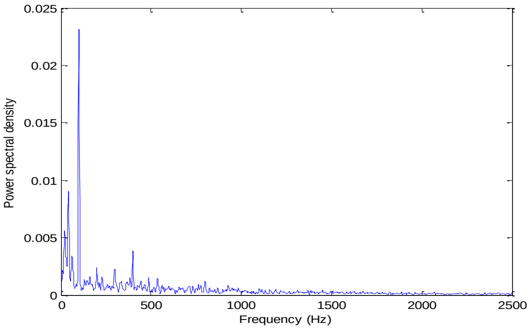
(c)	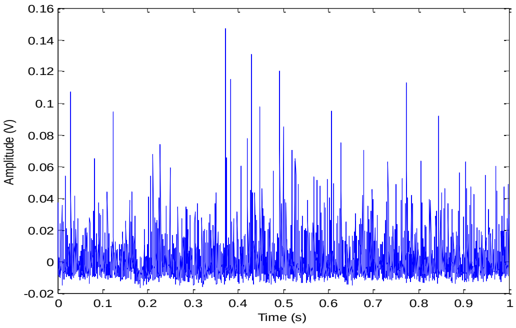	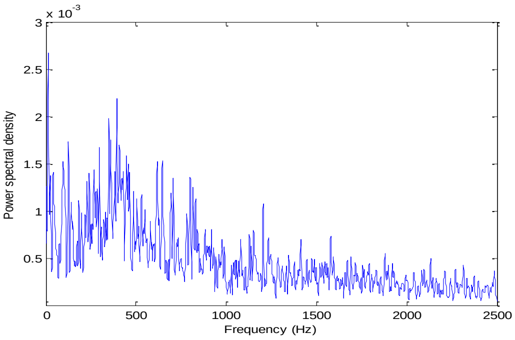
(d)	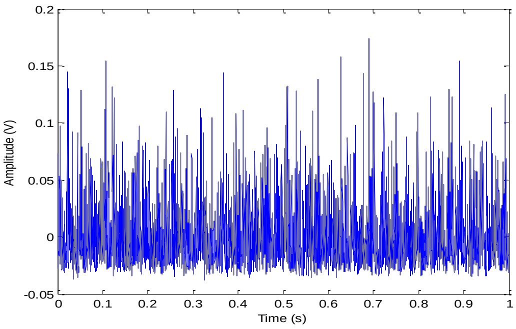	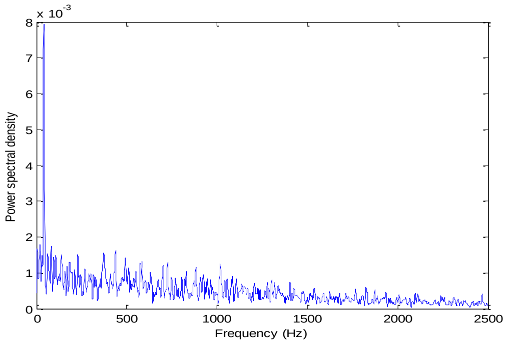

Figure 6.16: Typical 1-second RMS AE signals for water impact and their corresponding normalized demodulated spectrum for flow speeds: (a) 4.2 ms^{-1}, (b) 6.8 ms^{-1}, (c) 10.2 ms^{-1}, and (d) 12.7 ms^{-1}

In order to quantify these demodulated spectra, a processing approach was devised based on categorisation of peak heights and their corresponding frequencies. For each flow rate, across the 20 records, all peaks in the spectrum were identified automatically by first applying an identification threshold of 5% the maximum peak heights and then obtaining each peak height and its corresponding frequency. The ten highest peaks in the spectrum were then taken along with their corresponding frequency values for each record. Next, the resulting 200 values of peak height and corresponding frequency for each combination were used as an input to a Matlab algorithm. The algorithm divided the frequency range into 20 Hz bins and allocated each peak height to the appropriate frequency bin, calculating the number of occurrences in each bin. The average peak height for each bin was then determined by dividing the sum of all peak heights by the number of occurences: ————————. **Figure 6.17** summarises the results, quantifying the two distinct frequency patterns described above. As can be seen in **Figure 6.17a** a very clear harmonic pattern occurs at low speed with a fundemantal frequency of 100 Hz and charactersied by a set of much smaller harmonics. At the next highest speed, **Figure 6.17b** a broader spectrum based on 42 Hz begins to emerge alongside the 100 Hz pattern noted in **Figure 6.17a**. At the highest speed, the 100 Hz pattern is absent and is replaced by the 42 Hz band plus some higher frequency components not on the 100 Hz series. The spectrum for the higher intermediate speed is slightly anomalous in that, although it contains a growing 42 Hz component, there are a number of other components present at higher intensity. Although the exact causes of this low frequency spectral behaviours are not entirely clear, it is likely that they are associated with the hydraulic behaviour of the flow loop. The rotational speed of the pump is 10 Hz, so this does not explain either the 42 Hz or 100 Hz frequencies, nor, indeed the very obvious pulsation at lower speed. In fact, the spiral shape of the mono pump impeller is specifically designed to eliminate flow pulsations. However, it is possible that any practical application will be on a system with its own hydraulic characteristics, so the flow loop provides an example of how such characteristics might be dealt with in attempting to monitor particle impingement.

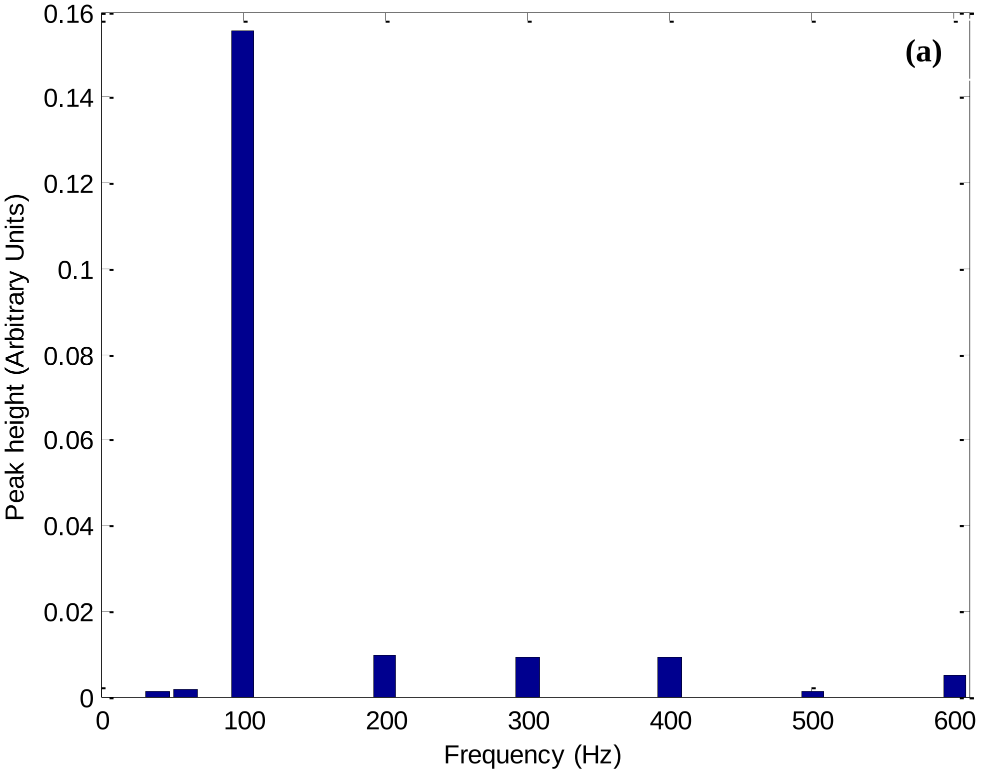
(a)
Peak height (Arbitrary Units)
0.16
0.14
0.12
0.1
0.08
0.06
0.04
0.02
0
0
100
200
300
400
500
600
Frequency (Hz)

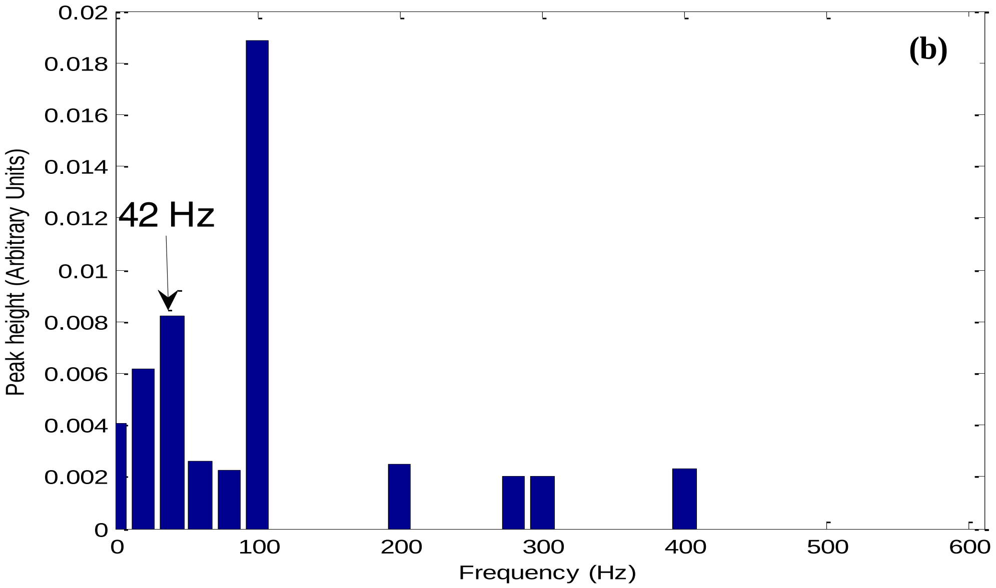
(b)
42 Hz
Peak height (Arbitrary Units)
0.02
0.018
0.016
0.014
0.012
0.01
0.008
0.006
0.004
0.002
0
0
100
200
300
400
500
600
Frequency (Hz)

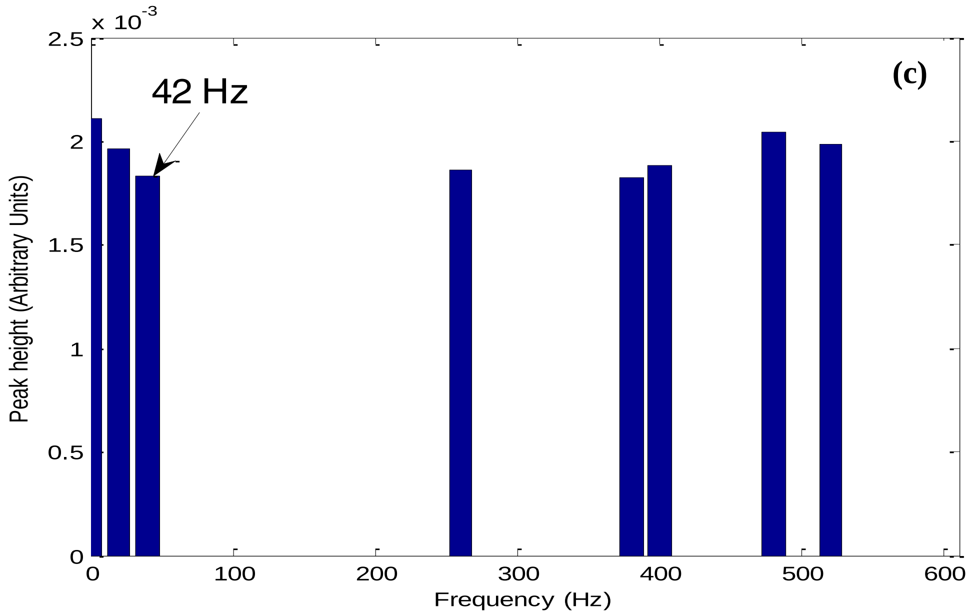

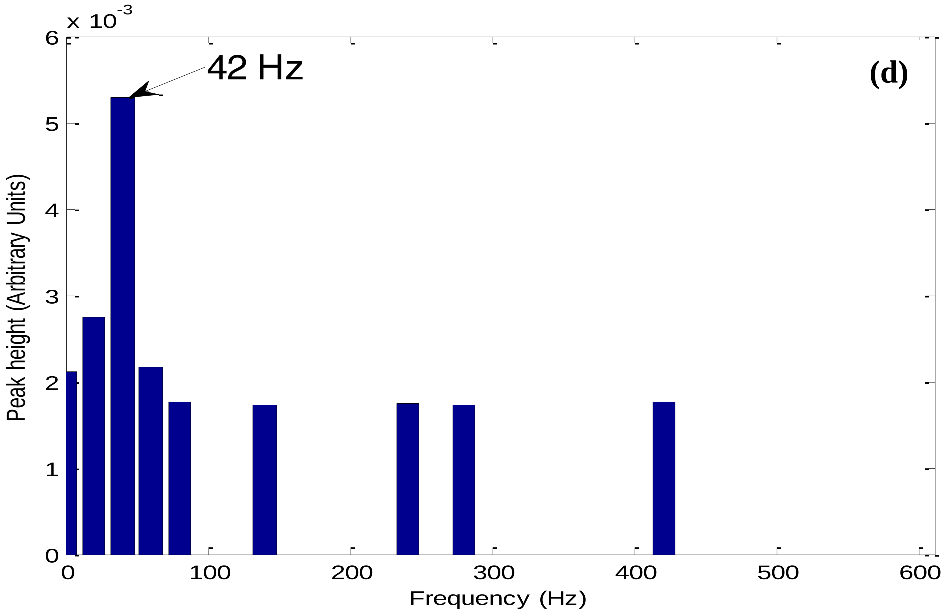

Figure 6.17: Distribution of the ten top frequency peak heights for water impingement at four flow speeds: (a) 4.2 ms^{-1}, (b) 6.8 ms^{-1}, (c) 10.2 ms^{-1}, and (d) 12.7 ms^{-1}

The proportion of oscillatory energy that is contained in the top 10 peaks for all flow speeds is shown in **Figure 6.18.** As can be seen, the remaining energy is quite high for the higher speeds indicating a generally more broadband distribution of energy.

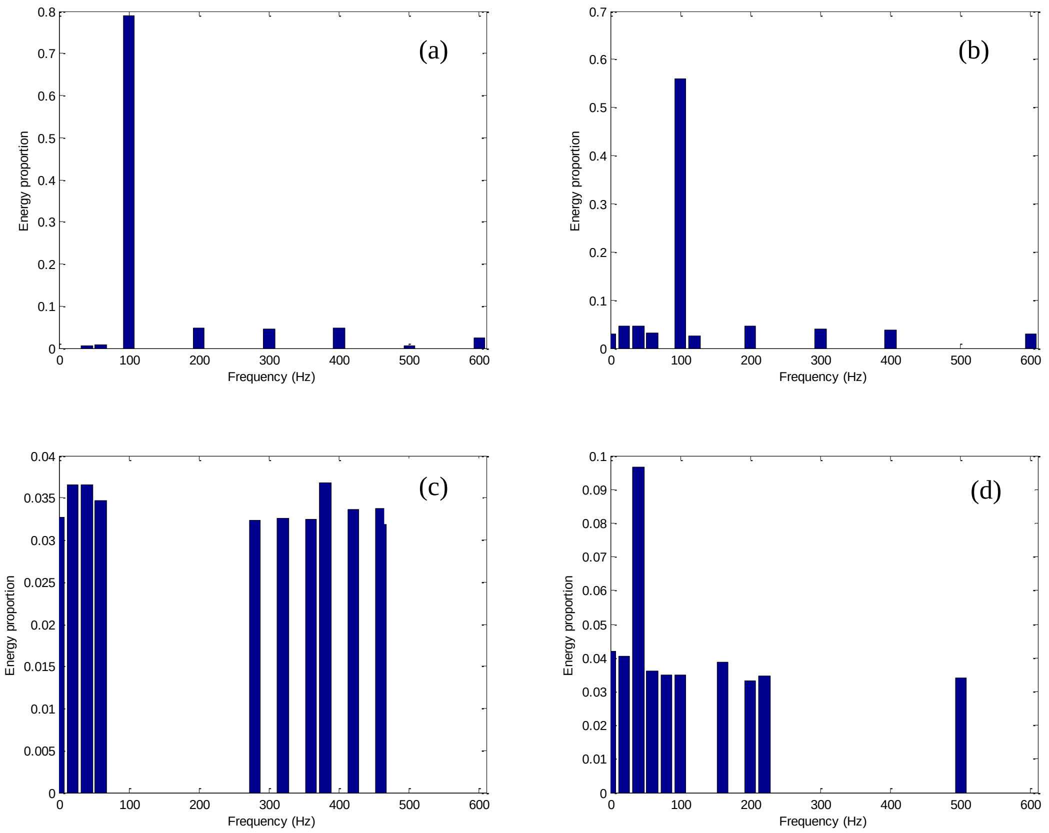

Figure 6.18: Proportion of the oscillatory energy contained in the top 10 peaks for water impingement at four flow speeds: (a) 4.2 ms^{-1}, (b) 6.8 ms^{-1}, (c) 10.2 ms^{-1}, (d) 12.7 ms^{-1}

Considering only the total AE energy analysis is not sufficient for practical situation, and bearing in mind the fact that the signal is not wholly continuous which indicates a dynamic effect which potentially contains information below and above the mean energy level, the total AE energy for slurry impingement signal was divided into static and oscillated parts.

As is obvious from the foregoing, any model for the AE arising from water impingement will consist of an oscillatory component and a static component. Therefore the total AE energy was divided into two parts, a static component E_{st} and an oscillatory component E_{osc}. The static component was simply obtained by calculating the average of the entire AE record. The oscillatory part was obtained by integrating the RMS of the 1-second averaged records using **Equation (3.1)**, once the static component had been removed (records such as those shown in **Figure 6.16**).

Figures 6.19 and **6.20** show the effect of flow speed on both the static and dynamic AE energy components, respectively. Since there is no particular reason to expect the hydraulic behaviour to show a power law dependence with flow speed, an exponential fit showing the dependence of AE energy components associated with (*v*-4.1) was used in the interest of obtaining a better fit, although the best fit power equation is also shown for each AE component. Thus, the AE energy associated with water impingement can be described by a mean level and an oscillatory component of energy .

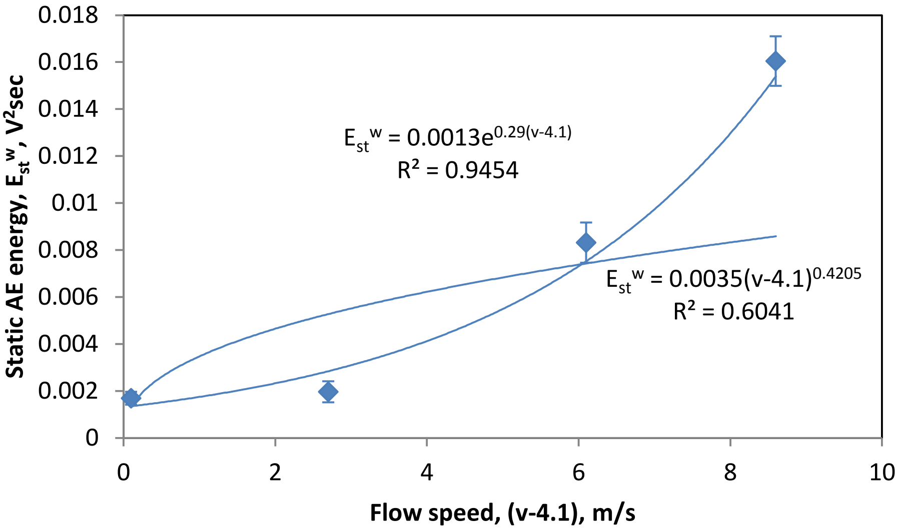

Figure 6.19: Effect of flow speed on static AE energy for water impingement showing the best power fit and the best exponential fit

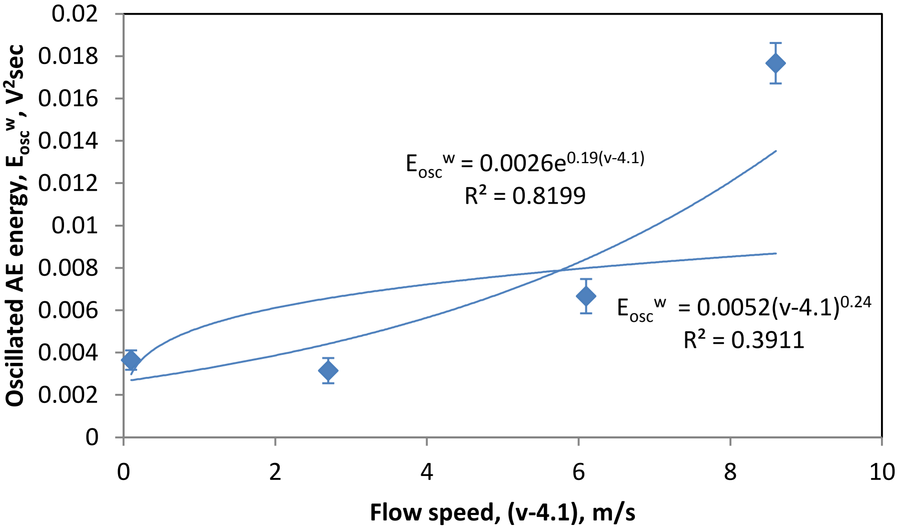

Figure 6.20: Effect of flow speed on oscillatory AE energy for water impingement showing the best power fit and the best exponential fit

6.3.2 Slurry impact analysis

A similar decomposition into static and oscillatory components (**Figure 6.21**) was used to analyse the AE from a particle-laden flow. The first stage in the analysis of particle-laden flow was to separate the two main components of the signal in a systematic way. To do so, the total AE energy for each record, was divided into its two main components the static component, and the oscillatory component, in the same way as was done for particle-free water. Each of these can be further divided accordingly into components due to particles E^p and due to water E^w.

The static energy associated with particle impact, , can be determined by subtracting the actual average values of the static energy of water impingement **Figure 6.19**, , from the total static energy of the slurry as: .

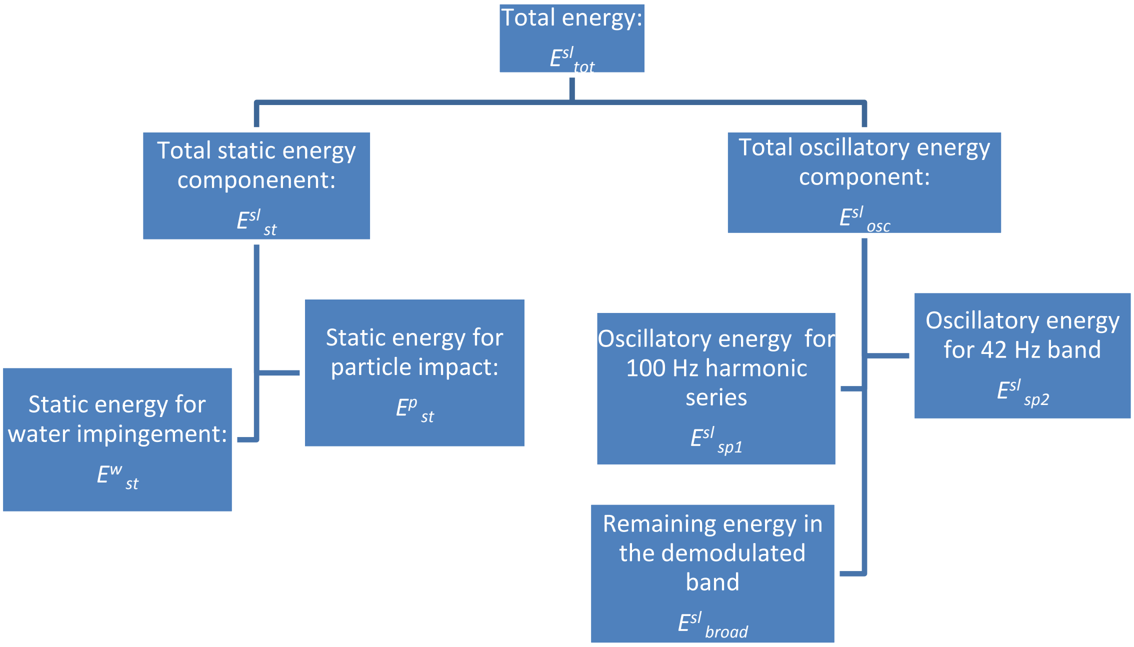

Figure 6.21: Schematic illustration of the decomposition of slurry impingement AE energy in the flow loop

Figures 6.22 to **6.25** show the effect of flow speed on the static AE energy associated with particle impacts for all particle sizes and nominal concentrations tested. As before, the best power law fit was used and the resulting exponents are shown in **Table 6.3**.

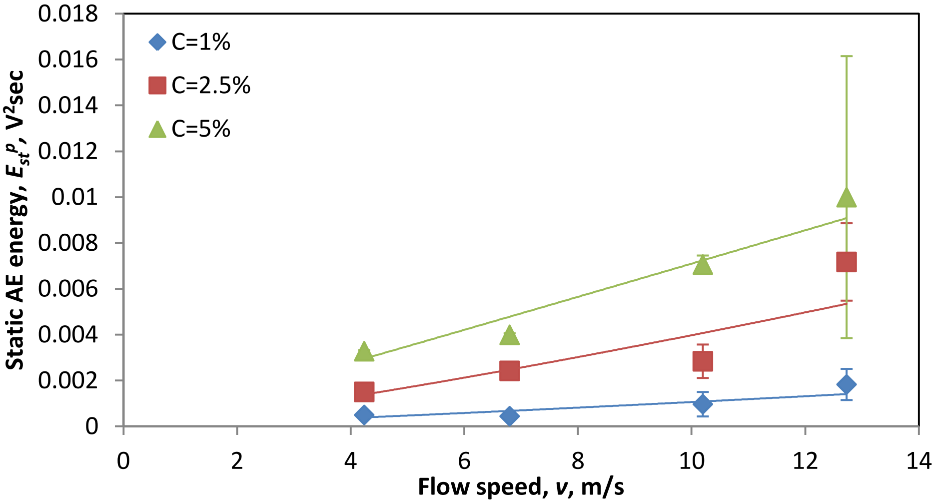

Figure 6.22: Effect of flow speed on the static AE energy for the three concentrations for particles in size range 212-250 µm

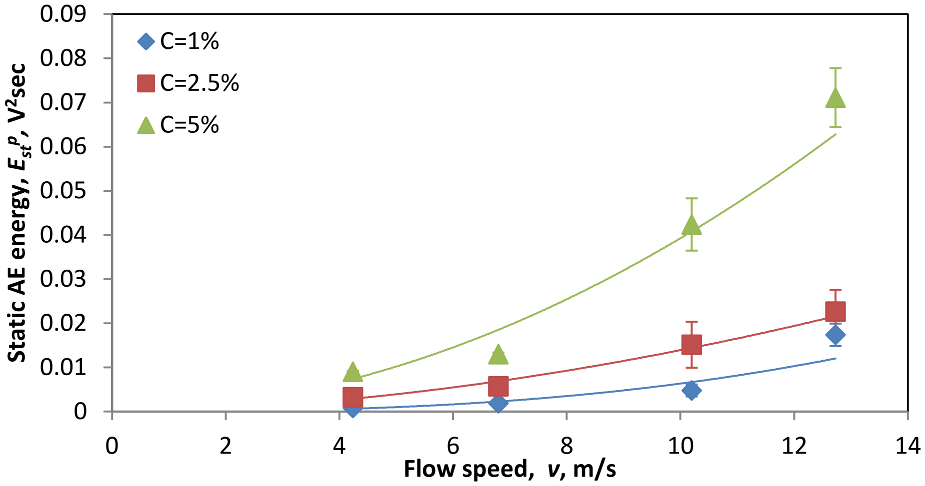

Figure 6.23: Effect of flow speed on the static AE energy for the three concentrations for particles in size range 300-425 µm

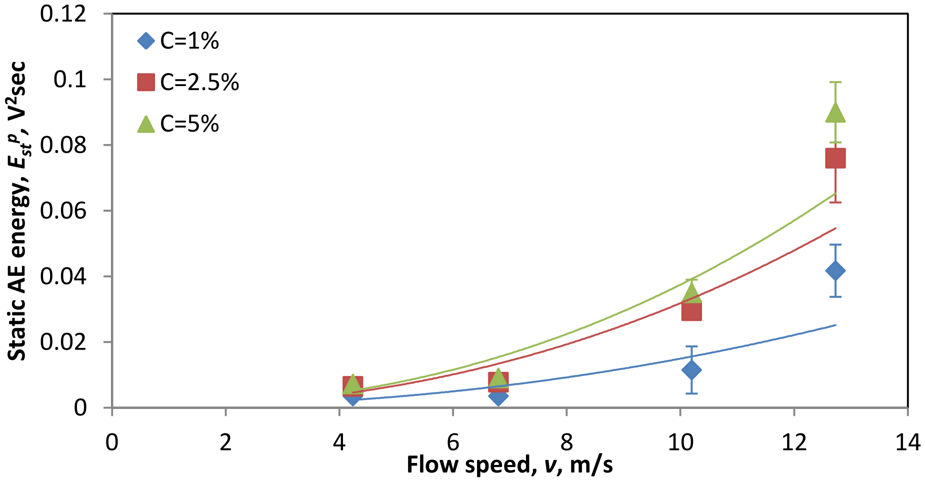

Figure 6.24: Effect of flow speed on the static AE energy for the three concentrations for particles in size range 500-600 µm

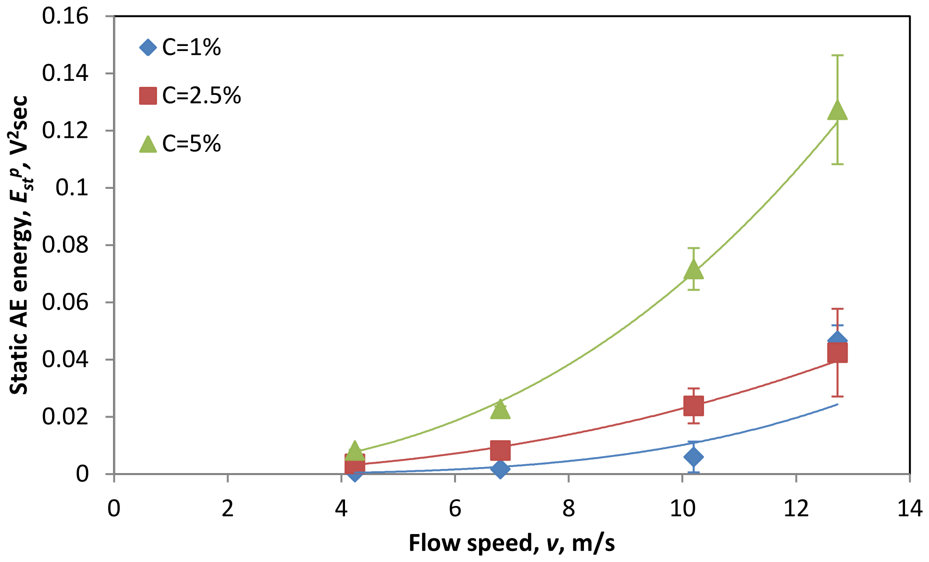

Figure 6.25: Effect of flow speed on the static AE energy for the three concentrations for particles in size range 600-710 µm

Particle size range (µm)	Nominal concentration (kg/m^3)	Flow speed exponent (*n*)	Curve fitting R^2 value (%)
212-250	1	1.18	75
	2.5	1.22	82
	5	1.03	93
300-425	1	2.6	93
	2.5	1.8	97
	5	1.95	93
500-600	1	2.1	78
	2.5	2.2	86
	5	2.3	87
600-710	1	3.6	89
	2.5	2.2	99
	5	2.5	99

Table 6.3: Exponent of flow speed dependence of the static component of measured AE energy for all flow loop tests

In order to examine if the energy for slurry impingement is carried in the same frequency bands as water impact, the dynamic slurry energy, was divided into three parts, the component associated with the 100 Hz harmonic series, , the component associated with the 42 Hz band, , and the remainder of the demodulated band (see **Figure 6.21**),

(6.4)

To decompose the oscillatory part of the AE, each record was band-pass filtered twice in the sp_1 and sp_2 bands using an infinite impulse response (IIR) digital filter of Chebyshev Type I , set with a fifth order low pass digital Chebychev filter and 0.9 peak to peak ripple in the bassband.

Figures 6.26 to **6.28** show the variation of the energy in each spectral component with flow speed for all particle size fractions and solid concentrations tested, along with the corresponding components for particle-free water. Over the range of flow speed, the dominant band is the broad oscillatory component, the 100 Hz band only being significant at lower flow speeds. The 42 Hz spectral component is always very small and increases with flow speed. There is particularly no difference between the various particle sizes and concentrations and particle-free water for this component, so it is of little use in detecting particle impacts. Unlike all the other spectral components, the 100 Hz band decreases with flow speed. **Figure 6.29** shows the effect of particle size and concentration on this spectral component at the lowest flow speed. As can be seen, the 100 Hz spectral component decreases with both the nominal particle concentration and particle size range indicating that the pump rotational speed effect on the AE recorded can be obscured by more particles in the mixture or bigger particle size range.

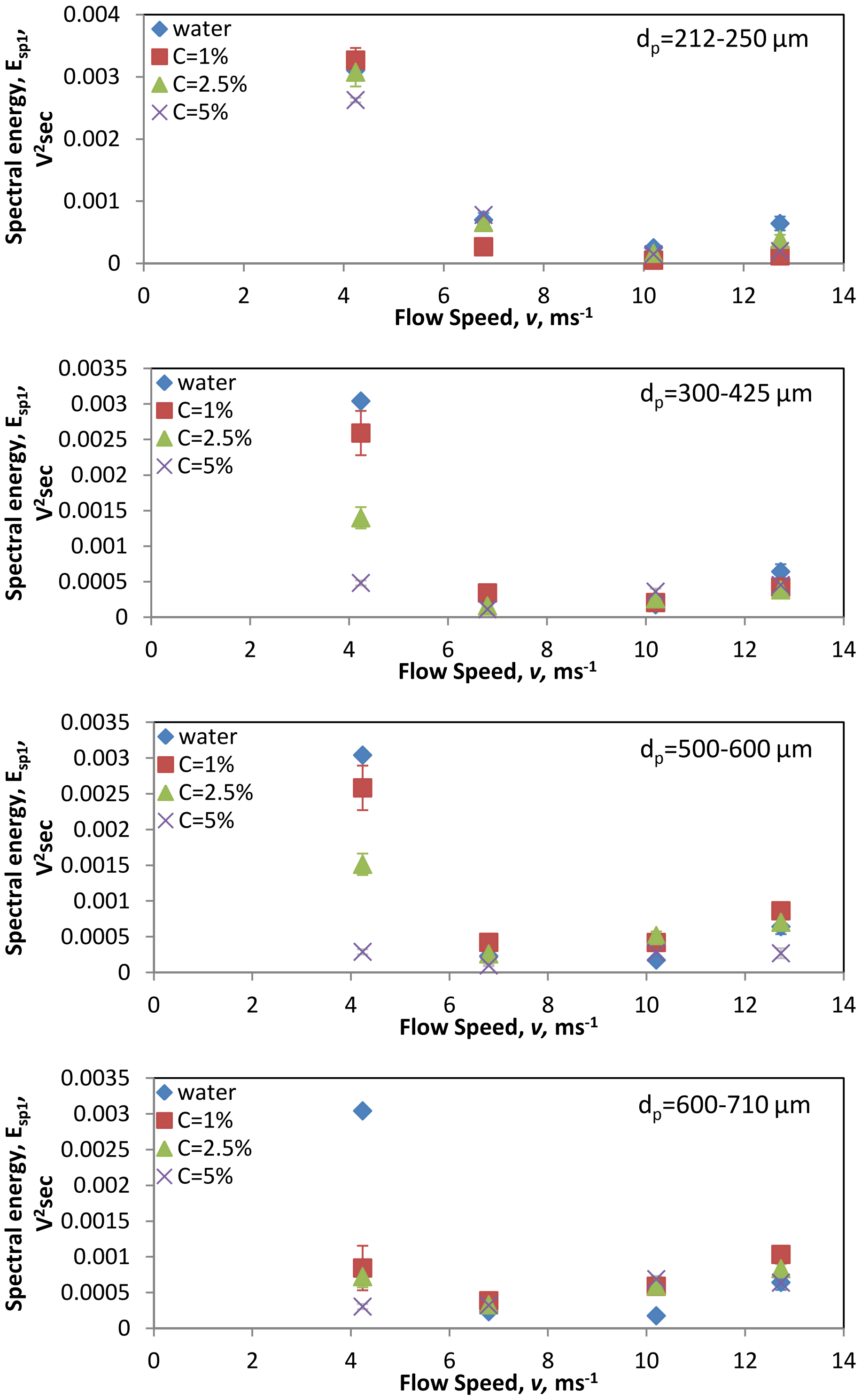

Figure 6.26: Effect of flow speed on the spectral AE energy, E_{sp1} , for the three concentrations and particle-free water for each of the particle size ranges shown

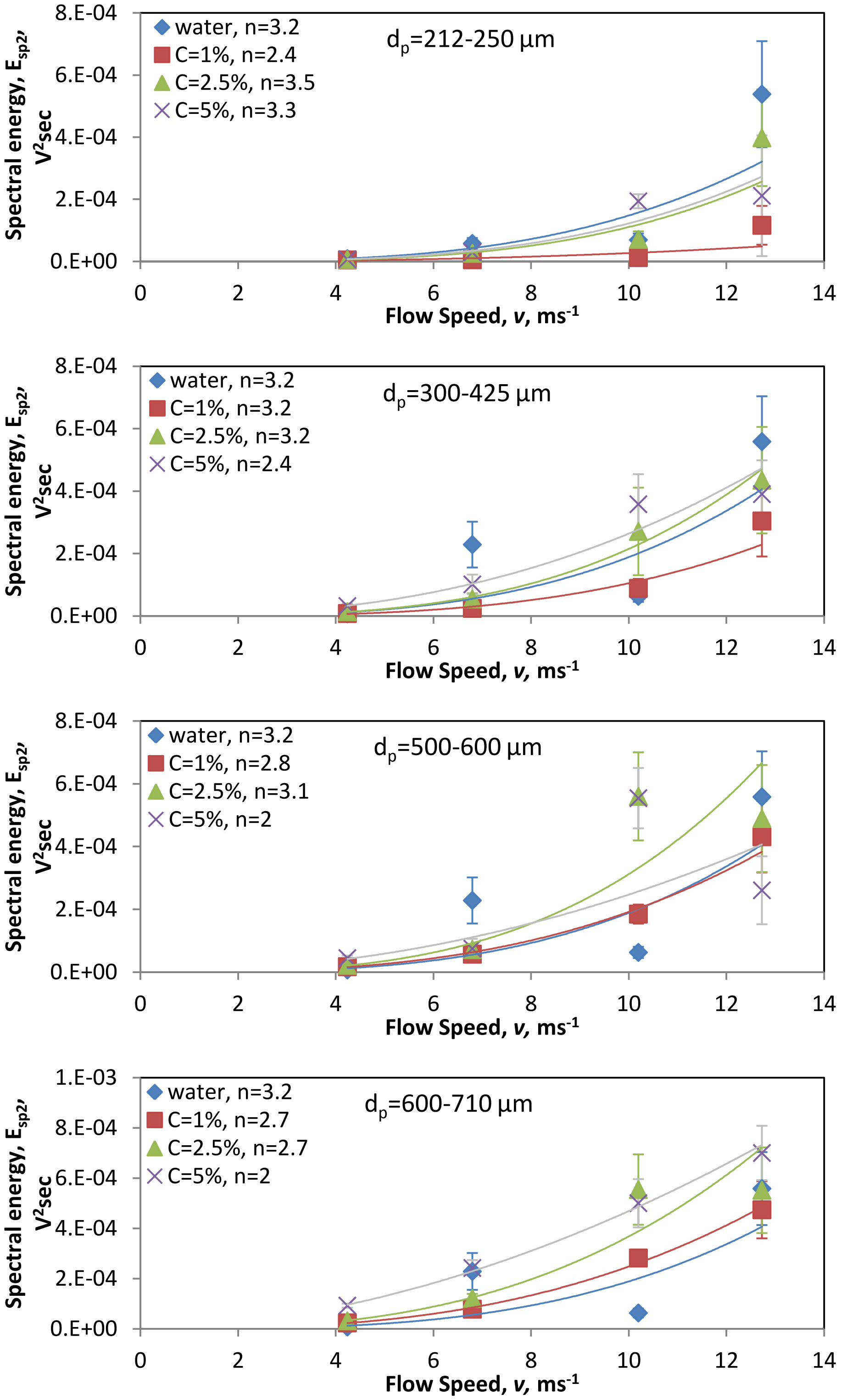

Figure 6.27: Effect of flow speed on the spectral AE energy, E_{sp2}, for the three concentrations and particle-free water for each of the particle size ranges shown

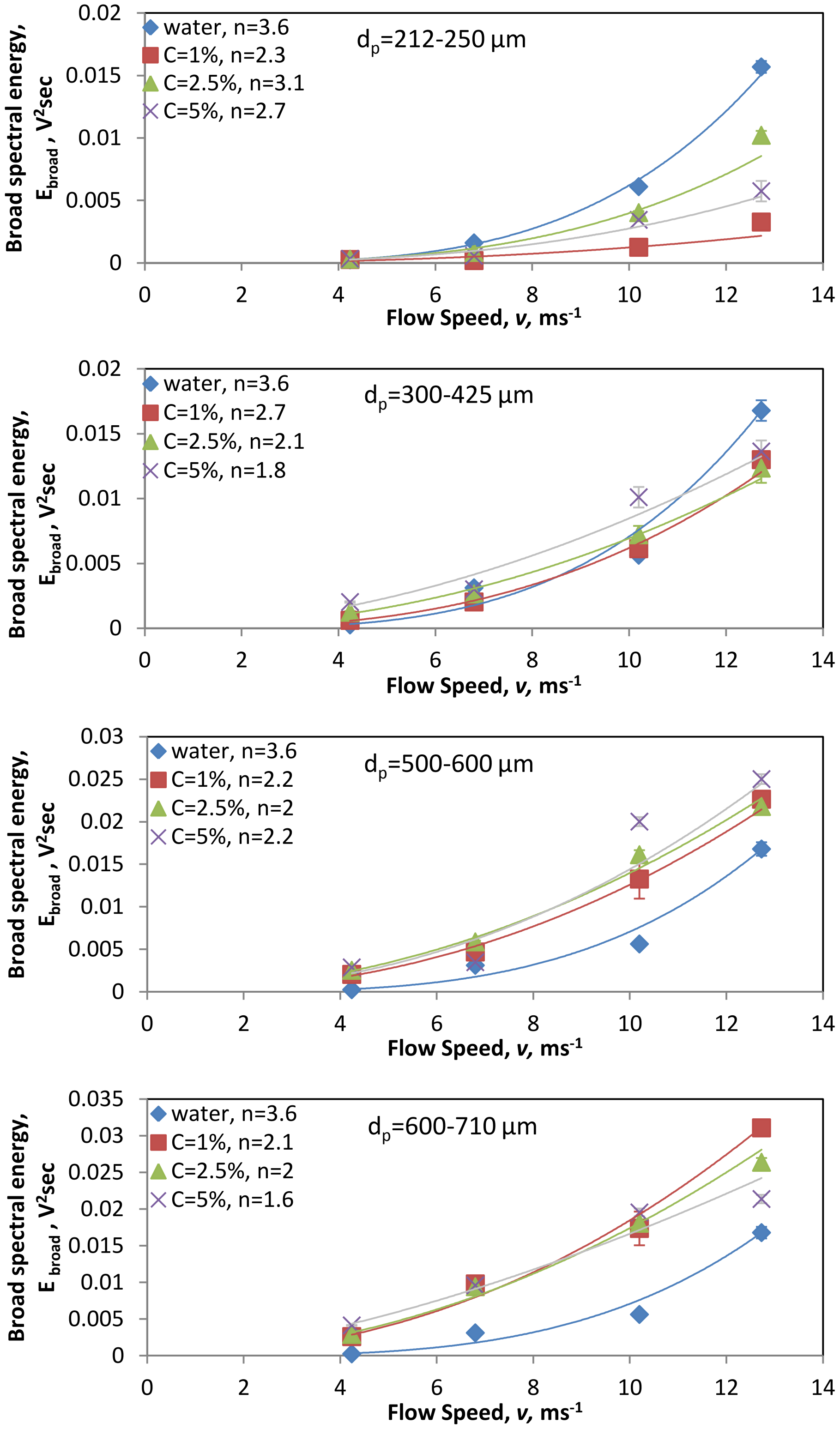

Figure 6.28: Effect of flow speed on the broad spectral AE energy, E_{broad}, for the three concentrations and particle-free water for each of the particle size ranges shown

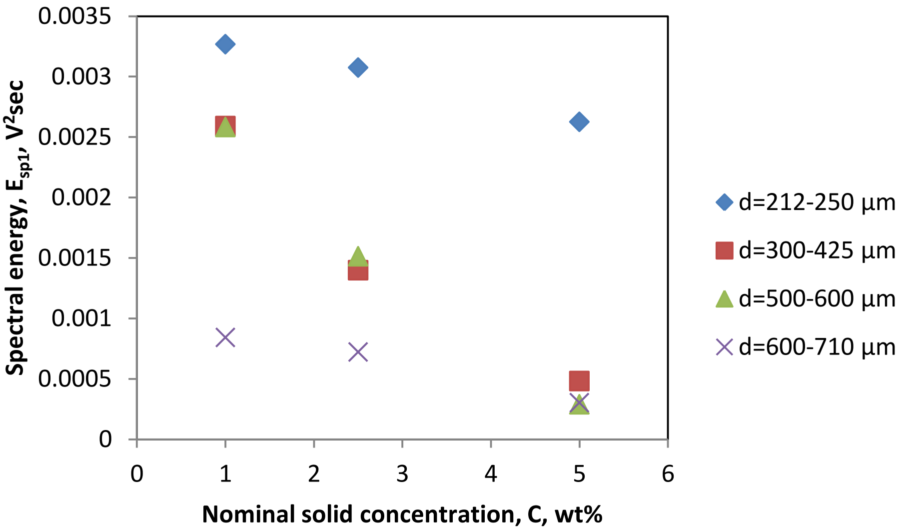

Figure 6.29: Effect of particle size and concentration on the spectral AE energy, E_{sp1} , for each of the particle size ranges at 4.2 ms^{-1} flow speed

6.3.3 Application of time series model to flow loop tests

The purpose of this section is to examine the applicability of the model to simulate (predict) AE energy in more practical environments and to assess any adjustments that need to be made in the processing techniques to use AE as a semi-quantitative diagnostic indicator for particle impingement in industrial flows. Besides the fact that the flow environment is different from the free jet tests, the target design is also slightly different, so the effects of these on the recorded energy both need to be assessed.

As with the slurry jet impingement experiments, what remains to be seen is whether the AE energy measured corresponds to what would be expected from the previously developed log-normal distribution function. Since the flow loop experiments involved a wider range of particle size ranges (up to 600-710 µm) than the slurry jet impingement experiments, the mean of the log-normal distribution shown in **Figure 5.12** was used here giving the mean AE energy:

The expected AE energy in a population of impacts, $E_{calculated}$, can now be obtained using the average particle arrival rate given in **Table 3.8** and the mean of the energy distribution function **Equation 6.2**. The measured AE energy associated with the particles, $E_{measured}$, was estimated by subtracting the background water jet energy E_w

from the integral of the signal, E as seen in **Equation 6.3**. The background water energy was estimated using **Equation 5.4**, where E_w was taken as the AE energy associated of the best fit power equations of both components of water impingement, static AE energy and oscillatory AE energy . As for the slurry impingement tests, the empirical model of Turrene and Fiset [94] was used to calculate the average particle speed for all the conditions studied (**Table 6.4**).

Particle size range (µm)	Flow speed (m/s)	Average calculated speed (m/s)
212-250	4.2	-
	6.8	0.3
	10.2	0.95
	12.7	1.43
300-425	4.2	0.1
	6.8	0.84
	10.2	1.8
	12.7	2.5
500-600	4.2	0.65
	6.8	1.75
	10.2	3.19
	12.7	4.24
600-710	4.2	0.98
	6.8	2.28
	10.2	3.99
	12.7	5.24

Table 6.4: Calculated particle arrival speed using the model of Turenne and Fiset [94]

Figures 6.30 to 6.33 show the correlation between the calculated and the measured AE energy for each of the particle sizes using the average calculated impact speed in **Table 6.4**. It is clear from these figures that the correlation slope approaches the expected value of unity with increasing particle size. This might be explained by the fact that smaller particle fractions (less inertia) are more vulnerable to influences of the fluid than bigger fractions (bigger inertia), which would change the impact angle and also the proportion of particles striking the surface, and this would also explain the lower measured values in **Figure 6.30** where uncontrolled behaviour of particles sweeping around the bend is more likely. **Figure 6.33** shows the average slope of the correlation between calculated AE energy and measured AE energy when taking all the data together. As can be seen, the slope is close to unity, although, the calculated (expected) AE energy is slightly overestimated. This might partly be explained by particle trajectories around the bend generally having an angle of incidence influenced by the bulk fluid flow, resulting in a greater proportion of particles having an angle of impact less than 90°, and thus overestimate in the calculated AE energy. Another possible reason might be that the hydraulic differences between the bend and the slurry impingement rig result in a smaller proportion of particles actually striking the target and contributing to AE energy due to a higher degree of particle interaction at or near the surface, resulting in particle collisions, reduced particle impact velocities and changed impact angles. Also, the effect of the slightly different design of the target at the bend might provide a leakage path for AE energy reducing the amount of measured AE energy. These factors have probably all contributed to the overestimate in the calculated AE energy and are those which would have to be taken into account in any real application of the technique as they are dependent on the design of the system being monitored.

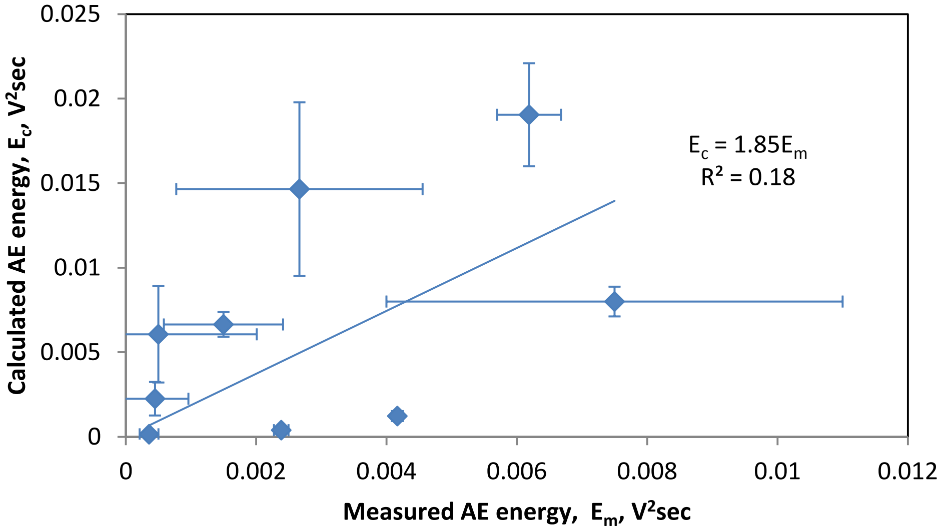

Figure 6.30: Calculated AE energy versus measured AE energy at particle size range 212-250 µm

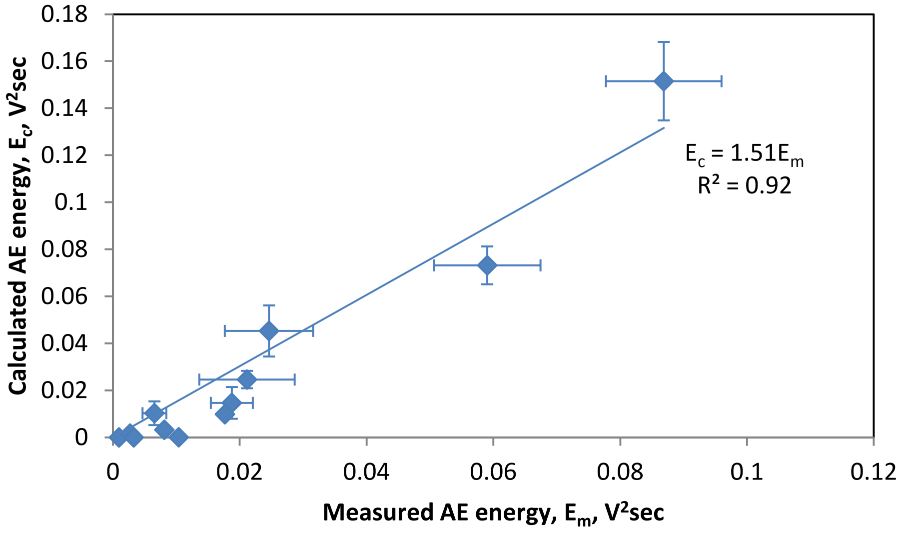

Figure 6.31: Calculated AE energy versus measured AE energy at particle size range 300-425 µm

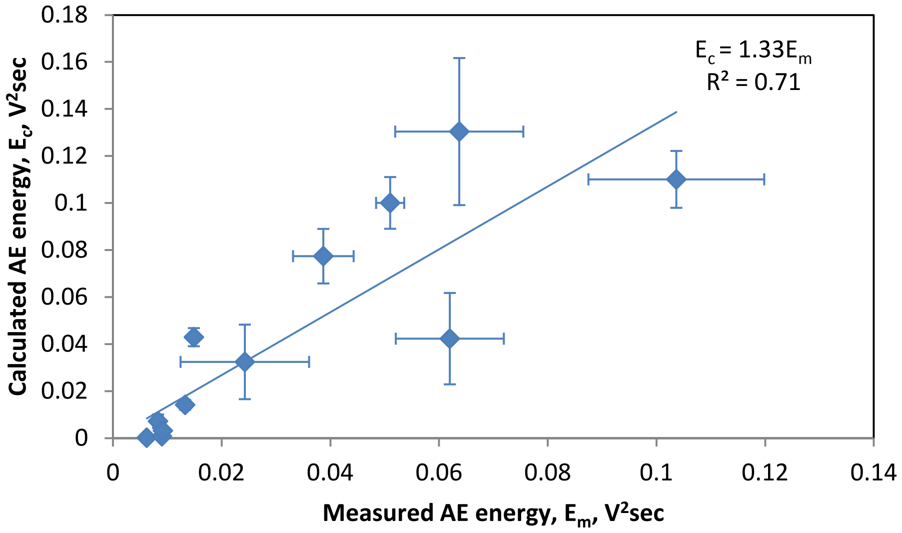

Figure 6.32: Calculated AE energy versus measured AE energy at particle size range 500-600 µm

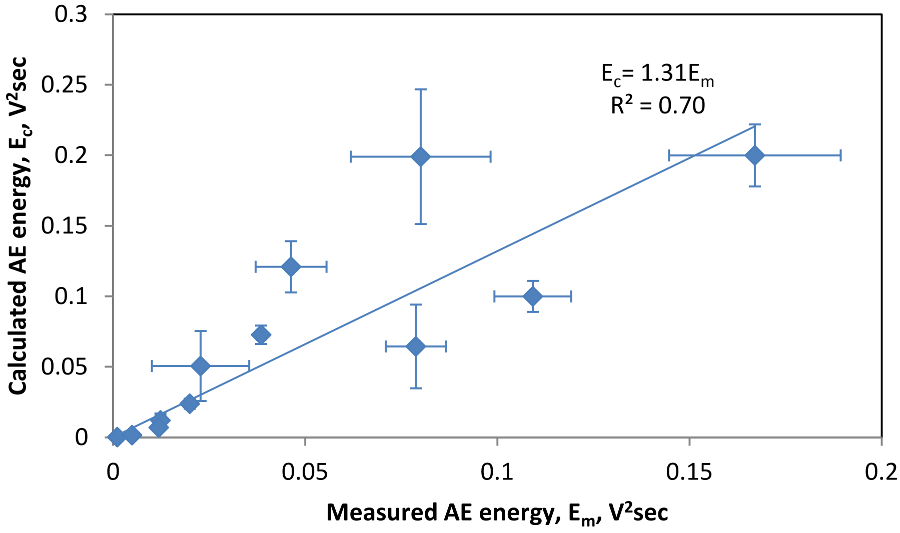

Figure 6.33: Calculated AE energy versus measured AE energy at particle size range 600-710 µm

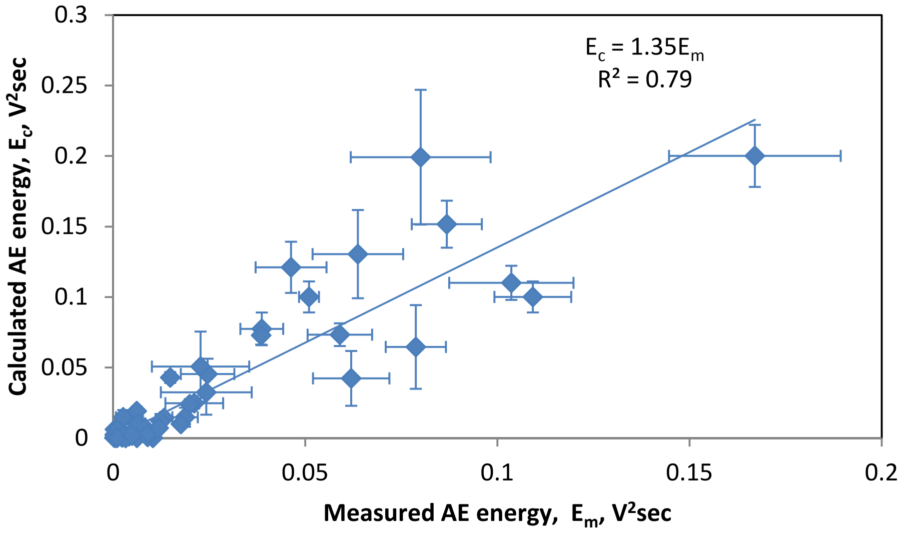

Figure 6.34: Calculated AE energy versus measured AE energy for all particle size ranges investigated

Chapter 7

Conclusions and Recommendations

In this work, two main types of experiments were carried out, AE monitoring of particle laden gas and AE monitoring of particle laden liquid, the tests with particle laden gas including free fall and free jet impingement and those with liquid including a free jet and pipe flow. A statistical distribution model describing the AE time series associated with a particle stream was developed, which allows a direct calculation for AE energy provided that the nominal mass and nominal speed of the impinging particles are known. The development and extension of this model to account for different particle carrier-fluids and to situations where particle arrivals cannot necessarily be resolved is considered to be the most important contribution of this study. The overall conclusion is that, provided appropriate calibrations are carried out, it is possible to develop an AE monitoring cell which will be able to measure the cumulative impingement energy (in terms of) in practical particle-laden flows. The main conclusions which led to this are outlined below followed by recommendations for future work.

7.1 Conclusions

The detailed conclusions are outlined below according to the order in which they are revealed in the thesis; dry impacts, time series model, slurry impacts and flow loop.

7.1.1 Free fall and preliminary airborne particle tests

7.1.1.1 Generally, AE offers the potential to monitor particle impact energy and thus assess the abrasive potential of dry particle flows.

7.1.1.2 For individual impacts, the AE energy was found overall to be proportional to the incident kinetic energy $\frac{1}{2}mv^2$ of the particles over a wide range of particle sizes (from 125 microns to 1500 microns) and incident velocities (from 0.9 ms^{-1} to 16 ms^{-1}) in accord with a number of other workers.

7.1.1.3 A distinct difference was found in the velocity exponent (assuming the diameter exponent to be 3) between multiple and individual impacts, the individual impacts generally giving higher energies per particle, This is attributed to particle interactions either in the guide tube or at the surface which modify the actual incident velocity from that assumed, and that effect has been observed by workers carrying out erosion experiments.

7.1.1.4 For the configuration used in this work, the diameter exponent was only valid up to particle sizes of around 1.5mm, above which it appears that a significant proportion of the incident kinetic energy was dissipated in whole body movement of the target.

7.1.2 Time series model

Acoustic emission has been used to measure and characterise the cumulative impact energy of particle streams impinging normally against a carbon steel target, with the following broad findings:

7.1.2.1 The temporal resolution was found to be determined by the design of the target plate, and individual particle analysis was only possible in records containing relatively few overlapping events.

7.1.2.2 For records where individual particle arrivals could be resolved, of the two time-domain processing techniques that were examined, the truncated distribution method was found to be the more effective.

7.1.2.3 Of the two distribution types examined, a lognormal distribution of AE energies was found to represent the observations better and this was consistent with literature findings on particle impact energy distributions from other areas of study.

7.1.2.4 The lognormal distributions of AE energy were calibrated against the expected kinetic energy at impact and validated against single particle findings. This resulted in a particle AE energy distribution function which could be calculated directly from the nominal mass and nominal speed of the impinging particles.

7.1.2.5 By inspection of the times series and the results of pencil-lead breaks, the pulse-shape function for an AE impact on the target plate could be determined and hence the particle time series could be simulated, irrespective of the amount of overlap. Comparison of the total energy in the recorded and simulated time series (including those in which the individual particles could not be resolved) showed generally good agreement, but with the simulations overestimating the energy by about 10% for small particles and underestimating by about 10% for large particles.

7.1.3 Slurry jet impingement tests

A series of slurry impingement tests were carried out to study the effect of particle size, flow speed, particle concentration, and impact angle, on the AE energy dissipated in a carbon steel target, with the following broad findings:

7.1.3.1 The main problem encountered in the use of the AE technique in slurry impact experiments, compared with air-directed jets, was the high degree of particle arrival overlap and the lower-than-expected (particle) signal to (water) noise ratio.

7.1.3.2 The measured AE energy was found generally to scale with the expected square of velocity, cube of particle size, linear with concentration and $\sin^2$ of nominal impact angle, but with weaker expression for smaller, slower particles.

7.1.3.3 The cumulative impact energy, discounting that due to the water, was a factor of at least ten lower than would be expected compared with similar experiments using an air-directed jet.

7.1.3.4 Correcting the actual arrival speed relative to the jet exit velocity using a published semi-empirical model gave calculated cumulative energies which were much closer to those observed.

7.1.3.5 Larger particles tended to give lower than expected cumulative energy, an observation that is attributed to drop-out of the particles relative to the fluid in the horizontally-directed jets.

7.1.3.6 Lower nominal angles of impingement tended to give lower than expected cumulative energy even when the normal component of the velocity is considered. This has again been attributed to the gravitational effect on both the slurry and the particles which will affect the vertical components of the velocity relative to the horizontal one.

7.1.4 Flow loop impingement tests

7.1.4.1 The measured AE energy was found overall to be proportional to the expected square of velocity, cube of particle size, and linear with concentration of the incident flow over a wide range of particle sizes (125-600 µm), flow speeds (4-12 ms^{-1}), and nominal concentrations (1-5 wt%), but, again, with weaker expression for smaller, slower particles.

7.1.4.2 The cumulative AE energy, due to water impingement, was approximately seven times higher than similar experiments using the slurry jet impingement test rig.

7.1.4.3 AE recorded by a sensor mounted on a pipe bend was strongly influenced by flow noise attributed to the hydraulic conditions in the pipe.

7.1.4.4 The raw AE power density spectrum varied systematically with the flow speed which indicates the potential of using AE as a monitoring indicator for hydraulic conditions.

7.1.4.5 Demodulated frequency analysis of the water impingement signals at different speeds showed two distinct patterns of spectral peaks in the demodulated signal.

7.1.4.6 A simple model for water impingement AE energy relative to flow speed was developed based on the static and oscillatory parts of the signal.

7.1.4.7 AE energy decomposition coupled with spectral peak filtering could be used on the static and oscillatory components of the particle flows to remove the fluid noise and to establish that both components showed speed, size and concentration exponents consistent with the slurry and airborne tests.

7.1.4.8 The mean of the AE energy distribution function for particle laden gas could again be generalised to account for particle laden liquid after correcting the actual arrival speed relative to the flow speed using a published empirical model.

7.1.4.9 The calculated AE energy (form the model) showed good agreement with the measured AE energy, but with the model overestimating the energy, particularly for smaller particles. The discrepancies could be traced to details of the design of the hydraulics and the target, and these are factors which would need to be accounted for in any practical application.

7.2 Future work

The work presented in this thesis contributes a strong grounding for future research in using the AE technique to monitor particle impact erosion in slurry handling systems.

The following recommendations are suggested for future research

- The AE energy model could be developed on the basis of the present study and could be tested in an industrial-scale flow loop to assess the degree to which the findings of this work are generic. Particular attention needs to be paid to the design of the monitoring cell and its local hydraulic environment.

- This study has considered mainly impacts between silica sand and a carbon steel target. It would be useful to examine the applicability of the model for a wider range of abrasives and target materials. It would also be useful to investigate the AE energy with a wider range of particle sizes and carrier fluids in order to improve the model predictive capability.
- The model should be examined for different impact regimes using different particle and target materials. In particular, there may be a scope for AE to distinguish between ductile and brittle erosion.

References

1. Aquaro D. *Erosion due to the impact of solid particles of materials resistant at high temperature.* Meccanica, 2006. **41**(5): p. 539-551.
2. Bitter J G A. *A study of erosion phenomena : part I.* Wear, 1963. **6**(1): p. 5-21.
3. Bitter J G A. *A study of erosion phenomena : part II.* Wear, 1963. **6**(3): p. 169-190.
4. Finnie I. *Erosion of surfaces by solid particles.* Wear, 1960. **3**(2): p. 87-103.
5. Hutchings I M. *Mechanisms of the Erosion of Metals by Solid Particles.* Journal of American Society for Testing and Materials, 1979. **664**: p. 59-76.
6. Hutchings I M, Macmillan N H and Rickerby D G. *Further studies of the oblique impact of a hard sphere against a ductile solid.* International Journal of Mechanical Sciences, 1981. **23**(11): p. 639-646.
7. Hutchings I M, Winter R E and Field J E. *Solid Particle Erosion of Metals: The Removal of Surface Material by Spherical Projectiles.* Proceedings of the Royal Society of London. Series A, Mathematical and Physical Sciences, 1976. **348**(1654): p. 379-392.
8. Papini M and Spelt J K. *Impact of rigid angular particles with fully-plastic targets Part I: Analysis.* International Journal of Mechanical Sciences, 2000. **42**(5): p. 991-1006.
9. Papini M and Spelt J K. *Impact of rigid angular particles with fully-plastic targets Part II: Parametric study of erosion phenomena.* International Journal of Mechanical Sciences, 2000. **42**(5): p. 1007-1025.
10. Meng H C and Ludema K C. *Wear models and predictive equations: their form and content.* Wear, 1995. **181-183**(2): p. 443-457.
11. Chen Q and Li D Y. *Computer simulation of solid particle erosion.* Wear, 2003. **254**(3-4): p. 203-210.
12. Clark H M and Hartwich R B. *A re-examination of the `particle size effect' in slurry erosion.* Wear, 2001. **248**(1-2): p. 147-161.
13. Feng Z and Ball A. *The erosion of four materials using seven erodents - towards an understanding.* Wear, 1999. **233-235**: p. 674-684.
14. Sundararajan G and Roy M. *Solid particle erosion behaviour of metallic materials at room and elevated temperatures.* Tribology International, 1997. **30**(5): p. 339-359.

15. Truscott G F. *A literature survey on abrasive wear in hydraulic machinery.* Wear, 1972. **20**(1): p. 29-50.
16. Levin B F, Vecchio K S, DuPont J N and Marder A R. *Modeling solid-particle erosion of ductile alloys.* Metallurgical and Materials Transactions A, 1999. **30**(7): p. 1763-1774.
17. Divakar M, Agarwal V K and Singh S N. *Effect of the material surface hardness on the erosion of AISI316.* Wear, 2005. **259**(1-6): p. 110-117.
18. Harsha A P and Thakre A A. *Investigation on solid particle erosion behaviour of polyetherimide and its composites.* Wear, 2007. **262**(7-8): p. 807-818.
19. Ferrer F, Faure T, Goudiakas J and Andres E. *Acoustic emission study of active-passive transitions during carbon steel erosion-corrosion in concentrated sulfuric acid.* Corrosion Science, 2002. **44**(7): p. 1529-1540.
20. Ferrer F, Idrissi H, Mazille H, Fleischmann P and Labeeuw P. *On the potential of acoustic emission for the characterization and understanding of mechanical damaging during abrasion-corrosion processes.* Wear, 1999. **231**(1): p. 108-115.
21. Ferrer F, Idrissi H, Mazille H, Fleischmann P and Labeeuw P. A *study of abrasion-corrosion of AISI 304L austenitic stainless steel in saline solution using acoustic emission technique.* NDT & E International, 2000. **33**(6): p. 363-371.
22. Duclos J B, Reuben R L and Steel J A. *A study of particle impacts in fluid flow using acoustic emission*. 2005, Heriot Watt University: Edinburgh.
23. Hou R, Hunt A and Williams R A. *Acoustic monitoring of pipeline flows: particulate slurries.* Powder Technology, 1999. **106**(1-2): p. 30-36.
24. Burstein G.T and Sasaki K. *Effect of impact angle on the slurry erosion-corrosion of 304L stainless steel.* Wear, 2000. **240**(1-2): p. 80-94.
25. Zhang L, Sazonov V, Kent J, Dixon T and Novozhilov V. *Analysis of boiler-tube erosion by the technique of acoustic emission: Part I. Mechanical erosion.* Wear, 2001. **250**(1-12): p. 762-769.
26. Head W J and Harr M E. *The development of a model to predict the erosion of materials by natural contaminants.* Wear, 1970. **15**(1): p. 1-46.
27. Johnson K L. *Contact Mechanics*. 1985, UK: Cambridge University Press.
28. Stronge W J. *Impact Mechanics*. 2000, Cambridge University Press, Cambridge.

29. Wu C Y. *Finite Element Analysis of Particle IMpact Problems*. PhD thesis. 2001, Aston University: Birmingham, UK.
30. Vu-Quoc L, Zhang X and Lesburg L. *A Normal Force-Displacement Model for Contacting Spheres Accounting for Plastic Deformation: Force-Driven Formulation.* Journal of Applied Mechanics, 2000. **67**(2): p. 363-371.
31. Tsai Y M. *Dynamic contact stresses produced by the impact of an axisymmetrical projectile on an elastic half-space.* International Journal of Solids and Structures, 1971. **7**(6): p. 543-558.
32. Tabor, D. *The Hardness of Metals*. 1951, Oxford University Press, Oxford.
33. Thornton C. *Coefficient of Restitution for Collinear Collisions of Elastic-Perfectly Plastic Spheres.* Journal of Applied Mechanics, 1997. **64**(2): p. 383-386.
34. Hutchings I M. *Energy absorbed by elastic waves during plastic impact.* Journal of Physics D: Applied Physics, 1979. **12**: p. 1819-1824.
35. Yigit A S and Christoforou A P. *On the impact of a spherical indenter and an elastic-plastic transversely isotropic half-space.* Composites Engineering, 1994. **4**(11): p. 1143-1152.
36. Stronge W J. *Rigid Body Collisions with Friction.* Proceedings of the Royal Society of London. Series A: Mathematical and Physical Sciences, 1990. **431**(1881): p. 169-181.
37. Shehadeh M F. *Monitoring of Long Steel Pipes using Acoustic Emission*, PhD thesis. 2006, Heriot Watt University: Edinburgh, UK.
38. Hunter S C. *Energy absorbed by elastic waves during impact.* Journal of the Mechanics and Physics of Solids, 1957. **5**(3): p. 162-171.
39. Reed J. *Energy losses due to elastic wave propagation during an elastic impact.* Journal of Physics D: Applied Physics, 1985. **12**: p. 29-37.
40. Tabor D. *The Hardness of Metals*. 1951, Oxford University Press, Oxford.
41. Wu C Y, Li L Y and Thornton C. *Energy dissipation during normal impact of elastic and elastic-plastic spheres.* International Journal of Impact Engineering, 2005. **32**(1-4): p. 593-604.
42. Thapa B, *Sand erosion in hydraulic machinery*. PhD thesis. 2004, Norwegian university of Science and Technology: Norway.
43. Yabuki A, Matsuwaki K and Matsumura M. *Critical impact velocity in the solid particles impact erosion of metallic materials.* Wear, 1999. **233-235**: p. 468-475.

44. Finnie I. *Some reflections on the past and future of erosion.* Wear, 1995. **186-187** (Part 1): p. 1-10.
45. Hutchings I M and Winter R E. *Particle erosion of ductile metals: A mechanism of material removal.* Wear, 1974. **27**(1): p. 121-128.
46. Winter R E and Hutchings I M. *Solid particle erosion studies using single angular particles.* Wear, 1974. **29**(2): p. 181-194.
47. Dhar S, Krajac T, Ciampini D and Papini M. *Erosion mechanisms due to impact of single angular particles.* Wear, 2005. **258**(1-4): p. 567-579.
48. Abouel-Kasem A. *Particle Size effect on Slurry Erosion of 5117 steels.* Journal of Tribology, 2011. **133**(1).
49. Al-Bukhaiti M A, Ahmed S M, Badran F M F and Emara K M. *Effect of impingement angle on slurry erosion behaviour and mechanisms of 1017 steel and high-chromium white cast iron.* Wear, 2007. **262**(9-10): p. 1187-1198.
50. Chevallier P and Vannes A B. *Effects on a sheet surface of an erosive particle jet upon impact.* Wear, 1995. **184**(1): p. 87-91.
51. Oka Y I, Nishimura M, Nagahashi K and Matsumura M. *Control and evaluation of particle impact conditions in a sand erosion test facility.* Wear, 2001. **250**(1-12): p. 736-743.
52. Oka Y I, Ohnogi H, Hosokawa T and Matsumura M. *The impact angle dependence of erosion damage caused by solid particle impact.* Wear, 1997. **203-204**: p. 573-579.
53. Oka Y I, Okamura K and Yoshida T. *Practical estimation of erosion damage caused by solid particle impact: Part 1: Effects of impact parameters on a predictive equation.* Wear, 2005. **259**(1-6): p. 95-101.
54. Oka Y I and Yoshida T. *Practical estimation of erosion damage caused by solid particle impact: Part 2: Mechanical properties of materials directly associated with erosion damage.* Wear, 2005. **259**(1-6): p. 102-109.
55. Shipway P H. *The effect of plume divergence on the spatial distribution and magnitude of wear in gas-blast erosion.* Wear, 1997. **205**(1-2): p. 169-177.
56. Shipway P H and Hutchings I M. *Influence of nozzle roughness on conditions in a gas-blast erosion rig.* Wear, 1993. **162-164**(1): p. 148-158.
57. Stevenson A N J and Hutchings I M. *Scaling laws for particle velocity in the gas-blast erosion test.* Wear, 1995. **181-183**(1): p. 56-62.

58. Deng T, Chaudhry A R, Patel M, Hutchings I M and Bradley M S A. *Effect of particle concentration on erosion rate of mild steel bends in a pneumatic conveyor.* Wear, 2005. **258**(1-4): p. 480-487.

59. Zhong Y and Minemura K. *Measurement of erosion due to particle impingement and numerical prediction of wear in pump casing.* Wear, 1996. **199**(1): p. 36-44.

60. ASTM standard, *G76-83(1989): Standard practice for conducting erosion tests by solid particle impingement using gas jets.* Annual book of ASTM standards, 1993. **03.02**: p. 313-317.

61. Andrews D R. *An Analysis of Solid Particle Erosion Mechanisms.* Journal of Physics, part:D, Applied Physics, 1981. **14**(11): p. 1979-1991.

62. Buttle D J and Scruby C B. *Characterization of particle impact by quantitative acoustic emission.* Wear, 1990. **137**(1): p. 63-90.

63. Deng T, Bingley M S and Bradley M S A. *Understanding particle dynamics in erosion testers--A review of influences of particle movement on erosion test conditions.* Wear, 2009. **267**(11): p. 2132-2140.

64. Clark H M. *The influence of the squeeze film in slurry erosion.* Wear, 2004. **256**(9-10): p. 918-926.

65. Clark H M and Wong K K. *Impact angle, particle energy and mass loss in erosion by dilute slurries.* Wear, 1995. **186-187** (2): p. 454-464.

66. Desale G R, Gandhi B K and Jain S C. *Improvement in the design of a pot tester to simulate erosion wear due to solid-liquid mixture.* Wear, 2005. **259** (1-6): p. 196-202.

67. Desale G R, Gandhi B K and Jain S C. *Effect of erodent properties on erosion wear of ductile type materials.* Wear, 2006. **261**(7-8): p. 914-921.

68. Gandhi B K and Borse S V. *Nominal particle size of multi-sized particulate slurries for evaluation of erosion wear and effect of fine particles.* Wear, 2004. **257**(1-2): p. 73-79.

69. Gandhi B K, Singh S N and Seshadri V. *Study of the parametric dependence of erosion wear for the parallel flow of solid-liquid mixtures.* Tribology International, 1999. **32**(5): p. 275-282.

70. Kovacevic R, Kwak H S and Mohan R S. *Acoustic emission sensing as a tool for understanding the mechanisms of abrasive water jet drilling of difficult-to-machine materials.* Proceedings of the Institution of Mechanical Engineers, Part B-Journal of Engineering Manufacture, 1998. **212**(1): p. 45-58.

71. Momber A W. *Wear of rocks by water flow.* International Journal of Rock Mechanics and Mining Sciences, 2004. **41**(1): p. 51-68.

72. Momber A W, Mohan R S and Kovacevic R. *On-line analysis of hydro-abrasive erosion of pre-cracked materials by acoustic emission.* Theoretical and Applied Fracture Mechanics, 1999. **31**(1): p. 1-17.

73. Oltra R, Chapey B and Renaud L. *Abrasion-corrosion studies of passive stainless steels in acidic media: combination of acoustic emission and electrochemical techniques.* Wear, 1995. **186-187**(2): p. 533-541.

74. Tian H H, Addie G R and Pagalthivarthi K V. *Determination of wear coefficients for erosive wear prediction through Coriolis wear testing.* Wear, 2005. **259**(1-6): p. 160-170.

75. Deng T, Li J, Chaudhry A R, Patel M, Hutchings I M and Bradley M S A. *Comparison between weight loss of bends in a pneumatic conveyor and erosion rate obtained in a centrifugal erosion tester for the same materials.* Wear, 2005. **258**(1-4): p. 402-411.

76. Wood R J K. *Erosion-corrosion interactions and their effect on marine and offshore materials.* Wear, 2006. **261**(9): p. 1012-1023.

77. Papini M and Dhar S. *Experimental verification of a model of erosion due to the impact of rigid single angular particles on fully plastic targets.* International Journal of Mechanical Sciences, 2006. **48**(5): p. 469-482.

78. Aquaro D and Fontani E. *Erosion of Ductile and Brittle Materials.* Meccanica, 2001. **36**(6): p. 651-661.

79. Shipway P H and Hutchings I M. *A method for optimizing the particle flux in erosion testing with a gas-blast apparatus.* Wear, 1994. **174**(1–2): p. 169-175.

80. Ciampini D, Spelt J K and Papini M. *Simulation of interference effects in particle streams following impact with a flat surface: Part I. Theory and analysis.* Wear, 2003. **254**(3-4): p. 237-249.

81. Ciampini D, Spelt J K and Papini M. *Simulation of interference effects in particle streams following impact with a flat surface: Part II. Parametric study and implications for erosion testing and blast cleaning.* Wear, 2003. **254**(3–4): p. 250-264.

82. Burzynski T and Papini M. *Analytical models of the interference between incident and rebounding particles within an abrasive jet: Comparison with computer simulation.* Wear, 2007. **263**(7–12): p. 1593-1601.

83. Burzynski T and Papini M. *Analytical model of particle interference effects in divergent erosive jets.* Tribology International, 2010. **43**(3): p. 554-567.

84. Gomes-Ferreira C, Ciampini D and Papini M. *The effect of inter-particle collisions in erosive streams on the distribution of energy flux incident to a flat surface.* Tribology International, 2004. **37**(10): p. 791-807.

85. Crespo E F. *Application of particle fracture energy distributions to ball milling kinetics.* Powder Technology, 2011. **210**(3): p. 281-287.

86. Brodie I and Rosewell C. *Theoretical relationships between rainfall intensity and kinetic energy variants associated with stormwater particle washoff.* Journal of Hydrology, 2007. **340**(1–2): p. 40-47.

87. Turenne S, Fiset M and Masounave J. *Effect of sand concentration on the erosion of materials by a slurry jet*. in *Wear of Materials - 1989, April 9, 1989 - April 13, 1989*. 1989. Denver, CO, USA: Publ by American Soc of Mechanical Engineers (ASME).

88. Fang Q, Xu H, Sidky P S and Hocking M G. *Erosion of ceramic materials by a sand/water slurry jet.* Wear, 1999. **224**(2): p. 183-193.

89. Iwai Y and Nambu K. *Slurry wear properties of pump lining materials.* Wear, 1997. **210**(1-2): p. 211-219.

90. Laitone J A. *Aerodynamic Effects in the Erosion Process.* Wear, 1979. **56**(1): p. 239-246.

91. Benchaita, M.T., P. Griffith, and E. Rabinowicz, *Erosion of Metallic Plate by Solid Particles Entrained in a Liquid Jet.* Journal of Engineering for Industry-Transactions of the ASME, 1983. **105**(3): p. 215-222.

92. Clark H M and Burmeister L C. *Influence of the squeeze film on particle impact velocities in erosion.* International Journal of Impact Engineering, 1992. **12**(3): p. 415-426.

93. Wong K K and Clark H M. *A model of particle velocities and trajectories in a slurry pot erosion tester.* Wear, 1993. **160**(1): p. 95-104.

94. Turenne S and Fiset M. *Modeling of abrasive particle trajectories during erosion by a slurry jet.* Wear, 1993. **162-64**(part B): p. 679-687.

95. Vallen H. *AE testing, fundamentals, equipment, applications [online]*, NDT.net (available at : http://www.ndt.net/article/az/ae_idx.htm).

96. Mba D and Rao R B K N. *Development of Acoustic Emission Technology for Condition Monitoring and Diagnosis of Rotating Machines: Bearings, Pumps,*

Gearboxes, Engines, and Rotating Structures. The Shock and Vibration Digest, 2006. **38**(1): p. 3-16.

97. Shehadeh M F. *Monotoring of long steel pipes using acoustic emission*, PhD thesis. 2006, Heriot-Watt University: Edinburgh, UK.

98. Schofield B H. *Research on the sources and characteristics of acoustic emission.* ASTM STP 505, 1972: p. 11-19.

99. Sikorska J. *The application of acoustic emission monotoring to the detection of flow condition in centrifugal pumps.*, PhD thesis. 2006, University of Western Australia, Perth, Australia.

100. Holroyd, T.J., The Acoustic Emission & Ultrasonic Monotoring Handbook. 2000, Oxford.

101. Boschetto A and Quadrini F. *Powder size measurement by acoustic emission.* Measurement, 2011. **44**(1): p. 290-297.

102. Ivantsiv V, Spelt J K and Papini M. Mass flow rate measurement in abrasive jets using acoustic emission. Measurement Science & Technology, 2009. 20(9) doi:10.1088/0957-0233/20/9/095402

103. Faisal N H A, Reuben R L and Alcock B. *AE monitoring and analysis of HVOF themal spraying process.* Jornal of Thermal Spray Technology, 2011: p. 1-14.

104. Mohan R S, Momber A W and Kovacevic R. *Detection of Energy Absorption during Abrasive Water Jet.* American Society of Mechanical Engineers, ASME, 1995. **3**(1): p. 69-86.

105. Boness R J and McBride S L, *Adhesive and abrasive wear studies using acoustic emission techniques.* Wear, 1991. **149**(1-2): p. 41-53.

106. Matsuoka K, Forrest D and Ming-Kai T, *On-line wear monitoring using acoustic emission.* Wear, 1993. **162-164**(1): p. 605-610.

107. Mechefske C K and Sun G. *Monitoring Sliding Wear using Acoustic Emission. International Congress on Condition Monitoring COMADEM 2001,* Manchester, UK.

108. Nivesrangsan P. *Multi-source, multi-sensor approaches to disel engine monitoring using acoustic emission*, PhD thesis 2004, Heriot Watt University: Edinburgh, UK.

109. Pollock A A. *Classical wave theory in practical AE testing.* Progress in Acoustic Emission III – Japanese Society of Non-Destructive Testing, 1986: p. 708-721.

110. Cochran W, Cooley J, Favin D, Helms H, Kaenel R, Lang W, Maling G, Nelson D, Rader C and Welch P. *What is the fast Fourier transform?* IEEE Transactions on Audio and Electroacoustics, 1967. **15**(2): p. 45-55.

111. Welch P. *The use of fast Fourier transform for the estimation of power spectra: A method based on time averaging over short, modified periodograms.* IEEE Transactions on Audio and Electroacoustics, 1967. **15**(2): p. 70-73.

112. McFadden P D and Smith J D. *Vibration monitoring of rolling element bearings by the high-frequency resonance technique — a review.* Tribology International, 1984. **17**(1): p. 3-10.

113. ASTM standard, *E976-99: Standard guide for determining the reproducibility of acoustic emission sensor response.* Annual Book of ASTM Standards, 1999. **3.03**: p. 395-403.

114. Brucato A, Grisafi F and Montante G. *Particle drag coefficients in turbulent fluids.* Chemical Engineering Science, 1998. **53**(18): p. 3295-3314.

115. Heuer V, Walter G and Hutchings I M. *A study of the erosive wear of fibrous ceramic components by solid particle impact.* Wear, 1999. **225-229**(1): p. 493-501.

Appedix A: AE sensor calibration certificate.

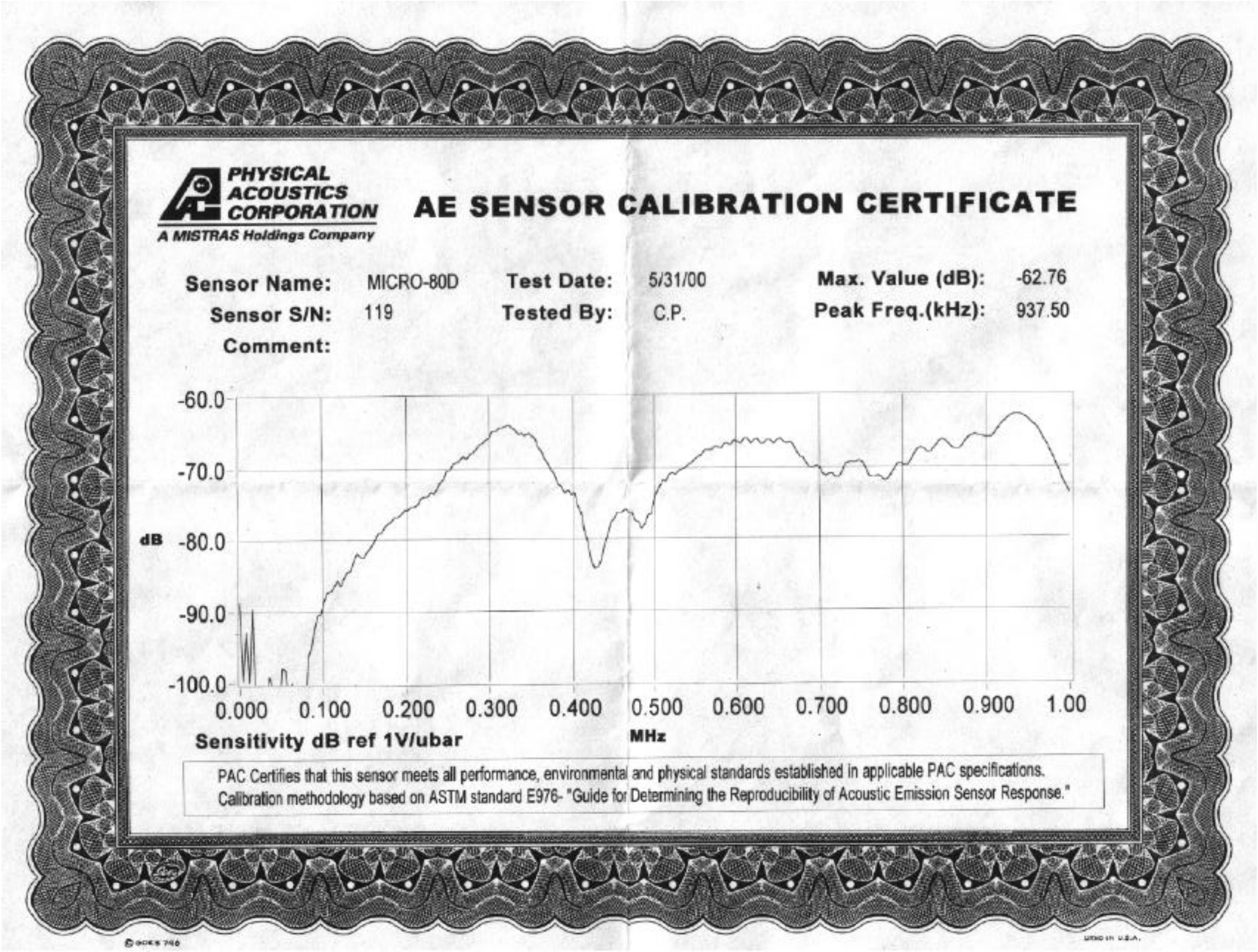

PHYSICAL ACOUSTICS CORPORATION
A MISTRAS Holdings Company

AE SENSOR CALIBRATION CERTIFICATE

Sensor Name:	MICRO-80D	**Test Date:**	5/31/00	**Max. Value (dB):**	-62.76
Sensor S/N:	119	**Tested By:**	C.P.	**Peak Freq.(kHz):**	937.50
Comment:					

PAC Certifies that this sensor meets all performance, environmental and physical standards established in applicable PAC specifications. Calibration methodology based on ASTM standard E976- "Guide for Determining the Reproducibility of Acoustic Emission Sensor Response."